Architectural control of ice-templated collagen scaffolds for cardiac regeneration

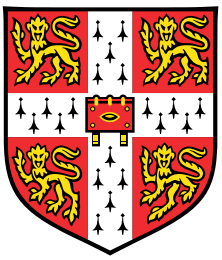

Jamie Cyr

Department of Materials Science and Metallurgy

University of Cambridge

This dissertation is submitted for the degree of

Doctor of Philosophy

Churchill College September 2020

Declaration

I hereby declare that except where specific reference is made to the work of others, the contents of this dissertation are original and have not been submitted in whole or in part for consideration for any other degree or qualification in this, or any other university. This dissertation is my own work and contains nothing which is the outcome of work done in collaboration with others, except as specified in the text and Acknowledgements. This dissertation contains fewer than 65,000 words including appendices, bibliography, footnotes, tables and equations and has fewer than 150 figures.

Jamie Cyr

September 2020

Abstract

Architectural control of ice-templated collagen scaffolds for cardiac regeneration

Jamie Cyr

A range of biomaterials and fabrication methods have been explored to produce biomimetic scaffolds to facilitate cardiac tissue regeneration. Ice-templated collagen scaffolds have demonstrated translational success in other clinical applications. The ice templating technique utilizes phase separation dynamics during solidification and subsequent sublimation of ice to produce scaffolds with interconnected porosity. Although composition has been found to be key to determining cellular response, both nano-scale and micro-scale surface features of ice templated collagen scaffolds have also been found to encourage cellular ingrowth and attachment. Previous research has introduced techniques to control pore size and anisotropy. To date, however, ice-templating has not been shown to allow control of architecture to the extent that it is possible to replicate the structure of more complex tissue morphologies such as the myocardium.

In this thesis, the underpinning physics of ice formation is leveraged to determine the final architecture of ice-templated collagen scaffolds. A controllable directional freezing apparatus was designed and built to enable fine control of the thermal environment during solidification. A relationship between the set thermal parameters and final pore architecture was established. This relationship enabled the production of structures with controlled pore alignment and size. The direct control and monitoring capabilities of the freezing apparatus enabled observations of intrinsic freezing kinetics. This insight allowed the solidification processes of anisotropic and isotropic ice-templating to be compared, and a link between the previously distinct fields was hypothesized.

A novel thermal control technique was developed that dictated ice growth directions and achieved complex lamellar orientation of ice-templated collagen scaffolds. A new mould

design was produced, with a heat-sink at the base and heat sources in the mould walls, which afforded three-dimensional thermal control during the solidification process. Ultimately, this created complex lamellar orientation of ice-templated collagen scaffolds. The technique is presented alongside a finite element model, developed as a predictive tool for the design of final lamellar orientation. Heat source moulds were used to introduce controlled thermal gradients during the solidification phase of the ice-templating process. Various heat source profiles were implemented and simulated. It was found that by introducing controlled complex thermal gradients during solidification, scaffolds with multidirectional pore orientations were produced, and the finite element simulation was found to accurately predict lamellar orientation. Taken together, the model and heat source freezing technique provide the opportunity for design and production of regenerative collagen scaffolds with tailored architectural morphologies.

After establishing a control protocol for producing structures with tailored local lamellar architecture, patches were tested by observing the effects of scaffold architecture on cellular behaviour and mechanical conformation to the dynamic movements of the heart. Cardiomyocytes (H9 hESCs) were seeded onto scaffolds with aligned and isotropic pore structures and the cell signalling patterns were then compared. It was determined that the biomimetic accuracy of the aligned scaffold improved the uniformity of calcium signalling in cardiomyocytes when compared with those on isotropic structures. These results indicate that myocardial function is enhanced by defined scaffold orientation.

The application of an *ex vivo* ovine cardiac perfusion model enabled direct observation of the native myocardial movement during the cardiac cycle. Through direct optical imaging and digital image correlation, collagen scaffolds were tested to assess their response to native myocardial deformation patterns. The strain dynamics of aligned and isotropic scaffold architectures were compared, and the efficacy of both glue and suture fixation methods were explored. It was determined that aligned scaffolds adhered with suture fixation complied with the native physio-mechanical environment. Similarly adhered isotropic scaffolds and patches adhered with glue, however, resulted in reduced deformation relative to the native myocardium.

The work in this thesis has established a novel freeze casting technique to afford specific three dimensional control of collagen scaffold alignment. The resulting scaffolds with directionally aligned pore architectures were found to enhance cellular and mechanical dynamics to better replicate the native behaviour of myocardial tissue.

Acknowledgements

I would particularly like to thank my supervisors, Professors Ruth Cameron and Serena Best, for their invaluable support, guidance and advice throughout this journey. They have created a fun and cohesive research environment within the Cambridge Center for Medical Materials group. I would additionally like to thank my fellow group members; Sheen, Rob, Matt and Tricia for always keeping me on my toes; Anke, Clare and Dan, for key advice and mentorship; Dave for patiently correcting my terrible spelling, and the rest of the group for both good advice and good company. Elsewhere in the department there have been a number of people who have helped make this project possible, particularly Wayne Skelton-Hough in the CCMM lab, Giovani Orlando, Simon Pipe and all of the workshop personnel who were always up for the challenge when I needed to design new equipment. Additionally, I would also like to thank Dr. Rob Thompson and Julia P*ü*rstle for the crash courses in strain tensors and digital image correlation, and for their constant willingness to answer my questions.

I gratefully acknowledge the financial support of the Gates Cambridge Foundation and The Jean Fine Spahr Fellowship for making my expedition to study at Cambridge not only a possibility, but a reality.

I would like to give ample credit and extend my sincerest gratitude to my collaborators, Dr. Maria Colzani and Dr. Clare Burdett, without whom much of this project would not have been possible. Dr. Maria Colzani, from the MRC Cambridge Stem Cell Institute, introduced me to numerous cell culture techniques and served as both a mentor and contributor for the cell studies presented in this thesis. Dr. Clare Burdett, shared her *ex vivo* cardiac model and acted as both a mentor and teacher for the *ex vivo* experiments in this thesis.

Outside of the lab there are a number of people and clubs to thank, all of whom positively contributed to my sanity throughout this adventure. The Gates Cambridge scholars community welcomed me to Cambridge with a bang and I am grateful to have been a part of such

a vibrant community composed of inspiring individuals. Particularly, I must thank Elyse for teaching me about every board game known to man and for all our adventures running along the river path. I would also like to thank the Gordon lab members for all the punting, barbecues and, of course, the classy evenings in spoons. Joe also deserves acknowledgment for bravely reading this whole thesis and patiently editing out every American 'z'. Finally, the amazing women on the CUAFC team have been a huge source of support and inspiration throughout this journey. A special thanks to my fellow Austrian, Connie, who was right there with me all the way from football trials to PhD submission.

Sam should get his own paragraph for his unwavering support and advice as I stumbled my way through these studies. He also gets extra points for patience in the final few months where pressure was at its highest and we were quite literally locked in together. I am really not sure I would have survived this process without his help. I am not kidding; it is likely that I would have starved.

Finally, and perhaps most importantly I need to thank my family. They have always demonstrated tremendous work ethics and perseverance, and challenged me to always seek out new adventures. I attribute all my achievements to the support and encouragement that they have provided over the last 26 years.

Table of contents

List of figures

List of tables

Chapter 1

Introduction

A clinical need exists for regenerative scaffolds to facilitate the repair of injured or diseased tissues and organs. In particular, heart disease is the leading cause of death in both industrialised nations and the developing world, accounting for approximately 31% of deaths worldwide according to the World Health Organisation [1]. Acute myocardial infarction results in a weakening of the collagen extracellular matrix (ECM) of the ventricular wall. Impairment to the myocardial wall is permanent, thus therapeutic options are limited and, in acute cases, the only treatment for congestive heart failure is a full cardiac transplant. Limitations in donor organ availability has motivated research into new strategies to repair the tissue damaged by cardiac infarction.

Three overarching aims have been identified for tissue repair materials, which are to provide: (*i*) an environment that enables targeted cellular migration, proliferation and differentiation; (*ii*) a high degree of permeability for efficient nutrient/cellular waste transport; and (*iii*) chemical and mechanical signalling that dictates de novo tissue formation and host remodelling [2, 3]. The field relies extensively on the production of porous 3D scaffolds which can be implanted to provide the appropriate environment for the regeneration of tissues and organs [4]. The regenerative scaffold should have properties similar to those of the native tissue as it

has been shown that the scaffold architecture dictates the final structure of the regenerated tissue [5, 6]. There is, therefore, a growing interest in the production of biomimetic scaffolds that facilitate the regeneration of tissues that are structurally consistent with the surrounding tissue.

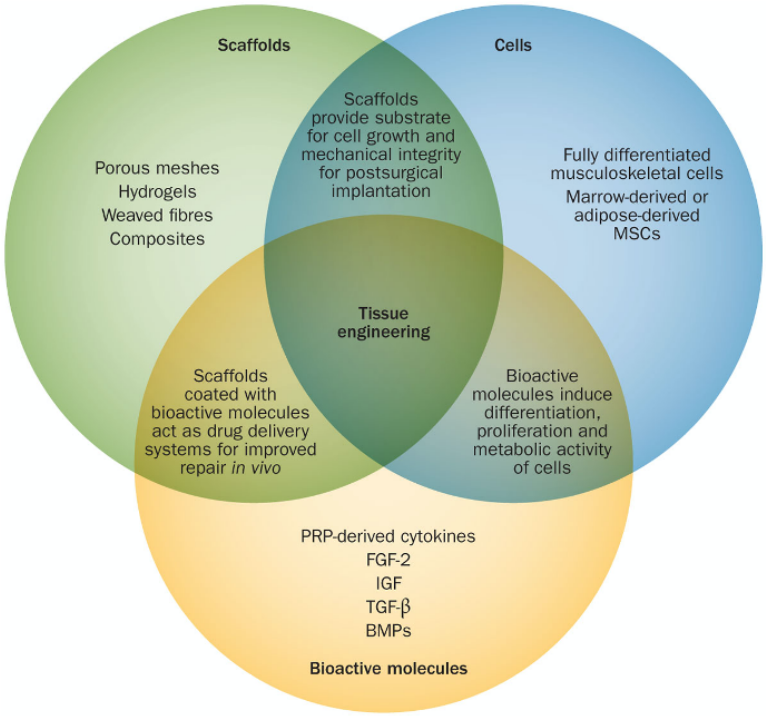

Fig. 1.1 Tissue engineering triad [7]

When applied to damaged tissue, a scaffold can support cellular in-growth and allow the healing process to proceed [8]. Ideally, the scaffold is resorbed in parallel with the healing process, such that, upon completion of regeneration, only native tissue remains [9]. Natural tissue consists of three primary components: cells, ECM, and signalling molecules. These components have been identified within the literature as the tissue engineering triad and are summarised in Figure 1.1 [4, 7, 10]. In essence, tissue regeneration constructs are designed to imitate this composition and encourage functional tissue repair.

Many tissues which would benefit from scaffold-facilitated regeneration are biomechanically complex [11]. Examples include interfacial tissue, such as the osteochondral interface in articulating joints, or muscular organs, such as the heart, which require several essential structures to restore function [12–17]. High levels of complexity in the tissues or organs targeted for repair necessitate fabrication methods that provide specific control over regenerative scaffold architecture. Many fabrication techniques have been developed to enable the fabrication of 3D scaffolds with interconnected porosity, ranging from particulate leaching techniques to electrospinning methods [18, 19]. Traditional methods for scaffold fabrication can enable the introduction of interconnected pores with tunable pore sizes and varying degrees of anisotropy. Control of complex pore architecture, however, has been a challenge [20].

The materials used for scaffold fabrication can be designed to optimise tissue engineered construct efficacy in clinical settings. Biomaterial properties dictate cellular interaction and adhesion, ECM secretion, re-vascularisation, and paracrine processes within an engineered construct [21]. Collagen is a natural biomaterial and serves as the main structural component of the native ECM. The material has an inherently diverse range of binding motifs that encourage cellular attachment and migration, as well as enabling further functionalisation with therapeutics and growth factors [22]. The ice-templating technique can be used to fabricate scaffolds from a wide range of materials. The use of a natural polymer in particular type 1 insoluble collagen has, however, demonstrated translational success for the regeneration of skin, nerve, and osteochondrial tissue [23]. The ChondroMimetic regenerative scaffold, for example, was used clinically to repair damaged cartilage in the knee [24].

Ice-templated scaffold fabrication is being explored for applications in a wide range of biomedical industries for the repair and reconstruction of skeletal tissues and organs [15, 24–27]. The ice-templating technique utilises the natural physics of ice formation to produce

porous interconnected scaffolds with a variety of pore sizes and morphologies [6, 28–30]. During the ice-templating process, an aqueous suspension is frozen. Due to the low solubility of impurities in ice, undissolved particles are pushed to the periphery of ice crystals during solidification. The resulting solid is a network of interconnected ice crystals encapsulated by the scaffold material. Thus, when the ice is removed via sublimation the final structure is an exact negative of the ice crystal network [31]. It has been shown that by understanding and controlling the ice formation during the solidification phase the final scaffold architecture can be controlled [32]. Variations in both the set freezing parameters and chemical or physical additives can enable final architectural features at multiple length scales to be tailored. Control over features such as pore size, interconnectivity, surface roughness and structural anisotropy can be achieved. Specific control of complex long-range pore organisation has not yet been reported.

The work in this thesis is predominantly focused on the design and fabrication of scaffolds for the repair of cardiac tissue, although much of the work is applicable to other complex tissue types. The development of an efficacious tissue engineered therapeutic patch that can facilitate regeneration of damaged myocardium and prevent end-stage heart failure is required [33, 34]. Reported outcomes of the use of cardiac patches have been modest but promising, but the clinical application of these techniques has been limited by a lack of vascularisation, immunogenicity, poor control of patch structure, and lack of appropriate physio-mechanical cues to promote cardiogenesis [10, 15, 35]. The specific and complex structural requirements for tissue functionality have made the engineering of functional regenerative cardiac tissue a challenge [21].

In this thesis, the design properties of type I collagen scaffolds for potential use in cardiac tissue repair are described. The literature review contextualises the longitudinal approach

taken in this work from architectural control of regenerative cardiac scaffolds through fundamental physical processes to the translational assessment of patch performance. Background information about collagen and its role in the intricate extracellular matrix of the myocardium is presented. The pathological structural degradation due to myocardial infarction is examined and the historical development of a therapeutic patch to structure cardiac regeneration is reviewed. Recent improvements in the understanding of the functional importance of extracellular structure on patch performance has increased the demand for fabrication methods that enable control of scaffold structure at multiple length scales. The ice-templating technique and its governing physical processes are presented at the end of the review as a possible avenue for tailored scaffold production. The culmination of the literature review with underpinning physics of ice-templating frames the work presented in Chapters 4 and 5.

Chapters 4 and 5 of this thesis explore the control techniques for anisotropic freeze-cast collagen scaffolds. The underlying ice physics is utilised to understand and manipulate the process of solidification and ultimately control the final scaffold architecture. In Chapter 4 the relationship between set freezing parameters and pore size, alignment, and uniformity within the final scaffold is explored. Subsequently, in Chapter 5 the fundamental physical processes are leveraged to develop a novel fabrication method that enables local and specific macro-architectural order, while maintaining the multi-scale features characteristic of the ice-templating technique. The fabrication technique is presented alongside a predictive finite element model that enables bespoke design of complex architectures with long range pore organization.

Enhanced control over complex pore orientations is particularly advantageous for the development of engineered cardiac tissue. Highly ordered structure in cardiac tissue constructs has been found to enable increased physiological behaviour in vitro, enhancing the relevance of

model systems for disease development and/or drug delivery. In the context of a therapeutic patch, biomimetic cellular organisation could enhance the integrative and functional capacity of regenerative scaffolds and direct the deposition of regenerated ECM. Chapters 6 and 7 of this thesis, explore the influence of anisotropy on regenerative cardiac constructs. In Chapter 6 the functional signalling and contractile capacities of cardiac constructs structured by pseudo-isotropic and aligned collagen scaffolds is directly compared at multiple length scales. Functional differences are highlighted at both a cellular and tissue level. In Chapter 7 an *ex vivo* cardiac model is used to evaluate the mechanical conformance to dynamic native myocardial deformations for different scaffold architectures. This work will help inform the design of regenerative cardiac constructs for applications both *in vitro* and in a translational capacity.

The aim of this work is to 1) develop ice templating techniques that afford improved architectural control over freeze cast collagen scaffolds; 2) Introduce a predictive quantitative model that can be leveraged to tailor scaffold architecture to better mimic native tissue structure; and 3) to test the hypothesis that cardiac regeneration, both from a cellular and physiomechanical perspective, will be improved by biomimetic architecture when compared to conventional isotropic structures.

Chapter 2

Literature Review

2.1 Collagen as a biomaterial

Collagen is the most abundant protein in the human body as it is the main structural component in the native extracellular matrix [36]. Collagen, a triple helical protein it, is composed of three polypeptide chains with at least one region of a repeated amino acid sequence $(\text{Gly–XY})_n$ where the X position is frequently proline and the Y position is often hydroxyproline [22, 37–39]. To date, 30 different collagen types have been identified [40]. Collagens are classified by their chemical structure and present in specific ratios within native tissue to dictate tissue specific physio-mechanical environments [38, 41].

2.1.1 Collagen structure

There are two main subfamilies of collagen namely fibrillar and nonfibrillar. These structural classifications are based on molecular packing and ultrastructure. Nonfibrillar collagens serve many purposes including, but not limited to, network formation, membrane formation, and membrane association [37, 40]. Collagen VII, for example, forms a hexagonal network in

Descemet's membrane while collagen VI forms a beaded filament that anchors the membrane of skeletal muscle cells to the extracellular matrix [40]. Another subclass of nonfibrillar collagens are the Fibril-Associated Collagens (FACIT) that associate with the surface of collagen fibrils and are believed to have a regulatory role on fibre dimensions and interactions [39, 40].

Fibrillar collagens are among the most abundant proteins in nature as they are the main functional support material of almost all connective tissue. The primary function of most fibrillar collagens is to provide three dimensional frameworks that confer mechanical strength, as well as signalling and organising functions for tissues and organs. The most common fibrillar collagens are types I, II,and III collagens. They contain long, uninterrupted $(\text{Gly–XY–})_n$ sequences and associate into a long triple helix known as a collagen monomer. Monomer formation is summarised in Figure 2.1a. in some tissues the monomers are associated into highly ordered fibrils. Lateral grouping of these fibrils results in thick fibres as described in Figure 2.1b [37, 38]. Most collagen fibrils in mature tissue are composed of several collagen types and are termed heterotypic. For example, cartilage contains fibrils of types II, XI, and IX or of types II and III, and skin is comprised of heterotypic fibrils of type I and III. The composition of collagen ECM changes with tissue type to dictate specific structure [38].

2.1.2 Collagen in the body

Collagen composition and orientation varies from tissue to tissue. Type I collagen fibrils are present in ligaments and tendons with traces of types III and V, and organised in parallel bundles of thick fibres for directional tensile strength. Conversely, in skin, fibrils are randomly oriented in the plane of the skin [38]. Type II collagen, in cartilage, forms thin fibrils that trap highly charged proteoglycans and water for resilience during compressive loading.

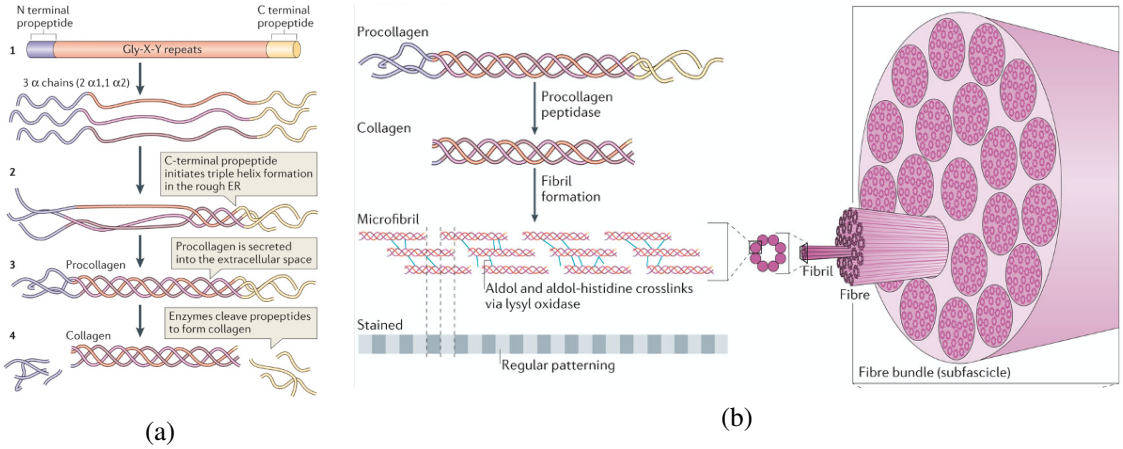

(a) (b)

Fig. 2.1 Fibrillar Collagen **(a)** Collagen monomer formation: 1) A standard fibrillar collagen molecule 2) Formation of the central triple helical structure of procollagen and collagen. 3) Procollagen is secreted into the extracellular space. 4) Procollagen is converted into collagen via cleavage of the N- and C-propeptides **(b)** Collagen fibre formation, collagen is assembled into cross-striated microfibrils that merge into mature fibrils, further bundling occurs to form fibres stabilized by FACIT collagens [37]

The collagen matrix in the myocardium consists mainly of types I and III collagens; type I collagen mainly provides rigidity, whereas type III collagen contributes to elasticity [41, 42].

Within the heart collagen molecules serve several functions. The primary function of which is that of supporting the muscle cells and blood vessels. Collagens also act as lateral connections between cells and muscle bundles to govern architecture and coordinate force. Furthermore, the respective tensile strength and resilience of myocardial collagens are important determinants of myocardial stiffness during both diastole and systole and serve to resist myocardial deformation, maintain shape and wall thickness and prevent ventricular aneurysm and rupture [41].

2.2 Characterisation of native structure and dynamics of the heart

2.2.1 Native myocardial structure

The myocardium has a complex 3D architecture comprising a cellular component supported by an intricate extracellular matrix that both contribute to the optimised contractile function of the heart [16]. Within the myocardium the most prevalent cell type is the cardiomyocyte, accounting for up to 30% of the total cellular population. Additional cell types include endothelial cells (ECs), pericytes, fibroblasts, and resident immune cells such as macrophage, B-cells, and T-cells [43, 44]. The cardiomyocytes serve as the fundamental contractile element of the tissue, individually shortening by $\sim$15% and thicken by only $\sim$8% during systole [16, 45]. However, myocyte contraction alone does not account for the functional ventricular contraction. Contraction of the left ventricle has been found to entail both longitudinal and circumferential shortening of between 10% to 25%, as well as greater than 35% thickening of the myocardium [16, 45]. These macro-functional dynamics are facilitated by the complex architecture of the ECM that imposes long range cellular order and directs electrical signalling propagation [44]. The ordered cellular structure of the myocardium is summarised in Figure 2.2.

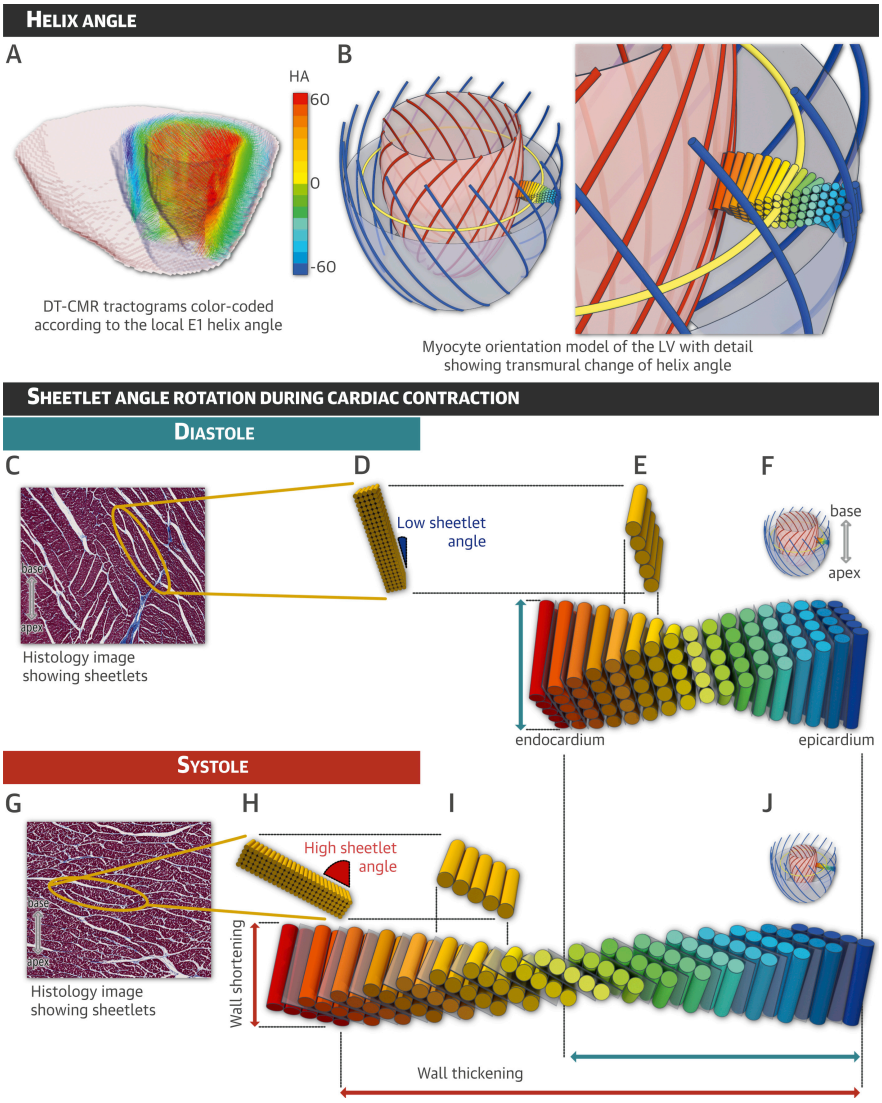

Fig. 2.2 Cardiac muscle organization **(A)** Multi-slice tractogram depicts the primary diffusion eigenvector (E1) direction color-coded according to the helix angle (HA) **(B)** Schematic diagram of the helical structure of cardiomyocytes with zoom. **(C-J)** Sheetlet angle (SA) rotation during cardiac contraction is depicted during **(C-F)** diastole and **(G-J)** systole with myocardial sheetlet microstructures shown in **(C)** relaxed and **(G)** contracted ex-vivo heart samples, a yellow ellipse surrounds a single sheetlet composed of closely packed cardiomyocytes (purple) bounded by shear layers (white). The sheetlet angle is defined as the angle between the sheetlet and the local epicardial left ventricular (LV) wall. Here, SA varied from a low value (SA $\sim 15^o$) in **(D)** diastole to a high value (SA $\sim 60^o$) in **(H)** systole. The colour coding indicates sheetlet orientation: blue is left handed epicardial helix; yellow is the mid-myocardium circumferential alignments; red is the right-handed endocardial helix; grey is the intervening cracks or shear layers. Data was collected with DT-CMR ¼ diffusion tensor cardiac magnetic resonance [16]

The heart wall is composed of a highly ordered ECM that contains three layers: the outermost epicardium, the myocardium, and the innermost endocardium [44]. Specifically, the microstructure of the left ventricular wall consists of cardiomyocytes embedded in a predominantly collagen matrix that forms anisotropic sheets of myocardial syncytia [46–50]. Figure 2.2 illustrates the orientation of the syncytium which has been found to vary smoothly as a function of tissue depth. The left-handed helical alignment that dominates the epicardial layer is shown in blue, the circumferential alignment observed in the myocardial layer is yellow, and the primarily longitudinal alignment of the endocardium is illustrated in red [51–53]. This highly ordered structure facilitates directional contraction and a twisting of the apex relative to the base during contraction; a function that optimises cardiac output [45]. The helical arrangement alone is, however, insufficient to explain the magnitude of ventricular wall thickening during systole [45]. A secondary organisation of cardiomyocytes consisting of laminar microstructures, 5 to 10 cardiomyocytes thick, termed sheetlets has been identified [54, 55]. The reorientation of these sheetlets during contraction has been proposed as the predominant mechanism to explain macroscopic wall thickening [16, 56, 57]. The directionally contractile behaviour of the myocardium facilitated by its complex extracellular architecture results in asymmetric deformation of the tissue during contraction [46–50].

In recent years new technologies have been developed to measure the *in vivo* deformation of the myocardium. For example, strain mapping has emerged as a clinical diagnostic and characterisation technique. Non-invasive imaging techniques can be used to perform cardiac strain imaging (CSI) such as ultrasound speckle-tracking echocardiography (STE), cardiac magnetic resonance image (cMRI) feature tracking, cMRI tissue tagging, and cardiac computed tomography (CCT) [58–60]. STE is the most popular technique because of its relatively simple implementation and clinical availability [58, 61]. The assessment of left ventricular longitudinal strain through STE and cMRI has been shown to predict significant coronary

heart disease, illuminate hypertrophy in systolic ventricular function, indicate risk of diabetic cardiomyopathy and highlight the site of infarction as shown in Figure 2.3a [59, 62, 63]. These methods typically involves capturing and processing planar cross-sectional views of the heart, meaning the deformation across the surface of the myocardium is not characterised. Soltani et al. 2018 [46], characterised the strains across the superficial epicardium of the right ventricle during open heart surgery. Direct optical imaging and speckle pattern tracking was used to perform full-field measurements of native myocardial principal strains, as shown in Figure 2.3b. A directional contraction was observed such the principal strains occurred concurrently in opposing directions with unequal magnitudes. In this study, strain was measured with reference to the contracted state and, therefore, the dominant strain was found to be in the positive direction as shown in Figure 2.3b. These measurements provided new insight into the biomechanics of the heart. The open heart surgery model, however, has a limited field of view and is not applicable to test myocardial reaction to novel pharmaceuticals or tissue engineered scaffolds. An improved understanding of native deformation, however, informs the design and production of biomimetic bioreactors that aid in cell development *in vitro* [11, 64–68]. Furthermore, strain analysis techniques can be utilised in characterising deformation and contractility regenerative tissue for comparison with native characteristics [69].

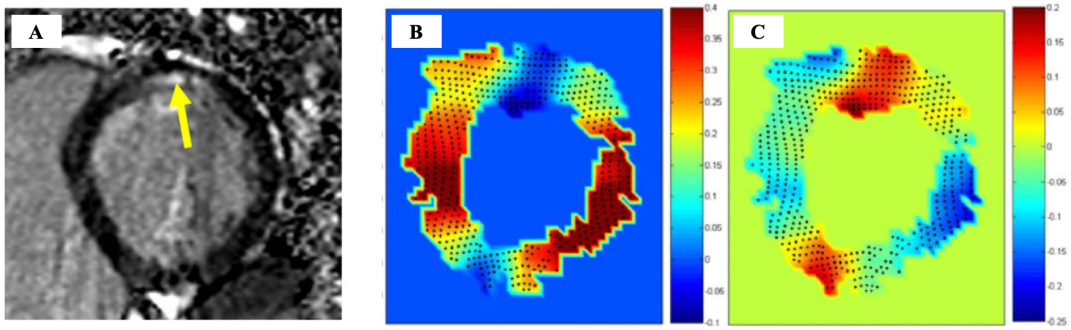

(a)

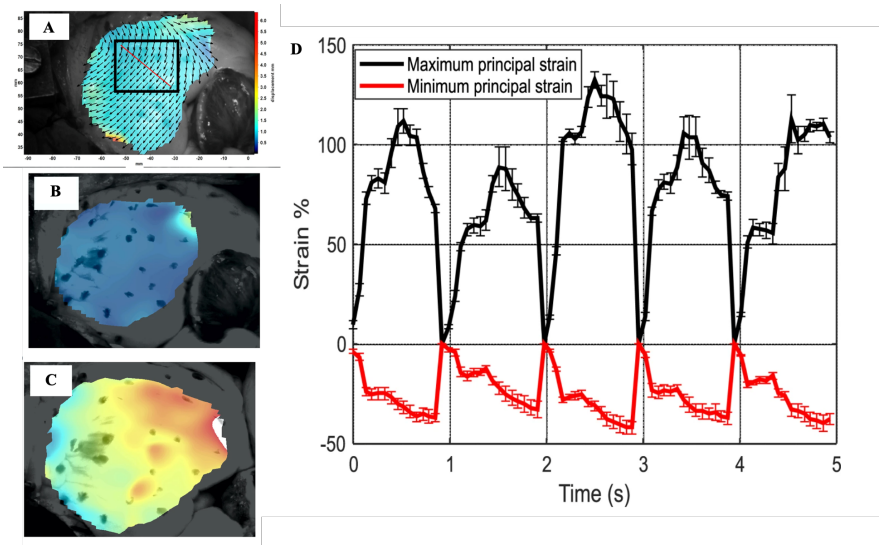

(b)

Fig. 2.3 **(a)** Three-dimensional (3D) Lagrangian strain map of the left ventricle with a myocardial infarction collected through cMRI data. **A** shows the myocardial infarction region at the subendocardium of the basal-posterior part of the heart (yellow arrow) **-C** shows the calculated strains from echocardiogram data. **B** radial and **C** longitudinal strains show a clear strain difference between the infarcted area and its neighbouring regions [59]. **(b)** Surface deformation strains collected through direct optical imaging **A** Original image from the heart overlain with displacement vectors and the vector length indicated by the colors. The black rectangle indicates where the average of the vector components, strain rate, principal strains, and tissue velocity were obtained from, and the red line shows the direction and length of the virtual extensometer used for extracting the data for fractional shortening **B** Displacement color heat maps for early systole stage **C** Displacement colour heat maps for end diastole stage **D** Average maximum and minimum principal strains obtained from the DIC analysis and the standard deviation error bars for each point [46]

The dynamics of the myocardium can also be visualised *in vivo* through Ca^{2+} transients and transmural gradients in membrane potential [25, 70–73]. Recently new technological developments have enabled the study of transmembrane potential, calcium transience and conduction velocity distributions across the width of the myocardium [72, 73]. Wen et al. 2018 used optical mapping to characterise dynamic electrophysiological behaviours in thin transverse slices of murine hearts treated with Ca^{2+} sensitive dye Rhod-2 and voltage sensitive dye RH237 [72]. It was shown that for both membrane potential and calcium signalling there was a significant signal duration gradient across the myocardial wall. Reduced signal durations were observed in the epicardium when compared with the endocardium. It was further found that through activation mapping of the thin transverse slices, arrhythmic behaviour could be identified in the epicardium and the endocardium [72]. A similar approach has been taken in the assessment of signalling capabilities of engineered tissues through optical imaging of Ca^{2+} florescence and wave form analysis [25, 70, 71]. Taken together recent developments of optical imaging techniques using both strain and electrophysiologic signalling have help to elucidate the complex dynamics of the native myocardium.

2.2.2 Myocardial infarct, the structural and functional effects

An acute myocardial infarction results in a weakening of the ECM within the ventricular wall which, in turn, results in chronic wall lengthening, thinning, and overall ventricular dilatation as shown in Figure 2.4 [10, 74–76]. Degradation of the myocardial wall is permanent due to the diminished regenerative capacity of adult cardiomyocytes, and the limited population of progenitor cells [3, 10, 77–80]. This ischemic damage causes the loss of cardiomyocytes (CMs) and the formation of fibrotic scar tissue that interferes with mechanical and electrical signal propagation leading to arrhythmia and subsequent heart failure [81].

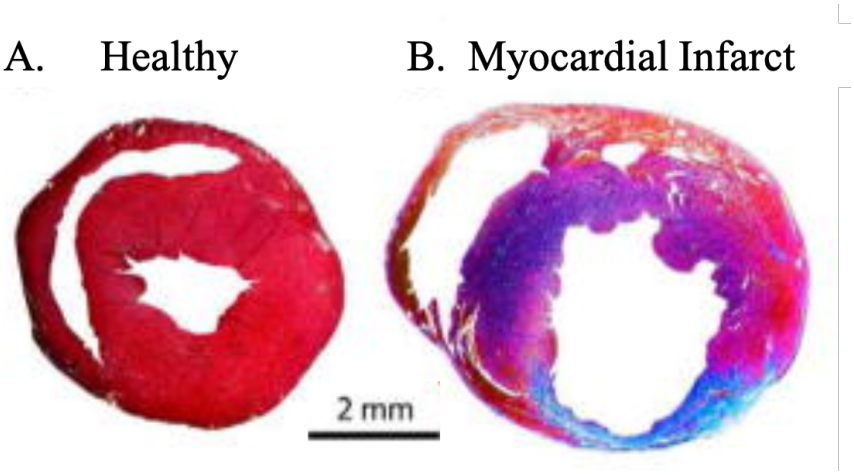

Fig. 2.4 Cardiac cross section of an **A** healthy and **B** myocardial infracted adult murine heart four weeks post injury stained with Masson's trichrome (TC, to label muscle fibers in red, collagen in blue, cytoplasm in pink, and nuclei in dark brown) [3]

Currently, therapeutic interventions, such as blood thinners, balloon angioplasty/stenting, and bypass grafting to restore coronary vascularisation, are ineffective in restoring function of ischemia-induced damages to the myocardium [44]. The only treatment option for end-stage heart failure is a full cardiac transplant. Limitations in donor organ availability and immunogenicity have motivated research into alternative therapies that can regenerate the damaged myocardium and prevent organ failure [10, 44, 82].

Direct cell delivery and the application of regenerative tissue constructs are two potential therapeutic interventions for cardiac regeneration [44]. Clinically, it has been demonstrated that intramyocardial injection or intravascular infusion of contractile cells such as myoblasts, or cardiomyocytes, and of non-contractile cells such as smooth muscle cells or human mesenchymal stem cells, can attenuate further damage to the myocardium and reduce the risk of heart failure [10, 83–85]. The efficacy of these cell delivery-based therapies is limited by low cell survival and engraftment rates as well as high incidence of anoikis or washout at the site of injury [86]. Data obtained from several studies have shown that cells delivered as a part of an engineered tissue construct can significantly enhance the cell survival and engraftment rate compared with direct cell delivery therapies [10, 87–91].

2.3 Tissue engineering for cardiac regeneration

Tissue repair constructs are being developed for a wide range of *in vivo* and *in vitro* applications [4, 35, 70, 92–95]. *In vitro*, cardiac micro tissues, organoids or organ on a chip systems enable a more complete understanding of disease development and drug efficacy [4, 96, 97]. Additionally, *in vitro* systems can be utilised for cell based therapies or biomedical studies on functional cell differentiation, environment cell interaction, cancer cell biology and drug delivery methodology [4, 98–101]. *In vivo*, engineered cardiac tissue, applied as a regenerative patch, has been shown to facilitate regeneration of native tissue after injury [3, 44, 82, 102, 103]. The efficacy of these model and regenerative systems has been limited by the capacity of engineered tissue to recapitulate the inter and intra cellular dynamics of the native myocardium.

The complex form and function of myocardial tissue has made the development of biomimetic engineered tissue for cardiac applications a unique challenge. It is now widely accepted that the mechanical, and architectural properties of tissue influence the intra-cellular and extra-cellular behaviour as well as cell-substrate interactions that ultimately dictate cellular adherence, phenotype and function [11, 67, 104–106]. For *in vivo* systems, biomimetic properties are integral as construct-host interactions can dictate the efficacy of engineered tissue [11, 44]. Native tissues are exposed to temporal stresses and strains, fluid pressure, fluid flow, and cellular/construct deformation [107–109]. It has been shown that mismatch between scaffold and native matrix properties can cause disruptions in signal propagation and mechanical discrepancies, as well as increased stress on the regenerative tissue due to boundary loading [11, 110]. Informed cardiac tissue design, therefore, requires a comprehensive understanding of the native myocardial architecture and its influence on tissue function to help characterise the diverse array of physical signals that cells may experience in vivo [11].

2.3.1 Engineered cardiac patch as a treatment for myocardial infarct

A promising avenue for cardiac tissue repair is the application of a regenerative patch to support the ventricular wall and template tissue regeneration. Figure 2.5 illustrates the anatomical sites of scaffold application to support the myocardium. Cardiac patch application, such as those illustrated in Figure 2.5, has been shown to encourage ventricular wall thickening, reduce cardiac wall stresses, and improve ventricular function after myocardial infarction [3, 50, 87, 111–113]. Cardiac scaffolds can be fabricated and functionalised through a range of techniques [10]. Each structure is designed to deliver healthy cells to the damaged area, facilitate tissue growth and serve as a template for new matrix deposition [4]. The clinical application of these techniques has been limited by several factors including a lack of control over scaffold structure, low re-vascularisation rates, high immunogenetic responses and insufficient capacity for the engineered construct to facilitate appropriate physio-mechanical cues to promote cardiogenisis [3, 114–116].

Current fabrication techniques

The efficacy of regenerative tissue is largely dependent on its material composition and structural architecture. The scaffold material should enable cellular adherence and proliferation with low immunogenicity [10]. Engineered structures also need to be sufficiently porous to enable nutrient and waste transport [117]. The regenerative scaffold architecture should replicate the native cardiac ECM, both chemically and mechanically to facilitate appropriate intercellular signalling and electromechanical coupling [44]. Finally, regenerative constructs should degrade in parallel with native extracellular repair processes, such that no toxic or immunogenic by-products are formed during resorption [44, 76, 118]. These features are commonly dictated by both chosen material and scaffold manufacture method [4].

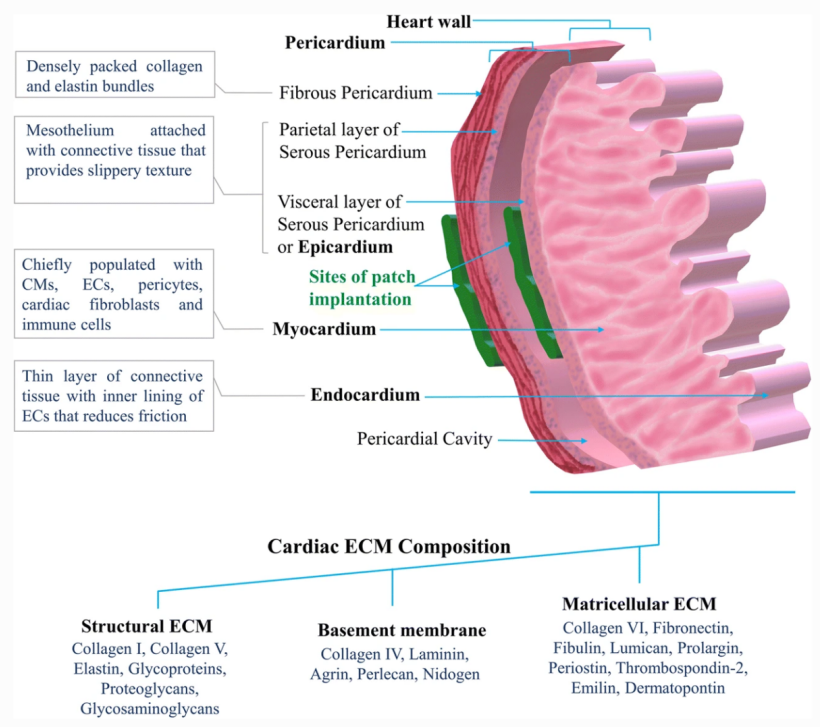

Fig. 2.5 Anatomical diagram of the Cellular and extracellular matrix (ECM) composition of the pericardium and heart wall as well as cardiac patch placement [44]

Scaffolds for cardiac tissue regenerative applications are commonly fabricated from either synthetic polymers or natural polymers [4]. Synthetic polymers such as poly-glycolic acid (PGA), poly-l-lactic acid (PLLA), and poly-lactic-co-glycolic acid (PGL) are also used to produce scaffolds for cardiac repair [119–121]. These materials have been shown to have predictable degradation rates and reproducible chemical and mechanical properties [10, 122–124]. Additionally, synthetic polymers are readily available and easily manipulated. Scaffolds can be fabricated with great precision to reflect the architecture of native tissue [125, 126]. Synthetic polymers, however, are found to induce persistent inflammatory reactions, toxic degradation pathways, and structural incompatibility with host tissue resulting in reduced tissue integration [4, 10, 127].

Natural polymers such as collagen, fibrin and alginate, on the other hand are inherently bioactive and provide a diverse array of binding and signalling motifs across the scaffold surface [10, 82, 118]. Scaffolds constructed from natural materials have, therefore, been shown to promote cellular migration, adhesion, proliferation and differentiation [22, 128, 129]. Natural polymers are often found to be non-toxic and degrade without the formation of harmful by-products and therefore over time allow host cells to produce native extracellular structures to replace the scaffold [4, 10]. The reduced inflammatory response associated with most natural polymers has enabled the clinical application of regenerative structures [24, 130]. Scaffolds composed of natural polymers, however, are challenging to fabricate and their architectures and mechanical properties are difficult to control [4].

Polymers used for cardiac tissue engineering, both natural and synthetic, have been fabricated in either gel form or solid state [10, 131]. Hydrogels are characterised by vast hydrophilic networks of polymer chains, often adopting a three-dimensional conformation due to the cross-linking [44]. Several materials are used in the fabrication of hydrogel scaffolds for cardiac patch engineering, including fibrin, collagen, gelatin, chitosan, Matrigel, and combinations thereof [44]. These materials allow for encapsulation of cells at a high density and can be polymerised around structural frames to form desired sizes and shapes [44, 132–134]. Hydrogels lack a defined architecture to guide cell assembly and therefore, the formation of hierarchical organisation that recapitulates the laminar architecture of the native myocardium is hampered [70, 135, 136]. Solid state tissue engineering in the form of a three-dimensional scaffolds, on the other hand, can provide mechanical cues that guide laminar tissue formation [70, 137–141].

As mentioned previously architectural control of cardiac scaffolds is integral to their downstream regenerative function. Scaffolds should be sufficiently porous to encourage cellular migration and enable efficient nutrient transport across the construct to avoid necrosis of the

core [110, 117, 142–145]. It has been found that pore diameters of $\sim$100 μm are optimal for cardiomyocyte populations. Angiogenesis, however, requires larger pore sizes of $\sim$300 μm to enable vascular development [10, 146–148]. Recently, hierarchical structural order has been identified as a key feature in cardiac scaffold fabrication [35, 50]. It has been shown that anisotropic scaffold structure can direct biomechanical and electrochemical signalling across the construct [35, 70]. Numerous methods for porous scaffold construction have been developed, including solvent casting/particle leaching, gas foaming, electrospinning, rapid prototyping and freeze drying [149]. Each method results in distinct scaffold structures as shown in Figure 2.6 and enables varying degrees of architectural control. While both solvent casting and gas foaming have been shown to result in scaffolds with high porosity, as shown in Figures 2.6 A-C, the control of pore interconnectivity and multi-scale architecture is limited [10, 150]. Electrospinning and freeze-casting techniques facilitate the production of scaffolds with structural features at multiple length scales, as shown in Figure 2.6 D & E. While there has been great progress in recent years, control over long range architectural organisation is still limited [50, 142, 151]. In contrast, rapid prototyping enables excellent long range architectural control, but, the technique is limited by a lack of structural features at the cellular level as shown in Figure 2.6 F [25, 152]. Currently, there is great interest in the development of a fabrication method for cardiac scaffold fabrication that enables architectural control at multiple length scales [152].

Therapeutic effects of regenerative cardiac tissue

In this section, implantation attempts are presented in chronological order to illustrate the development over time of the therapeutic effects of the regenerative cardiac patch. The regenerative efficacy of engineered cardiac tissue has been continuously improving over the past two decades. Kelley et al.1999 first demonstrated that the application of a poly(propylene)

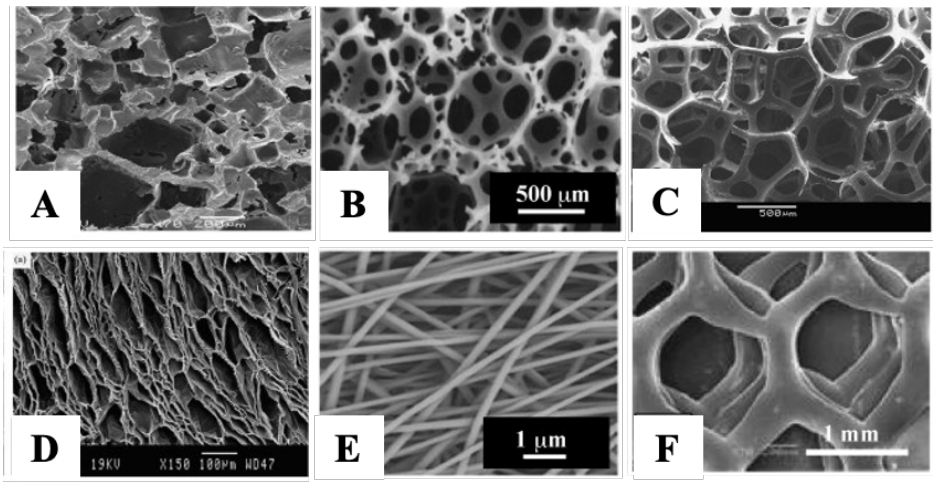

Fig. 2.6 Typical porous structures produced by different scaffolding techniques. (A) salt/sugar particle leaching (PLA); (B) paraffin template (paraffin microsphere leaching (PLA) [250]; (C) chemical reactant gas foaming (polyurethane); (D) thermally induced phase separation (TIPS)/freeze drying (PLA); (E) electrospinning (PCL); (F) 3D Printing (PLGA); [10]

(Marlex) mesh around the heart after infarct, acting to inhibit left ventricular dilation, preserved the ventricle geometry and function in an ovine model [153]. A year later, Leor et al. 2000 seeded foetal rat myocardial cells onto isotropic freeze dried alginate scaffolds and implanted the constructs into rat hearts affected by myocardial infarct. It was found that, after nine weeks, the addition of cells encouraged neovascularisation and host integration [154].

In the same year, Zimmerman et al. 2000 presented a technique to produce spontaneously and coherently beating 3-dimensional engineered heart tissue by seeding neonatal rat cardiomyocytes onto a ring shaped collagen hydrogel [155]. These scaffolds were later fitted around rat hearts after myocardial infarction [156]. It was found that after 14 days of implantation the engineered tissue was heavily vascularised, and after 28 days electrical coupling had occurred between the graft and the host. Additionally, the engineered tissue was found to prevent further ventricular dilation and induce systolic wall thickening of infarcted myocardial segments [103]. In 2008, cardiac patch efficacy was tested clinically in the Myocardial Assistance by Grafting a New Bioartificial Upgraded Myocardium (MAGNUM) phase I

clinical trial, where isotropic collagen patches seeded with bone marrow cells were sutured into ten patients with postischemic left ventricular scarring. Results showed that patients treated with the patch had increased left ventricular wall thickening by 33%, reduced cardiac wall stresses, and improved diastolic function [157]. These early results were promising. Chronic limitations, however, such as low cell density, survival and construct contractile force compounded with high inflammatory responses, prevented clinical application.

Holladay et al 2012 introduced several growth factors to isotropic freeze dried collagen type I scaffolds seeded with mesenchymal stem cells to promote cell maturity, survival and reduce the inflammatory response. The constructs were adhered to rat hearts with induced myocardial infarcts. The functionalised collagen scaffolds reduced inflammatory response, increased infarct wall thickness, and increased the left ventricular ejection fraction as shown in Figure 2.7a [158]. While these results seem encouraging no significant changes were observed in infarct size. This lack of correlation between functional improvement and infarct size was also observed in many other studies that predated the efforts of Holladay et al 2012 [159–162]. In 2015 Menasche et al. published the first clinical case report in which human embryonic stem cells were amplified and cardiac-committed prior to seeding onto an isotropic fibrin scaffold in order to improve patch function. The scaffold was implanted into a 68-year-old patient suffering from severe heart failure. After 3 months, improved left ventricular ejection fraction was observed without further complications such as arrhythmia, tumor formation, or immunosuppression related adversities [33]. The outcomes of these studies, and others demonstrating the use of cardiac patch application to improve ventricular function after injury, have been modest but promising [3, 50, 87, 111, 113]. Extensive clinical application of these techniques has been limited. Reported shortcomings include vascularisation, immunogenicity, poor control of patch structure, and lack of appropriate physio-mechanical cues to promote cardiogenisis [3, 114–116, 118]

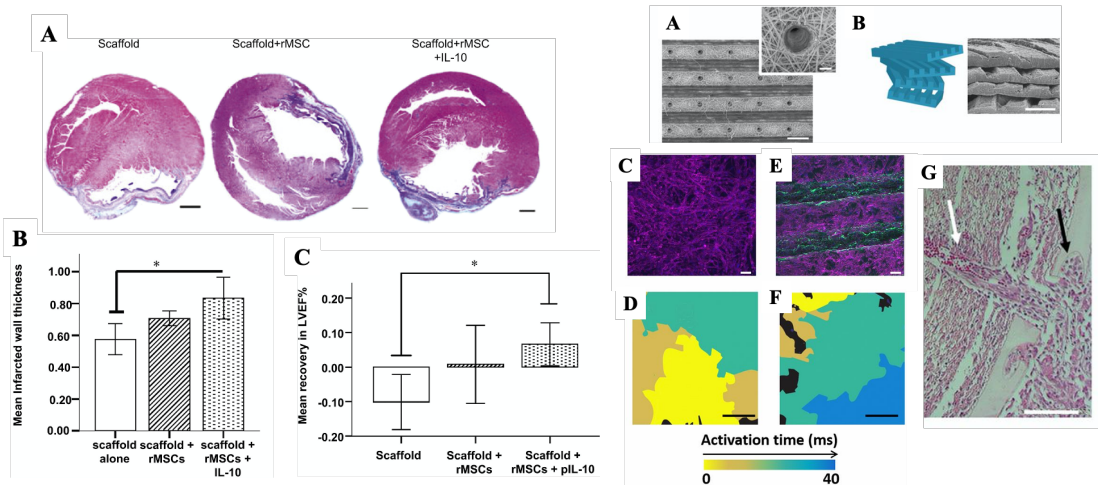

(a) (b)

Fig. 2.7 Translational applications of cardiac patches **(a)** The effects of cell seeding and growth factor fuctionalisation of a type 1 collagen cardiac patch on infarcted rat hearts. **A** Histologica (Masson's Trichrome staining) analysis of infarct size and severity within the left ventricle in the groups treated scaffold alone, scaffold +rMSCs, and scaffold + rMSCs + pIL-10. **B** Quantitative analysis of mean wall thickness in each group. **C** Quantitative analysis of mean recovery in LVEF% [158]. **(b)** Modular assembly and performance of an aligned albumen patch **A** SEM images of grooved scaffolds with microholes **B** Schematics (Left) and SEM micrographs (Right) of grooved electrospun scaffolds stacked with a slight angle shift **C** - **E** cellular structure and electrical signalling dynamics for **C**-**D** planar and **E**-**F** grooved scaffolds. Immunofluorescence images sow α-sarcomeric actinin (pink). Heat maps show **D** randomly oriented electrical signal propagation of an engineered cardiac tissue within the planar scaffolds and **F** anisotropic propagation within the grooved scaffolds. **G** Infiltration of a host blood vessel containing red blood cells (white arrow) into the engineered construct (black arrow).

Cell-focused strategies have historically been applied to promote cardiomyocyte maturation to improve the functional capacity of the cardiac patch. However, in recent studies, engineered tissue structure has emerged as an important cell signalling regulator that can promote proliferation as well as electrophysiological and structural maturation [163, 164]. The development of polymeric hydrogel bioinks and the growing popularity of bioprinting as a mode of scaffold fabrication has enabled an increased understanding of the importance of macro-scale architecture in cardiac tissue engineering. Jang et al. 2017 fabricated stem cell-laden patterned patches with human cardiac progenitor cells encapsulated in polycapro-

lactone. It was found that 3D printed patches exhibited enhanced cardiac function. They also reduced cardiac hypertrophy and fibrosis, increased migration from the patch to the infarct area, and capillary formation resulting in improved cardiac function when compared with nonpatterned patches. These results demonstrated that the patterned patch architectures provided artificial cardiac niches that facilitated cardiac tissue repair [165]. Fleischer et al. 2017 also highlighted the importance of scaffold architecture by designing a cardiac patch constructed from layers of electrospun albumen scaffolds with laser patterned grooves [50]. The scaffolds were layered with offset orientations to replicate the helical structure of the myocardial wall and seeded with cardiac cells isolated from neonatal rats. It was found that the grooved scaffolds facilitated cell alignment and directional electrical signal propagation as shown in Figure 2.7b. The addition of growth factors was also found to improve vascularisation *in vivo*. These studies have motivated new interest in understanding the influences of substrate structure on cardiomyocyte behaviour.

Fleischer et al. 2017 constructed a cardiac patch through the modular layering of patterned albumen films seen in Figure 2.7b [50]. It was shown that scaffolds composed of anisotropically patterned layers mimicked both the stiffness and mechanical anisotropy of the native myocardium. It was also found that cardiac cells cultured within these layers assembled into aligned and elongated cardiac bundles resembling the natural tissue morphology and facilitating directed signal propagation as shown in Figure 2.7b. No spontaneous beating, however, was reported [50].

Understanding the importance of anisotropy

Although translational studies in cardiac tissue engineering only recently began utilising anisotropic architecture to improve tissue function, the structure–function relationships in cardiac muscle for *in vitro* systems has been a topic of interest for decades [71, 137, 139, 166–

168]. Rohr et al. 1991 demonstrated that patterned cultures that constrain the cell monolayer in two dimensions can regulate source–sink relationships in cardiomyocyte signalling, resulting in unique propagation of action potential wavefronts [137]. Similarly, work done on neonatal rat ventricular myocytes cultured on fibronectin patterned through microabrasion showed that alignment of the ECM potentiated the elongation and alignment of cultured myocytes. The cells formed anisotropic monolayers that propagated excitation wavefronts faster in the longitudinal direction relative to the transverse direction [139]. Topographical micropatterning of substrates has since been shown to direct the self-organisation of cardiomyocytes into muscle tissue with a hypertrophic phenotype [167, 169]. Specifically, geometric cues in the ECM have been shown to act as boundary conditions that regulate myofibrillogenesis. The resulting two dimensional structural formations can be seen in Figure 2.8a A-C [168, 170, 171]. Consequently parallel alignment of bundled myofibrils has been found to enhance contractile strength as shown in Figure 2.8a D [172]. Feinberg et al. 2012 demonstrated that structural alignment cues influence the inter-cellular and intra-cellular organisation of cardiomyocytes by combining image analysis of sarcomere orientation with muscular thin film contractile force assays. Sarcomere-generated force was found to increase as a function of tissue anisotropy. The observed relationship was larger than would be anticipated from enhanced calcium handling and increased uniaxial alignment alone. These reports suggest that boundary conditions imposed on myocardiocytes by a two-dimensional extracellular environment are an important regulator of cardiac tissue form and function [71].

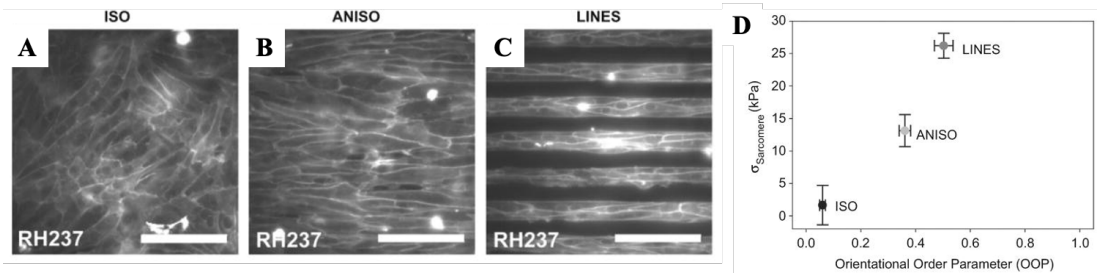

(a)

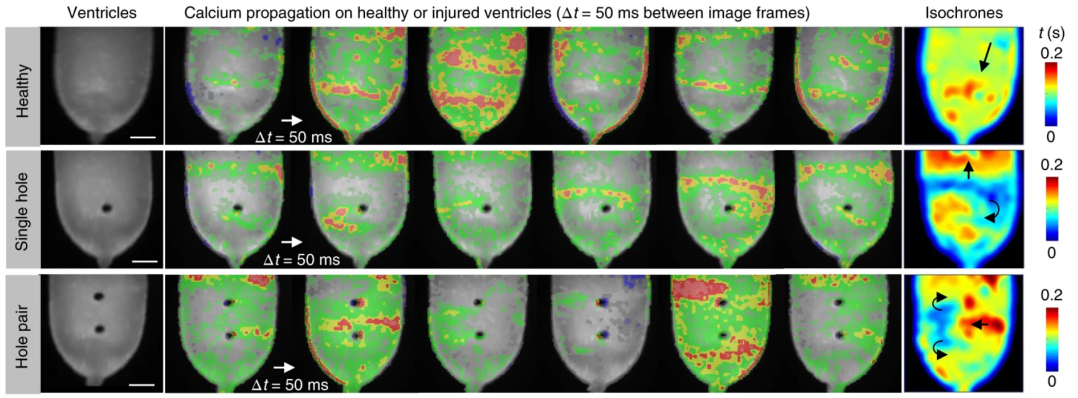

(b)

Fig. 2.8 Functional influence of anisotropy **(a)** 2D tissues composed of cells with clearly defined borders that reflect the engineered alignment **A** isotropic **B** anisotropic and **C** lines. Plot of orientational order parameter (OOP) verses sarcomere contractile stress for each tissue type. [71] **(b)** Calcium wavefront propagation on a healthy (top) or injured (middle and bottom) tissue-engineered NRVM ventricle. The uninjured ventricle exhibited plane waves with a peak-to-peak spatial period of 5 mm (top). Subsequent 1 mm diameter biopsy punch injury of this ventricle resulted in circular anatomical defects that generated pinned spiral waves. The single-hole injury (middle) generated a single spiral wave whereas the hole pair (bottom) generated counter propagating spiral waves that converged and propagated through the inter-hole region with each cycle. Black arrows in isochrone images indicate direction of calcium wave rotation and propagation. Scale bars, 3 mm [70]

Some recent studies have emerged demonstrating increased physiological functionality in three dimensional anisotropic tissue engineering [35, 50, 70, 97]. Macqueen et al. 2018, motivated by mimicking the native myocardial architecture, engineered 3D ventricle scaffolds that were shown to promote cardiomyocyte assembly into functional 3D tissue-engineered ventricle chambers. The ventricle scaffolds were found to direct signal propagation, and

describe the arrhythmia in the presence of injury as shown in Figure 2.8b. Additionally, contractile behaviour was observed and cyclic pressure volume changes were reported. The thin ($\sim$30μm thick) structure, however, limited the contractility of the construct [70]. Finally, Liu et al. 2020 demonstrated that anisotropy of the cellular micro-environment influences the contractile force of 3D printed methacrylated gelatin constructs. It was shown that cells printed in a grid pattern produced reduced contractile force when compared to cells printed into parallel lines. The influences of structural architecture on signalling dynamics, cellular development and phenotyping were not explored [35]. These recent studies support the hypothesis that biomimetic structural properties dictate the form and influence the function of engineered cardiac tissue. The technical complexity of scaffold engineering, however, has meant that the isolated functional and developmental effects of architectural organization in engineered cardiac tissue have not yet been systematically studied. Little is, therefore, known about the direct influence of structure on specific functionality of engineered tissue.

2.3.2 Current limitations in cardiac tissue engineering

The field of cardiac tissue engineering has made several breakthroughs in the past 20 years, expanding the potential for tissue regeneration in future human and model medical systems. Despite improvements in cell fate designation and cellular maturity, significant hurdles remain in establishing and maintaining sufficiently high cellular densities within engineered tissue [2]. Specifically, vascularisation has been identified as a major concern. In particular, the metabolic rate of cardiomyocytes necessitates a dense capillary system in the cardiac tissue [173]. Scaffold functionalisation with growth factors such as VEGF and FGF has shown encouraging results. Improvements in scaffold architectural design and pre-vascularisation may significantly increase both cellular and graft survival as well as promote functional integration with the native myocardium [2, 44]. In addition to patch viability, optimisation

of engineered tissue function is also necessary for translational application. The heart is an organ with excellent biomechanical properties to support high pressure and produce significant contractile force [2]. The electrical function and contractile force generated by engineered cardiac tissues currently falls well below desired levels and is compounded by inconsistent electrical integration with the host myocardium [44]. Introducing biomimetic anisotropy to engineered tissue structure is hypothesised to improve both the functional contractile limitations such as contractile strength as well as electrical coupling between native and engineered tissue. There is, however, a lack of fabrication methods that enable architectural control of three dimensional scaffolds at multiple length scales [152].

2.4 Ice templating

As mentioned previously tissue engineering scaffolds require a porous matrix with high interconnectivity to support cellular in-growth and efficient nutrient transport [110, 117, 142–145]. The structure should also provide sufficient physio-mechanical support to enable native function at both a cellular and tissue level until full integration and regeneration are achieved [174]. A variety of methods have been developed to produce biomaterial scaffolds in an attempt to replicate tissue structures. Many scaffolds, however, have features at a single length scale, not hierarchical structures consisting of features on multiple length scales. Scaffolds with hierarchical structures better resemble biological tissues and have been demonstrated to enhance cell function [152, 175–177]. The freeze-casting technique is highly appealing for its ability to produce hierarchical structures with topographical characteristics at multiple length scales. Freeze-casting is independent of scaffold substrate because it is a physical process. The process is, therefore, conserved for a variety of materials such as ceramics, metals, or polymers.

To date the literature around freeze-cast collagen scaffolds has been split into two sectors pertaining to the production and control of isotropic and aligned structures. Isotropic structures are characterised by a homogeneous sponge-like architecture with equiaxed pores [31, 178, 179]. Anisotropic structures, however, are characterised by aligned morphologies, with columnar pore structures [30, 142, 180]. These variations in scaffold morphology are motivated by the variety of structures observed in native human tissue [181–183] as it is necessary to replicate the structure of the native ECM to ensure the regeneration of functional tissue with a biomimetic morphology [110, 184].

Freeze-cast structures are produced during the solidification of a colloid or suspension. The porous structure is a result of the low solubility of impurities in ice, such that during crystal formation the suspended particles are pushed to the periphery of the ice crystal. The resulting solid is a network of interconnected ice crystals encapsulated by the particle material. When the ice is then removed *via* sublimation the final structure is an exact negative of the ice crystal network. It follows that by controlling the ice formation during the solidification step the final scaffold architecture can be controlled [31, 32, 185]. Techniques have been established to control pore size [32, 179, 186], wall thickness [187], surface roughness [188] and interconnectivity [117, 188] across several length scales. Freeze casting is a comparatively straightforward physical process based on benign, biocompatible liquid carriers such as water. For this reason all classes of materials can be processed [174].

2.4.1 Solidification

Solidification occurs in two stages, the formation of a stable nucleus and subsequent crystal growth. Both impact the porous structure created through the freeze-casting process. Nucleation is the process by which the first crystal is formed and occurs stochastically making

it difficult to control. Once nucleation has occurred, crystal growth ensues [31]. The rate and direction of crystal growth is sensitive to the thermal environment of the suspension [185]. Following the completion of solidification, the crystal structure continues to evolve. Remodelling occurs below the equilibrium melting temperature, and is dependent on many factors, such as temperature, time, and composition of the solution. Both the solidification and crystal remodelling processes can be further controlled through the utilisation of additives that alter the chemical and physical properties of the suspension [31].

Nucleation

In order for the initial nucleus crystal to form, the system needs to overcome three main barriers of formation: the reduction of entropy within the scheme, the increased strain energy and the increased inter-facial energy at the interface between the solid and the liquid [189]. For this reason, liquid systems below the melting temperature exist in a metastable state. An increasing number of molecules cluster into a locally ordered structure [189, 190]. When the cluster grows large enough, stable bonds are formed and latent heat is released as described in Figure 2.9 [31, 189, 190].

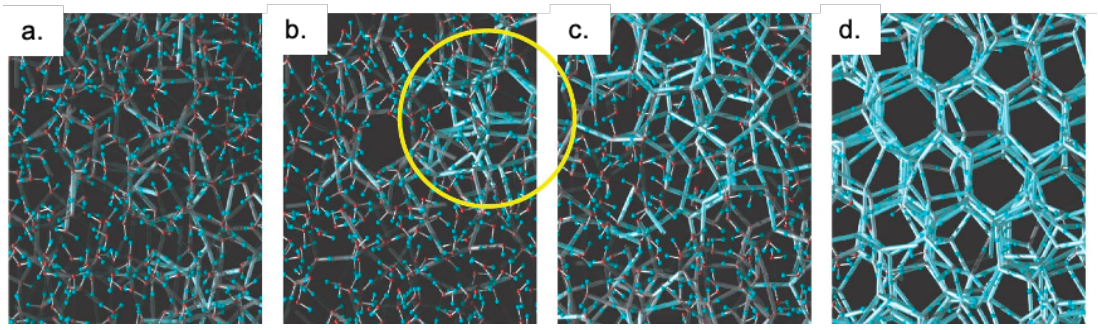

Fig. 2.9 Computational simulation results for the solidification of water at time **a.** 208 ns, **b.** 256 ns **c.** 290 ns, and **d.** 320 ns. Initial nucleus formation was observed after 256 ns (circled region), subsequently stable hydrogen bonds are formed [190]

Nucleation can occur at any temperature below the melting temperature (0 ^{o}C). The probability of a nucleation event, however, increases as the temperature decreases. The temperature at which the stable nucleus occurs is referred to as the nucleation temperature [31, 189]. Within

the literature, a positive correlation between the nucleation temperature and the size of the stable nucleus has been identified [31, 191].

In freeze-casting systems, nucleation is widely acknowledged to be critical in determining whether scaffolds are isotropic or anisotropic [28, 29, 192]. Husmann et al. 2015, demonstrated that the thermal environment of a 1 wt % collagen suspension at the time of nucleation was predictive of the structural composition of the final scaffold [193]. It was shown that when all of the suspension had cooled below the melting temperature at the time of nucleation, an isotropic pore structure was achieved. When large thermal gradients were present and only a fraction of the suspension had cooled below the melting temperature at the time of nucleation, an ice front was developed. The development of an ice front resulted in partially anisotropic pore structures. Subsequent to nucleation, crystal growth has been shown to influence the final pore morphology of both isotropic and anisotropic ice-templated scaffolds [32, 179].

Crystal growth

In order to obtain porous structures, particles in the suspension must be rejected during crystal formation. This phenomenon has been studied extensively with various model suspensions [32, 194–196]. Thermodynamically, in order for rejection to occur there must be a net increase in free energy if the particle is engulfed by the solid:

$$\Delta\sigma = \sigma_{sp} - (\sigma_{lp} + \sigma_{sl}) > 0 \tag{2.1}$$

where σ_{sp}, σ_{lp} and σ_{sl} represent the interstitial free energies of the solid-particle, liquid particle and solid-liquid interface, respectively.

It has been shown that for slow crystal growth rates, this thermodynamic relationship is enough to predict particle entrapment or rejection [195, 197]. To enable particle transport to the periphery of the crystal, however, a liquid film of sufficient thickness is required between the solid phase and the particle. The thickness of this liquid film has been found to have a negative relationship with the velocity of crystal growth, such that as crystal growth speeds increase, the thickness of the liquid film decreases [32]. Therefore, there is a critical velocity, v_c, for particle rejection, above which particles are entrapped by the growing crystal. A simple model has been identified between the critical velocity and the force balance at the particle/ice interface:

$$v_c = \frac{\Delta\sigma d}{3\eta r}\left(\frac{a_0}{d}\right)^n \tag{2.2}$$

where a_0 is the average intermolecular distance in the film, d is the overall thickness, η is the solution viscosity, r is the particle radius and n is an empirically determined exponent that has been found to vary between 1 and 5 depending on the model system [32, 195].

The interactions that govern particle rejection are summarised in Figure 2.10. For directional solidification the critical velocity for collagen suspensions has previously been reported as 20 μm^2. The determination of critical velocity in isotropic systems is comparatively more difficult due to the lack of a measurable ice front [198]. In either case, however, it has been found that variations in freezing kinetics below v_c have a large impact on the pore size.

2.4.2 Freeze-casting kinetics

The kinetics of crystal growth in both isotropic and anisotropic systems are dictated by several factors including temperature, heat flow and suspension composition. The crystal growth rate is found to increase when the temperature of the suspension is reduced. Furthermore,

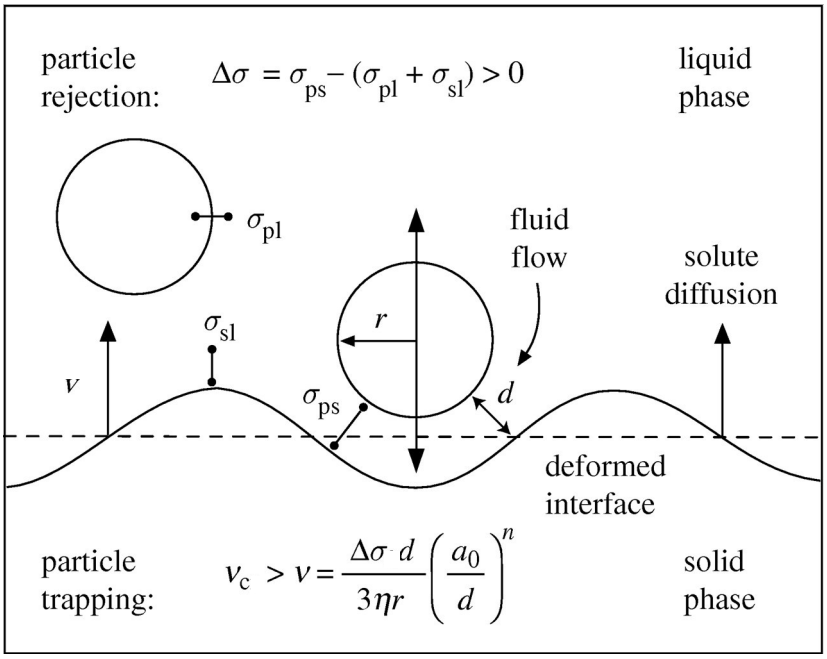

Fig. 2.10 Schematic of particle–freezing front interactions that govern particle rejection [174]

the thermal environment also affects the rate of growth by governing how efficiently the heat is removed from the system [179, 199]. Distinct methods have been developed to describe the freezing kinetics for isotropic and anisotropic systems.

Isotropic freeze-casting kinetics

In isotropic freeze-casting, crystal growth occurs in the absence of significant thermal gradients and when the entire suspension has cooled below the melting temperature prior to any nucleation event. The low temperature of the suspension means that the overall latent heat outweighs heat removal and two crystal growth phases can be observed. Initially, rapid crystal growth from the nucleation site occurs in dendritic fashion and spreads throughout the supercooled suspension [193]. The initial crystal growth rate is found to be positively correlated with the degree of suspension supercooling [31, 200–202]. Rapid crystal growth

results in a large latent heat release that raises the suspension temperature to the melting temperature [179]. Part of the initial ice skeleton may melt following this phase of growth [193, 203]. Subsequently, secondary ice growth occurs from the dendritic ice skeleton and is dependant on the heat removal capacity of the thermal environment [193].

In 2014, Pawelec et al. demonstrated that the freezing kinetics of the secondary crystal growth phase are responsible for determining the pore size of isotropic freeze-cast structures. The time at equilibrium parameter was defined to describe the time between nucleation and complete solidification, designated to occur at $-1.5\ ^{o}$C [31]. It was found that suspensions that spent greater time at equilibrium during solidification resulted in larger pore sizes irrespective of mould geometry or suspension volume.

Directional freeze-casting kinetics

Directional crystal growth occurs in the presence of sufficiently large temperature gradient, such that only a small volume of the suspension is undercooled prior to nucleation. In the absence of a dendritic skeleton dispersed throughout the suspension volume to structure crystal growth after nucleation, an interfatial front is developed between the liquid and solid phases. As heat is removed from the system, crystal growth progresses perpendicular to the phase front [203]. The development and progression of the solidification front in directional freeze-casting has been widely studied in ceramic systems and has been found to directly influence the pore structure of the final freeze-cast material.

Deville et. al. 2007, identified three stages of ice growth in the formation of unidirectional freeze-cast alumina structures: planar growth, columnar growth, and lamellar growth as shown in Figure 2.11 [32]. Due to the physical nature of the ice-templating process these evolutionary stages of crystal morphology during the freeze-casting are generalisable to

most materials. Evidence of similar stages has been documented in ice-templated collagen scaffolds [142].

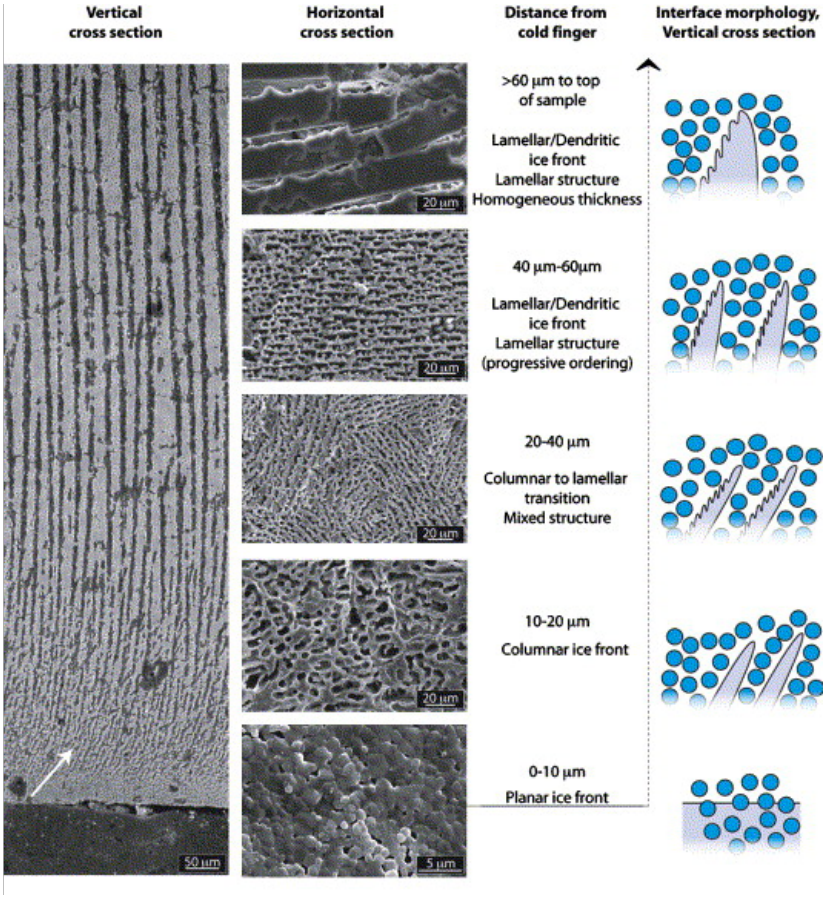

Fig. 2.11 Final architecture of a freeze-cast alumina structure correlated to the evolutionary phases of ice front morphology. Horizontal cross-sections further illustrate the solid liquid interface morphology [32]

When the colloid is initially introduced to the cold finger, rapid ice growth occurs at a velocity higher than the critical velocity for particle rejection. This causes a thin, dense isotropic region (0-10 μm) to form where particles are trapped in the planar solidification front. Rapid ice growth is not sustained as the latent heat, released by the crystal formation, and the thermal mass of the liquid slurry, slows the freezing velocity to below the critical velocity and

particles are rejected from the solidifying crystals. The rejected particles build up ahead of the phase interface and locally pin the ice front, triggering a transition to a columnar ice front [32].

In the columnar stage, collagen particles are trapped between the ice crystals creating a pattern across the surface. Differences in thermal conductivity between the material particles and the solid phase mean that local temperature gradients arise. These thermal gradients, in conjunction with latent heat released upon solidification, result in undulations in the freezing front surface [174, 204]. A build up of rejected particles also causes a local increase in particle concentration just ahead of the freezing front, which decreases the melting temperature of the colloid and creates a zone of constitutional supercooling ahead of the front [205]. The result is rapid anisotropic crystal growth as shown in Figure 2.11.

The ice growth direction is dictated by two factors; firstly, the hexagonal crystal structure of ice and secondly, the presence of a sufficiently high temperature gradient. Ice crystals have a preferential growth direction, meaning that the crystal will grow 100 times faster in the basal plane (a-, b-axis) than in the perpendicular direction (c-axis). The freezing process is, therefore, more efficient for crystals that are oriented with their a-axis parallel to the temperature gradient. This causes the columnar phase to transition to a lamellar phase. In the lamellar phase, ice crystals with a-axes that align with the thermal gradient will grow at the expense of crystals with alternative orientations, and ice propagation will occur upward as vertical lamellar crystals with horizontal c-axes [32, 206].

Pore size The rate of freezing front progression and lamellar growth is correlated with crystal size, and ultimately influences the pore sizes observed in the freeze-cast structure [31, 32]. Efficient heat removal from the system results in a rapid freezing front velocity. The fast freezing front velocity causes an increase in the concentration of rejected particles ahead of the front resulting in an increase in constitutional supercooling ahead of the growing

crystals [174]. As the crystals grow more rapidly in their preferential direction, growth on the c-axis is increasingly limited, resulting in thinner lamellae. Conversely, as the crystal growth slows there is more time for diffusion of particles, allowing coarser lamellae to form [32].

A power–law relationship has been identified in the literature between the average lamellae spacing λ and freezing front velocity v where $\lambda \propto v^{-n}$ and where n is specific to the freeze-casting system [32, 185, 187, 207–210]. Deville et al. 2007 identified that the parameter n was influenced by particle size, where 100 nm alumina particles produced $n = 0.6$, however, when the particle sizes doubled the relationship increased to $n = 1$ [32].

Architectural control with collagen

Pore size In recent years, directional freeze-casting has been applied to the production of large scale (>20 mm in height) freeze-cast collagen scaffolds. Pawelec et al 2017, explored the relationship between freezing front velocity and final pore size of aligned 7.5 wt% collagen scaffolds with and without the addition of hydroxyapatite and ethanol [142]. Pawelec identified a power-law relationship of $n = 0.85$ for collagen suspensions in the presence of ethanol, irrespective of hydroxyapatite addition. In the absence of ethanol, however, no relationship was observed. Divakar et al 2019, explored the power-law relationship with a 2 wt% collagen suspension, however, no freezing front velocity was measured. Instead the final scaffold pore size was correlated to the set cooling rate at the base of the mould. A power law of $n = 0.2$ was identified [199].

Pore orientation The relationship between the temperature gradient and directional crystal growth, has been further utilised to fabricate structures with bidirectional pore orientations.

Studies have shown that by varying the size, shape and location of the heat sink within the solidifying system pore orientation can be manipulated. Davidenko et al. 2012, established a graded distribution of cooling power across the base of a 1 wt% collagen suspension [211]. In addition to a large vertical gradient greater than 35 ^{o}C, a lateral temperature difference across the width of the suspension of greater than 10 ^{o}C was established. As a result, the lamellar orientation of the resultant pore structure was bidirectional, angled in the direction of the thermal gradient as shown in Figure 2.12a. Similarly, Pot et al. 2015, utilised a graded distribution of cooling power at the base of a 7 wt% collagen suspension, however, a comparatively small lateral temperature difference of less than 2 ^{o}C across the width of the suspension was established [212]. The reduced lateral temperature difference relative to the large vertical temperature difference measured to be greater than 20 ^{o}C was not found to be sufficient to result in bidirectional lamellar orientation of the final freeze-cast scaffold [212].

The influence of the heat sink shape and location on pore orientation has also been explored. Campbell et al. 2017, introduced a localised heat sink at the base of a 1 wt% collagen suspension [213]. The sink had an inverted conical geometry and was located in the centre of the slurry base. The resultant freeze-cast scaffold was found to have radial lamellar orientation, where lamellar channels were observed to originate at the tip of the heat sink cone and fan out throughout the scaffold volume as illustrated in Figure 2.12b [213]. Divakar et al. 2019, reported moderate success in the production of radially aligned freeze-cast structures. Collagen scaffolds (2 wt%) were cast in cylindrical moulds, where the wall and base of the mould were designed to act as heat sinks. A radial structure with an inclined pore morphology was reported for a set cooling rate of 1 ^{o}C min^{-1}. It was observed, however, that the structure was not conserved for all set thermal parameters, and that both rapid (10 ^{o}C min^{-1}) and slow (0.1 ^{o}C min^{-1}) set cooling rates resulted in reduced regularity in the pore orientation [199]. The variations in structural regularity could be attributed to varying

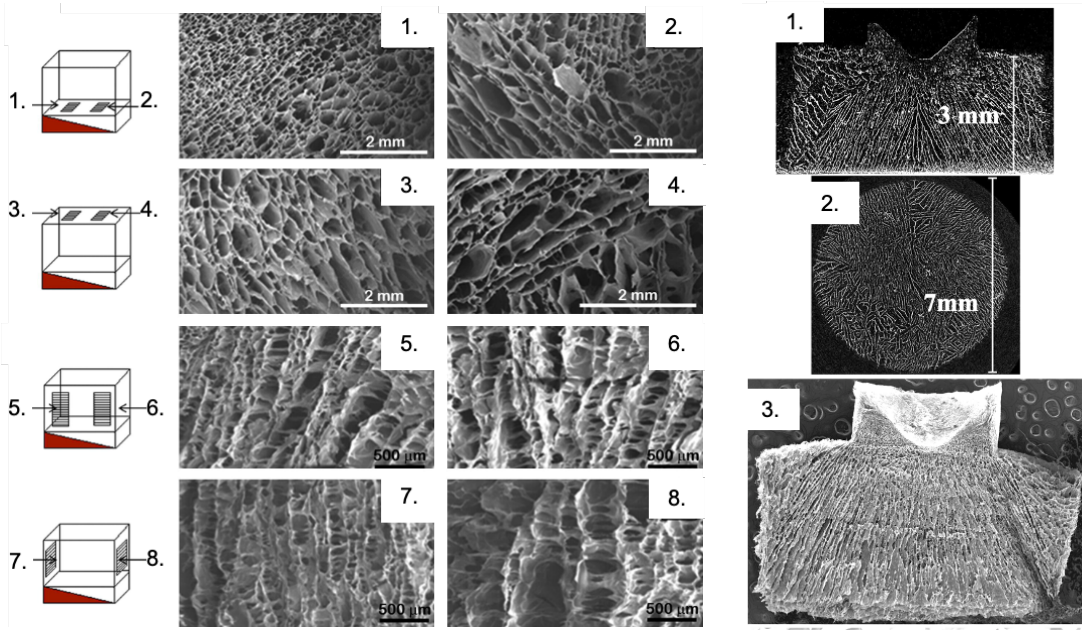

(a) (b)

Fig. 2.12 Manipulation of pore orientation **(a)** Bidirectionally aligned freeze-cast collagen scaffold, 1.-4. show transversal cross sections, 5.-8. show longitudinal cross sections, bidirectional lamellar orientation is evident in 5. where the wedge mould system resulted in a large lateral thermal gradient component [211] **(b)** Radially aligned freeze-cast collagen scaffold, 1. and 2. show reconstructed μCT images of transversal and horizontal planes of the scaffold 3. shows an SEM micrograph of the transversal plane [213]

degrees of undercooling present within the system prior to nucleation, and/or poor control over the thermal gradient magnitude and direction at the time of solidification. However, further study is needed.

2.4.3 Post solidification crystal dynamics

Following solidification further remodelling can occur through surface and bulk molecular diffusion. Three broad categories of molecular movement have been identified, namely attrition, agglomeration, and Ostwald ripening [214]. Attrition is a mechanical process in which ice crystals are broken down into smaller crystals [189]. Agglomeration is the process by

which smaller particles fuse together, resulting in large particles; agglomeration is limited to long time periods greater than one hour [191]. Oswald ripening is the growth of large crystals at the expense of smaller ones. Within the literature this process is also commonly referred to as recrystallisation and annealing. Oswald ripening results in macroscopic coarsening of the ice structure and is driven by the reduction of both the chemical potential of small radii and the inter-facial energy within the system [189, 215]. Attrition and agglomeration processes can be avoided. Oswald ripening, however, is always observed to some degree during freezing and post solidification at temperatures above the glass transition temperature.

2.4.4 Practical methods for control of solidification

Numerous methods have been developed to manipulate the physical process of freeze-casting, and control the pore morphology, size and orientation of ice templated structures. The techniques utilised in the literature can be divided into three main categories, and these are, cooling method, mould design, and chemical/physical additives. Through the variation and combination of these experimental parameters, an extensive tool-kit for structural control has been compiled within the literature.

Cooling method

The cooling method influences the degree of undercooling prior to nucleation, as well as the presence and orientation of thermal gradients within the suspension. To achieve isotropic structures, cooling methods with low cooling rates and/or reduced thermal variability have been developed. The most common method for producing ice-templated scaffolds with equiaxed pore structures, is a shelf-ramping freeze drier or lyophiliser [117, 130, 216]. The method is highly versatile, and allows both the set freezing temperature and the set cool-

ing rate to be varied independently [216]. The insulated thermal environment within the freeze-drier also enables an increase in thermal homogeneity within the suspension as it cools which reduces the development of thermal gradients and enables the development of isotropic structures. Although lyophilisation is the most popular method of isotropic structure production, anisotropy has also been achieved. Pawelec et al. 2014 explored the effects of filling height on final scaffold structure for 1 and 0.5 wt% collagen scaffolds frozen in a freeze-drier [216]. It was found that the freeze-drier enabled homogenous cooling of samples with filling heights between 5 and 15 mm, such that at the time of nucleation all parts of the suspension had cooled below the melting temperature. However, a filling height of 20 mm resulted in only part of the suspension cooling below the melting temperature at the time of nucleation and anisotropy was observed at the top of resultant scaffold [216].

Similarly, cold baths can be used to produce both isotropic and anisotropic structures [142, 212, 217]. Yuan et al. 2009 demonstrated that by varying the cooling rate of 3 wt% chitosan suspensions, the final pore morphology could be influenced [217]. It was shown that a slow cooling rate of 0.83 ^{o}C min^{-1} resulted in uniform cooling throughout the suspension with no significant thermal gradients. This resulted in an isotropic pore morphology in the final ice-templated scaffold, irrespective of set bath temperature. Conversely, large temperature differences across the cooling suspension were observed for quenching protocols with fast cooling rates between 28 and 60 ^{o}C min^{-1}. These protocols resulted in crystal growth in the direction of the temperature gradient, and ultimately, an aligned pore morphology [217].

The cooling methods to produce anisotropic structures have been developed to maintain and control thermal gradients within the cooling suspension. Directional crystal growth is most commonly achieved through the use of a controllable heat sink, either a cold bath [142, 212]

or a cold finger [185, 199]. Most experiments described in the literature use a one-sided freezing system in which the top of the mould remains exposed to the ambient environment as shown in Figure 2.13a [188, 199, 207, 218, 219]. Divakar et al. 2019 utilised a single cold finger to achieve directional solidification of 2 wt% collagen suspensions [199]. It was observed that the vertical temperature difference established within the suspension due to the heat sink at the base of the mould, provided by the cold finger, and the heat source at the top of the mould, provided by the ambient environment, was sufficient to elicit directional crystal growth and an aligned pore morphology. Further control of the thermal environment within the suspension during directional solidification has been achieved through the application of a two-sided cold finger set up. The main advantage of two-sided freeze-casting systems, in which the bottom and top of the suspension are contacted by controlled heat sinks with independently variable temperatures, is that the temperature gradient and freezing-front velocity within the sample can be better controlled [187, 185]. Waschkies et al. 2009 demonstrated that by programming the temperature at both the base and the top of a 30 vol% alumina suspension, the vertical temperature difference across the suspension could be prescribed and stabilised throughout the duration of the solidification process, ultimately leading to increased pore size homogeneity in the final freeze-cast structure [185].

The cooling method has been shown to influence pore size uniformity in both isotropic and anisotropic ice templating systems. It has been shown that rapid freezing rates result in largely uniform pore sizes throughout the resultant structure. At reduced cooling rates, however, pore sizes have been found to vary between the top and bottom of the final structure. O'Brien et al. 2004 demonstrated that by increasing the cooling rate of a 0.5 wt% collagen suspension from 0.6 to 0.9 ^{o}C min^{-1} pore sizes were found to decrease from 130 to 90 μm and a reduction in the pore size coefficient of variance from 0.151 to 0.128 was reported [220]. It has further been documented that the suspension volume does not all cool at the same time and that reduced cooling rates at the top of the suspension often lead to statistically significant

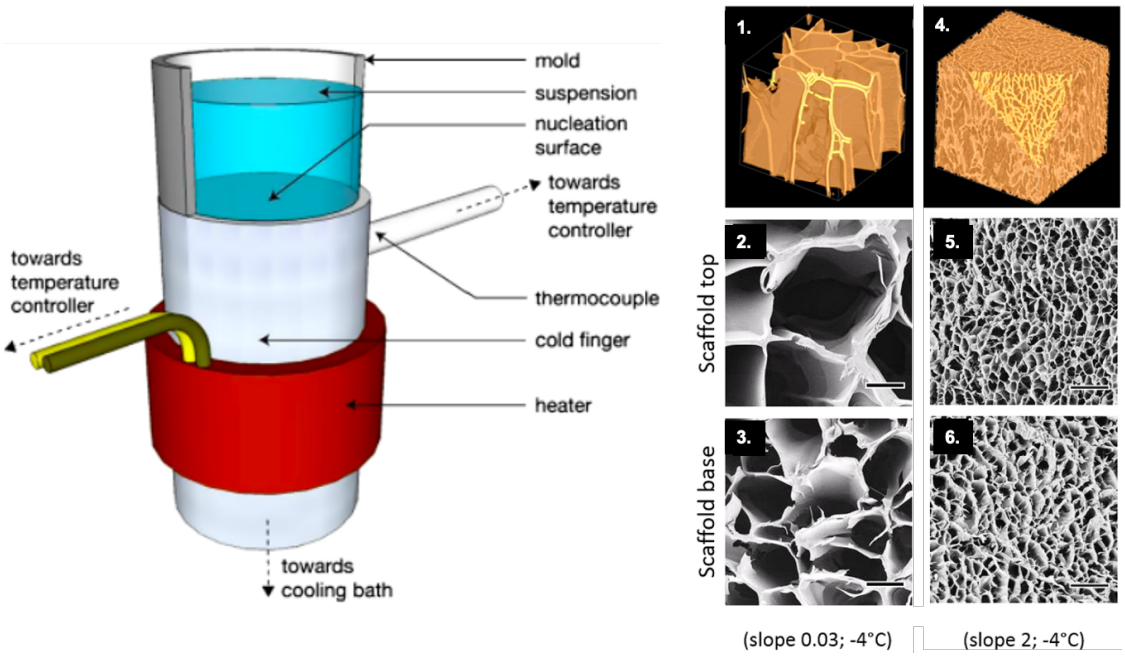

(a) (b)

Fig. 2.13 Freezing set-up and scaffold pore structure **(a)** Schematic of a controllable one-sided freezing system for directional freeze casting [188] **(b)** Pore structure of directionally solidified 7.5 wt% collagen scaffolds with cooling rates of 0.03 ^{o}C min^{-1} (1.-3.), and 2 ^{o}C min^{-1} (4.-6.); 1. and 4. show μCT reconstructions and remaining images show SEM micrographs; scale bars 200 μm. [142]

differences between the pore sizes measured at the base and the top of the scaffold [179, 221].

A similar result has been observed in directional freeze-casting systems. Pot et al. 2015 demonstrated that 2 wt% collagen suspension cooled rapidly via quenching at low temperatures of -196 and -78 ^{o}C produced scaffolds with homogenous pore sizes [212]. Pawelec et al. 2017 also observed pore size uniformity in 7.5 wt% collagen scaffolds directionally solidified with a set cooling rate of 2 ^{o}C min^{-1}. When the cooling rate was reduced, however, to 0.03 ^{o}C min^{-1} the resultant scaffolds were found to have significantly larger pore sizes at the top of the structure, relative to the base as shown in Figure 2.13b [142]. These pore size variations, resulting from both isotropic and anisotropic freeze-casting methods, can

be attributed to the efficiency of heat removal afforded by the cooling method during the solidification process and its consequent effect on crystal growth kinetics.

Mould design

In addition to cooling method, numerous variations in mould design have been developed to influence the final pore architecture of freeze-cast scaffolds. Husmann et al. 2015 demonstrated that the thermal environment within the suspension can be influenced by varying the thermal conductivity of the mould geometry [193]. Mould designs have also been developed to increase the homogeneity of the thermal environment within the suspension. In 2013, Pawelec demonstrated that introducing an air gap between the base of the mould and the cold source, while simultaneously introducing a thermally conductive sleeve around the walls of the mould, resulted in increased pore size homogeneity for isotropic structures frozen at slow cooling rates [179].

Anisotropic pore structures, on the other hand, have been produced in a freeze-drier environment by exaggerating thermal gradients within the cooling suspension. Davidenko et al. 2012 demonstrated that a mould with a thermally conductive shelf contacting base and thermally insulating walls, will result in a vertically aligned pore structure in 1 wt% collagen scaffolds [211]. Similar moulds are used outside the freeze-drier in conjunction with controllable heat sink set-ups for directional freeze-casting [187, 199, 212].

2.4.5 Additives

In combination with mould design, additives are also used to influence the solidification dynamics, and consequently the final structure of ice-templated materials. Additives can be

used to affect both nucleation and crystal growth kinetics. Nucleation agents are used to increase the probability of the occurrence of a nucleation event within a narrow temperature range [222, 223]. Silver iodide (AgI) and Pseudomonas syringae are common nucleation agents, however, a wide range of additives haven been used; from iron ore to river sand [222–224]. Nucleation agents are effective *via* various mechanisms. AgI for example, has a crystal structure that resembles ice and acts as a template for ice crystal formation. Conversely, sand and iron ore introduce surface roughness that increase the number of sites available for heterogeneous nucleation [222].

Additives are also effective during the crystal growth stage of solidification. They can be used to affect the growth kinetics and crystal microstructure as well as the topology of the solid-liquid interface. Additives influence several physical processes such as the phase diagram of the solvent, the inter-facial energies of the solid/liquid and particle/liquid boundaries, the degree of under-cooling ahead of the freezing front, the viscosity of the solvent and the forces between ceramic particles in the suspension. Through manipulation of these processes, several microstructural features can be altered including the thickness and separations between pore walls, the roughness of the pore walls at multiple length scales, and in anisotropic structures, the presence and density of bridges between lamellae [188, 225].

Through their influence on the interfacial energies, additives can be used to alter the final architecture of freeze-cast structures from lamellar (e.g. no additive, trehalose or sucrose) to cellular (e.g. gelatin, glycerol or a combination of sucrose and acid citric acid). Beyond the overall architecture, additives can be used to modify the roughness of the pore walls. The addition of sodium chloride (NaCl) has been shown to result in sharp faceted microstructure due to the close proximity of the eutectic point to the melting point [188]. Conversely, the addition of carbohydrates such as sucrose and/or trehalose results in a second glassy phase between -40 and -50 ^{o}C. Structures prepared in the presence of these additives exhibit

rounded, smooth surface features [188]. Additionally, sucrose and trehalose modify the interfacial energies and the degree of undercooling ahead of the solidification front. This affects the morphology of the growing crystal, promoting homogenous growth of regularly distributed dendrites into the pore wall surface. In contrast, addition of ethanol leads to pocket-like dendrites across the pore walls [188]. The effect of additives on interfacial tension and interparticle forces can lead to splitting and healing of crystal tips, resulting in the encapsulation of particles and the formation of bridges between lamellae. Trehalose, for example, has been found to promote a high density of thin bridges, while sucrose leads to a low density of thick bridges for ceramic samples prepared with a cold finger cooling rate of 10 ^{o}C min^{-1} [188].

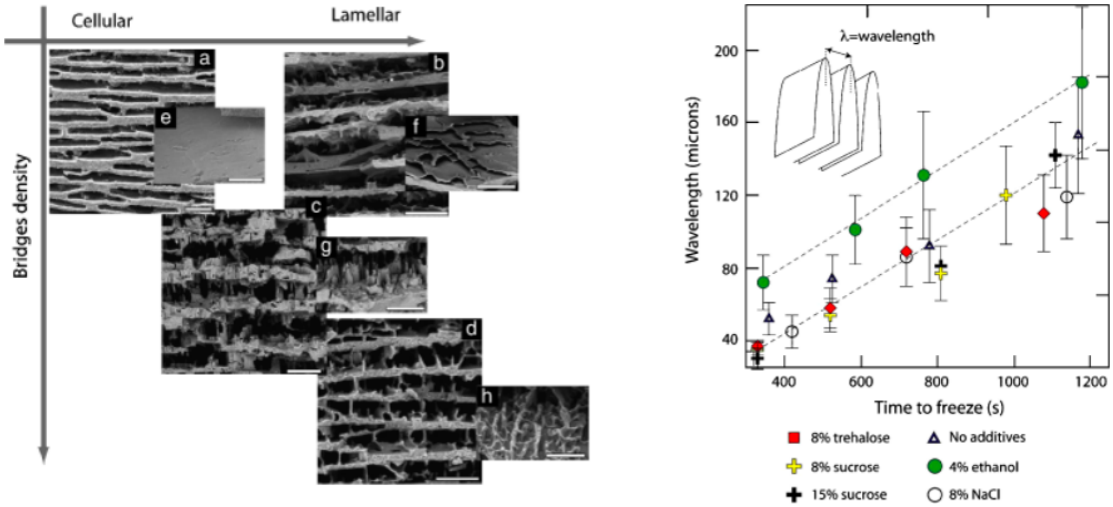

(a)

(b)

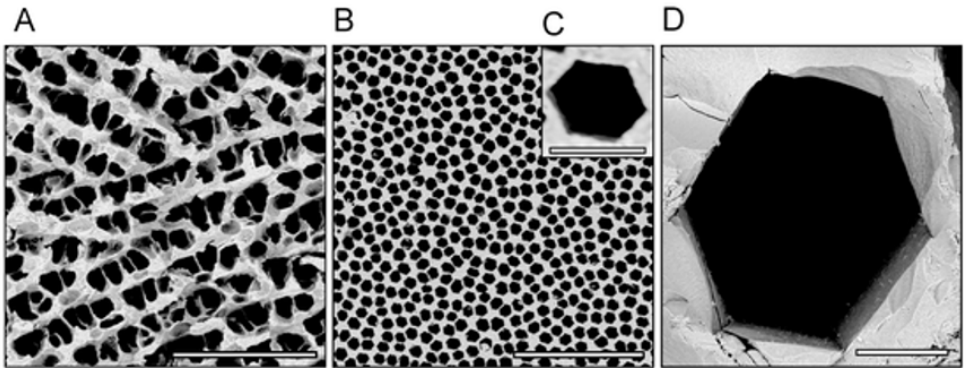

(c)

Fig. 2.14 Structural effects of additives **(a)** Scanning electron micrographs demonstrating the effects of different additives on changing the structure from lamellar to cellular, as well as on the surface roughness and density of bridges between lamellae in directionally freeze-cast alumina structures *a.* sucrose and citric acid resulted in a cellular structure with very smooth ceramic walls; *b.* ethanol resulted in a smooth roughness of the lamellar walls; *c.* sodium chloride resulted in a sharp and rough lamellae surface; and *d.* sucrose resulted in a large degree of bridging. Insets *e.–h.*: Details of the surface roughness of the lamellae. Scale bars: a. 50 μm, b. 100 μm, c. 100 μm, d. 50 μm, e. 50 μm, f. 100 μm, g. 100 μm, h. 100 μm [188] **(b)** Lamellar spacing (wavelength) versus time-to-freeze for 2-cm-tall samples with different additives. Error bars represent the standard deviation [188] **(c)** SEM micrographs taken of the transverse cross section of ice-templated yttria-stabilized zirconia scaffolds without (A) and with (B-D) zirconium acetate addition [226]. Scale bars: A, B, D: 50 μm, C: 5 μm

Despite the significant influence of additives on microstructural features of ice-templated materials, the relationship between the pore size and the ice front kinetics has been found to be largely independent of the additives, with the exception of ethanol which has been shown to result in increased pore sizes [142, 188]. The underlying reasons for this behaviour are not yet fully understood. It has been hypothesised, however, that the effect is a consequence of the coexistence of a liquid and a solid crystal phase at low temperatures. Another exception is the addition of zirconium acetate (ZrAc), which has recently been shown to inhibit planar crystal growth along the a-b plane, resulting in hexagonal columnar crystals that result from slow expansion along the c-axis [226–228]. The affects of additives are summarised in Table 2.1.

Complex architecture

Recently there has been a increased interest in producing ice-templated structures with complex architecture. The application of unidirectional freezing, bidirectional freezing and radial freezing, were discussed in section 2.4.2. In addition to the engineering of freeze cast structures by controlling the thermal environment, external magnetic [232], electric [233], and acoustic [234] fields can be used to further alter the solidification process [235].

Magnetic field aligned freeze-casting is used to fabricate anisotropic magnetic ceramic scaffolds with a hierarchy of architectural alignment in multiple directions. Nelson et al. 2020 used a weak rotating magnetic field, applied normal to the ice growth direction in a uniaxial freezing apparatus, to achieve a long-range helical architecture in porous Fe_3O_4 scaffolds [232]. The conformity of lamellar alignment to the orientation of the applied magnetic field enables direct and specific control of macrostructural morphology. The technique, however, is limited to structures composed of magnetic materials [235]. Electric fields have

Table 2.1 Summary of structural affect of additives

Additive	Physical process	Effect	Mechanism	Reference
Iron ore	Nucleation	↑ Nucleation temperature	↑ Surface roughness ↑ Available nucleation sites	[222]
Sand				[222]
Silver Iodide	Nucleation	↑ Nucleation temperature	Template for crystal formation	[223]
Pseudomonas syringae	Nucleation	↑ Nucleation temperature	Seed nucleation	[224]
Gelatin	Growth Kinetics	↑ Cellular macrostructure	↑ Viscosity ↑ Interfacial energies	[188]
Glycerol	Growth Kinetics	↑ Cellular macrostructure	↓ Melting temperature ↑ Interfacial energies	[188]
Carbohydrates	Growth Kinetics	↑ Dendrite regularity ↑ Smooth surface features	↓ Melting temperature ↑ Mushy zone ↓ Interfacial energies	[188, 229, 230]
Sucrose	Growth Kinetics	↑ Bridge thickness	↓ Interfacial energies ↑ Interparticle forces	[188, 230]
Trehalose	Growth Kinetics	↑ Bridge quantity	↓ Interfacial energies	[188, 229]
Citric Acid	Growth Kinetics	↑ Cellular macrostructure (+ carbohydrate)	↑ Interparticle forces	[188, 231]
Sodium chloride	Growth Kinetics	↑ Rough surface features	↑ Eutectic behaviour	[142, 188]
Ethanol	Growth Kinetics	↑ Pore size	↑ liquid solid coexist at low temperatures	[188]
Zirconium acetate	Growth Kinetics	↓ Pore size Pore shape	↓ Preferential growth	[226, 227]

also been used to influence the final architecture of freeze-cast structures. The technique imparts a temperature gradient, thus controlling the growth path of ice crystals. Electric fields oriented perpendicular to the freezing direction have been shown to produce angled ice crystal growth in an alumina suspension [233]. In contrast, applying electric fields parallel to the solidification direction produces alumina scaffolds with bilayered dense/porous regions [236]. Similarly, standing ultrasonic wave fields have also been shown to affect lamellar architecture [234, 235]. The standing pressure wave that results from the acoustic radiation force, drives particle movement to low pressure regions within the suspension. Ogden et al. 2019 applied the technique in the solidification of a titanium oxide (TiO_2) suspension and the resulting scaffolds exhibited a distribution of concentric rings with alternating dense and porous morphologies [234].

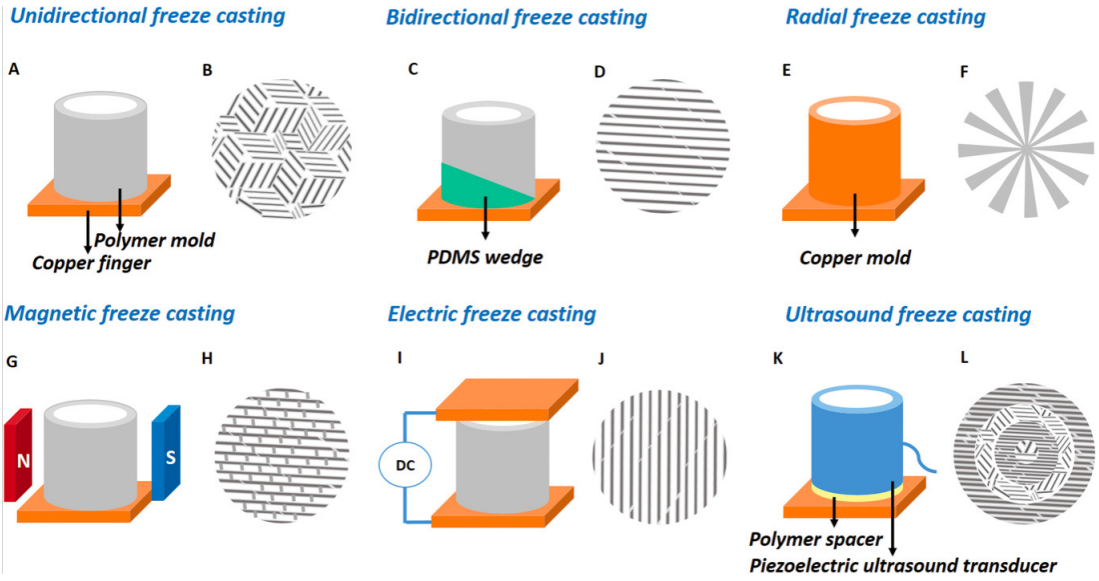

Fig. 2.15 Schematics of freeze-casting architectural control techniques and corresponding microstructures on the transverse plane of resulting scaffolds; A,B) unidirectional, C,D) bidirectional, E,F) radial, G,H) magnetic, I,J) electric and K,L) ultrasound freeze casting [235]

Of further note, localised surface macrostructure can be dictated through patterning techniques. Prior to freezing, patterning of the mould base has resulted in a corresponding pattern present on the base surface of the resultant scaffold [150, 188]. Chen et al. 2016 used ice-particulate patterning to establish a hierarchical honeycomb-like structure at the base of freeze-cast collagen scaffolds [150]. The ice-particulate method can also be used to introduce macro-scale porosity throughout the structure by suspending ice spheres in a super cooled suspension prior to solidification, however, long range lamellar organisation is sacrificed [150].

In addition to monolithic structures, macrostructures such as microspheres [237], fibers [238], meshes [239] and other complex geometries [235] with porous microstructures, have been achieved through the combination of freeze-casting with other processing techniques such as electrospraying [240], electrospinning [241] or additive manufacturing [152]. Although significant material and processing limitations have been reported [235], the increasing volume of micro-structural and macro-structural control techniques for the freeze-casting system is encouraging. There is, however, a lack of physically inherent and spatially specific architectural control techniques for tissue engineering applications.

2.4.6 Functionalisation

Ice-templated scaffolds for tissue engineering are commonly made of natural polymers with inherent bioactivity, such as type I collagen. Collagen scaffolds naturally have a diverse array of signalling and binding motifs, that encourage cellular attachment and migration. The biochemical and physio-mechanical composition of ice-templated scaffolds can be further tailored through chemical functionalisation. Scaffolds can be decorated with therapeutic drugs [36, 242], growth factors [243], signalling proteins/molecules [244] and/or structural proteins [245, 246].

It has been shown, that the natural degradation of collagen scaffolds can be used to enable prolonged drug delivery and growth factor release. Mullen et al. 2010 evaluated the potential of ice-templated collagen scaffolds loaded with insulin-like growth factor-1 as a controlled delivery device. It was found that after an initial burst release within the first 24 hours the scaffold provided a slow, sustained growth factor release was observed over 14 days [243]. Furthermore, functionalising scaffolds with signalling proteins can encourage tissue specific cellular differentiation.

Incorporating growth factors and other biomimetic molecules into the scaffold systems is commonly used to further induce differentiation. Collagen hydrogels with increasing amounts of fibronectin encouraged increased outgrowth of stem cells and endothelial-like phenotyping [247]. Similarly, additions of laminin have been shown to increase cardiac differentiation, while the combination of fibronectin and laminin induce osteogenic differentiation [247, 248]. It has been further shown that incorporation of glycosaminoglycans (GAGs) with varying levels of sulphation can influence cellular metabolic activity and gene expression [244].

The structural composition of ice-templated collagen scaffolds can also be influenced through chemical functionalisation. Cross-linking with different concentrations of EDC (1-ethyl-3-(3-dimethylaminopropyl-carbodiimide hydrochloride) and NHS (N-hydroxy-succinimide) has been shown to influence mechanical strength and stiffness of the final structure [249]. Scaffold stiffness has been shown to affect cell differentiation [250], morphology [251] and migration [252–254]. Increased mechanical stiffness has been shown to lead to increased osteogenic expression, as high substrate elasticity and stiffness guide cells toward osteogenic lineages [250]. Scaffolds with low stiffness, however, have been shown to better encourage neural and myocyte lineages [250]. Increased cross linking in the past has reduced cellular viability. Work done by Bax et al. 2016 [246] and Shepherd et al. 2017 [255] have, however,

demonstrated that reduction in cross-linking percentage or incorporating fibrinogen into ice-templated collagen scaffolds, can drastically improve cellular viability while maintaining mechanical strength.

2.5 Summary

There is a need for the development of engineered cardiac tissue to facilitate regeneration of functional myocardial tissue after infarct. Early translational success is motivating, but clinical application has been limited in part by insufficient control over engineered tissue architecture to replicate the native hierarchical features of the myocardium. Recent studies have explored the influences of anisotropy on cardiac tissue engineering and have demonstrated improved phenotypic and functional capacities. The influences of scaffold anisotropy on tissue behaviour, however, has not yet been systematically studied and therefore the relationship is not fully understood. This is partly due to the limitations in scaffold fabrication capacities.

Numerous fabrication methods have been explored, however, further research is needed to develop a biomaterial scaffold with controlled architecture at multiple length scales. Ice-templated collagen scaffolds have shown significant translational success. Collagen, as a natural biopolymer, encourages cellular migration, proliferation and attachment, as well as provides ample opportunity for functionalisation. Collagen scaffolds fabricated through ice-templating are characterized by open interconnected porous morphologies with hierarchical features at the nano-scale and micro-scale. The surface features that result from ice-templating have been found to encourage cellular attachment and integration into the engineered scaffold, while the macro-scale porosity enable efficient nutrient waste transport. Various techniques have been developed to manipulate and control the freeze-casting process

and, consequently, the final architectural structure of resultant scaffolds. Control techniques for features such as pore size, pore shape, surface roughness and interconnectivity have been well established. However, to date, complex architectural control over macro-scale pore structure remains a significant challenge.

Chapter 3

Collagen scaffold production and performance characterization

The majority of work reported on ice-templated collagen scaffolds utilise a cold shelf freeze drier to control the set temperature [117, 130, 216]. While thermal parameters can be programmed, the freeze drier setup often has a limited temperature range and the closed insulated environment limits the independence of thermal and spatial variables during solidification as well as physical access to the sample. For directional solidification, the use of a programmable cold finger circumvents these limitations. Solidification on a cold finger enables direct access to the sample for monitoring and manipulation purposes while also decoupling the thermal and spatial variables such that complex thermal environments can be induced. This chapter details the design and fabrication of a bespoke freezing apparatus to enable improved control over the directional solidification process. The basic methods for producing and analysing collagen scaffolds are also presented, and these methods are used throughout the remainder of this thesis.

3.1 Collagen scaffold production

3.1.1 Freezing equipment design and construction

Controlled directional ice propagation was achieved through the utilisation of a bespoke freezing apparatus. The rig was designed to directionally freeze large scale (2 cm diameter 3 cm height) collagen suspensions by creating and maintaining a temperature gradient between the top and bottom of the suspension. The apparatus designed and utilised in this work was modelled after the single cold finger device used by Deville et al. 2006 [187, 207].

The controllable heat sink and mould system are depicted in Figure 3.1a and the dimensions of the freezing apparatus are summarized in Figure 3.1b. The cooling bath was constructed of rolled steel (cut and welded to specification) and was contained within an insulating polystyrene box. The cold finger system was cooled by liquid nitrogen. Due to the high volatility of liquid nitrogen, a buffer bath of 95% ethanol was designed around the cold finger to provide sustained cooling power after nitrogen evaporation. The temperature at the top of the cold finger was controlled via a proportional–integral–derivative (PID) controller made by Eurotheum 2400 connected to a 20 V ring heater.

Custom moulds were designed to interface directly with the top of the cold finger. Copper was chosen as the material of both the cold finger and the mould base because of its high thermal conductivity. A uniform thermal profile across the suspension was achieved through the utilization of polycarbonate for the mould walls. Polycarbonate has a similar thermal diffusivity (0.144 $mm^2\ s^{-1}$) to that of water (0.143 $mm^2\ s^{-1}$) [256]. The copper base of the mould was enamelled with a thin layer of RS Black Epoxy Potting Compound to; *i)* bond the mould walls to the mould base; and *ii)* protect the collagen suspension from copper contamination. A high vertical temperature difference was achieved by exposing the top of the mould to the ambient environment.

A second freezing apparatus was designed to scale up production of collagen scaffolds. The second freezing apparatus was designed to provide four individually controllable freezing interfaces and had dimensions summarised in Figures 3.1c and 3.1d. Each interface was controlled with an OMEGA CN32PT-304 PID controller interfaced with Platinum software.

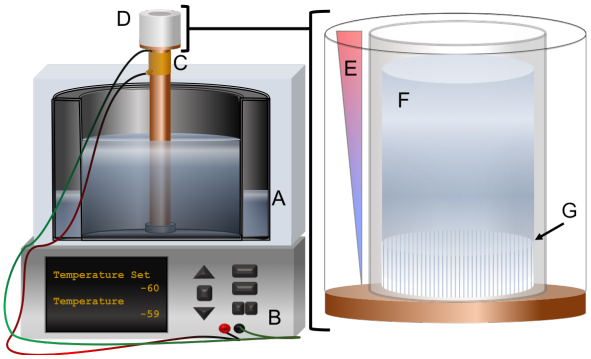

(a)

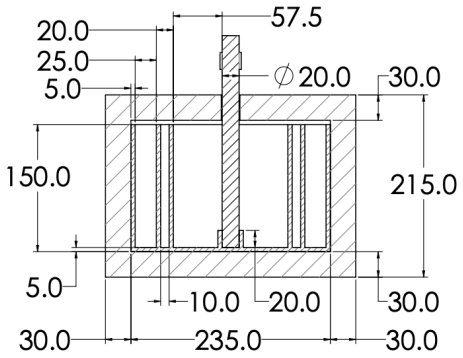

(b)

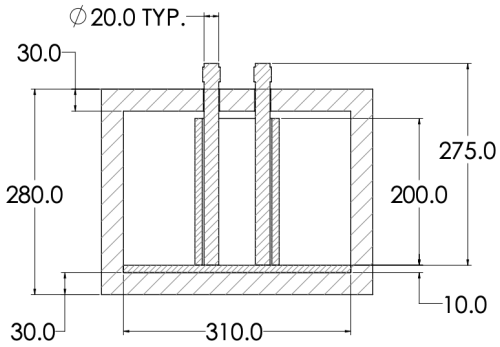

(c)

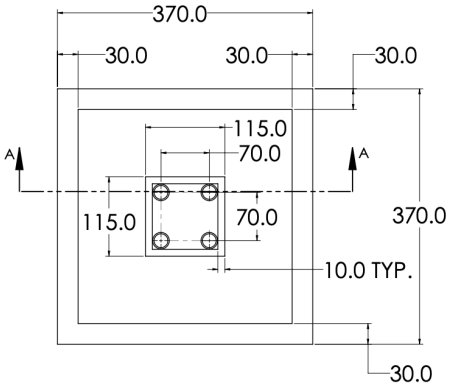

(d)

(e)

Fig. 3.1 Controlled freezing setup **(a)** and **(b)** original freezing apparatus **(a)** schematic of the setup *A.* cooling bath with liquid nitrogen (outer compartment) and ethanol buffer (inner compartment) *B.* PID temperature controller *C.* ring heater that regulates the temperature at the top of the cold finger *D.* mould *E.* vertical temperature gradient within the mould *F.* the collagen slurry *G.* solidification front in plane with the mould base **(b)** the dimensions of the original freezing apparatus **(c)** and **(d)** the second freezing apparatus dimensions **(c)** from a cross sectional side view and **(d)** top view **(e)** an image of the second freezing apparatus in use

3.1.2 Collagen scaffold production

A 1 wt% suspension of insoluble type I bovine dermal collagen (Devro) was prepared in a 0.05 M acetic acid solution (Sigma-Aldrich UK). The collagen was left to swell in solution at 4 ^{o}C for 24 hours prior to blending at 22,000 rpms for 6 minutes. Gas was then removed from solution using a vacuum chamber (VirTis SP Scientific Wizard 2.0) ramped from 750 torr to 2000 mtorr over 10 minutes. The slurry was allowed to equilibrate to room temperature (25 ^{o}C).

Isotropic

Collagen slurry was pipetted into standard 24-well plates (Corning, NY, USA), 2 mL per well (8 mm filling height). Well plates were placed on a teflon block (10 mm thickness) and frozen in a freeze drier (VirTis SP Scientific Wizard 2.0), shelf temperature -30 ^{o}C for 3 hours.

Aligned

Collagen slurry (9 ml) was pipetted into cylindrical polycarbonate moulds (20 mm internal diameter, 10 mm wall thickness, 30 mm height) bonded with RS black epoxy potting compound to a copper base (40 mm diameter, 2 mm thickness) as shown in Figure 3.1a. The mould was loaded onto the PID temperature controlled cold finger described in Section 3.1.1. The top of the mould was exposed to the ambient environment.

Lyophilisation

Once freezing was completed the mould was removed from the cold finger and immediately placed onto a cold freeze drier shelf (-30 ^{o}C) (VirTis SP Scientific Wizard 2.0) to avoid any melting. The scaffolds were dried at 0 ^{o}C under a vacuum of less than 100 mtorr for 20 hours.

Cross-Linking

Cross-linking was carried out using an EDC/NHS (1-ethyl-3-(3–dimethylaminopropyl) carbodiimide N-hydroxysuccinimide) chemistry (both reagents from Fisher Scientific). A molar ratio of 5:2:1 EDC:NHS:COOH groups in collagen has been identified as the standard 100% cross linking regimen [246, 255, 257]. Varied percentages of the standard e.g. 30% (15:6:10 EDC:NHS:COOH), were used to cross link the scaffolds in this thesis. Cross-linking reagents were dissolved in 95% ethanol and scaffolds were soaked for 2 hours within the mould. Scaffolds were washed (5 x 5 min) with deionised water.

After cross-linking, scaffolds were freeze dried (VirTis SP Scientific Wizard 2.0) a second time with a cooling rate of 0.2 ^{o} C min^{-1} to a primary freezing temperature of -20 ^{o}C. Drying occurred at 0 ^{o}C under a vacuum of less than 100 mtorr for 20 hours.

3.2 Collagen scaffold characterization

3.2.1 Thermal freezing profile

Temperature data was collected with k-type thermocouples at 4 second intervals. Thermocouples were adhered to the internal wall of the mould. Data was collected with an Omega RDXL6SD-USB data logger. All thermal profiles were visualised in MATLAB R2020a.

3.2.2 Imaging

X-ray micro-computed tomography (μCT) images (Skyscan 1172) were taken of each complete scaffold with a voltage of 25 kV, current of 138 μA and a pixel size of 5.46 μm. Reconstructions of μCT images were performed with NRecon software by Skyscan.

Scanning electron microscopy micrographs were taken of scaffolds. Prior to imaging, collagen scaffolds were sputter coated with gold for 2 min at a current of 20 mA. All micrographs were taken using a JEOL 820, with a tungsten source, operated at 10 kV.

3.2.3 Pore size

Quantitative pore size analysis was completed on regions of interest of 2.5 x 2.5 x 6.5 mm^3 from each region of the final reconstructed μCT image as shown in Figure 3.2. ImageJ software was used to binarise and watershed each of the nine sections and particle analysis was employed to compile pore size data. The pore sizes were analysed and visualised in MATLAB R2020a.

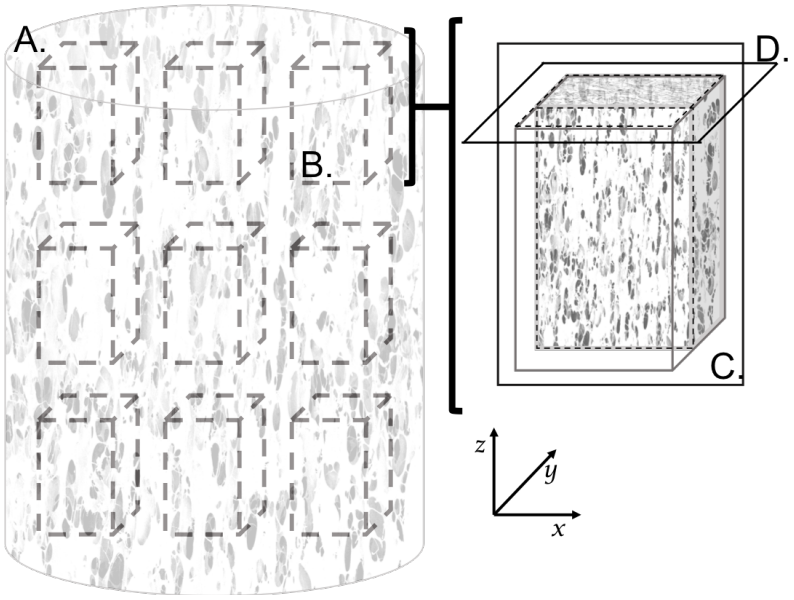

Fig. 3.2 Region of interest designations for freeze dried collagen scaffolds *A.* were analysed in nine regions of interest *B.* Pore size analysis was conducted on sequential slices along the x,y plane *D.* for each region of interest. Alignment quantification was conducted on sequential slices along the x,z plane *C.* for each region of interest.

3.2.4 Alignment

Fast Fourier Transforms were used to asses pore alignment according to the method laid out by Ayres et. al 2008 [258]. The μCT image stacks of the regions of interest shown in Figure 3.2 were sliced along the xz-axis (longitudinal plane) and 2D fast Fourier transform analysis was performed in ImageJ. Radial sums of the resultant transform were collected and pixel intensity for each radial direction was normalised by the minimum to enable comparison between samples. The normalised intensity profiles were plotted in MATLAB R2020a to show the degree of alignment for each radial direction. Here, the degree of preferential alignment was termed ε_{AOP} and utilised to compare between samples.

3.2.5 Pore Orientation

Fourier Transform analysis via the Directionality plug in for ImageJ was used to assess the lamellar orientation of resulting collagen scaffolds. Directionality histograms were calculated for each slice in the xz-axis (longitudinal plane) for each volume of interest shown in Figure 3.2. The mean lamellar direction and standard deviation were calculated for each volume of interest with Matlab R2020a.

3.2.6 Digital image correlation and strain analysis

Strain analysis was performed with Ncorr digital image correlation software run on MatlabR2020a. The reference image was redefined during diastole after each beat. The Green-Lagrange strain tensor was exported, and the principal strains were calculated through diagonalisation in MatlabR2020a. The principal strain calculation and physical representation can be seen in Figure 3.3.

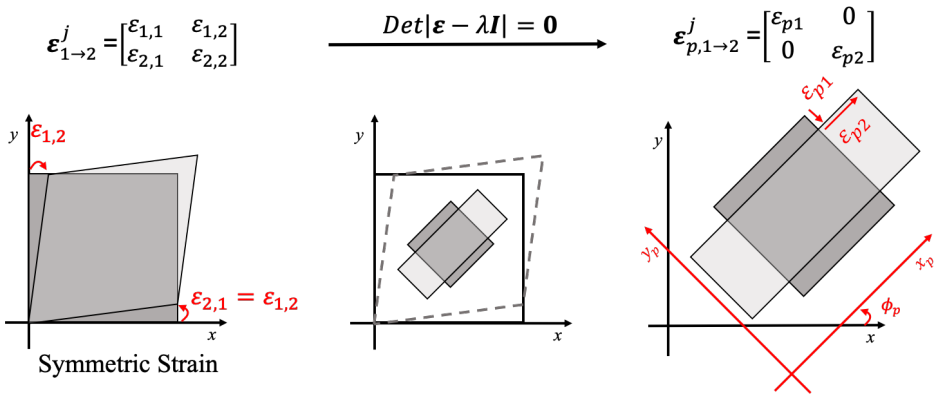

Fig. 3.3 Component strain calculations. ***left*** Shows the symmetric strain matrix with indicated undeformed (opaque) and deformed (translucent) unit square. ***middle*** Shows the deformation on the principal axis ***right*** Shows the principal strains and their directions as well as the principal axis rotation.

Chapter 4

The influence of thermal parameters on pore size and alignment

4.1 Introduction

Many tissues and organs display inhomogeneous and anisotropic structure. The anisotropy of native tissue contributes to specific function as the extracellular structure plays an important role in cellular response, phenotype, and adherence [110, 128, 247]. For this reason, there is great interest in developing tissue engineered scaffolds for regenerative medical application that mimic the ordered hierarchical structure of native tissue. Scaffold porosity and pore size has been shown to play a large role in supporting targeted cellular differentiation, orientation, and function. The pore size determines the availability of ligand binding sites. Pores need to be large enough to allow cellular migration within the construct. Pore sizes, however, also need to be small enough to establish a sufficiently high specific surface area, and a minimal ligand density for the binding of a critical number of cells within the scaffold [4, 259, 260]. Different cell types have varying pore size requirements. For example, while 100 μm pore diameter is optimal for cardiomyocyte function [261, 262], nerve cells require far smaller pores between 5 and 30 μm [263, 264]. It has been further shown that graded pore sizes can

be favourable for bone regeneration and interface tissue [261, 265–267]. Similarly, specific regenerative functions are influenced by pore size [4]. Sufficient porosity is required for the diffusion of nutrients into the scaffold and the removal of cellular waste products. While some studies have stated that pore sizes larger than 300 μm are necessary for vascularisation [146–148], excessive pore size may hinder vessel formation due to an inability of endothelial cells to bridge across the structural gap [268]. The specificity of pore size requirements for various tissue engineering applications demands a comprehensive and detailed understanding of the processing parameters that dictate pore size in the production of freeze cast scaffolds.

To date, the literature around freeze-cast collagen scaffolds has been split into two sectors pertaining to the production and control of isotropic and aligned structures. As discussed in Section 2.4.2, Pawelec et. al 2014 [179] introduced a universal parameter for the control of pore sizes in isotropic ice templated structures. In contrast, anisotropic freeze-casting pore sizes are controlled by the freezing front velocity induced during solidification [32, 142, 174, 185]. The great majority of work on understanding the anisotropic freeze casting system has concerned high concentration ceramics [32, 185, 188, 269]. Ice-templating is a largely physical process and, therefore, insights from studies in ceramic systems can be applied to the freezing of low concentration polymer suspensions, however, post solidification processing procedures such as sintering complicates direct comparisons. In recent years, researchers have introduced the technique to the production of ice templated polymer scaffolds for regenerative medical application. Two main procedures have been adopted to create anisotropic structures. The first is freezing with a constant set temperature at the base of the mould [151, 212, 218]. The second is freezing with a linearly decreasing set temperature at the base of the mould [142, 199].

Waschkies et al. 2009 [185] compared the freezing front progression of an alumina colloid for a single heat sink at the base of the mould held at a constant temperature and a dual heat sink set-up with linearly reduced temperatures programmed at both the top and bottom of the mould. It was found that using the constant base protocol, the freezing front velocity reduced as the front progressed away from the heat sink. However, a dual cold finger set-up with linearly decreasing temperatures linearised the freezing front progression. Significant differences between the final structures produced under each protocol were identified. The pore size and uniformity were found to be better controlled by the linearly decreasing temperature profile [185].

This chapter explores the relationship between freezing protocol and final structure for ice-templating with low wt% polymer suspensions. The constant base temperature and linearly decreasing base temperature protocols are compared. The resulting freezing front velocities, pore sizes, and alignment are used to characterise the fundamental differences between the two techniques, identifying the strengths and weaknesses of each approach and contextualising the results in the field of ice-templating.

4.2 Experimental methods

The basic methods for scaffold production and characterisation, discussed in Chapter 3 were followed unless otherwise stated. While the set freezing protocol varied, filling volume remained constant at 9 ml 1 wt% collagen suspension.

4.2.1 Scaffold production

Directional freezing of the collagen slurry was executed with the freezing apparatus presented in Section 3.1.1. A 1 wt% collagen suspension was prepared according to the protocol specified in Section 3.1.2. Two freezing protocols were executed; the base of the mould was either set *i)* to hold at a constant temperature ($dT_B/dt = 0$), or *ii)* to decrease at a constant rate ($dT_B/dt = k$) where k is constant. The experimental set up is summarised in Figure 4.1.

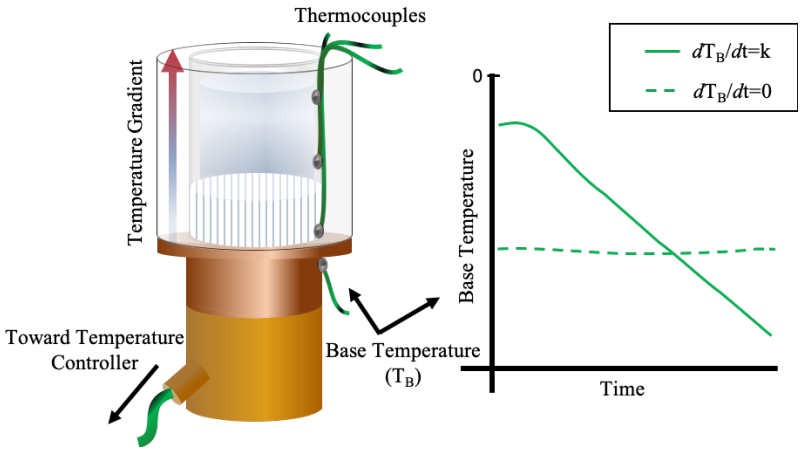

Fig. 4.1 Directional freeze-casting set-up illustrating the directional temperature gradient and the varied set thermal profiles at the base of the mould

i) The temperature at the base of the mould was held at a constant temperature (T_B). Five conditions were tested -10, -20, -30, -50, and -80 ^oC. For each condition, the cold finger temperature was stabilised prior to mould introduction and held constant for the duration of the freezing process.

ii) The temperature at the base of the mould was programmed to decrease at a constant rate (dT_B/dt) after mould introduction. The heat sink temperature was initially stabilised at -10 ^oC and held for 1 minute. The temperature was reduced at a constant rate for the duration of

the freezing process. Five rates were tested, namely -0.2, -0.5, -1, -3, and -5 ^{o}C min^{-1}.

Once freezing was completed, scaffolds were dried according to the protocol presented in Section 3.1.2.

4.2.2 Freezing time comparison between pure water and collagen suspension

The time until complete solidification (termed "freezing time") was recorded for the directional freeze casting of both D.I. water and 1 wt% collagen suspension prepared as described in Section 3.1.2. The freezing apparatus described in Section 3.1.1 was programmed to have a constant base temperature of -60^{o}C.

4.2.3 Measurement of solidification font progression

Temperature data were collected during the freezing process for each protocol to ensure that a vertical temperature gradient within the mould was achieved. Thermocouples (k-type) were placed at a height of 0 and 26 mm within the mould (total height 30mm). Temperature readings were taken at 4 second intervals during freezing.

Time-lapse footage was taken of the solidification progression for each experimental condition. Cylindrical polycarbonate moulds were filled with 9 ml of water. Water was chosen instead of the collagen suspension because both liquids have comparable thermal and solidification properties. The visual contrast, however, between pure ice and water is higher than between solidified and liquid collagen slurry [179, 193, 270]. The freezing progression was imaged at 10 second intervals with a GoPro Hero 5 camera as shown in Figure 4.2 for each

of the freezing protocols described in Section 4.2.1.

Time lapse footage was binarised with ImageJ software and the freezing front position and velocity were analysed with MATLAB R2020a.

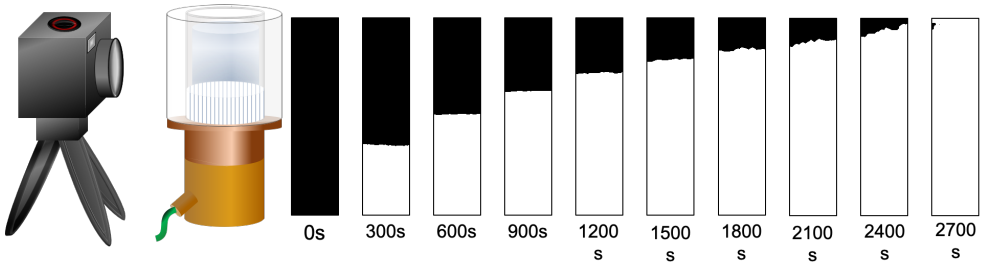

Fig. 4.2 Time-lapse tracking set up **(a)** images were taken of the ice propagation process at 10 second intervals. Shown is the binarised freezing front (white) progression every 5 minutes under the $T_B = -30^oC$ condition.

4.2.4 Structural characterisation

Qualitative pore size distributions were assessed via CTVox colour scale display. A 0.5 x 1 x 15 mm rectangular region of interest was selected across the middle of the scaffold and binarised in CTAN software via Otsu thresholding. The binary image was rendered in three dimentions in the CTVox software and the pores were colour coded according to size for visual assessment of relative pore size variation.

Quantitative pore alignment and pore size analysis was carried out as described in Sections 3.2.4 and 3.2.3 respectively.

4.2.5 Analysis

A minimum of three separate trials of each freezing condition were executed for both collagen scaffold production and freezing front progression analysis to ensure reproducibility.

4.3 Characterization of the solidification process

The solidification process was characterised. Time dependent temperature readings were recorded to verify the presence of a temperature gradient across the height of the suspension. The corresponding ice front progression behaviour was measured for each freezing condition and the freezing front velocity profiles were calculated. The solidification characteristics are later used to explain observed structural differences of resultant collagen scaffold for varying solidification conditions.

4.3.1 Freezing time comparison between pure water and collagen suspension

To enable a comparison between structural and freezing front data the freezing times of a 1 wt% collagen suspension and D.I. water were compared for solidification with a constant base temperature of -60 ^{o}C. No significant difference between freezing times observed as shown in Figure 4.3.

4.3.2 Influence of thermal parameters on solidification

Temperature readings taken from the bottom and top of the slurry during the freezing process are shown in Figure 4.4 for both a constant base temperature protocol (T_B =-10 ^{o}C shown

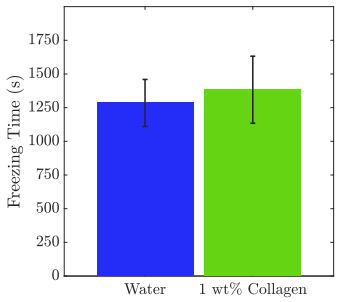

Fig. 4.3 The freezing times of D.I. water (N=4) and a 1 wt% collagen suspension (N=3), error bars show standard error

in Figure 4.4a) and a linearly decreasing base temperature protocol (dT_B/dt=-0.2 ^{o}C min^{-1} shown in Figure 4.4b). The slowest freezing conditions were selected for each freezing protocol to illustrate the minimum difference in temperature between the bottom and top of the slurry. While both freezing protocols produced significant vertical temperature differences, the linearly decreasing base protocol achieved a more stable temperature difference across the height of the slurry for the duration of the freezing process as seen in Figure 4.4c.

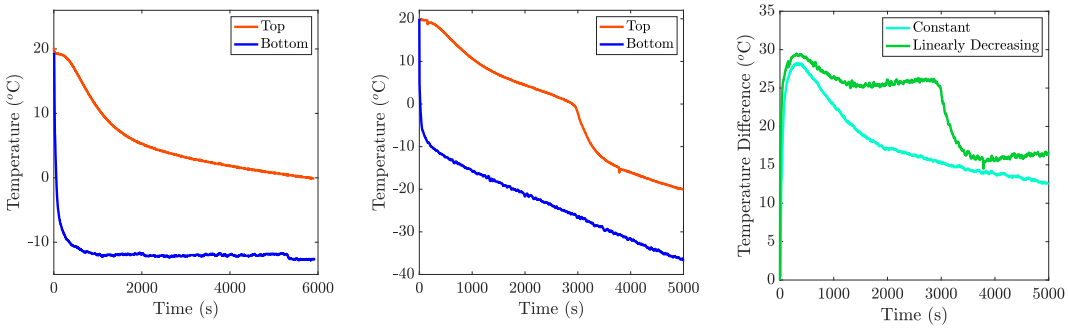

Fig. 4.4 Temperate profile during slurry solidification. **(a)** constant base temperature (T_B=-10 ^{o}C). **(b)** linearly decreasing base temperature (dT_B/dt=-0.2 ^{o}C) **(c)** vertical temperature difference for each protocol

Freezing Front Progression

The freezing protocol was found to significantly influence the freezing front progression. The constant base temperature protocol resulted in a nonconstant freezing front progression curve, such that, the freezing front initially progressed rapidly for approximately 200 seconds and subsequently slowed for the remainder of the solidification process for all base temperature conditions as shown in Figure 4.5a. It was found that the freezing front position curve amplitude was negatively correlated to the base temperature. The T_B =-80 ^{o}C protocol was found to freeze the fastest in 1070 seconds, while the T_B =-10 ^{o}C protocol had the slowest freezing time of 5830 seconds.

The rate of freezing for the constant temperature base condition was initially high and then found to rapidly reduce and gradually approach zero until solidification was complete as shown in Figure 4.5c. The average freezing front velocity was found to increase as the set base temperature decreased as shown in Figure 4.5c.

The linearly decreased base temperature condition resulted in a more linear front progression curve. The rate of cooling was found to be positively correlated with the rate of freezing front progression as shown in Figure 4.5b. The $dT_B/dt = -5$ ^{o}C min^{-1} condition had the shortest freezing time of 980 seconds while the $dT_B/dt = -0.2$ ^{o}C min^{-1} had the longest freezing time of 4540 seconds. It followed that the freezing front velocities observed for the linearly decreasing base temperature protocols were more constant than those of the constant base temperature protocol. Furthermore, the rate of temperature reduction was positively correlated with the freezing front velocity as shown in Figure 4.5d.

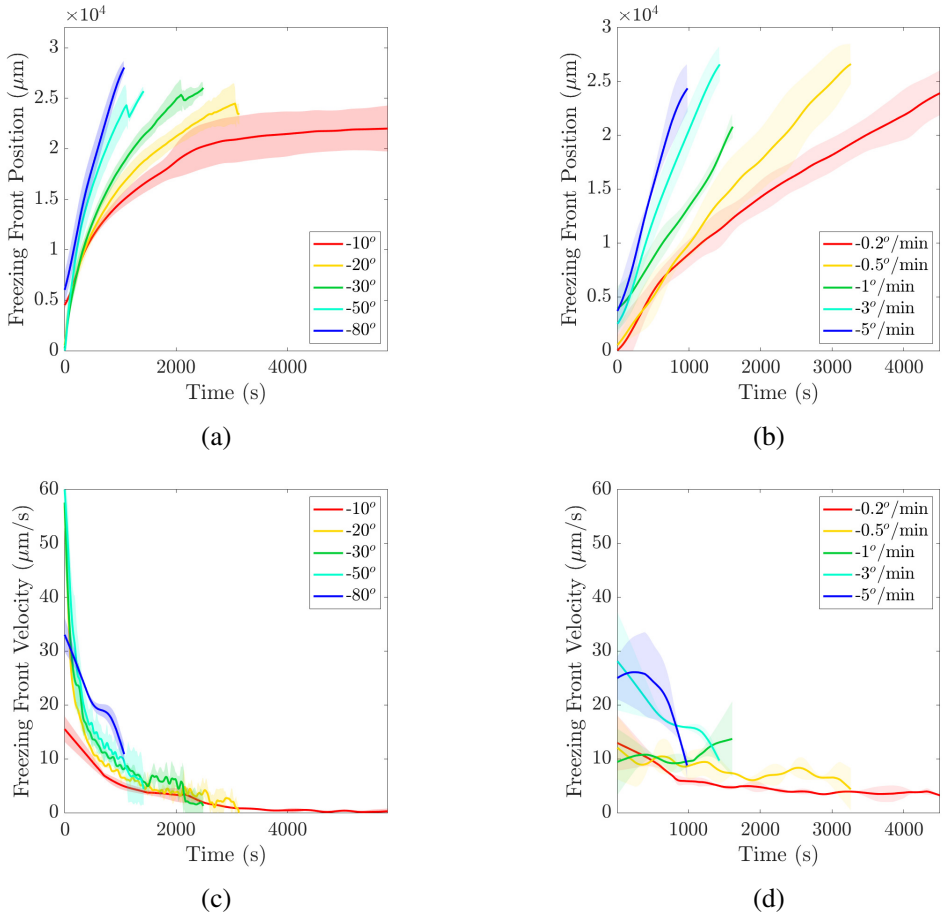

Fig. 4.5 Freezing front progression and velocity for different freezing protocols. The freezing front position over time for **(a)** the constant base temperature condition and **(b)** the linearly decreasing base temperature conditions. The freezing front velocity over time for **(c)** the constant base temperature condition and **(d)** the linearly decreasing base temperatures condition. Experimental repeats for the constant base temperatures T_B =-10, -20, -30, -50, and -80: N=3, N=4, N=4, N=4, N=3 respectively; and linearly decreasing base temperature dT_b/dt = -0.2, -0.5, -1, -3, and -5: N=3, N=3, N=4, N=3, N=3 respectively

4.4 Collagen scaffold architectural results

Reconstructed μCT images were used to asses the final scaffold architecture. The final pore architecture was characterised by pore size, defined as the diameter of the lamellar channels observed on the xy-plane (transverse) and the degree of lamellar alignment in the xz-plane (longitudinal). Figures 4.6a and 4.6b display the resultant lamellar architecture

for each freezing condition of the constant base temperature and linearly decreasing base temperature protocols respectively. All scaffolds had significant lamellar alignment in the xz-plane. The pore structures in the xy-plane display honey-comb like features, signifying that plate formation during freezing was avoided. It was observed that for both protocols variations in the base temperature influenced the pore sizes of the final scaffold as shown in Figure 4.6.

4.4.1 Degree of alignment

Fast Fourier transform analysis of μCT images from each scaffold were used to assess the degree of alignment achieved by each directional freezing condition. Figures 4.7a and 4.7b show that all scaffolds were aligned throughout the structure, irrespective of the base temperature protocol. It was found, however, that scaffolds produced with a linearly decreasing base temperature protocol were more consistently aligned, with an average ε_{AOP} of 0.52$\pm$0.07, than scaffolds produced with a constant base temperature, with an average ε_{AOP} of 0.45$\pm$0.09. The quality of structural alignment was found to be sensitive to the constant base temperature protocol. The set freezing temperature was found to have a negative correlation with alignment quality, such that the set base temperature of -10 ^{o}C produced the most aligned structure with an ε_{AOP} of 0.57$\pm$0.14 while the set base temperature of -80 ^{o}C resulted in the least aligned structure with an ε_{AOP} of 0.36$\pm$0.07. Conversely, for the linearly decreasing base protocol the quality of structural alignment had little variation across all freezing rates, with only the 0.2 ^{o}C min^{-1} protocol resulting in significant increase in alignment quality. Fourier analysis also revealed the direction of lamellar alignment. It was observed that lamellae were aligned perpendicular to the base of the mould and parallel to the induced temperature gradient for all freezing conditions as shown in Figure 4.7.

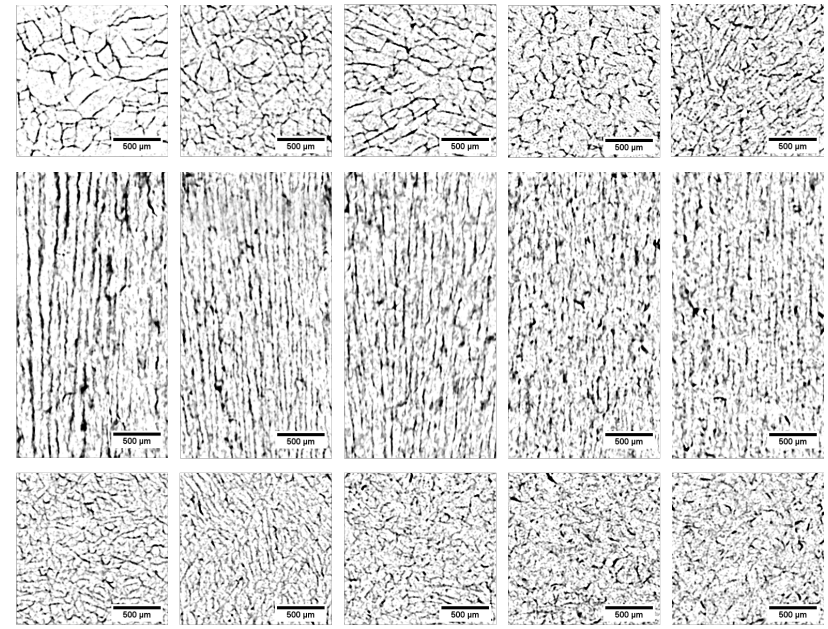

(a)

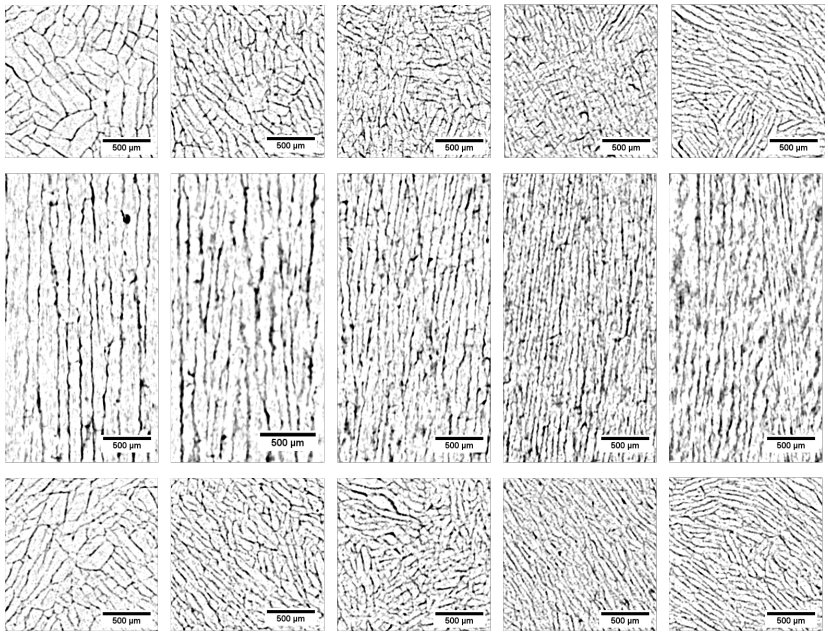

(b)

Fig. 4.6 The reconstructed μCT images of collagen scaffolds produced with **(a)** a constant base temperature and **(b)** a linearly decreasing base temperature protocol. For both **(a)** and **(b)** transverse cross sections of the pore structure at the base of the mould are depicted on the bottom, longitudinal cross sections are depicted in the middle and transverse cross sections of the pore structure at the top of the mould are depicted on the top. All scale bars are 500 μm

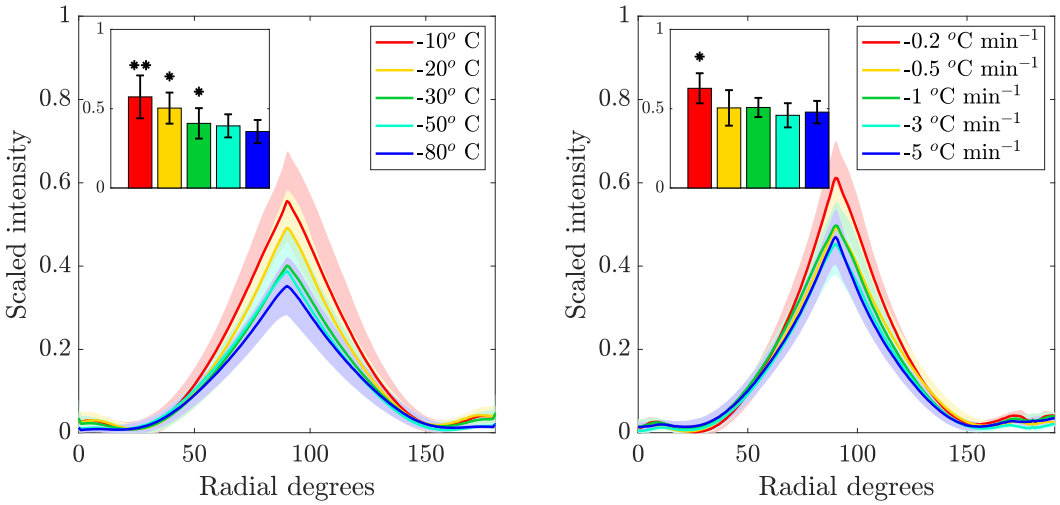

Fig. 4.7 Fast Fourier transform analysis of μCT slices along the xz-plane of each scaffold. Pixel intensity is plotted against orientation angle inserts display the maximum alignment value (ε_{AOP}) for each freezing condition **(a)** constant base temperature, * indicates statistical significance from the -80 ^{o}C condition, ** indicates statistical significance from both the -80 ^{o}C and -30 ^{o}C conditions **(b)** linearly decreasing base temperature, * indicates statistical significance from the -5 ^{o}C min^{-1} condition. Experimental repeats for the constant base temperatures T_B =-10, -20, -30, -50, and -80: N=3, N=3, N=3, N=3, N=3 respectively; and linearly decreasing base temperature dT_b/dt = -0.2, -0.5, -1, -3, and -5: N=3, N=3, N=3, N=3, N=3 respectively

4.4.2 Influence of thermal parameters on mean pore size

Variations in both the constant base temperature protocol and the linearly decreasing base temperature protocol were found to influence the pore size of the resultant collagen scaffold. For the constant base temperature protocol it was found that the temperature of the cold finger was positively correlated with the pore size as shown in Figure 4.8a. Similarly, for the linearly decreasing base temperature protocol, the rate of cooling, dT_B/dt influenced the final pore sizes as shown in Figure 4.8b. While both freezing protocols achieved a similar range of final pore sizes, the average pore size was more sensitive to changes in the linearly decreasing base temperature protocol than to changes in the constant base temperature protocol.

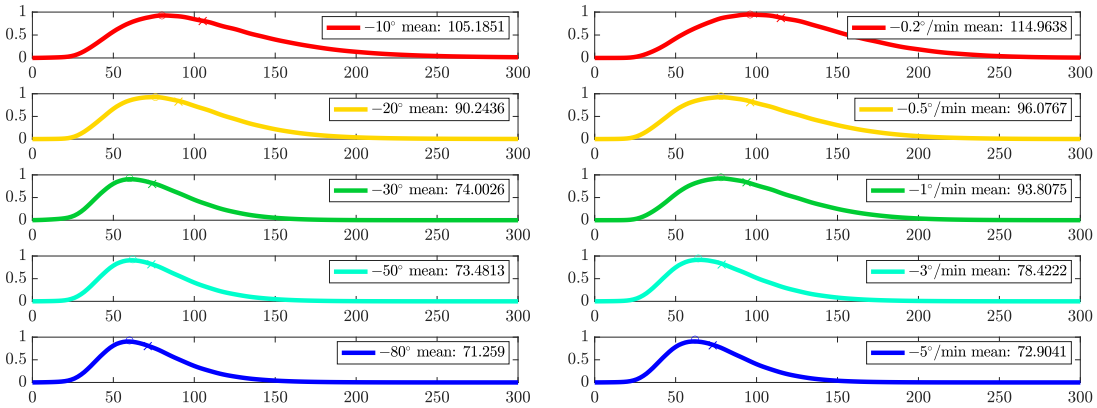

(a) (b)

Fig. 4.8 Pore size probability distributions for different freezing conditions. The mean and mode are shown on each distribution by a 'x' and 'o' respectively. **(a)** The pore size distributions for scaffolds produced under constant base temperature conditions. **(b)** displays the pore size distribution for scaffolds produced with a linearly decreasing temperature profile. Experimental repeats for the constant base temperatures T_B =-10, -20, -30, -50, and -80: N=3, N=3, N=3, N=3, N=3 respectively; and linearly decreasing base temperature dT_b/dt = -0.2, -0.5, -1, -3, and -5: N=3, N=3, N=3, N=3, N=3 respectively

4.4.3 Influence of thermal parameters on structural uniformity along the freezing direction

The pore size uniformity of the final collagen scaffolds varied significantly depending on the freezing protocol. Figure 4.9 displays longitudinal pore size representations of rapid freezing conditions ($T_B = -80\ ^o$C and $dT_B/dt = -5\ ^o$C min^{-1}) and slow freezing conditions ($T_B = -10\ ^o$C and $dT_B/dt = -0.2\ ^o$C min^{-1}) and highlights variations in intra-scaffold pore size uniformity. Both the $T_B = -80\ ^o$C and the $dT_B/dt = -5\ ^o$C min^{-1} conditions produced uniform structures as shown in Figures 4.9a and 4.9b respectively. Sow freezing rates, however, resulted in structural differences between freezing protocols. The structure frozen with $T_B = -10\ ^o$C displayed a large range of pore sizes across the height of the structure, with lamellar coarsening observed towards the top of the scaffold as shown in Figure 4.9c. Conversely, the $dT_B/dt = -0.2\ ^o$C min^{-1} structure displays increased pore size uniformity as shown in Figure 4.9d.

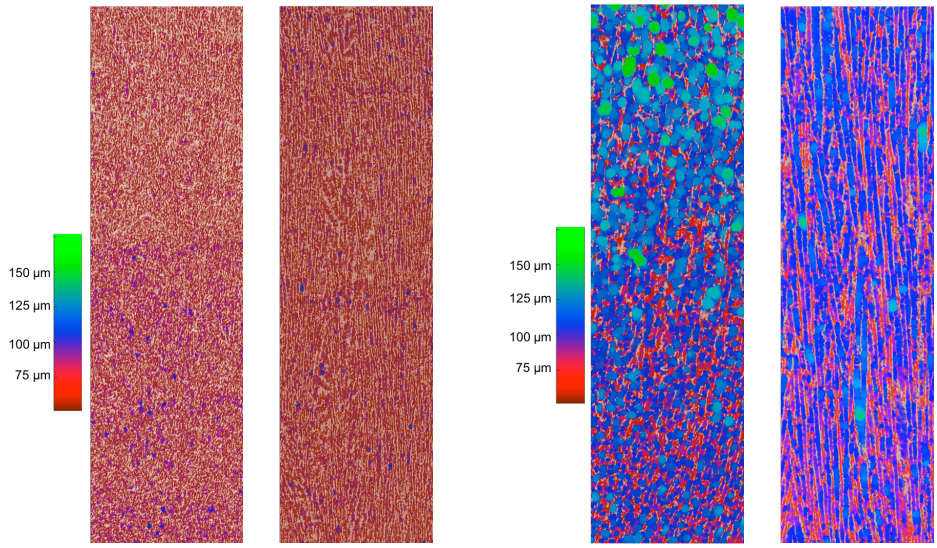

Fig. 4.9 Reconstructed μCT data taken from the middle of the scaffolds created under varied freezing conditions. Colours refer to pore size. **(a)** and **(c)** display resultant structures from a constant base temperature protocol **(a)** T_B=-80 ^{o} and **(c)** T_B=-10 ^{o}, **(b)** and **(d)** display the resultant architecture of the linearly decreasing base temperature protocols **(b)** dT_B/dt =-5 ^{o}C min^{-1} and **(d)** dT_B/dt =-0.2 ^{o}C min^{-1}.

Intra-scaffold structural uniformity was further assessed through comparison of the mean pore sizes observed at the top and the bottom of resultant collagen scaffolds for each condition. For rapid freezing conditions, little difference between regional pore sizes was observed. As freezing times increased, however, it was found that pore size uniformity was influenced by freezing protocol. While both protocols produced a positive correlation between the mean pore size of the total scaffold, the scaffolds resulting from the constant base temperature protocol displayed increased variability in pore sizes between the bottom and top as shown in Figure 4.10a. In contrast, the linearly decreasing base temperature protocol resulted in improved structural uniformity for conditions with longer freezing times as shown in Figure 4.10b. Both protocols resulted in a positive correlation between the mean pore size of the final scaffolds and the average pore size difference between the top and bottom of the scaffold as shown in Figure 4.10c. The constant temperature base protocol, however, resulted in significantly larger pore size differences across the height of the scaffold as freezing times increased.

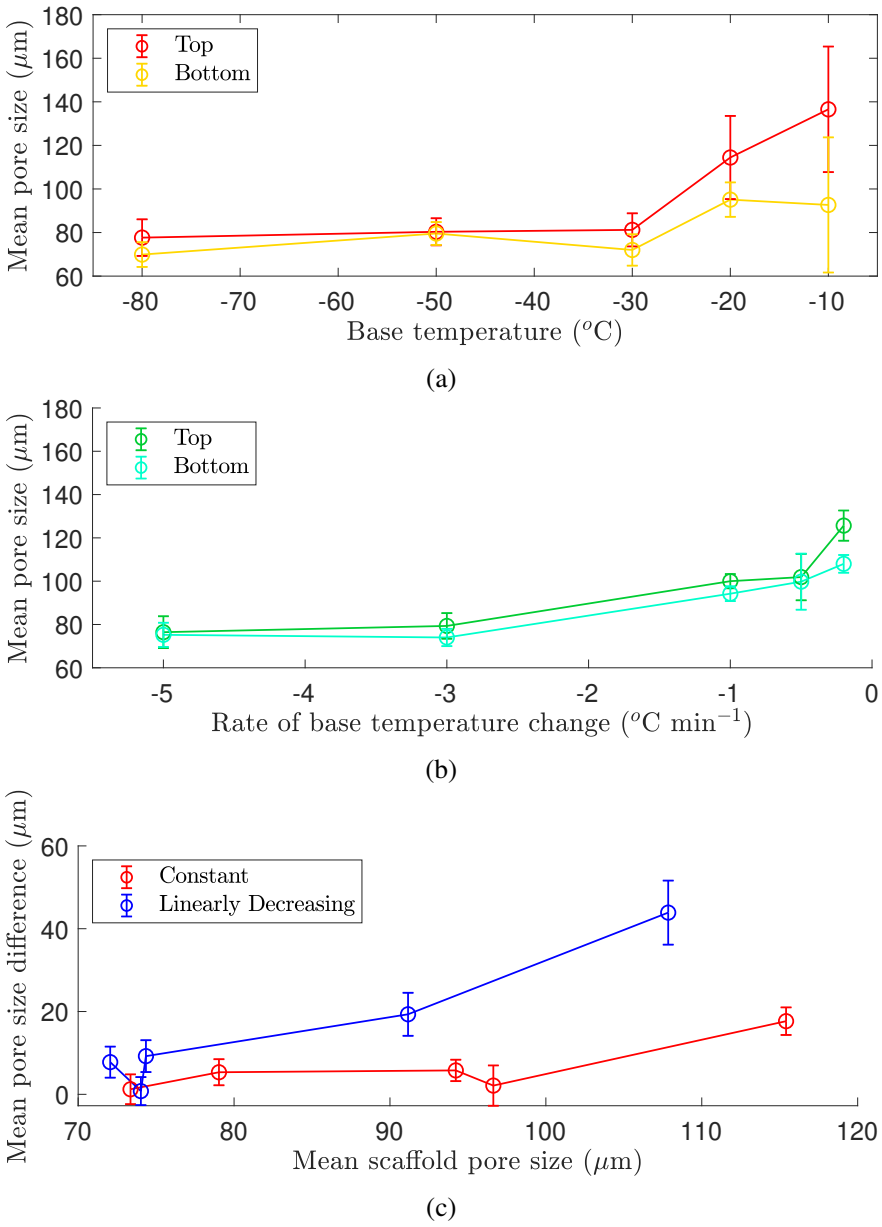

Fig. 4.10 Intra-scaffold pore size variation was assessed for each condition**(a)** constant base temperature freezing protocol and **(b)** linearly decreasing base temperature freezing protocol. Protocols were compared by visualising **(c)** the intra-scaffold pore size variation against the mean pore size of the whole scaffold.

4.5 Discussion

The influence of freezing protocol on the final architecture of large freeze-cast collagen scaffolds was explored. Two protocol types were compared. One being freezing with a

constant base temperature and the other being freezing with a linearly decreasing base temperature. Both cooling regimes resulted in significant vertical temperature gradients within the suspension and, consequently, a unidirectional pore structure with lamellae alignment perpendicular to the base of the mould. Each protocol, however, resulted in distinct freezing front progression profiles. Variations in each protocol were found to strongly influence the pore sizes of final collagen scaffolds. The linearly decreasing base temperature resulted in significantly increased control in final pore size as well as structure uniformity. In contrast, the constant temperature base protocol resulted in scaffolds with graded pore sizes that increased in size from the bottom to top of the scaffold.

The distinct pore compositions of each protocol can be linked to the fundamental process of ice formation and the thermodynamics of ice propagation during the freeze casting process. Specifically, both the freezing front velocity and the presence of a thermal gradient have been shown to have a significant influence on the final pore architecture of directional freeze-cast structures [32, 142, 207, 185]. These control mechanisms can be further explained by exploring the parameters that influence the thermodynamic process of ice growth.

4.5.1 Controlling the freezing front kinetics

Significant differences in freezing front progression behaviour was observed between the two freezing protocols presented. The constant base temperature protocol resulted in a logarithmic shaped freezing front progression curve with initially high freezing front velocities that rapidly reduced and slowly approached zero until the solidification was complete. On the other hand, the linearly decreasing base temperature protocol resulted in largely linear freezing front progression curves with increased stability in the freezing front velocity. These differences can be attributed to the efficiency of heat removal through the base of the mould for each protocol.

As the freezing front progresses away from the heat sink the efficiency of heat removal decreases proportionally. This is due to the insulating properties of the ice growing between the freezing front and the heat sink. Therefore, for the constant base temperature protocol, the heat sink efficiency will reduce as the front progresses causing the freezing front velocity to reduce over time, resulting in the progression curves observed in Figure 4.5a. For linearly decreasing base temperature conditions, the reduction in heat sink efficiency caused by the progression of the freezing front away from the heat sink is offset by reduction of the set temperature overtime. The consistent increase in cooling power therefore, dictates the rate of freezing front progression during the solidification process resulting in distinct freezing front velocities for each rate of cooling as shown in Figure 4.5d.

4.5.2 Pore alignment and orientation

It has been shown that a sufficiently high temperature gradient will dictate lamellar growth direction in ice templated collagen systems [142]. It was found that both the constant base temperature and the linearly decreasing base temperature protocols produced significant vertical thermal gradients within the suspension. The observed temperature difference shown in Figure 4.4c was established via continued heat removal from the base of the mould and convective heating from the ambient air at the top of the mould. The temperature difference observed for the linearly decreasing base temperature protocol was more consistent throughout the freezing process. This can be attributed to a continued increase in cooling power to offset the reduction in heat removal efficiency as the freezing front progressed away from the mould base. Despite the discrepancies in gradient amplitude for the two protocols, it was expected that the thermal gradients produced for both conditions would be sufficiently high to result in vertical lamellae alignment of the final collagen scaffold.

While the relationship between vertical temperature gradients and longitudinal lamellar alignment has been documented, to date little has been done to quantify the observed alignment. Fourier transform analysis was used to measure the degree of lamellar alignment for both the constant base temperature and the linearly decreasing base temperature protocols. The parameter ε_{AOP} was adapted from the work of Ayres et al. 2008 to illustrate the degree to which the lamella are aligned [258]. Furthermore, the x-axis location of the primary pixel intensity peak describes the orientation of lamellar alignment.

While all scaffolds were found to be aligned perpendicularly to the mould base throughout the structure as shown in Figure 4.7, the freezing protocol was found to influence the degree of pore alignment observed in the final scaffold. Slow freezing protocols were found to result in significantly increased pore alignment for both the constant and linearly decreasing base protocols. It was also found that the linearly decreasing base protocols resulted in more consistent alignment for each freezing condition. This result can be attributed to the improved stability in the vertical temperature difference during solidification facilitated by the linearly decreasing base temperature protocol as shown in Figure 4.4c.

4.5.3 Pore size

The pore sizes of freeze-cast collagen scaffolds were influenced by both freezing protocols. The linearly decreasing base temperature regimen, however, provided more specific control of the average pore size as shown in Figure 4.8. Additionally, the linearly decreasing base temperature protocol resulted in less variability in pore size across the final scaffold as shown in Figure 4.10. This result was caused by the differences in freezing front velocity profiles for the two protocols. As previously discussed in Section 4.5.1, the linearly decreasing base temperature protocol resulted in more constant freezing front velocities that were distinct

for each condition whereas the constant base temperature protocol resulted in nonconstant freezing front velocities that varied drastically during the course of freezing as shown in Figures 4.5c and 4.5d.

Variability in freezing front velocity will allow for different degrees of lamellar coarsening to occur in different regions of the final collagen scaffold, resulting in a structure with a large degree of pore size variation as illustrated in Figure 4.11a. Specifically, the pore sizes at the bottom of the structures produced with a constant base temperature protocol were observed to be finer than those produced at the top of the structure. This follows from the shape of the freezing front velocity curves. For all of the constant base temperature conditions, the freezing front velocity was high during initial freezing and rapidly reduce over time as shown in Figure 4.2. This pattern of freezing allows for increased horizontal crystal expansion during the later stages of solidification and subsequently a final scaffold architecture with larger pore sizes at the top of the structure as observed in Figure 4.10.

The linearly decreasing base temperature protocol was shown to produce more stable freezing front velocities during the solidification process due to the more consistent heat removal from the solid-liquid interface as shown in Figure 4.5d. Each distinct freezing front velocity resulted in different degrees of horizontal crystal expansion and, therefore, distinct pore sizes in the final collagen scaffolds. Furthermore, the consistency of the freezing front velocity during the solidification process resulted in reduced variability in pore sizes between the bottom and the top of the scaffold as shown in Figure 4.10c.

The relationship between pore size λ and freezing-front velocity v for directional freeze-casting has been described as $\lambda \propto v^{-n}$ and is further discussed in section 2.4.2. Recently, this relationship has been explored for freeze-cast collagen systems. The freezing front velocity

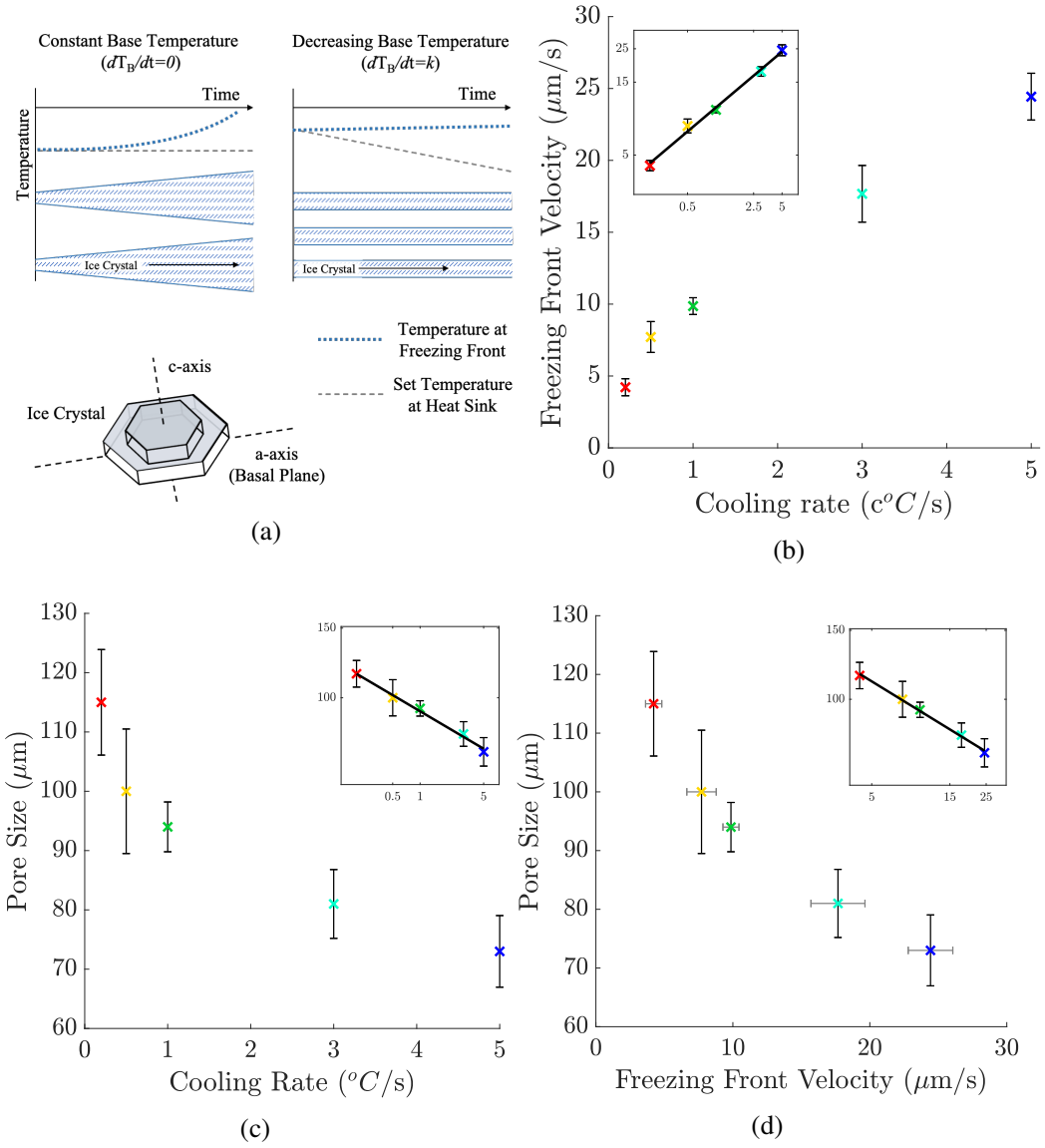

Fig. 4.11 Pore size and processing variable **(a)** illustration of the crystal growth and expansion for both freezing protocols **(b)** the relationship between freezing front velocity and set cooling rate. **(c)** the relationship between pore size and freezing rate $\lambda = kv^{-n}$ where n=0.13 **(d)** the relationship between pore size and freezing front velocity $\lambda = kv^{-n}$ where n=0.26

parameter has, however, been difficult to measure. Pawelec et al. 2017 used temperature data at fixed vertical intervals to extrapolate the measurement. While a power law relationship of n=0.85 was established for collagen systems in the presence of ethanol, none was observed without the antifreezer additive [142]. More recently, Divakar et al. 2019 studied the pore

sizes of directionally freeze-cast 2 wt% collagen scaffolds at varying cooling rates, however, no measurement of freezing front velocity was made. Instead the pore size was correlated to the set cooling rate at the base of the mould and the power law relations ship was observed with n=0.2 [199]. Although both studies confirm that pore size can be influenced through variation in set cooling rates, there is a need to further understand the relationship between freezing front and pore size in ice templated collagen systems.

The results presented here for the linearly decreasing base temperature protocol expand the understanding of the power-law relationship for the pore size and freezing front velocity in collagen scaffolds. The mean freezing front velocities and the rate of cooling were compared and each parameter was correlated to the resultant pore size of final scaffolds for each of the linearly decreasing conditions as shown in Figure 4.11c-4.11d. The relationship between the freezing front velocity (v μms^{-1}) and the cooling rate (c ^{o}C s^{-1}) were not found to be linear. Instead a logarithmic curve was observed where $c = v^{0.5}$ as seen in Figure 4.11b. It follows that while the pore size was related to both the rate of cooling and the freezing front velocity for each linearly decreasing base temperature condition, the exponent for power-law relationship for the freezing front velocity (n=0.26) was higher than that of the cooling rate (n=0.14). This is shown in Figures 4.11c and 4.11d respectively. These results are consistent with those presented by Divakar et al 2019 [199]. By identifying the relationship, however, between pore size of low wt% collagen scaffolds with the freezing front velocity, the relationship is independent of processing equipment. Furthermore, by demonstrating the relationship between the freezing front velocity and the cooling rate two things are achieved; *i)* contextualisation is provided for the work done by Divakar et al 2019, and *ii)* future experimental design can be informed to achieve targeted pore size control.

4.5.4 Comparison of freezing kinetics for anisotropic and isotropic systems

The power-law relationship between pore size and freezing front velocity for aligned freeze-cast structures is conserved for all applications (from high concentration metals and ceramics to low percentage polymers). The relationship is further supported by the thermodynamics of ice crystal formation, where slower crystal formation times allow for increased c-axis expansion and subsequently larger pore sizes. Taken together, the robust and reproducible relationship between pore size and the time scales of ice-crystal formation implies the possibility of a generalisation that could link the processing parameters used for anisotropic and isotropic ice-templating.

Pawelec et. al 2014 proposed a universal link between final pore size and time at equilibrium in isotropic freeze-cast collagen scaffolds. It was found that pore size was positively correlated with time at equilibrium with a relationship of $\lambda = \tau^{1/n}$ where n was found to be 4.8 ± 1.7 for isotropic collagen structures [179]. Time at equilibrium was defined as the time between nucleation and the completion of solidification, or the velocity at which the isotropic structure solidifies. Isotropic structures are produced in the absence of a high thermal gradient therefore, preferential crystal growth directions are not aligned. The degree of c-axis crystal expansion, however, still dictates the final pore size of resultant ice-templated scaffolds [32, 199]. Slower solidification and thus greater times at equilibrium result in a increased crystal expansion along the c-axis. Conversely, rapid freezing and low times of equilibrium provide limited opportunity for c-axis growth resulting in smaller pore sizes. The findings of Pawelec et. al 2014 are shown in Figure 4.12a [179].

The time at equilibrium parameter and the freezing front velocity parameter, therefore, describe and predict the degree of crystal expansion occurring during the ice-templating process

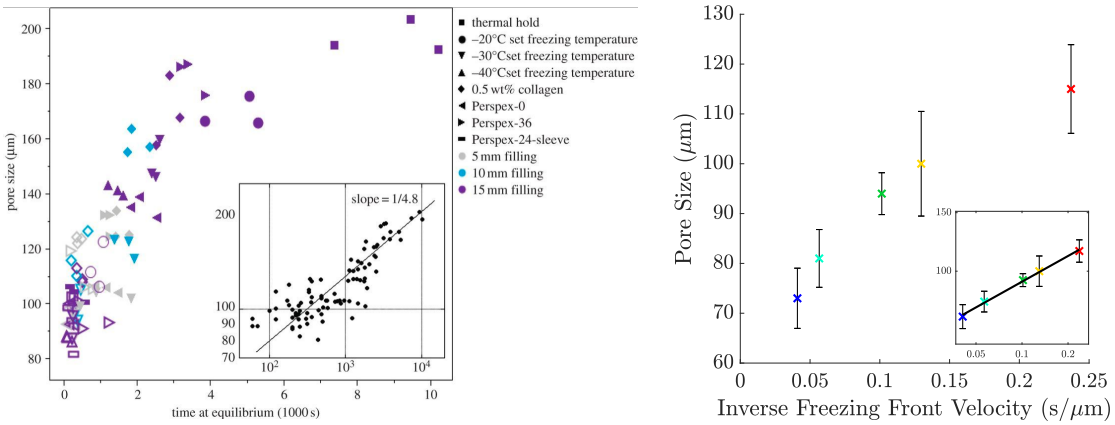

(a) (b)

Fig. 4.12 Freezing front velocity and time at equilibrium **(a)** the power law relationship between pore size and time at equilibrium for isotropic scaffolds, adapted from [179] **(a)** the power-law relationship between pore size and the inverse freezing front velocity

of isotropic and aligned structures respectively. The theoretical agreement between the two processes results in a union of the two halves of the freeze casting field, such that the freezing front velocity is inversely proportional to the time at equilibrium, $kv^{-n} = \tau$. By examining the relationship between pore size and inverse freezing front velocity a logarithmic curve was observed such that $\lambda = kv^{-n}$ where n=3.8$\pm$1.4 as shown in Figure 4.12b. The relationship was comparable to the resulting correlation between time at equilibrium and pore size for isotropic structures presented by Pawelec et. al in 2014 [179].

Considering the isotropic and anisotropic freeze casting systems in terms of the governing ice crystal formation kinetics provides a link between the two branches of the freeze-casting field and unites the relationship between freezing protocol and final scaffold architecture for two distinct structure types. The hypothesis presents further opportunities for tailored complex structure design that seamlessly combine isotropic and aligned regions of the same structure. This link enhances the possibility for interdisciplinary communication between the two distinct bodies of research.

4.5.5 Pore size uniformity

The pore size uniformity of each freezing protocol was assessed by comparing the mean pore size at the bottom of the scaffold to that at the top. At rapid freezing rates for both protocols, no pore size discrepancies were observed between the top and bottom of the resultant scaffolds. At slower freezing times, however, the linearly decreasing base temperature protocol was found to produce a higher degree of pore size uniformity across the final scaffold than the constant base temperature protocol as shown in Figure 4.10. This result is consistent with the robust relationship between pore size and freezing front velocity described above. The linearly decreasing base temperature protocol maintained a relatively constant freezing front velocity during solidification. The freezing front velocity profile of the constant base temperature protocol was, however, characterised by initially rapid front progression and a subsequent drop in freezing front velocity as the front moved away from the cold source, slowly approaching zero until the completion of solidification.

While pore size uniformity is required to establish homogeneity in permeability and mechanical properties across the scaffold [271–273], there has been recent interest in the production of graded scaffolds with variable pore sizes from the top to the bottom. Preiss et all 2012 developed a protocol to produce graded freeze cast zirconia toughened alumina structures [269]. Graded ceramic structures can be used as filtration devices [274], planar solid oxide fuel cells [275], or as preforms to infiltrate with a second phase to build a graded composite [276]. From a tissue engineering perspective, graded polymer scaffolds, such as those produced under the constant base temperature protocol, could be used in vitro as cell sieves, layered tissue culture systems to test drug delivery or co-culture systems [277–280]. Additionally, increased interest has been paid to the design and production of complex hierarchical tissue morphologies for regenerative medical applications because graded scaffolds form an ideal structures for interface tissue repair [280].

4.5.6 Conclusion

Two freezing protocols, a constant and linearly decreasing base temperature, were compared in the production of aligned freeze-cast collagen scaffolds. Resultant collagen scaffolds were found to be aligned irrespective of protocol. Slower freezing protocols, however, were found to improve the degree of alignment present in the final structure. Overall, the linearly decreasing base temperature protocol produced more consistent alignment irrespective of freezing rate. On the other hand with the constant base temperature protocol, the degree of alignment was found to increase with the set freezing temperature. Control over the degree of alignment has not previously been reported and could be an important parameter in tissue engineering as tissue structure and organisation has been shown to influence function. Irrespective of protocol longer freezing times produced increased pore sizes. The linearly decreasing base temperature protocol designated more specific control over the final scaffold pore sizes. The constant base temperature protocol was found to produce graded pore structures with larger pore sizes observed at the top and smaller pore sizes at the bottom.

The relationship between pore size and freezing front velocity for 1 wt% collagen scaffolds was identified to be a power law relationship with an exponent of n=0.26. This result was contextualised within the literature and compared to the isotropic control parameter time at equilibrium. By considering both systems through the perspective of fundamental physics, the control parameters were compared and a fundamental link was postulated. The relationship between set cooling rate and freezing front velocity was also explored to enlighten experimental design for the fabrication of ice-templated collagen scaffolds with tailored pore sizes and distributions. Taken together, the improved understanding of processing parameter influences on aligned ice-templated collaged scaffold structure will improve the specificity with which scaffolds can be tailored to fit specific application criterion.

Chapter 5

Design and control of complex hierarchical structures

5.1 Biomimetic collagen scaffolds with tailored and controlled complex architectures

The fabrication of regenerative scaffolds that replicate the structure and function of native tissue has proven a great challenge in recent years. An increasingly large body of literature has demonstrated the importance of organ-specific structure at multiple length scales [25, 182, 281–283]. The biomimetic and physiomechanical properties of regenerative scaffolds have also been shown to improve cellular phenotyping [67], cellular function [50], native matrix deposition [4], and regenerated tissue function [96]. For these reasons the efficacy of engineered regenerative constructs is greatly influenced by the capacity of engineered scaffolds to replicate the complex native extracellular environment [6, 25, 50, 282–287].

Precise architectural control of regenerative medical constructs has been attempted through a range of techniques. These include laser patterning [50], electrospinning [288], 3D printing

[25], and ice-templating [150, 289], however, significant limitations have been reported. Bioprinting has demonstrated achievements in producing precisely controlled complex extracellular features at a macroscopic scale. This technique, however, is greatly limited by spatial resolution and cannot replicate nanoscale and micro-scale surface features [152]. Lyophilization and electrospinning have been shown to successfully produce hierarchical structures with high resolution at multiple length scales, although, to date there is a distinct lack of precise control over complex macroscopic architecture [142, 199, 211].

Recent improvements in understanding the importance of spatial specificity and controlled complex architecture in tissue engineered scaffolds has resulted in increased interest in the application of 3D bioprinting. While specific control of scaffold structure has been achieved through 3D printing techniques due to the extrusion process, 3D printed scaffolds typically comprise of smooth solid struts that do not promote cellular adhesion [152, 290, 291]. Lee et al. 2019 addressed this issue by incorporating gelatin microparticles from the support bath into 3D printed collagen, resulting in a textured strut surface [25]. Improved cellular integration was achieved when compared to tradition 3D printed constructs with no surface morphology, though struts maintained a solid composition, determined by the diameter of the extrusion needle. This characteristic limited the degree of scaffold permeability and reduced cellular interaction across the structure [152]. Wang et al. 2020 developed a novel integrated method (Freeze Fresh) that combines 3DP and freeze-casting to produce 3DP scaffolds with microscale architecture and high permeability characteristic of freeze cast structures while maintaining a printed strut design [152]. However, the dependence of the technique on 3D printing technology means it is limited by the range of bio-inks available, high cost and protocol complexity.

Freeze-casting circumvents the complexity and high cost of 3D printing by leveraging the natural thermodynamics of the ice solidification process to define the multi-scale hierarchical architecture of resultant scaffolds. Manipulation of physical and chemical conditions during freezing has been shown to influence pore size [32, 179, 186], wall thickness [187], surface roughness [188], and interconnectivity [117, 188]. Some architectural diversity has also been demonstrated through ice templating, including isotropic [117, 130, 179], unidirectionally aligned [30, 142, 199], and radially aligned [199, 213, 289] pore morphologies. Furthermore, a strong relationship between thermal gradients and pore orientation has been established [199, 211, 292]. Techniques have also been established to dictate the surface morphology of ice templated structures through patterning of the freezing surface [150, 188]. To date, despite the well-defined thermodynamic process no specific three dimensional control over complex lamellar orientation has been reported.

The robust connection between the architecture of the final porous structure and the physics of ice growth has motivated a large body of research into mathematical modelling of the freeze-casting process. Recently, one dimensional particle diffusion models [293], phase field simulations [294, 295], molecular dynamical simulations [296], and finite element methods [193] have been developed to study the ice-templating process. These simulations have contributed an improved understanding of the ice-templating process and can be used as a tool in the experimental design of freeze-cast materials. Huang et. al. 2018 presented a phase-field model that accurately described the dendritic behaviour of anisotropic unidirectional crystal growth [294]. The simulated results accurately described the resultant wall thickness and lamellar wavelength of experimentally produced freeze-cast silica carbide structures [294, 297]. The phase-field approach is mathematically complex and computationally expensive making it liable to limitations in processing power and difficult to apply as an experimental design tool. Conversely, Husmann et al. 2015 used a simple finite element

approach to predict pore structure of isotropic scaffolds based on the cooling profile within various moulds. While this approach is less exhaustive, the simplicity of the approach makes it a useful and accessible tool in experimental design [193].

Here, a relationship between the final freeze-cast scaffold architecture and thermal gradients present within the mould during freezing is hypothesised. It is theorized that the lamellar structure of collagen scaffolds can be controlled by manipulation of the thermal environment during freezing. It is further hypothesised that a simple finite element model of the time dependant solidification processes can be utilized as a predictive tool to indicate the final three dimensional structure of ice templated collagen scaffolds. The aim of this chapter is, therefore, two fold. The first objective is to develop a controllable freezing apparatus in which an asymmetric thermal environment can be achieved and collagen scaffolds with complex lamellar architectures can be produced. The second objective is to develop a representative three dimensional finite element model that can recapitulate the thermal environment during the freezing process and therein predict the final lamellar structure of ice templated collagen scaffolds. To achieve these goals a novel technique is presented to provide fine control over final lamellar orientation in freeze-cast collagen scaffolds. The method utilises controlled heat sources integrated into casting moulds to enable full three dimensional control of the thermal environment during solidification, and is presented alongside a simple but predictive finite element simulation. The simple finite element model illustrates the dynamic thermal environment during the solidification process and predicts the lamellar architecture of resultant collagen scaffolds. The agreement between the simulation and the final scaffold architecture enables the computational design and control of freezing to give bespoke, specifically designed structures with complex pore morphologies. Three distinct thermal environments of increasing complexity are demonstrated to illustrate design specificity. Initially a no source condition is tested to verify the model's predictive capabilities.

Subsequently, two complex thermal environments are implemented and the influences on final pore architecture are compared to simulated thermal environments. Finally, the thermal processing conditions are varied to demonstrate localized control of scaffold structure. The aim of this work is to; *i)* introduce a novel experimental protocol to provide targeted and precise control of lamellar orientation in freeze-cast collagen scaffolds for regenerative medical applications; and *ii)* demonstrate a simple predictive simulation tool that, when applied to the novel heat source moulds presented, can be used to design and produce freeze-cast structures with specific, complex, multidirectional lamellar orientations.

5.2 Experimental methods

The basic methods for scaffold production and characterization, found in Chapter 3 were followed unless otherwise noted. While the set freezing protocol varied, filling volume remained constant at 9 ml of 1 wt% collagen suspension.

5.2.1 Design and fabrication of a novel multidirectional freeze casting system

Custom cylindrical polycarbonate moulds were designed to facilitate complex thermal gradients within the mould during collagen slurry solidification. Moulds were constructed of three main parts, an external polycarbonate tube (height 30 mm, external radius 20 mm, internal radius 12 mm), a slurry contacting polycarbonate tube (height 30 mm, external radius 12 mm, internal radius 10 mm), and a copper disc (height 2 mm, radius 20 mm). The external tube was bonded with RS black epoxy potting compound to the copper base, while the slurry contacting tube was fit snugly within the external tube, and free to slide in and out of the mould as shown in Figure 5.1a.

Heaters were incorporated into the external surface of the slurry contacting tube. Two 8x8 mm square depressions 1 mm deep were machined into the external surface of the slurry contacting tube at the locations shown in the model geometry Figure 5.1b. Patch heaters were constructed of PT100 (RS) resistors adhered to the centre of an 8x8 mm square of copper foil. The foil and resistors were glued into the slurry contacting tube with Electrolube Thermal Bonding Epoxy. The power outputs of the resistive heaters were individually controlled with a Tenma 72-10480 DC power supply set to implement a constant current across the resistors for the duration of the freezing process.

5.2.2 Collagen scaffold production

Directional freezing of the collagen slurry was executed with the freezing apparatus presented in section 3.1.1 with a base temperature set at -60 ^{o}C. A 1 wt% collagen suspension was prepared according to the protocol specified in section 3.1.2. Three thermal conditions were implemented to assess the effects of complex thermal gradients on ice-templated collagen scaffold architecture, namely *i)* a no source condition; *ii)* a single source condition where 0.075 A were applied to the P_T heater; and *iii)* a dual source condition where 0.075 A were applied to both the P_T and P_B heaters respectively. Additionally, the heat source power output was tested as an architectural control parameter. The power output for the single source condition was set to 0.1, 0.2, 0.55, and 0.65 W. Temperature data were collected for each condition with k-type thermocouples at 4 second intervals.

Once freezing was completed, scaffolds were dried according to the protocol presented in section 3.1.2.

5.2.3 Model set-up

Comsol Multiphysics 5.0 was used to create a simple finite element phase change simulation of the solidification process during freeze-casting. Novel heat source moulds were drawn and meshed within the simulation and boundary conditions were applied for experimental consistency. Three thermal environments were simulated for comparison with experimental results.

Geometry and material properties

A four-part geometry was drawn in Comsol Multiphysics 5.0. The mould was modelled in three parts with a disc base, an inner slurry contacting tube, and an external tube with dimensions described in Figure 5.1b. The external surface of the slurry contacting tube was partitioned with two square regions of 8 mm width to model the heat sources in the more complex simulations. The collagen slurry (9 ml) was modelled as a cylinder of height 28.5 mm nested within the internal tube. Thermal ties were imposed on all contacting surfaces with the form union function. The geometry was meshed with a physics defined 'finer' tetrahedral mesh, with a maximum element size of 1.5 mm and a minimum element size of 0.1 mm.

Materials properties were imposed for consistency with experimental conditions. The thermal properties of copper were imposed onto the disc at the base of the mould and the thermal properties of polycarbonate were imposed onto both of the tubular mould parts shown in Figure 5.1b. The thermal properties of collagen slurry have been shown to behave comparably to those of water [193, 270]. The nested cylinder was, therefore, assigned phase change properties of water, shown in Table. 5.1 and Figures 5.1c-5.1d.

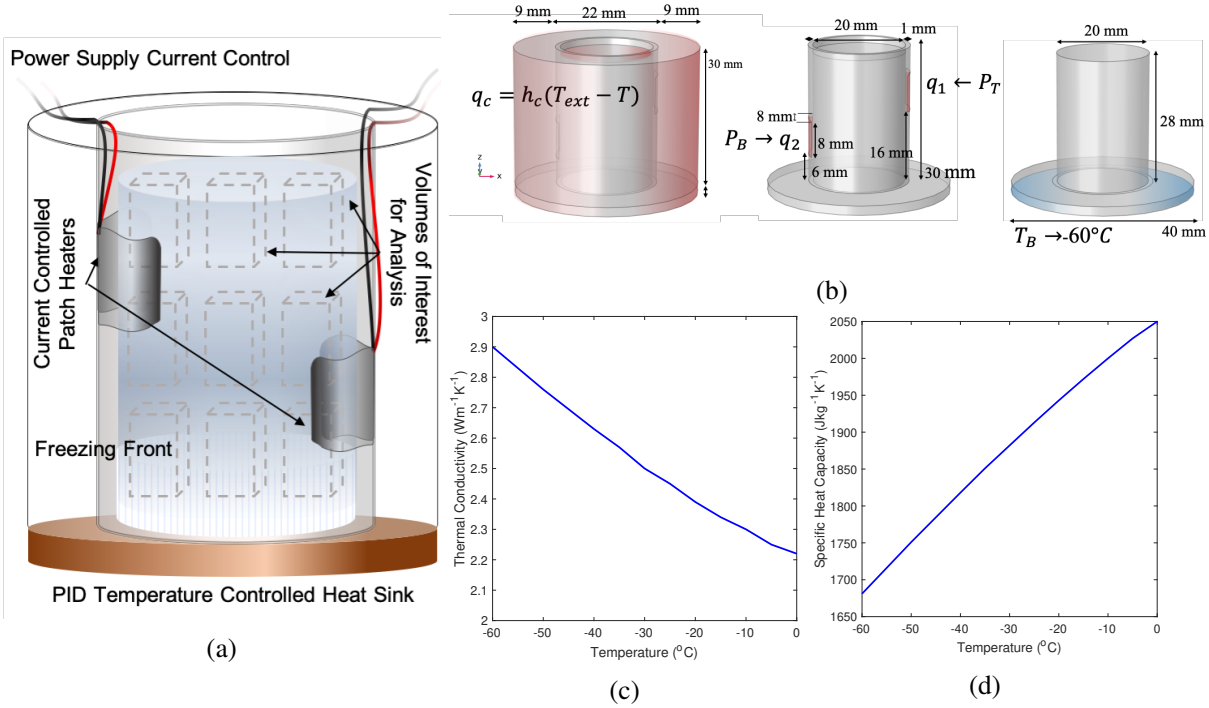

Fig. 5.1 Experimental methods and simulation. **(a)** Novel heat source moulds, cooled via PID controlled heat sink. Volumes of interests for analysis are depicted within the slurry. **(b)** Experimentally analogous boundary conditions and four part mould-slurry geometry imposed in the finite element simulation. **(c-d)** Temperature dependant material properties. **(c)** Thermal conductivity of ice. **(d)** Specific heat capacity of ice.

Table 5.1 Material property assignments

Material	Thermal Conductivity k (W m^{-1} K^{-1})	Density ρ (kg m^{-3})	Specific Heat Capacity C_p (J kg^{-1} K-1)
Polycarbonate	0.2	1200	1200
Copper	401	8960	390
Slurry$_l$	0.6	997	4200
Slurry$_s$	$k^i(T)$	918	$C_p^i(T)$

Boundary conditions

An initial temperature of 22 ^{o}C was imposed on the whole simulation geometry. Experimental conditions were simulated through boundary conditions. Convective heat flux was used to simulate the heat transferred between the ambient air and the model geometry,

$$q_c = h_c(T_{ext} - T)$$

where T_{ext} is the ambient temperature considered, to be 24 ^{o}C, T is the temperature of the air contacting surface, and h_c is the convective coefficient. The convective coefficient has been shown to lie between 5 and 30 $\mathrm{Wm^{-2}K^{-1}}$ [193, 298]. It was found that $h_c = 27.5$ $\mathrm{Wm^{-2}K^{-1}}$ produced the most experimentally consistent results. A Dirichlet boundary condition ($T_B = -60^o$C) was imposed at the base of the mould to act as a heat sink. The Dirichlet boundary condition was imposed with a step function that transitions from the initial temperature to the heat sink temperature in 0.1 seconds, to avoid discontinuities in the simulation.

Three thermal profiles were assessed where different heat source conditions were imposed onto the square regions on the external surface of the slurry contacting tube (P_T,P_B Figure 5.1b). Each region was set to establish one of three conditions namely: the no source condition, $P_T = P_B = 0$, the single source condition, $P_T = 0.55$ W, $P_B = 0$ W and the dual source condition $P_T = P_B = 0.55$ W. The boundary conditions of the simulation are summarised in Figure 5.1b.

Time-dependent simulation

A time period of 3000 seconds was simulated, where temperature values were calculated at 1 second intervals. The three dimensional diffusion equation was used to calculate the

temperature at each time point,

$$\rho C_p \frac{\partial T}{\partial t} + \nabla(-k\nabla T) = Q \tag{5.1}$$

where, T is temperature, t is time, Q is the sum of all heat sources in the system and ρ, C_p and k are the thermal properties of the material, summarised in Table 5.1. During the phase transition the respective material properties are combined with the phase change function (equation 5.6) to facilitate a smooth transition between phases,

$$\sum_{i=1}^{N} \theta_i = 1 \tag{5.2}$$

$$\rho = \sum_{i=1}^{N} \theta_i \rho_i \tag{5.3}$$

$$k = \sum_{i=1}^{N} \theta_i k_i \tag{5.4}$$

$$C_p = C_{p,1}(1-\alpha(T)) + C_{p,2}\alpha(T) + L_{i\rightarrow i+1}\frac{d\alpha}{dT} \tag{5.5}$$

where,

$$\alpha = \frac{1}{2}\frac{\theta_{i+1}\rho_{i+1} - \theta_i \rho_1}{\rho} \tag{5.6}$$

$\alpha(T)$ ranges from 0 to 1 for pure liquid and pure solid elements respectively. In the above equations, material properties, density, thermal conductivity and specific heat capacity are denoted, ρ, k, and, C_p respectively. Additionally, N represents the number of phases and θ represents the phase proportion, eq. 5.2. Work done by Pawelec et al. 2014 demonstrated that the phase transition for a 1 wt% collagen suspension occurs gradually across a broad temperature range centred around 0 ^{o}C. These results show that the majority of the entropy shift that occurs during the phase transition is contained within a 4 ^{o}C interval [179]. There-

fore, the simulated phase transition in this work was defined to occur during a 4 ^{o}C transition interval, during which latent heat (333.5 kj kg^{-1}) was released.

The diffusion equation 5.1 was solved at each time step in conjunction with relevant phase change properties and the resulting temperature for each mesh element was stored. The final time-dependent temperature and temperature gradient solutions for all three of the thermal conditions described above were exported for analysis.

5.2.4 Analysis and model validation

The simulated and experimental freezing processes were analysed for comparison. Time-dependent temperature data from regions of interest were collected after the completion of the simulation and compared to the temperature date collected experimentally. Furthermore, the local temperature gradient profile at the time of solidification was collected from the simulation results and compared to the final lamellar structure of the experimentally produced freeze-cast collagen scaffolds.

Orientation characterization

Scanning electron microscopy micrographs and X-ray micro-computed tomography (μCT) images were taken according to section 3.2.2 for orientation analysis. Reconstructed μCT data were segmented into volumes of interest as shown in Figure 5.1a.

Fourier Transform analysis via the Directionality plug in for ImageJ was used to assess the lamellar orientation of resulting collagen scaffolds. A directionality histogram was calculated for the x-z plane for every slice in each volume of interest. The mean lamellar direction and standard deviation were calculated for each volume of interest with Matlab R2020a.

Identification of predictive indicators

The simulated time dependent temperature data was analysed in Matlab R2020a for comparison with experimental results. Time dependent temperature data were averaged over a 2 mm cubic region at specific locations to correlate with thermocouple placement during experimental solidification.

Cross sectional thermal profiles were visualised by sectioning the slurry component of the geometry such that the average temperature was taken across the y-direction for the range y=-1 mm to y=1 mm. The resulting temperatures on the x-z cross section were visualised as a contour plot with intervals of 5 ^{o}C at various time points.

The temperature gradient directions at the time of transition between the liquid and solid phase ($t_{l\rightarrow s}$) were extracted for comparison with experimental results. To avoid the localized effects of latent heat release, $t_{l\rightarrow s}$ was set to be the time at which each mesh element reached 0.5 ^{o}C. Gradient fields were visualised on the cross section as above and averaged over each of the nine areas of interest produced by dividing the x and z-axes into thirds for comparisons with experimental analysis as shown in Figure 5.1a.

5.2.5 Statistics

Three repetitions of each freezing condition were executed. All data are reported as the mean $\pm$ standard deviation. A confidence interval of 95% was used throughout.

5.3 Results: Unidirectional alignment and simulated predictions

Resultant lamellar architecture of scaffolds produced under the no source freezing condition were compared to simulation results to assess the predictive properties of the numerical model. The time dependent temperature profile as well as the thermal gradient field at $t_{l\rightarrow s}$ were expected to indicate the thermal behaviour of the solidifying slurry, and predict the final lamellar orientation of the resultant ice-templated collagen scaffold.

5.3.1 Heat transfer coefficient assignment

The heat transfer coefficient (h_c) describes the thermal interaction between the modelled geometry and the external environment. It has been shown that the value lies within a range of 5 to 30 $\mathrm{Wm^{-2}K^{-1}}$ [193]. To best describe the system presented here the steady state temperature at the top of the collagen suspension after freezing was recorded and compared to the analogous simulated values for the no source condition. The results can be seen in Table 5.2. It was found that the assignment of the value h_c=27.5 $\mathrm{Wm^{-2}K^{-1}}$, most accurately described the steady state behaviour of the experimental results.

5.3.2 Thermal Environment

Temperature data were collected at the top and bottom of the slurry during collagen suspension solidification under the no source condition and compared to simulated results as shown in Figures 5.2a-5.2d. Similar temperature profiles were observed between the simulation and experimental results, where the bottom of the slurry was found to rapidly drop to the set temperature at the base of the mould while the top of the slurry was observed to cool more slowly. Solidification times varied for experimental results and complete solidification for the no source conditions was found to occur after 1380$\pm$250 seconds. In the following

Table 5.2 Parameter (h_c) estimation

h_c value	Simulation Results		Experimental results		
	SS Temp (^{o}C)	Freezing time (s)	Sample Number	SS Temp (^{o}C)	Freezing time (s)
20	-22.3	1455	1	-18	1650
22.5	-20.7	1485	2	-17.7	1158
25	-19.5	1500	3	-19.6	1340
27.5	-18.3	1515		mean: -18.4 $\pm$1	mean: 1383$\pm$249
30	-17.2	1545			

conditions an exemplar temperature profile will be presented for comparison with simulated results. For the thermal profile presented in Figure 5.2a, complete solidification, indicated by a sharp increase in the rate of cooling, occurred at t=1300 seconds. Solidification was observed to occur after t=1515 seconds for the simulation result as illustrated in Figure 5.2c. Figures 5.2b and 5.2d show that a large temperature difference of 50-70 ^{o}C between the top and bottom of the collagen suspension during the solidification process for both the experimental and simulated results.

Agreement between simulated and experimental thermal behaviour indicates that the simulated thermal distribution can be used to describe the thermal environment of the collagen suspension during solidification. A cross sectional view of the solidification simulation shows the heat distribution within the system. The cooling front can be seen to be oriented parallel to the base of the mould and progresses from the bottom of the suspension to the top as shown in Figure 5.2e.

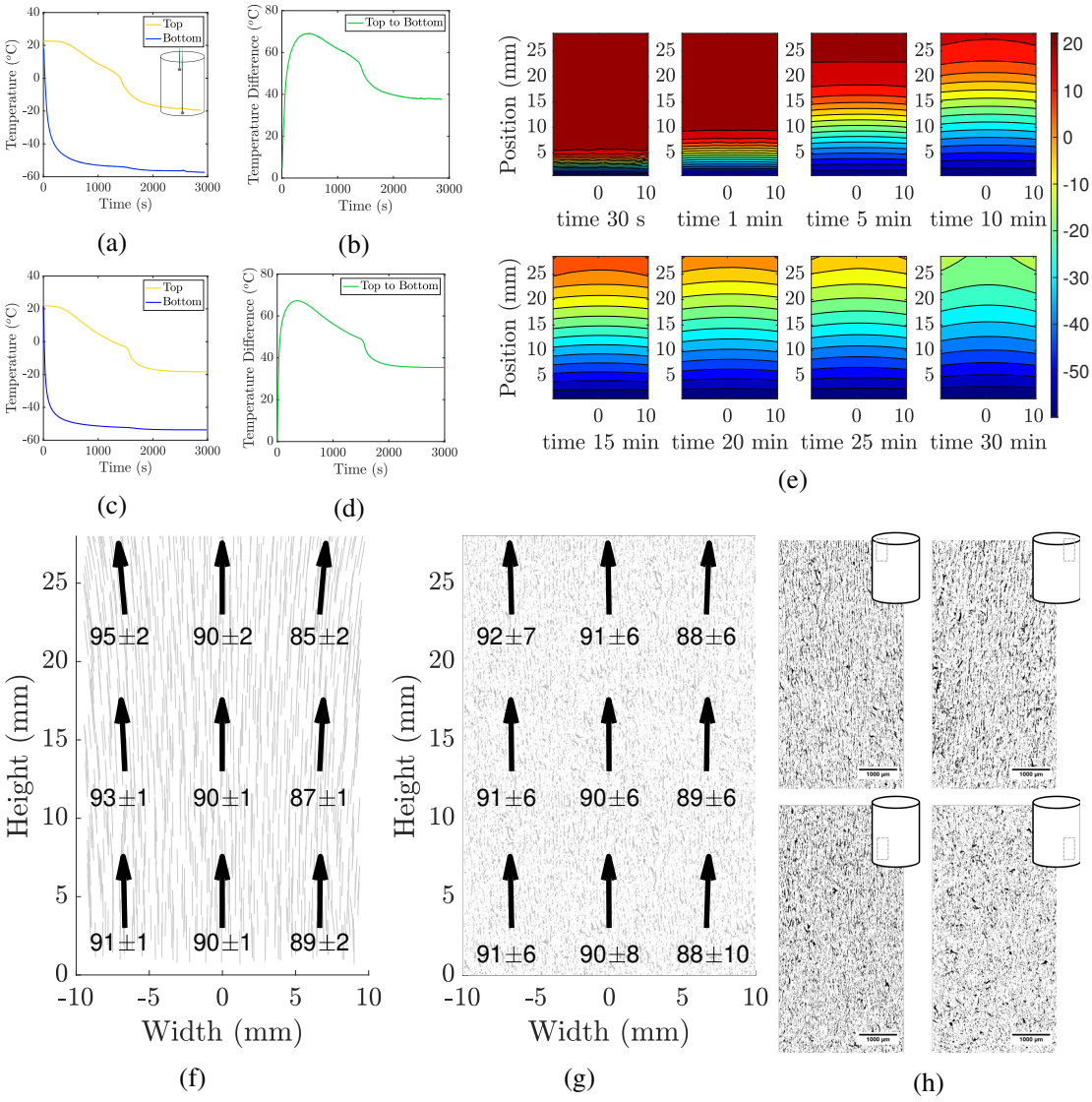

Fig. 5.2 No source results. **(a)**-**(d)** Temperature results under the no source condition for **(a)**,**(b)** experimental measurements**(c)**,**(d)** and simulated profiles. **(a)** and **(c)** display the temperature at the top and bottom of the slurry. **(b)** and **(d)** Display the temperature difference across the height of the slurry. **(e)** Cross-sectional temperature contours during solidification under the no source condition. **(f)** The simulated temperature gradient profile at $t_{l\rightarrow s}$. **(g)** Lamellar orientation throughout the final scaffold. Large arrows in **(f)** and **(g)** represent the average orientation direction for each section of the slurry. **(h)** μCT images of the final lamellar structure of resultant collagen scaffolds. Images sliced on the x-z-plane for different regions of the structure, indicated on each insert. All scale bars are 1000 μm

5.3.3 Lamellar Prediction

The simulated temperature distribution across the three dimensional suspension was used to produce a gradient vector field to describe local gradient orientations. The three dimensional vector field describes the thermal gradient across each mesh element at $t_{l\rightarrow s}$ shown in grey in Figure 5.2f. The gradient field was observed to display uniform orientation, in which vectors align normal to the base of the mould, at 90 ± 1^{o}, perpendicular to the thermal contours observed in Figure 5.2e. For comparison with the final lamellar architecture of collagen scaffolds, the average gradient direction was calculated for each region of interest as shown in 5.2f. The orientation of each region of interest was found to be close to normal with some systematic variations in mean vector direction where regions proximal to the mould walls were observed to subtly point outward. The effect intensified as the position along the z-axis increased. Therefore, a structure with lamellar orientation normal to the base of the mould was predicted with subtle outward orientations at the periphery of the scaffold.

5.3.4 Lamellar Structure

The direction of the lamellar alignment for freeze-cast collagen structures produced under the no source condition was analysed for each region of interest. The final lamellar structure is summarised in Figures 5.2g and 5.2h. Uniform alignment was observed with an average orientation of 90 ± 2^{o}, normal to the base of the mould. No significant deviation was found. A subtle tendency for outward orientation, however, was observed in peripheral regions as shown in Figure 5.2g and 5.2h.

5.4 Results: Implementation of complex thermal environments

Novel heat source moulds were implemented to explore the influence of complex thermal environments on the resultant lamellar architecture of ice templated collagen scaffolds. The model was also expanded to describe the presence of more complex thermal environments. The thermal and architectural results of the *single source* and *dual source* conditions are presented in this section.

5.4.1 Single heat source environment

Asymmetric thermal environment

The constant current applied to the heater at the top of the mould (P_T) produced a local disruption in the vertical temperature gradient. The thermal disruption is evident in the time dependant temperature profiles for both the experimental measurements and simulated results as shown in Figure 5.3a-5.3d. Temperatures at the top and bottom were comparable to the no source condition. Due to the increased thermal load caused by P_T, solidification at the top of the suspension occurred later, at t=1910 seconds and t=1770 seconds for the experimental example and simulated data respectively. The temperature differences between the top and bottom of the suspension were also observed to exceed that of the no source condition as shown in Figure 5.3b.

For both the experiment and the simulation, the temperature adjacent to the P_T increased initially before cooling and solidifying at 2500 seconds and 2250 seconds respectively as shown in Figures 5.3a and 5.3c. The region opposite P_T behaved similarly to the top of the suspension resulting in a significant temperature difference of between 25 and 30^{o}C across the width of the mould during solidification as seen in Figures 5.3b and 5.3d.

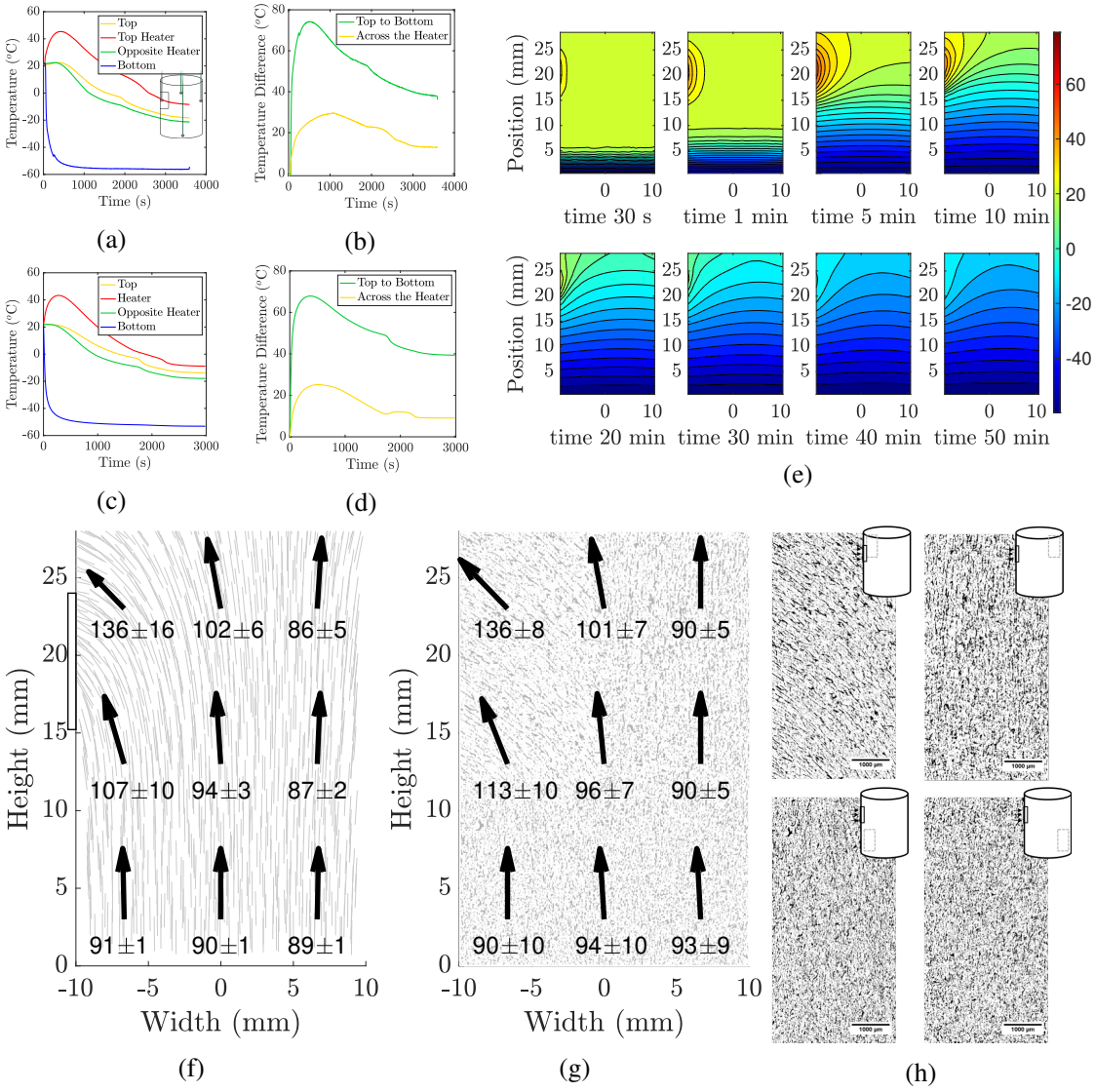

Fig. 5.3 Single source results. **(a)**-**(d)** Temperature results under the single source condition for experimental measurements**(a)&(b)** and simulated profiles **(c)&(d)**. **(a)** and **(c)** display the temperature at the top and bottom of the slurry as well as proximal and directly opposite the heat source. **(b)** and **(d)** Display the temperature difference across the height of the slurry and across the width of the slurry at the height of the heat source. **(e)** Cross-sectional temperature contours during solidification under the single source condition. **(f)** The simulated temperature gradient profile at $t_{l\rightarrow s}$. **(g)** Lamellar orientation throughout the final scaffold. Large arrows in **(f)** and **(g)** represent the average orientation direction for each section of the slurry. **(h)** μCT images of the final lamellar structure of resultant collagen scaffolds. Images viewed on the x-z-plane for different regions of the structure, indicated by inserts. All scale bares are 1000 μm

The effect of the P_T heat source on the thermal environment can be seen in Figure 5.3e, illustrating the cross sectional thermal contouring of the cooling suspension at specific time points. A locally asymmetric thermal environment was induced, where the bottom portion of the slurry displayed a similar behaviour to the *no source* condition with contour lines oriented parallel to the base of the mould. At the top of the slurry, however, the contour lines were observed to bend around the source throughout the cooling process. The region proximal to P_T was last to cool below 0^oC, and the local contour lines were oriented parallel to the mould wall as shown in Figure 5.3e.

Prediction of complex lamellar structure

The localised asymmetry was also visible in Figure 5.3f, illustrating the gradient vector field for $t_{l\rightarrow s}$. It was found that gradients proximal to the source were observed to point in the direction of P_T, whereas gradients opposite P_T and at the bottom of the suspension maintained the normal orientation observed in the no source condition. For comparison with the lamellar architecture of resultant collagen scaffolds, the mean vector orientation was calculated for each region of interest and are summarised in Figure 5.3f. The gradient vectors in regions of interest proximal to the heat source were observed to deviate from normal, the mean vector orientation of the two regions of interest adjacent to the heater (top and middle) was 121 ± 13^o, a deviation of 31^o from normal. It was observed that the adjacent region in the middle of the suspension was less sensitive than the top region. Therefore, lamellar architecture is predicted to maintain normal orientation in regions distant from the heat source. However, proximal to P_T it is expected that lamellae will bend in the negative x direction as a result of the induced thermal gradients.

Controlled lamellar structure

The P_T heat source induced asymmetric and spatially variable lamellar alignment in the resultant collagen scaffold. Figures 5.3g and 5.3h show that lamellae proximal to the source were observed to bend toward P_T. The mean strut orientation of the two regions of interest adjacent to the heater was 125 ± 6^o, a deviation of 35^oC from the normal direction. Normal lamellar alignment, near 90^o, was observed opposite to P_T and at the bottom of the scaffold. These results are consistent with the simulated prediction shown in Figure 5.3f.

Scaffolds produced under the no source condition, shown in Figure 5.4a, display unidirectional lamellar alignment with microporosity in strut walls. This is consistent with micro-scale and nanoscale surface features that have been shown to encourage cellular attachment and increase scaffold permeability [152]. The multidirectional freezing process induced by the peripheral heat source maintained the micro-scale and nano-scale surface features characteristic of ice templating, while specifically dictating local macro-scale lamellar alignment resulting in a hierarchical structure with defined complex architecture, shown in Figure 5.4b.

5.4.2 Dual heat source environment

Asymmetric thermal environment

The time dependent temperature data for the dual source freezing condition and analogous simulation were measured adjacent to and directly opposite both heaters, namely: P_T and P_B, as shown in Figure 5.5a-5.5d. Experimentally, the temperature of the suspension adjacent to both heaters rapidly increased to 55^o C and 50^o C for P_T and P_B respectively before reducing for the remainder of the solidification process. The initial temperature elevation was found to be lower in simulated results with 44 ^{o} C and 35 ^{o} C for P_T and P_B respectively. Despite

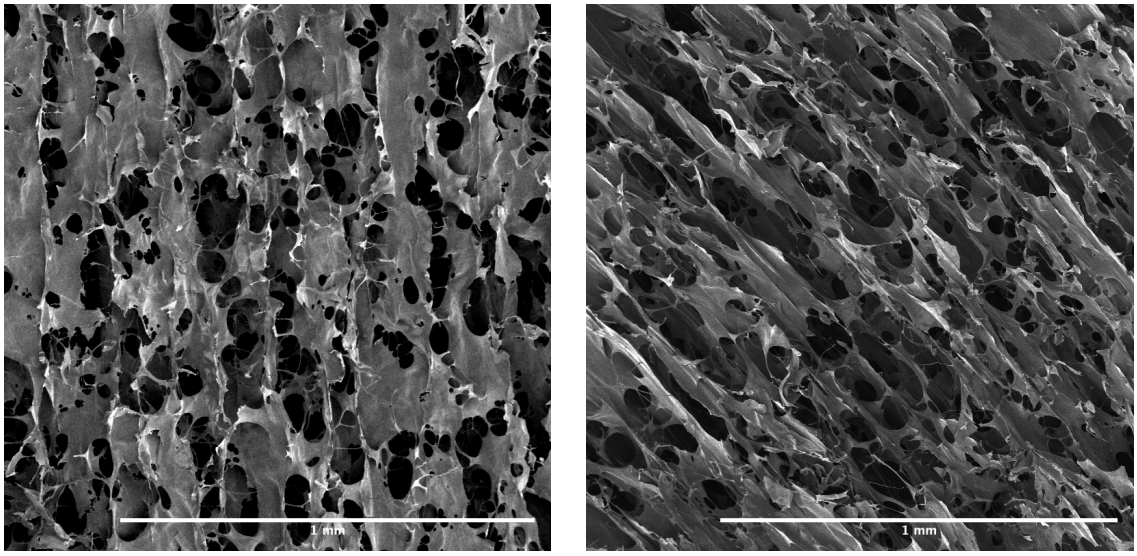

(a) (b)

Fig. 5.4 SEM micrographs at 50-times magnification of the resultant lamellar structure for **(a)** the no source condition and **(b)** the single source condition proximal to the heat source. Micrographs illustrate the porous microstructure as well as the ordered macrostructure achieved through the directional ice-templating technique. All scale bars are 1mm

the observed differences in thermal profiles between simulation and experiment, significant temperature differences across the width of the mould were observed in both.

The temperature difference across the width of the mould at the height of P_B showed an early peak of 34^{o}C and 18^{o}C prior to 500 seconds before stabilising at 15^{o}C and 6^{o}C for the measured and simulated temperature results respectively as shown in Figures 5.5b and 5.5d. The P_T heat source produced a more sustained temperature difference between 24^{o}C and 18^{o}C experimentally and 20^{o}C and 10^{o}C in the simulation.

The resultant thermal contours for the antiparallel temperature gradients are visualised on the x-z cross section in Figure 5.5e. The cooling front was observed to bend around P_B and then fold across to approach P_T. While both heat sources caused local disruptions in the contour profile, the contour lines were largely parallel to the base of the slurry in regions opposite the heat sources.

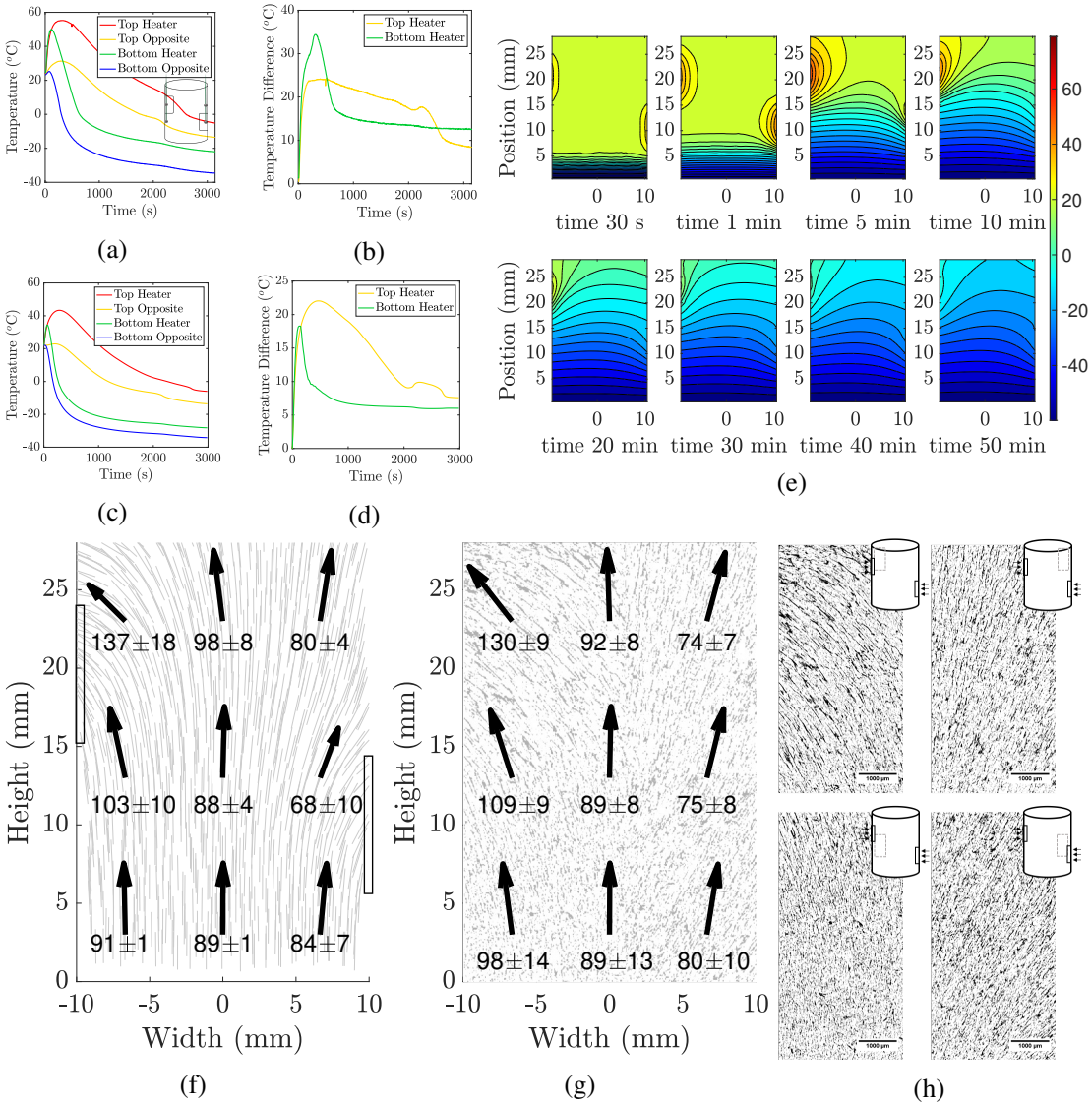

Fig. 5.5 Dual source results. **(a)**-**(d)** Temperature results under the dual source condition for experimental measurements**(a),(b)** and simulated profiles **(c),(d)**. **(a)** and **(c)** display the temperature proximal and directly opposite each heat source. **(b)** and **(d)** Display the temperature difference across the width of the slurry at the height of each heat source. **(e)** Cross-sectional temperature contours during solidification under the dual source condition. **(f)** The simulated temperature gradient profile at $t_{l\rightarrow s}$. **(g)** Lamellar orientation throughout the final scaffold. Large arrows in **(f)** and **(g)** represent the average orientation direction for each section of the slurry. **(h)** μCT images of the final lamellar structure of resultant collagen scaffolds. Images viewed on the x-z-plane for different regions of the structure, indicated by inserts. All scale bars are 1000 μm

Prediction of complex lamellar structure

The temperature gradient field for $t_{l\rightarrow s}$ showed that gradient vectors deviated from normal in both the positive and negative x directions as shown in Figure 5.5f. The average gradient vector orientations for the two regions proximal to each heat source were calculated to be 120 ± 15^o and 76 ± 8^o for P_T and P_B respectively. Given the complex multidirectional gradient vector field, the resultant lamellar structure of the dual source condition was expected to have a spatially variable lamellar architecture with local lamellar orientations that deviate from normal in both directions.

Controlled lamellar structure

The presence of two antiparallel temperature gradients across the width of the slurry had a significant impact on the direction of ice-crystal growth, and subsequently, the lamellar architecture of the freeze-cast collagen scaffolds. Lamellar alignment was observed to orient toward each heat source as shown in Figures 5.5g and 5.5h. The average lamellar orientations for the two regions proximal to each heat source were 120 ± 6^o and 76 ± 6^o for P_T and P_B respectively. Figures 5.5g shows that the final lamellar orientation was in agreement with predicted results for all regions of interest.

5.5 Power input as a control parameter for lamellar orientation

The influence of the heat source power on the thermal environment, and the lamellar orientation of freeze-cast collagen scaffolds was assessed by varying the power input of the P_T source in both the simulation and experimentally. The power input was found to have a

significant influence on final lamellar orientation, such that as power input to P_T increased, lamellae were found to be oriented increasingly outward, toward P_T. This relationship was also observed in simulated gradient vector fields. It was found that in both experimental measurements, shown in Figures 5.6a-5.6d and simulated results, shown in Figures 5.6e-5.6h the region of interest at the top of the suspension was more sensitive to the heat source than the region of interest in the middle. The power input to the system was also positively correlated with the temperature difference across the suspension for both the experiment and the simulation, shown in Figure 5.6i and Table 5.3. It was found, however, that the temperature difference across the width of the mould was systematically underestimated in the simulation. Similarly, while increased power output also correlated with increased solidification time in both the experiment and simulation, the simulation systematically underestimated the time of complete phase transition at all power levels.

Table 5.3 Experimentally measured freezing and architectural characteristics influenced by power input to the heat source

	Deviation from normal ($\lvert 90^o - Angle^o \rvert$)		Temperature difference $\Delta T(t_{l\to m})$		Time of complete phase transition ($t_{l\to s}$)	
Power	Exp.	Sim.	Exp.	Sim.	Exp.	Sim.
0.1 W	$14\pm7\ ^o$	$13\pm3\ ^o$	$13\ ^o$C	$3\ ^o$C	1700 s	1620 s
0.2 W	$29\pm9\ ^o$	$20\ \pm5\ ^o$	$15\ ^o$C	$5\ ^o$C	2000 s	1710 s
0.55 W	$35\pm6\ ^o$	$32\pm9\ ^o$	$17\ ^o$C	$11\ ^o$C	2500 s	2250 s
0.72 W	$51\pm7\ ^o$	$44\pm10\ ^o$	$20\ ^o$C	$15\ ^o$C	3400 s	2800 s

The relationship between lamellar orientation and the temperature difference across the suspension was also explored for the two peripheral heat sources in the dual source condition. It was found that the positive correlation observed in the single source condition with varied power input was not supported by the dual source condition as shown in Figure 5.6j.

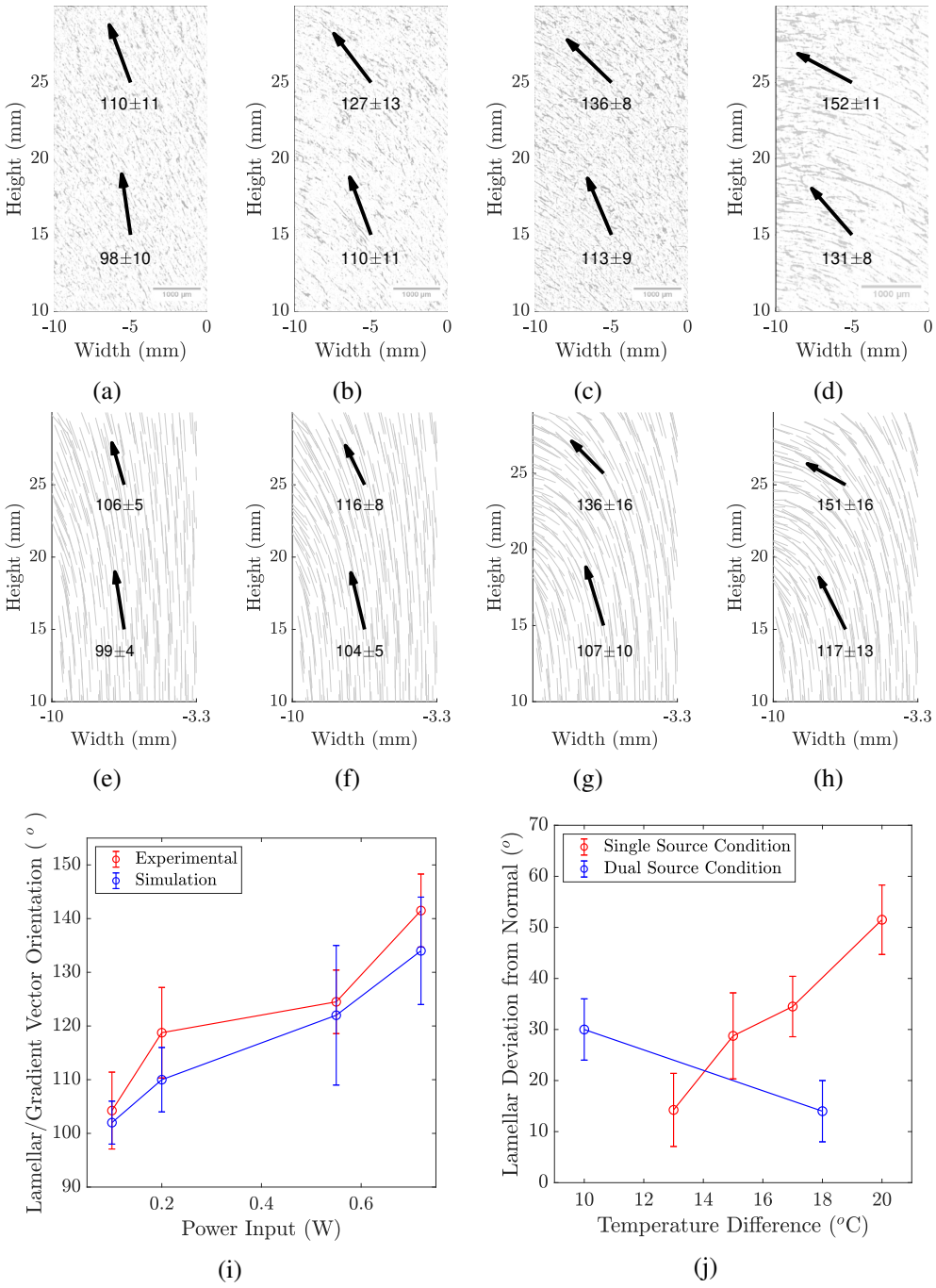

Fig. 5.6 Heat source power input as a control parameter. **(a)-(d)** Final scaffold lamellar orientation proximal to the heat source for varied power input to the single source condition. Large arrows represent the average gradient orientation of each section for **(a)** 0.1 W, **(b)** 0.2W, **(c)** 0.55 W, **(d)** 0.72 W **(e)-(h)** Simulated temperature gradient profile at $t_{l\rightarrow s}$ proximal to the heat source for analogous power input as **(a)-(d)**. **(j)** Lamellar orientation and prediction for varied power input. **(j)** Temperature difference verses lamellar deviation from normal for the single source condition (red) with varied power input and each of the two heaters in the dual source condition (blue) with equal power input: blue-left) P_T and blue-right) P_B.

5.6 Discussion

5.6.1 Implications and influences on the field of bioengineering and freeze-casting

A novel technique to establish fine control over local lamellar orientation in freeze-cast collagen scaffolds was introduced. The use of custom controllable heat source moulds resulted in the presence of complex thermal environments during the solidification stage of the ice-templating process. By dictating the thermal environment during solidification, the ice growth direction was controlled and collagen scaffolds with specific and complex multidirectional orientations were produced.

A simple finite element model was employed to explore the influence of the novel heat source moulds on the thermal environment within the suspension during solidification. The resulting simulations further supported the link between thermal gradient direction at the time of solidification and the final lamellar orientation of freeze-cast collagen scaffolds. Agreement between simulated thermal gradient fields and final scaffold architecture illustrate the design capabilities of a simple finite element model in achieving tailored collagen scaffold architecture through the novel thermal control system.

The control capabilities of the heat source mould system were demonstrated by varying power input. A correlation between lamellar orientation and heat source power was identified. This behaviour was accurately predicted by the simulation, supporting the use of the finite element model as an experimental design tool.

5.6.2 Predictive qualities of the model

The simulated gradient vector field at $t_{l\rightarrow s}$ agreed with the lamellar orientation from experimentally produced collagen scaffolds for all conditions. This robust relationship confirms the link between thermal environment and lamellar orientation hypothesised in the literature [32, 211] and further advances the understanding of the ice-templating process. Specifically, the agreement between the final lamellar structure and the simulated thermal environment at $t_{l\rightarrow s}$ lends weight to the use of simulation tools to further understand the influence of boundary conditions on the dynamic thermal environment within the mould during the freezing process. Furthermore, the predictive qualities of the simulation encourage the use of simple descriptive models as experimental tools in the design of complex multidirectional freeze-cast structures.

The simulation results, while largely in accordance with experimental findings, were subject to limitations. Within the simulation, the phase change entropies were balanced using the apparent specific heat method, which, while computationally straightforward, has been shown to limit the accuracy of the results [299, 300]. Phase change inaccuracies possibly contributed to the discrepancies observed between simulation and experiment for solidification times. Fitting the phase transition to observed thermal data, however, is beyond the scope of this work. Additionally, due to the spatial variability of lamellar architecture and the simulated gradient vector field, orientation measurements were found to be sensitive to sampling location. Discrepancies between average gradient direction and average lamellar orientation are confounded by variation in sampling volume location discrepancies between the model and the reconstructed μCT data. Despite these limitations, the simulation was found to be predictive of final lamellar orientation given experimentally analogous imposed boundary conditions.

5.6.3 Correlating thermal environment with lamellar orientation

Three thermal conditions were assessed for the influence of thermal control on final lamellar architecture in freeze-cast collagen scaffolds. The implementation of directional freezing in ice templated scaffolds has been widely shown to result in an aligned lamellar structure with normal orientation to the base of the mould [30, 142, 199]. The resultant scaffold architecture for the no source condition presented in this work is in agreement with the literature. It has previously been hypothesised that lamellar orientation is influenced by thermal gradients during solidification [199, 211, 292]. However, tailored multidirectional structures with locally controlled architectures have not yet been reported. The novel heat source mould design presented in this work provides localised control of resultant lamellar orientation of collagen scaffolds, while maintaining the porous interconnected microstructure that is characteristic of the ice templating technique.

The introduction of a localised heat source altered the ice crystal growth direction such that crystals with preferential growth directions in line with the induced thermal gradient, grew at the expense of crystals with alternative orientations [32]. Fine control of the local thermal environment during solidification afforded the production of collagen scaffolds with tailored architecture and localised control of lamellar orientation.

The power input to the peripheral heat source was varied to test power output as an architectural control parameter. Heat source power was correlated with lamellar orientation, seen in Figure 5.6i. This relationship is a consequence of the magnitude of the thermal gradient induced by the heat source. Small power inputs resulted in small lateral gradient components causing a minor change in orientation. Conversely, larger power inputs caused a large change in orientation.

Varying the power input directly influenced the temperature difference observed across the mould, shown in Figure 5.6j. Using the lateral temperature difference is applicable when comparing results produced with the same source geometry. When thermal geometry changes, for instance between the single source condition and the dual source condition, the process is more complex. The deviation from normal of the resulting lamella for the dual source condition had a negative correlation with the observed lateral temperature difference at $t_{l\rightarrow s}$. This result illustrates the importance of a full three dimensional understanding of the thermal environment during freezing. The reduced correlation between lateral temperature difference and the deviation of lamellar alignment from normal is due to variations in the thermal gradient component magnitudes at the freezing front. The lateral temperature difference (18 ^{o}C) across the mould at P_B was high. However, lamellar orientation was found to deviate only 14 ± 6^{o} from normal in the region proximal to the source as shown in Figure 5.6j. The proximity of the heat source to the heat sink at the base of the mould resulted in large vertical gradient components that contributed to the resultant gradient direction. The final gradient vector direction is the component sum of all present thermal gradient at the freezing front and, therefore, for complex three dimensional environments, simple one dimensional temperature readings are insufficient to fully describe the local gradient orientation. The complexity of the system substantiates the importance of predictive models that can describe the complete thermal environment and be used as design tools during the production of freeze-cast structures with specific complex multidirectional morphologies.

5.6.4 Looking forward

Taken together the local control of lamellar orientation achieved through the application of the novel thermal controlled mould system and the predictive properties of the simple finite element model presented, allows for a greater degree of specificity in freeze-cast structures.

The technique can be scaled and combined with the control mechanisms already established for pore size [32, 142, 186], lamellar thickness [187, 199], and interconnectivity [117, 188]. This could produce specific structures with targeted complex architectures for regenerative medical scaffolds that mimic the hierarchical structures observed in complex tissue types. By pairing the design protocol with the predictive model, it follows that target structures can be visualised and designed through simulation, and that heat source moulds can be programmed to input the necessary dynamic thermal conditions to produce highly specific structure orientations.

Although the implications for the design of hierarchical and architecturally specific collagen scaffolds for a wide range of regenerative medical applications are important, the technique is not limited to ice-templated collagen scaffolds. The relationship between temperature gradient and lamellar orientation has been observed in all directional freeze-cast systems and the technique presented here can be universally applied. By altering the lamellar orientation seamlessly within a structure, the resulting strength, stiffness, and other related properties can be tailored to specific applications. This introduces a new tool for the development of freeze cast materials with spatially varied properties.

5.7 Conclusion

This work presents a novel system for creating controlled, multidirectional lamellar alignment in ice-templated collagen scaffolds. This was achieved by introducing heat sources and sinks to specific regions of the mould, which enables complex thermal gradients to develop during solidification. Specifically, local lamellae were observed to align in the direction of local thermal gradients. This enables complex hierarchical structures to be produced in a single step process, which has been a major goal of tissue engineering for some considerable time.

The heat source mould technique was presented alongside a finite element simulation of the solidification process under analogous boundary conditions. The temperature gradient direction immediately prior to the phase transition was found to be predictive of the final lamellar orientation of experimentally produced collagen scaffolds. Both the model and experimental system were sensitive to the power input of the heaters, evidencing that control over thermal power is an effective strategy in designing final scaffold architectures. The finite element model and novel heat source mould system allow for targeted and specific design of complex structural morphologies which have not been achievable up until now with the ice-templating technique. This approach will ultimately allow specific hierarchical structures to be input into the model, which will be able to specify the combination of heat sources and sinks required, with the necessary power inputs and durations, to achieve the personalised structures that are required for successful tissue engineering.

Chapter 6

The influence of scaffold anisotropy on engineered cardiac tissue function

6.1 Introduction

The complex three dimensional architecture of the native myocardium is responsible for directional contractions with asymmetric strain profiles [46–50]. A more detailed review of cardiac tissue engineering and the impact of architectural control can be found in section 2.3.1. Briefly, translational designs for a regenerative cardiac patch have, historically, been structured by pseudo-isotropic scaffolds or gels [103, 157, 158]. Recent investigations, however, have shifted toward the use of anisotropic structures, demonstrating increased cellular organisation and function [10, 35, 50, 70, 71, 125, 301]. While both architectural morphologies are currently being explored in the literature, due to the technical complexity of scaffold engineering the isolated functional effects of three dimensional architectural organisation in engineered cardiac tissue have not yet been studied systematically. Therefore little is known about the direct influence of structure on specific functionality of regenerative tissue.

In this chapter a direct comparison is made between the cellular and long range functional effects of pseudo-isotropic and aligned structural morphologies in the field of cardiac tissue engineering. To guide cell attachment and impart a hierarchical tissue organisation three dimensional collagen scaffolds are utilised and populated with pluripotent stem cell (PSCs) derived cardiomyocytes. In order to enable a direct comparison between scaffold morphologies, an ice-templated parent scaffold with unidirectional alignment was fabricated, from which the inherent planar asymmetry was utilised to produce thin patches that were characterised by either pseudo-isotropic or anisotropic pore architectures. The use of single scaffold fabrication technique to produce both structures ensures that other physio-mechanical features are held constant as far as possible, and the influences of pore architecture on tissue level and cellular level function can be assessed independently.

The effects of scaffold architecture were characterised at multiple length scales. At tissue level, electrical signal propagation and deformation behaviour were compared. The functional differences between structure morphologies were then assessed at a cellular level to better understand the differences in tissue level performance. Phenotypic cellular maturity was characterised through RNA analysis and physiological cellular development and organisation were measured through sarcomeric organisation, cellular alignment, and gap junction formation. This chapter describes a systematic comparison of the functional and cellular affects of isotropic and aligned scaffold structures [70, 302–305].

6.2 Methods

The work in this chapter was done collaboratively with Dr. Maria Colzani at the Wellcome-MRC Cambridge Stem Cell Institute, in Cambridge, UK. Dr. Colzani's greatly appreciated contributions are specified in this section.

6.2.1 Collagen scaffold preparation

Scaffold fabrication

A 1 wt% suspension of insoluble type I bovine dermal collagen (Devro) was prepared according to the protocol laid out in section 3.1.2. The collagen suspension (9 ml) directionally freeze-cast using the controllable heat sink and mould system described in section 3.1.1. The heat sink was programmed to hold at -10 ^{o}C for 1 minute followed by cooling at a rate of 0.2 ^{o}C min^{-1}. The top of the mould was exposed to the ambient environment. After solidification, scaffolds were dried, imaged and then cross linked to 5% according to the protocols described in section 3.1.2.

Scaffold imaging

Prior to cross-linking scaffolds were imaged with both scanning electron microscopy and X-ray micro-computed tomography (μCT) as described in section 3.2.2. Reconstructions of μCT data were used to assess the structural alignment and pore size of the parent scaffold according to the protocols described in sections 3.2.3 & 3.2.4

Scaffold slicing

Scaffolds were punched with an 8 mm biopsy punch and sliced to a thickness of 500–700 μm. Aligned structures were cut such that the circular face of the scaffold was parallel to the longitudinal plane of structural alignment. Pseudo-isotropic scaffolds were cut such that the circular face of the scaffold was parallel to the transverse plane of structural alignment as shown in Figure 6.1.

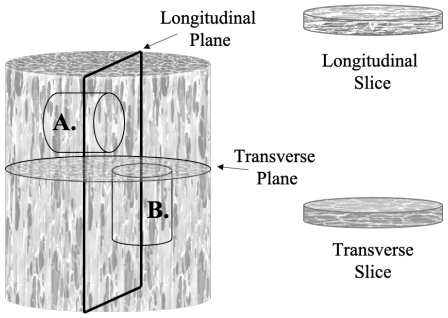

Fig. 6.1 Schematic of scaffold slicing geometry, **A.** is the biopsy punch orientation for longitudinal slices, **B** is the biopsy punch orientation for transverse slices

6.2.2 Cell line generation and culture conditions

CH9 hESCs were maintained and differentiated according to protocols described by Iyer et al. 2015 [306] and Mendjan et al 2014 [307]. An overview of the procedure is as follows: H9 hESCs were seeded into 12 well plates coated with Matrigel (Corning) filled with CDM-BSA supplemented with ROCK inhibitor (Millipore, 1 μm) at a density of 10^5 cells cm^{-2}. Media was changed after 3 hours to CMD-BSA, supplemented with FGF-2 (20 ng ml^{-1}), Activin-A (50 ng ml^{-1}), BMP-4 (10 ng ml^{-1}, R&D) and LY294002 (10 μM Tocris). Media was changed again after 42 hours to CDM-BSA supplemented with FGF-2 (8 ng ml^{-1}), BMP-4 (20 ng ml^{-1}), Retinoic Acid (SIMGA, 1 μM), endo-IWRI (1 μM, TOCRIS). Cells were maintained with this media, refreshed every 48 hours, for 4 days. Media was changed to CDM-BSA supplemented with FGF-2 (8 ng ml^{-1}), BMP-4 (20 ng ml^{-1}) for an additional 2 days. Media was then changed to CDM-BSA with no cytokines and replaced every 48 hours. Spontaneous beating is generally observed 8-10 days after seeding. The cellular differentiation and preparation was done by Dr. Maria Colzani.

6.2.3 Cardiac cell selection

Differentiated cardiac cells were metabolically selected via lactate selection. Media was removed from beating cardiomyocytes on 14 day. The wells were washed with PBS and

TryPLE (Life technologies) (500 ul per well in a 12 well plate) was added. Plates were incubated at 37^o C for 8-12 minutes, until dissociated. CDM BSA and DNase (DNase I Solution (1 mg/ml) cat. 7900 Stemcell Technologies) diluted to 1:500 stock (1mg/ml) was added, 1 ml per well. Cells were collected in a falcon tube and centrifuged (3 minutes at 1200 rpm). Cells were resuspended in CDM BSA to a concentration of $1x10^6$ cell/ml. Rock inhibitor (Y-27632 cat. 11573560 Millipore) (1:1000) was added. Cells were plated in a 6 well plate ($2x10^6$ cells/well) and incubate at 37^o C for 8-12 hours. Media was removed from wells and lactate media (DMEM without Glucose/pyruvate with non-essential amino acid (cat.554084 Gibco) (1:100 from stock solution) and Sodium lactate (cat. L7022-10G SIGMA) (1:250 from 1M stock,4 mM final concentration)) was added (2 ml/well). Cells were incubated in lactate media for 96 hours, media was refreshed after 48 hours.

The lactate selected hESC-derived cardiomyocytes were pelleted via centrifugation and resuspended in Fixation/Solubilization solution (BD Cytofix/Cytoperm Fixation/Permeabilization Kit, Biosciences) for 20 mins at 4^oC. Cells were then pelleted by centrifugation and resuspended in 1X BD Perm/Wash Buffer containing anti-Cardiac Troponin-T APC antibody or Isotype control (Miltenyi Biotech) and incubated for 2 hours at 4^oC. Cells were washed three times in 1X BD Perm/Wash Buffer, and then resuspended in phosphate buffered saline containing 0.1% BSA and 2 mM EDTA. Data was acquired on BD LSRFortessa^{TM} Flow Cytometer and analysed with FlowJo^{TM} v9. The cellular selection and flow cytometry was done by Dr. Maria Colzani.

6.2.4 Cell seeding onto the scaffold

Scaffolds described in section 6.2.1 were sterilised in 70% EtOH for 30 min. The EtOH was removed by PBS washing 3x5 minutes prior to scaffold conditioning with cell culture media

(CDM BSA) for 1 hour in preparation for cell seeding. Cardiomyocytes were dissociated using TrypLE (Life technologies) and seeded at a density of 2 x 10^6 cells per scaffold in CDM BSA supplemented with ROCK inhibitor 1 μM. The cellular seeding onto scaffolds was done by Dr. Maria Colzani.

6.2.5 Viability

PrestoBlue Cell Viability Reagent (Thermo Scientific) was added to culture media according to the manufacturer's instructions after 7 days of culture. Cells were incubated with the dye for 4 hours. Media was then sampled and fluorescence at 560 nm was analysed using VICTOR Multilabel Plate Reader (Perkin Elmer). Media containing PrestoBlue incubated in empty wells was used as background control. The cell viability staining and imaging was done by Dr. Maria Colzani.

6.2.6 Live cellular dynamic measurements

Fluo-4 AM calcium dynamics recording

Fluo-4 AM (10 μg/ml, Life technologies) was added to the cell culture media, on day 7 of culture, for 30 min at 37 ^{o}C. Videos were recorded on an Axiovert inverted microscope (Zeiss) using a Sony LEGRIA camera. Scaffolds were recorded both un-paced and paced at frequencies of 1 or 1.5 Hz using c-PACE EM pace (IONOPTIX). The Fluo-4 AM calcium dynamics imaging was done by Dr. Maria Colzani.

Structural deformation recording

Bright field videos were recorded on an Axiovert inverted microscope (Zeiss) using a Sony LEGRIA camera. The bright field video recording was done by Dr. Maria Colzani.

6.2.7 Live cellular dynamic analysis

Fluo-4 AM calcium video analysis

Video analysis was performed in MatlabR2020a. Fluorescence intensity was normalized and mean intensity was plotted against time. Both intensity peak frequencies and Fast Fourier Transform analysis were used to calculate pulse rate. For samples that did not exhibit spatial deformation during calcium fluorescence, pulse rates were also calculated for each pixel to indicate global signalling uniformity. Individual pulse times were recorded for each pixel and the temporal signalling uniformity in space was visualised through isochrones in MatlabR2020a.

Strain analysis

Strain analysis was performed on bright-field video samples according to the protocol laid out in section 3.2.6. The scaffold structure under bright-field provided a reliable speckle pattern with sufficient contrast for analysis. A subset radius of 30 pixels and spacing of 5 pixels was used with high strain enabled.

6.2.8 Immunocytochemistry

Cell-seeded constructs were washed once in PBS then fixed for 1 hour with 4% PFA. The cells were subsequently permeabilised with 0.1% Triton (Sigma), 0.5% BSA (Sigma) in PBS for 15 min before blocking with 3% BSA (Sigma) in PBS for 1 hour. Incubation with primary antibody (diluted accordingly) was then performed. Constructs were then washed in PBS and incubated overnight with the appropriate secondary antibody, or phalloidin where appropriate, overnight. Constructs were then washed and stained with DAPI (Sigma, 1 μg/ml) for 1 hour

Table 6.1 Antibodies

Antibody	Supplier	Cat. Number
mouse monoclonal anti Cardiac Troponin T (I)	Abcam	Ab8295
Rabbit polyclonal Anti-Connexin 43 (I)	Abcam	ab11370
Rabbit polyclonal Anti sarcomeric α-actinin (I)	Abcam	ab68167
Phalloidin - 555	Abcam	ab68167
Chicken anti-mouse 488 (II)	Life Technologies	A-21200
Donkey anti-rabbit 568 (II)	Life Technologies	A10042

prior to imaging. Micrographs were obtained using an SP-5 confocal microscope (LEICA). Primary (I) and secondary (II) antibodies are listed in Table 6.1. The florescence staining and imaging was done by Dr. Maria Colzani.

6.2.9 Immunofluorescence Analysis

Sarcomeric development

Individual sarcomere chains were isolated from confocal images showing α-actinin such that the sarcomere band spanned the height of the region of interest. Fluorescence intensity was normalised by the minimum fluorescence (f_0) such that, $f_{norm} = (f/f_0) - 1$. The mean fluorescence intensity signal was plotted against the length of the sarcomere chain and the relative prominence of each intensity peak was measured in MatLabR2020a to calculate sarcomere intensity. Sarcomere width was defined as the signal wavelength.

Cellular alignment

F-actin staining was used to characterise cellular spreading and cytoskeletal alignment. The F-actin orientation and coherence of cardiomyocytes after 7 days of culture was measured for 50 μm^2 sections (27 measurements were taken per scaffold) with the OrientationJ plugin for ImageJ. The intra-scaffold variance was calculated for each individual scaffold.

Gap junction density

Immunofluorescence staining of Connexin-43 was used to visualise gap junction structures through fluorescence microscopy. Mature gap junctions were counted with particle analysis in ImageJ. The gap junction density for 200 μm^2 regions of interest was calculated in MatlabR2020a for each scaffold.

Cell density

Dapi stained nuclei were counted with particle analysis in ImageJ. The cell density for 200μm^2 regions of interest was calculated in MatlabR2020a for each scaffold.

6.2.10 RNA extraction, retrotranscription and RT-qPCR

RNA was extracted using GenElut Mammalian Total RNA Miniprep Kit (Sigma) according to the manufacturer's instructions. RNA (100 ng) was subsequently retrotranscribed to complementary DNA (cDNA) using Maxima First Strand cDNA Synthesis Kit (Thermo scientific). RT-qPCR was performed using Fast SYBR Green Master Mix on a 7500 Real-Time PCR System using GAPDH as a housekeeping gene. All primers were designed to span an intron-exon junction, and are listed in Table 6.2. The relative expression of mRNA was obtained using the ΔCt method. The RNA extraction and RT-qPCR was done by Dr. Maria Colzani.

Table 6.2 RNA Primers

Gene	Fw primer	Rev primer
hGAPDH	AACAGCCTCAAGATCATCAGC	GGATGATGTTCTGGAGAGCC
MYH7	ACTGCCGAGACCGAGTATG	GCGATCCTTGAGGTTGTAGAGC
MYH6	GCCCTTTGACATTCGCACTG	GGTTTCAGCAATGACCTTGCC
TNNI1	CCGGAAGTCGAGAGAAAACCC	TCAATGTCGTATCGCTCCTCA
TNNI3	TTTGACCTTCGAGGCAAGTTT	CCCGGTTTTCCTTCTCGGTG
SCN5A	GAGCTCTGTCACGATTTGAGG	GAAGATGAGGCAGACGAGGA
RYR2	ACAACAGAAGCTATGCTTGGC	GAGGAGTGTTCGATGACCACC
SERCA2A	ACAATGGCGCTCTCTGTTCT	ATCCTCAGCAAGGACTGGTTT
MYL2	TACGTTCGGGAAATGCTGAC	TTCTCCGTGGGTGATGATG
MYL7	CCGTCTTCCTCACGCTCTT	TGAACTCATCCTTGTTCACCAC

6.2.11 Statistics

Data are presented from 3 repetitions performed in triplicate. A t-test with a 95% confidence interval was used to determine statistical significance.

6.3 Results

6.3.1 Scaffold architecture

The mean pore size for scaffolds prior to cross linking was designed to be optimal for cardiomyocytes and measured to be 117 ± 9 μm [10]. Distinct scaffold architectures were observed across the transverse and longitudinal planes of the directionally freeze cast scaffolds. On the transverse plane the pores structure was found to be composed of homogenous and equiaxed pores, while on the longitudinal plane the pore structure was found to be composed of unidirectionally aligned pores as shown in Figures 6.2a and 6.2b respectively. Figure 6.2c shows the resultant intensity plots for the alignment analysis for each slicing plane. Significantly increased alignment was measured for the longitudinal plane, $\varepsilon_{AOP} = 0.66 \pm 0.08$ when compared to the transverse plane, $\varepsilon_{AOP} = 0.18 \pm 0.06$. It follows that scaffolds sliced to discs with 8 mm diameter and 500-700 μm thickness were dominated by the pore architecture

present on the circular face of the structure while all other physio-mechanical properties such as pore size, strut wall thickness, porosity, permeability and interconnectivity, were maintained. Scaffolds sliced parallel to the longitudinal plane will be referred to as aligned and scaffolds sliced parallel to the transverse plane will be referred to as pseudo-isotropic as illustrated in Figure 6.1. Scaffold properties were measured prior to cell-seeding. For clarity, the term scaffold will be used to refer to the structure without cells while the term construct will be used to refer to the scaffold structure in addition to cardiomyocytes.

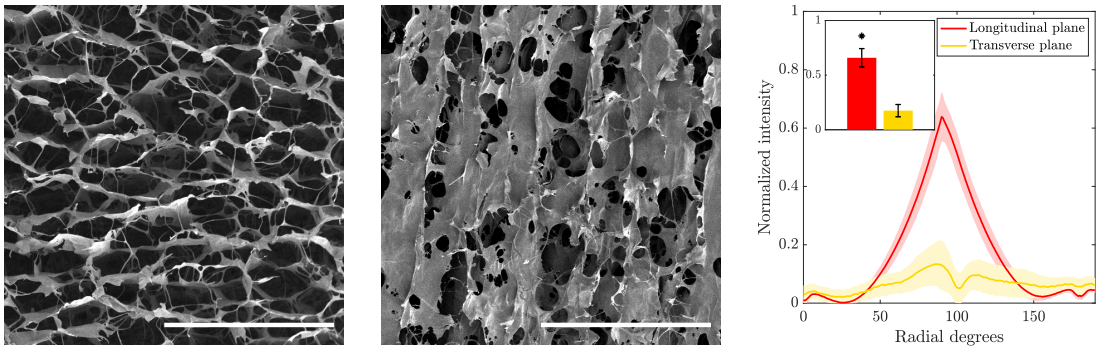

(a) (b) (c)

Fig. 6.2 SEM micrographs of scaffold structure in the **(a)** transverse plane and the **(b)** longitudinal plane (scale bars 500 um) **(c)** proportion of alignment at each radial orientation, insert shows the maximal alignment proportion for each slicing plane (N=3)

6.3.2 Cardiac selection

Representative samples of differentiated and selected cells were assessed for the cardiac specific marker, Troponin-T, via flow cytometry. It was found that greater than 90% of lactate selected cells were Troponin-T positive as shown in Figure 6.3.

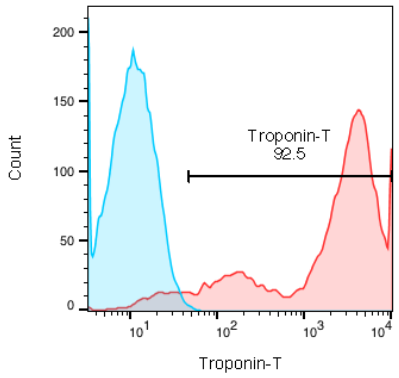

Fig. 6.3 A representative distribution of Troponin-T positive cells measured via flow cytometry. Blue indicated the control cells stained with an IgG antibody*control*; red indicates the Troponin-T positive cells within the lactic selected sample.

6.3.3 Tissue-level performance

Cell density

The cell density of each construct was calculated, to verify comparable cellular viability across conditions. Figures 6.4a & 6.4b show equal cell densities for each condition as measured through Almar Blue fluorescence intensity and nucleus density respectively.

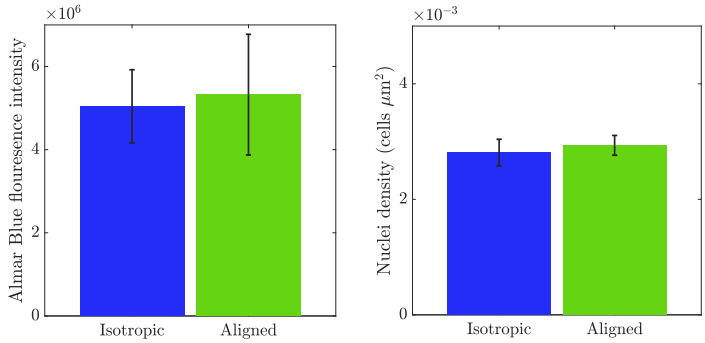

(a) (b)

Fig. 6.4 Engineered construct viability and cellular density measured through **(a)** Florescence intensity of Almar Blue (aligned N=4, pseudo-isotropic N=5) and **(b)** nuclei density (N=8 for both conditions) for each construct architecture; error bars represent standard error

Spontaneous electrical signalling

Calcium imaging is used as a surrogate for action potential visualisation in cardiac tissue engineering. Here, spontaneous calcium transience was used to assess the effects of scaffold structure on the long range electrical function of engineered cardiac tissue. Figures 6.5a and 6.5b show mean fluorescence intensity over time. Fast Fourier Transform analysis was used to determine the pulse rate of the fluorescence signal for each scaffold. It was found that the constructs with aligned architecture enabled a more regular pulse profile and a significantly greater pulse rate ($0.55\pm$ 0.09 Hz) than the pseudo-isotropic condition ($0.33\pm$ 0.03 Hz) as seen in Figure 6.5c.

The influence of scaffold architecture on the spatial uniformity of spontaneous electrical signalling was explored through pulse rate heat maps, visualised across the region of interest (ROI), as shown in Figures 6.5d-6.5g. It was found that pseudo-isotropic constructs resulted in a non-uniform spatial distribution of pulse rates. Figure 6.5d demonstrates the patchy distribution observed for pseudo-isotropic samples, where some regions were found to pulse more frequently than others, resulting in a high spatial variance as shown in figure 6.5e. The same observation was true for all pseudo-isotropic constructs. In contrast, aligned constructs resulted in largely uniform spatial distributions of pulse rates and reproducibly small spatial variances as shown in Figures 6.5f-6.5h. In addition to the pulse rate, the intra-pulse spatial uniformity of electrical signalling was characterised. Figures 6.5i-6.5l show the isochrones and temporal histograms for time of peak fluorescence within a global pulse. The pulses sampled are specified by green boxes in Figures 6.5a and 6.5b. It was found that the construct architecture similarly influenced the electrical dynamics within a single pulse, the performance of pseudo-isotropic constructs was characterized by large spatial variance and patchy isochrones, whereas aligned constructs resulted in predominantly concurrent signalling across the field of view as shown in Figure 6.5m. These results indicate

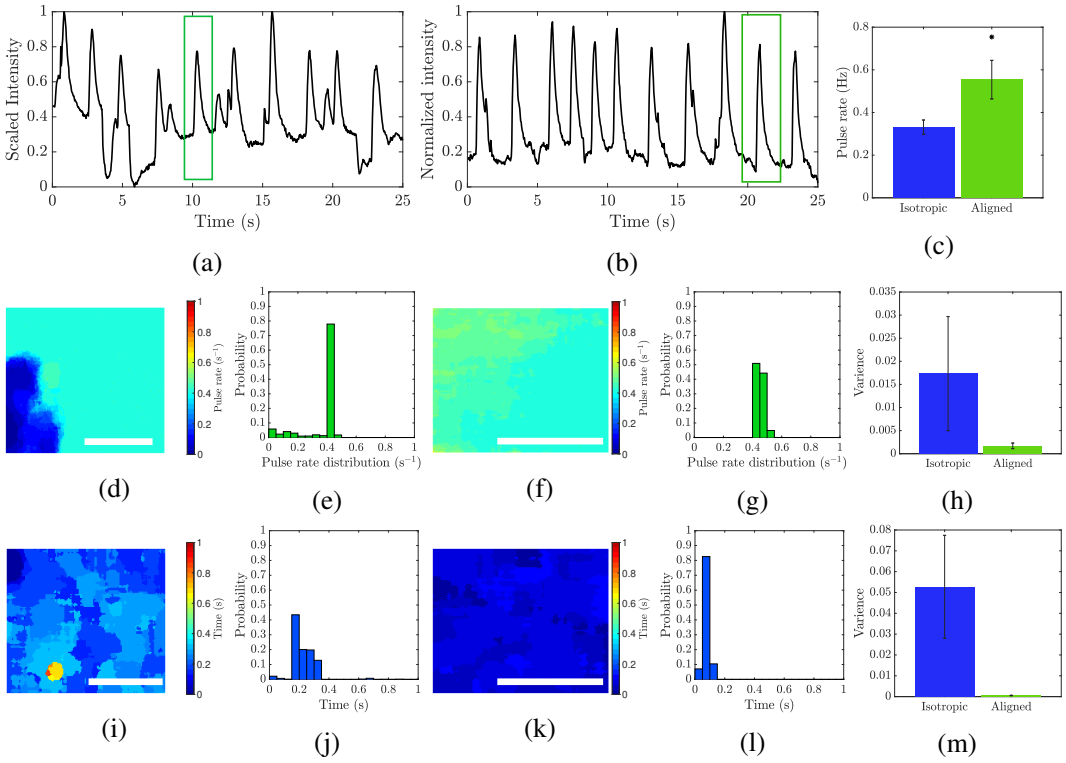

Fig. 6.5 Live Fluo-4 AM calcium staining was performed on immature cardiomyocytes derived from H9 hESCs after 7 days of culture, video recordings of fluorescence dynamics were used to asses the temporal and spatial signalling uniformity **(a)** & **(b)** mean fluorescence intensity in time for cardiomyocytes on pseudo-isotropic and aligned scaffolds respectively **(c)** pulse rate for all pseudo-isotropic (N=8) and aligned (N=5) samples **(d)-(g)** illustrate pulse rate in space and associated histogram for **(d)** & **(e)** a pseudo-isotropic construct and **(f)** & **(g)** an aligned construct **(h)** spatial variance of the pulse rate for pseudo-isotropic (N=5) and aligned (N=3) constructs **(i)-(l)** illustrate the time of peak fluorescence in space within a single pulse, designated by the green boxes in **(a)** & **(b)**, and associated histogram for **(i)** & **(j)** pseudo-isotropic constructs and **(k)** & **(l)** aligned constructs **(m)** spatial variance of time of peak fluorescence within a pulse for all pseudo-isotropic (N=5) and aligned (N=3) constructs; Scale bars represent 0.2 mm; error bars represent standard error

that the spontaneous electrical signalling dynamics of engineered cardiac tissue are greatly influenced by the underlying scaffold structure, and that improved signalling uniformity was achieved in the aligned construct.

Paced electrical signalling

The influence of scaffold architecture on electrical signalling dynamics was also characterised in a field paced environment. The transient calcium fluorescence for pacing at 1 Hz and 1.5 Hz are shown in Figures 6.6a-6.6c and Figures 6.6d-6.6f respectively. It can be seen that calcium signalling on pseudo-isotropic structures, irrespective of pacing frequency, displayed reduced regularity in calcium cycling when compared to results for anisotropic samples. Additionally, while the dynamic signalling on anisotropic constructs was able to conform to the external pacing frequency at both 1 and 1.5 Hz, pseudo-isotropic constructs were not found to conform with a pacing frequency of 1.5 Hz as shown in Figure 6.6f. The influence of scaffold structure on paced signalling dynamics were also characterised through waveform dynamics.

The calcium signalling fluorescence wave form was characterised by the temporal characteristics, time to peak, and time to 90% decay, illustrated in Figure 6.6g. For both pacing frequencies it was found that the temporal wave characteristics for calcium signalling on aligned constructs were shorter relative to that of pseudo-isotropic constructs, as shown in Figures 6.6h-6.6k. The reduced temporal waveform characteristics observed for aligned constructs indicate an increase in signalling synchronicity, and reactivity for both external pacing frequencies.

Dynamic strain

Contractility is an increasingly important parameter, used to assess the physical performance of cardiac tissue constructs [69]. Here, the characteristic strain profiles for each scaffold architectural morphology were compared. Scaffold architecture was found to dramatically influence the deformation profiles and therefore, resultant principal strains of the engineered

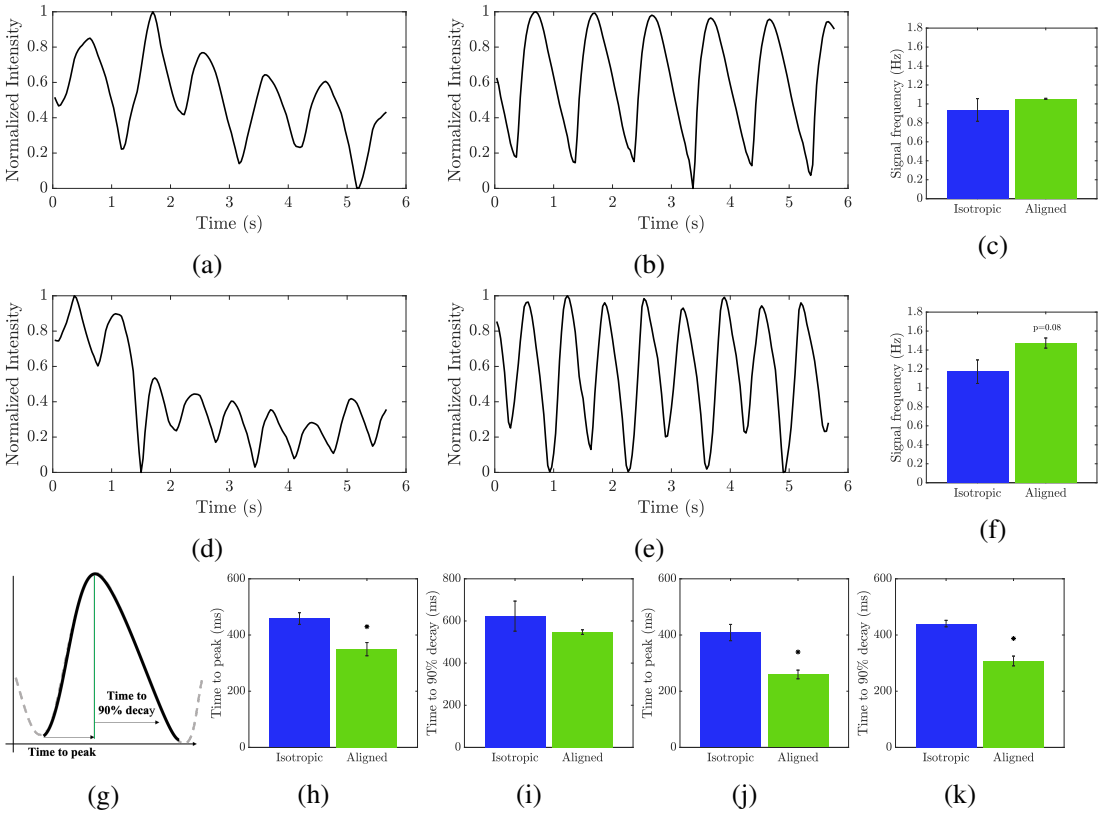

Fig. 6.6 Paced calcium dynamics **(a)**-**(b)** normalized fluorescence intensity analysis with pacing at 1 Hz for **(a)** pseudo-isotropic and **(b)** aligned constructs **(c)** mean signal frequency for each structure **(d)**-**(e)** normalized fluorescence intensity dynamics with pacing at 1.5 Hz for **(d)** pseudo-isotropic and **(e)** aligned constructs **(f)** mean signal frequency for each structure **(g)** waveform diagram **(h)**-**(k)** waveform analysis of intensity dynamics for pacing at **(h)** & **(i)** 1 Hz and **(j)** & **(k)** 1.5 Hz; all error bars represent standard error; all experimental repartitions were done with an N=3

constructs. Principal strains for pseudo-isotropic constructs were found to occur concurrently with equal and opposite magnitudes, indicating no net surface area change during the contraction as shown in Figure 6.7a. The average strain magnitude at maximal contraction was 0.015 with a maximal contractile strain rate of $0.1\ t^{-1}$ and relaxation strain rate of $0.05\ t^{-1}$ as shown in Figure 6.7b. Heat maps of the spatial distribution of principal component magnitudes at peak strain illustrate a high variability in component strains across the construct surface. Figures 6.7c and 6.7d show a representative spatial distribution of strain, where the

patchy profile is reminiscent of the spatial distributions for calcium dynamics observed in the previous section. Furthermore, no uniformity was observed in the strain direction, shown by the overlaid vector field in Figures 6.7c and 6.7d.

The strain dynamics that resulted from aligned constructs sharply contrasted the results for pseudo-isotropic samples. Principal strains for anisotropic constructs were also found to occur concurrently. Figure 6.7e, however, shows that strain magnitudes during contraction differed dramatically, indicating a net negative surface area change during contraction. It was observed that the average strain magnitude at maximal contraction for ε_1 (0.15) was ten times greater than the orthogonal component, ε_2 (0.015). A similar relationship was observed in the strain rate profile, where the strain rates for ε_1 reached a maximal contractile rate of $1.15\,t^{-1}$ and relaxation rate of $0.75\,t^{-1}$. The strain rates observed in ε_2, on the other hand, were dramatically reduced as shown in Figure 6.7f. To further understand the influence of structural anisotropy on the strain dynamics, the principal strain orientation was compared to the scaffold orientation. It was found that ε_1 was parallel to the scaffold architecture alignment, indicated by a white arrow in Figure 6.7g. Figure 6.7j showing that the aligned construct morphology resulted in a significantly increased directional contraction, and Figure 6.7l illustrates a significant increase in coordination of the deformation. The directional deformation dynamics observed for the anisotropic construct condition are consistent with previously reported deformation profiles of native cardiac tissue *in vivo*, where ε_1 is shown to be 2.5 times greater than ε_2 [46].

The shape of the total tissue strain rate over time has been identified as an important indication of functional cardiac tissue. For native tissue three characteristic points have been identified: *i)* a global minimum during peak systole (SRs), *ii)* a global maximum with reduced magnitude during disatole (SRe) and *iii)* a small maximum during the isovolumetric contrac-

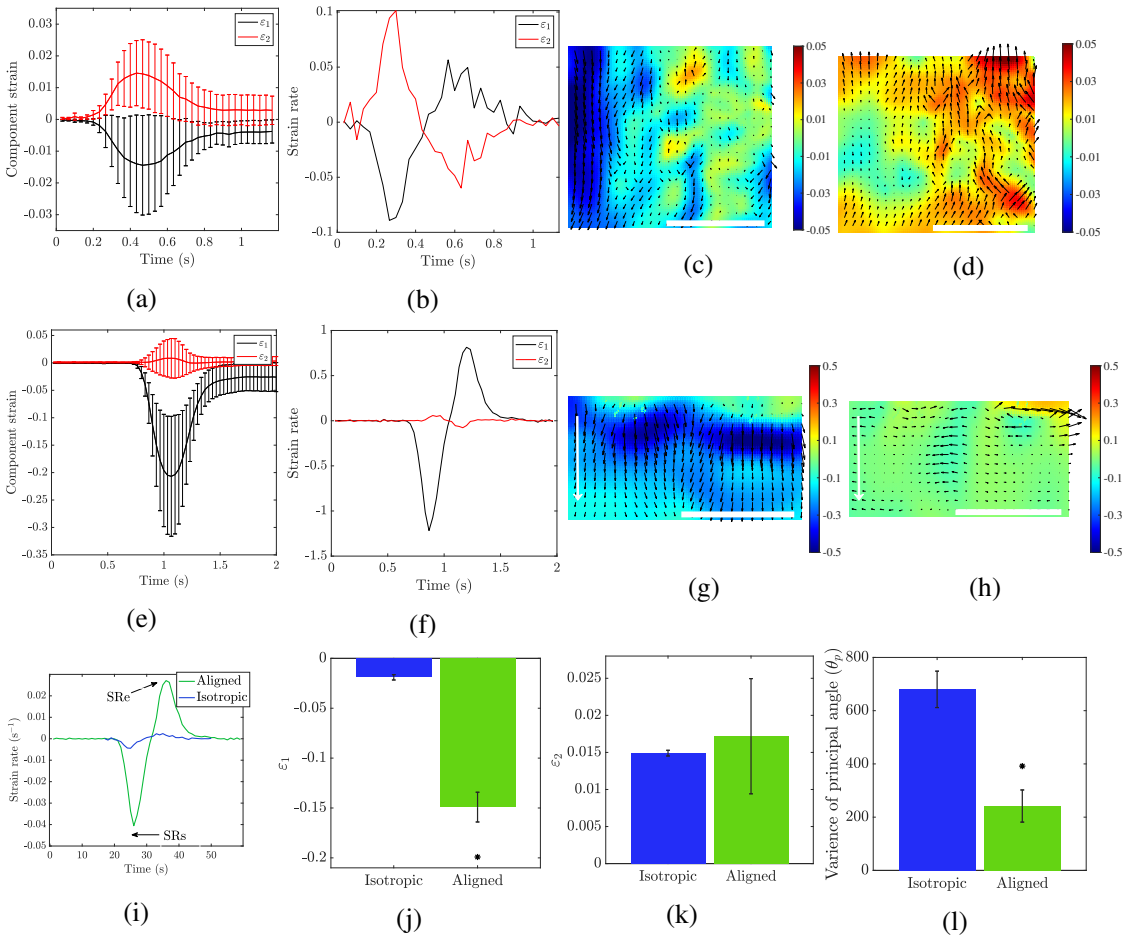

Fig. 6.7 Live bright field imaging was performed on immature cardiomyocytes derived from H9 hESCs after 7 days of culture, video recordings were used to asses the construct deformation during contraction. Strain dynamics for **(a)-(d)** pseudo-isotropic constructs and **(e)-(h)** aligned constructs; **(a)** & **(e)** principal component strain in time (error bars show standard deviation within the region of interest), **(b)** & **(f)** mean strain rate for each principal component strain, **(c)** & **(g)** spatial colour map for ε_1 at maximum strain, **(c)** & **(g)** spatial colour map for ε_2 at maximum strain, **(i)** maximum ε_1 for all pseudo-isotropic and aligned constructs **(j)** maximum ε_2 for all pseudo-isotropic and aligned constructs, **(k)** variance of principal strain direction for all pseudo-isotropic and aligned constructs. For heat maps; scale bar is 1 mm; error bars represent standard error; all experimental repartitions were done with an N=8

tion of diastole (SRa) [46]. Figure 6.7i shows the total strain rate for both an aligned and pseudo-isotropic construct. With the exception of the intermediate peak due to isovolumetric contraction (SRa), this strain rate shape is consistent with the strain rate produced with the

aligned construct, where SRs and SRe were found to be -0.04 and 0.025, approximately 44% and 83% of physiologically recorded values respectively [46]. The labelling of key physiological strain characteristics can be seen in Figure 6.7i. Taken together, strain dynamics provided a useful tool in characterising the contractile deformation of engineered tissue and enabling comparisons with native tissue. It was found that aligned constructs recapitulated the strain and strain rate patterns observed during typical cardiac function.

6.3.4 Characterisation at a cellular level

Cellular phenotypic maturity

At tissue-level length scales, structural anisotropy was found to influence both signalling dynamics and functional deformation. To further understand the influence of structural anisotropy on regenerative cardiac constructs phenotypic and functional development was also characterised at a cellular level. Gene expression analysis was performed through qPCR for the radioiodine receptor-Ca^{2+} release channel (RYR), cardiac α-myosin heavy chain (MYH6), β-myosin heavy chain (MYH7), Troponin-I 1 (TNNI1) and Troponin-I 3 (TNNI3). Expression of RYR was found to be elevated in cells seeded on aligned structures relative to pseudo-isotropic as shown in Figure 6.8a. Additionally, it was found that relative expressions on both the TNNI an MYH axese indicated that higher levels of phenotypic and developmental maturity were achieved by cells seeded on aligned structures relative to pseudo-isotropic as shown in Figures 6.8b & 6.8c.

Intra- and extra-cellular organisation

Due to its role as the contractile unit of the cardiomyocyte, sarcomeric development is commonly assessed to characterise functional cellular development in engineered cardiac

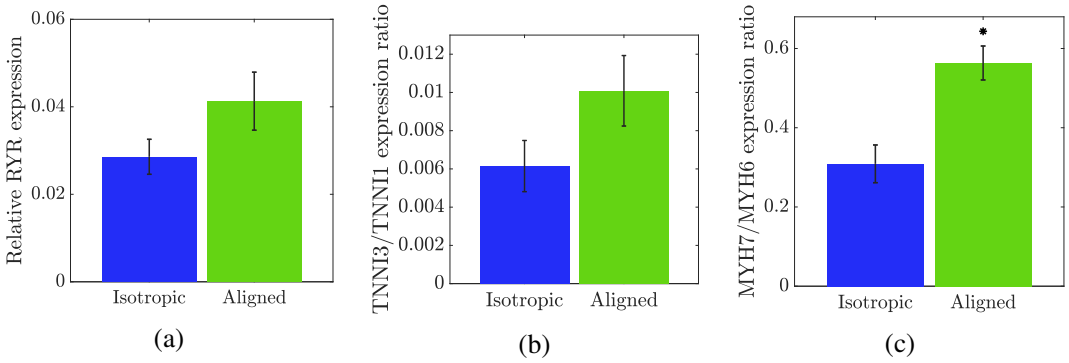

Fig. 6.8 Gene expression **(a)** relative RYR expression **(b)** cardiac troponin (TNNI3) to slow twitch troponin (TNNI1) expression ratio **(c)** myosin composition MYH7 to MYH6 expression ratio for each construct morphology; error bars show standard error; all experimental repartitions were done with an N=3

tissue [140, 171, 308]. Here, sarcomeric development was analysed through the localisation of the contractile protein α-actinin, to understand the influence of extracellular order on functional intracellular structure formation. It was found that cells seeded onto pseudo-isotropic scaffolds displayed reduced banding prominence and organisation when compared with those on aligned structures as shown in Figures 6.9a-6.9d. A significant difference in sarcomere prominence was observed; additionally, a positive trend between alignment and sarcomere length was also found as illustrated in Figures 6.9e & 6.9f. Reduced banding prominence and spacing indicates a reduced state of sarcomere development and has been shown to reduce intracellular contractile force [140, 308]. In addition to sarcomere maturity, construct contractility has also been correlated with intra and intercellular orientation uniformity [140].

The effects of extracellular structure on cellular orientation and intercellular alignment, were analysed through orientation analysis of the actin cytoskeleton. It was observed that cells seeded on the pseudo-isotropic structure exhibited no preferential orientation direction as shown in Figures 6.10a-6.10d, whereas, those on aligned scaffolds conformed to the extracellular structural alignment and displayed increased orientation uniformity as shown in Figures 6.10e-6.10h. Cellular coherence measurements illustrate the degree to which cellular

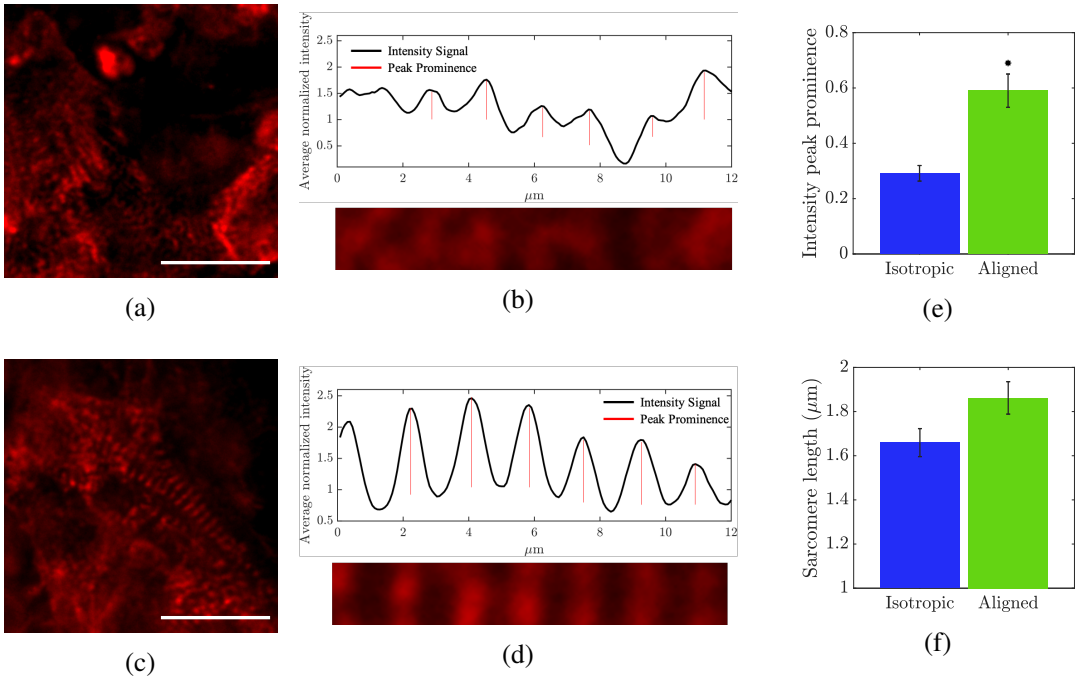

Fig. 6.9 Immature cardiomyocytes derived from H9 hESCs stained for α-actinin after 7 days on **(a-b)** pseudo-isotropic scaffolds and **(c-d)** aligned scaffolds; scale bars represent 20 μm **(b)** and **(d)** demonstrate the quantification of sarcomeric organization through relative intensity peak prominence along a single sarcomere chain **(e)** relative intensity peak prominence (sarcomere intensity) **(f)** sarcomere length for cells on aligned (N=4) and pseudo-isotropic (N=3) scaffolds; error bars represent standard error

structures uniformly align, while orientation variance describes the distribution of cellular orientations present within the construct as illustrated in Figure 6.10i. Figures 6.10j and 6.10k show that cardiomyocytes were found to align with increased cellular coherence and intercellular uniformity on aligned constructs relative to pseudo-isotropic structures. These results help to explain the differences in tissue deformation observed above, and the strong, directional contraction that resulted from the aligned construct.

Directional contraction is facilitated by uniform cellular orientation, however, continuous signal propagation is essential for concurrent cellular contraction and optimised contractile force. The intercellular signalling capacity of aligned and pseudo-isotropic constructs were

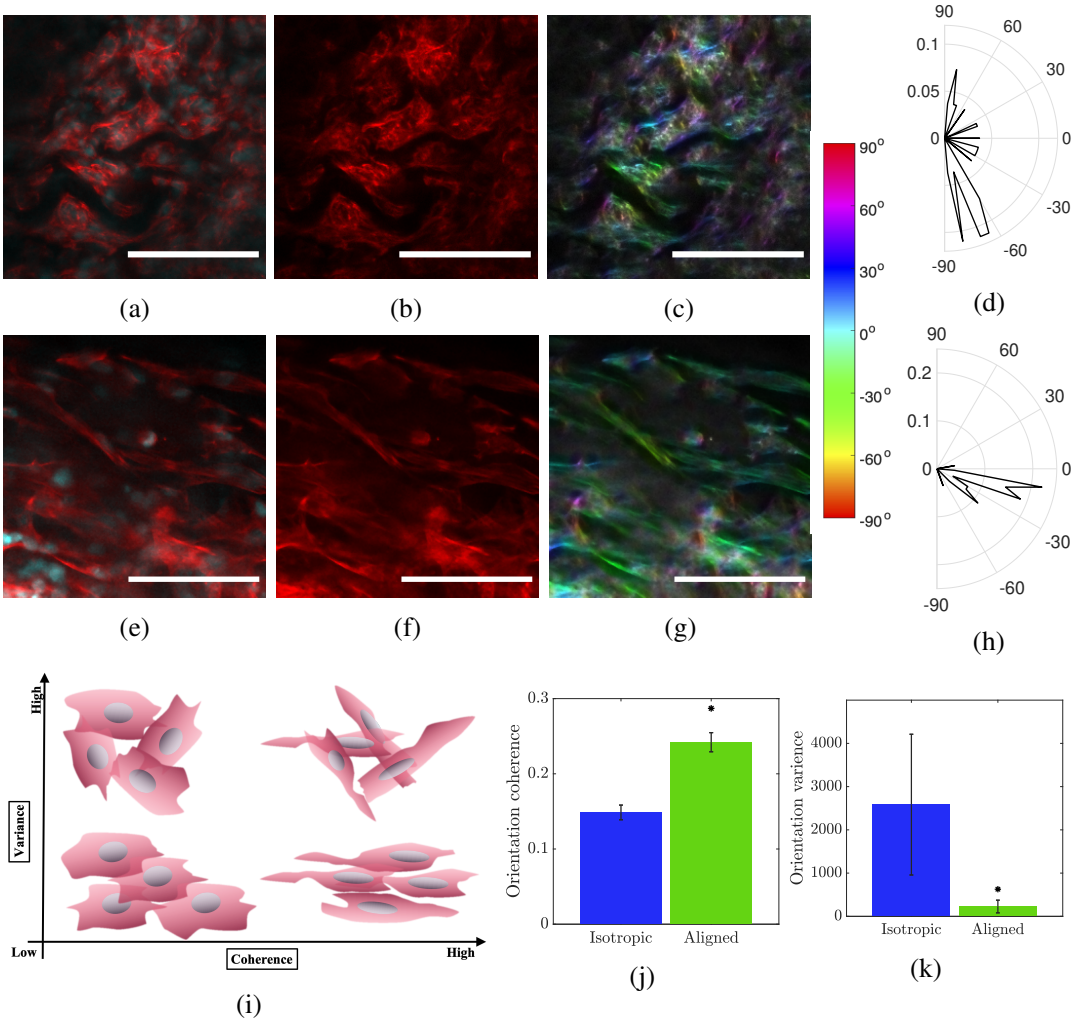

Fig. 6.10 Immature cardiomyocytes derived from H9 hESCs stained for actin (phalloiden, red) and cell nuclei (dapi, blue) after 7 days on **(a)-(c)** pseudo-isotropic scaffolds and **(d)-(f)** aligned scaffolds; scale bars represent 100 μm **(a)** &**(d)** composite image **(b)** & **(e)** Isolated Phalloiden channel showing actin organisation **(c)** &**(f)** actin orientation colormap resulting from Fourier transform orientation analysis over a moving pixel average of 2 pixels **(g)** &**(h)** polar histograms of the actin orientation of cardiomyocytes within a single scaffold **(g)** pseudo-isotropic and &**(h)** aligned **(i)** diagram of coherence and variance **(j)** average actin orientation coherence for all pseudo-isotropic and aligned samples **(k)** average actin orientation variance for all pseudo-isotropic and aligned samples; error bars represent standard error; all experimental repartitions were done with an N=5

compared by assessing the presence of connexin-43, the protein that comprises gap junctions.

Due to the immature nature of the seeded cardiomyocytes gap junctions were expected to

appeared as punctuated structures where a high density of connexin-43 was present rather than the distinctive perimeter pattern of intercalated discs observed in mature cells [309]. Figures 6.11a-6.11d illustrate early focal concentrations of connexin-43 that is indicative of early gap junction development [309, 310]. The prevalence of gap junction structures was compared between conditions and it was found that aligned structures facilitated a higher density of early gap junctions relative to pseudo-isotropic structures, as shown in Figure 6.11e. This result is consistent with the higher signalling uniformity observed for aligned structures.

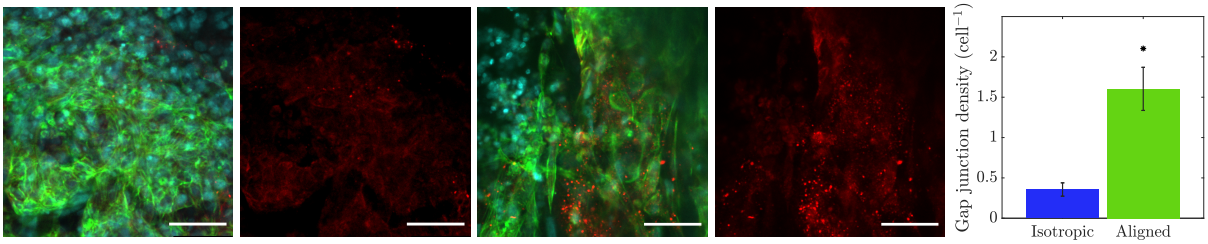

(a) (b) (c) (d) (e)

Fig. 6.11 Immature cardiomyocytes derived from H9 hESCs stained for Dapi (blue) Troponin (Green) and Connexin (red) after 7 days on **(a)-(b)** pseudo-isotropic scaffolds and **(c)-(d)** aligned scaffolds; scale bars represent 50 μm **(a)** & **(c)** Composite images **(b)** & **(d)** isolated connexin channel showing gap junction structures **(e)** gap junction density for all pseudo-isotropic (N=5) and aligned (N=4) samples; error bars represent standard error

6.4 Discussion

The field of cardiac tissue engineering has made rapid progress in recent years, expanding the potential for tissue regeneration in future human and model medical systems. Clinical application of a regenerative cardiac patch is, however, limited largely by an insufficient capacity for regenerative constructs to replicate the signalling and physio-mechanical dynamics of native tissue, as well as impart appropriate physio-mechanical cues to promote cardiogenisis, maturation and engraftment [3, 114–116]. Currently, the electrical function

and contractile force generated by engineered cardiac tissues falls well below desired levels and is compounded by inconsistent electrical integration with the host myocardium [44]. Through a direct comparison, it was demonstrated, here, that optimisation of scaffold structure can improve the biomimetic signalling and contractile functionality of regenerative cardiac constructs. These results provide a direct comparison between current tissue engineering design methodologies, and further elucidate the influences of scaffold architecture on the performance of engineered cardiac tissue.

The dynamic functionality of the heart arises from the contraction of cardiomyocytes arranged in distinct orientations by a highly ordered ECM [35, 311]. To date, however, the isolated functional effects of architectural organisation in engineered tissue have not been systematically studied. In order to accurately compare the effects of scaffold architecture on engineered tissue constructs efforts need to be made to conserve physio-mechanical properties across conditions, such that the architectural order is the only variable. Here, the inherent geometric asymmetry of directionally freeze-cast three dimensional collagen scaffolds, with pore sizes optimised for cardiomyocytes [10], was utilised to produce thin scaffold discs dominated by distinct architectural morphologies as shown in Figure 6.2c. The use of a single parent scaffold for both architectural conditions ensures that micro-scale and nano-scale scaffold features are conserved between conditions while the long-range structural anisotropy is varied. Each structure was seeded with cardiomyocytes, and the functional and cellular dynamics of the engineered constructs were compared. By performing a systematic comparison at multiple length scales the recent studies in anisotropic cardiac design can be contextualised, and future design methodologies in preclinical cardiology and regenerative medical research can be informed [70, 302–305].

The influence of architectural morphology on the electrochemical signalling capacity of each construct was explored through live calcium fluorescence, where calcium wave propagation is considered analogous to action potentials [25, 71, 35]. Furthermore, calcium signalling patterns have been shown to vary depending on the anatomical region of the myocardium, a result observed through transverse cardiac slicing and optical imaging [72, 73]. For this reason spatial and temporal signalling patterns are of great importance when assessing the translational potential of regenerative cardiac patches. The spatial and temporal homogeneity of fluorescence dynamics were used to compare the long range effects of each scaffold morphology on spontaneous calcium signalling and conductivity. Figures 6.5d-6.5m show that the pseudo-isotropic condition resulted in poor spatial uniformity for both pulse rate and intra-pulse time of peak intensity when compared to the aligned condition. The patchy signalling profiles produced by the pseudo-isotropic condition indicate that signalling propagation across the scaffold surface is hindered by the pseudo-isotropic structure. This result is consistent with findings presented by Macqueen et al. in 2018 [70]. It was demonstrated that when the aligned structure of electrospun PCL/gelatin scaffolds was interrupted, for example by a punched hole in the scaffold, calcium signalling patterns, measured through florescence, were greatly influenced. The temporal uniformity of calcium florescence was found to be reduced. Furthermore, the temporal disruption was found to increase when additional holes were punched into the scaffold [70]. In contrast, the aligned constructs were found to encourage a continuous and uniform signalling profile. These results help to indicate the signalling and contractile functionality of each structure type, and are in agreement with results presented by Feinberg et al. in 2012 who showed that the transition from isotropic tissue organization to increased uniaxial alignment was associated with enhanced calcium handling in two dimensions [71].

Field pacing was also utilised to test the conformance of construct signalling dynamics to external stimuli. It was found that while both conditions conformed to pacing at 1 Hz, the aligned construct was more sensitive to the 1.5 Hz pacing frequency as shown in Figure 6.6f. Through waveform analysis it was also found that the aligned constructs facilitated a more punctuated signal, with a faster time to peak and time to 90% decay profile when compared to the pseudo-isotropic condition as shown in Figures 6.6h-6.6k. Taken together the results of both spontaneous and paced signalling dynamics demonstrate that aligned structures facilitated an improved capacity to direct a synchronous electrochemical signal and conform to external pacing. When considering the *in vivo* environment, the capacity for regenerative cardiac constructs to translate electrical signals across the damaged myocardium is paramount. Here, aligned structures would enable uniform signal transduction whereas pseudo-isotropic structures were found to disrupt the signal propagation which resulted in arrhythmia-like behaviour [70, 138, 312].

A similar trend was observed when the tissue level contractile function of the two tissue morphologies was compared. Contractility is an emerging parameter that describes the dynamic function of engineered cardiac tissue. Contractility is commonly measured with force. Current force measurement techniques, however, are compromised by the complex mechanical and biochemical contribution of the extracellular structure [301, 313]. Recently, the deformation and contractility of the native myocardium has been characterised through strain and strain rate. These parameters circumvent the limitations associated with force measurements and have enhanced the understanding of myocardial function through direct optical methods [46, 69].

The direction and rate of strain produced by regenerative constructs were compared to that of native tissue to further understand the ability of engineered tissue to recapitulate native

mechanical performances. It was found that contractile functionality was significantly improved by extracellular alignment as shown in Figures 6.7a-6.7h. Aligned cardiac tissue constructs facilitated not only increased deformation, but additionally a defined and directed synchronous contractile behaviour that resulted in tissue densification and surface area reduction as indicated by the increased magnitude of ε_1 relative to the orthogonal component in Figure 6.7e. This deformation behaviour matches previously reported surface deformation characteristics of *in vivo* cardiac tissue [46]. The directional contraction in native tissue optimises cardiac output [181]. In addition to the strain dynamics, strain rate has also been identified as an important parameter when characterising cardiac tissue function [46]. Figure 6.7i shows the tissue strain rate for both the pseudo-isotropic and aligned constructs, and it can be seen that the aligned construct produced a more physiologically relevant profile when compared to the pseudo-isotropic construct. The differences in contractile function can be attributed to the degree of long range cellular order facilitated by each scaffold structure. In two dimensions it has been shown that cellular alignment encourages intercellular sarcomere coherence, which in turn results in directed contractile force [71]. In contrast, the lack of long range structural organisation in the pseudo-isotropic construct hampered the development of directional deformation. This deformation characteristic, in a translational setting, would reduce the mechanical coupling between the engineered tissue and host myocardium.

The cells used in this chapter were derived from a hESC line. There are ethical limitations associated with use of hESCs. Embryonic stem cells are derived from pluripotent cells of the early human embryo, therein, destroying the embryo [314]. The ethical limitations of this method has fuelled the development of induced pluripotent stem cells (iPCs). iPSC are derived from skin or blood cells that have been reprogrammed back into an embryonic-like pluripotent state, enabling the development of an unlimited source of any type of human cell, a technique developed in 2006 [315]. The H9 line of hESCs was produced in 1998 by Dr.

J. A. Thomas [314]. The line is immortal and has been maintained for the last two decades. It follows that differentiation protocols for hESCs have been better established than those of iPSCs [316]. The H9 hESC line was approved for clinical trials a short time after it's development and hESCs have well established usage in translational science [317]. There are numerous clinical trials currently utilizing hESCs for therapeutic benefit. Initially the use of iPSC in a clinical setting was slowed by the use of viral vectors to reprogramme somatic cells into a pluripotent state [316]. However, more recently viral free programming methods have been established and efficient differentiation protocols have been developed. Currently, a few iPSC based clinical trials have been approved, however this number is expected to increase rapidly [316, 317]. While the relatively robust clinical history of hESCs makes these cell lines appealing for translational research such as the development of a cardiac patch, recent advancements of iPSCs has made them a viable option for translational medical research and a consideration for future studies as the results in this thesis should be reproducible with an iPSC cell type.

The functional differences between conditions were further explored at a cellular level. Gene expression analysis showed that cells seeded onto aligned scaffolds showed increased cellular cardiogenisis and maturity. The RYR protein is responsible for the smooth endoplasmic reticulum (SR) calcium efflux mechanism that initiates contraction. Elevated expression of this calcium handling gene on aligned constructs, as shown in Figure 6.8a, helps to explain some of the differences in signalling dynamics and signalling waveform observed between conditions. Additionally, phenotypic development was characterised by observing the ratio between the gene expression for the sarcomere protein isoforms TNNI and MYH. The TNNI protein is part of the troponin complex of thin filaments in striated muscle cells, where it prevents myosin binding in the relaxed state. The relative expression of TNNI3 (cardiac troponin) to TNNI1 (slow twitch troponin) indicates cardiac phenotyping. The myosin

composition is governed by the MYH gene expression, where the relative expression of MYH7 and MYH6 indicates developmental maturity. Figures 6.8b and 6.8c show that aligned constructs facilitated increase cellular cardiogenesis and maturity.

In addition to increased cellular maturity, aligned constructs were also found to increase the intra-cellular and intercellular order as well as cellular communication infrastructure. Figures 6.9e and 6.9f demonstrate the increased sarcomere organisation observed on aligned constructs which has been shown to correlate with cellular contractility [71]. Furthermore, the aligned constructs were found to facilitate improved intercellular organisation and alignment across the scaffold as indicated by a significant increase in orientation coherence and decrease in orientation variance shown in Figures 6.10j & 6.10k. The differences in sarcomere development and cellular organisation help to explain the increased contractile function observed on aligned constructs. Similarly, the differences in signalling dynamics can be explained by the increased prevalence of early gap junction structures on aligned constructs as illustrated by Figure 6.11e. Gap junction structures help facilitate intercellular communication. The increased appearance of focal densities of connexin-43 staining is consistent with previously published studies [309, 310]. Johannes Bargehr et al 2019 demonstrated that injection of both cardiomyocytes and hESC derived epicardial cells into rat hears after infarct resulted in early gap junction formation between the native tissue and the injected cells as well as between implanted cells. These early gap junctions were indicated through focal densities of connexin-43 florescence staining[310]. These results contextualize the staining patterns observed in this chapter. The improved gap junction development observed on the aligned scaffolds can, therefore, help explain the improved signalling transduction observed within this condition.

These results raise some important questions about the mechanism by which tissue architecture improves cellular phenotyping and maturity. It has been postulated that extracellular boundary conditions regulate cellular function through the coordination of sarcomeres at an intercellular level [35, 71]. This does not explain the increased cellular maturity observed on aligned structures as the immediate cellular environment and scaffold structure at a micro-scale and nano-scale are largely the same due to the common scaffold origin. A recent study by Bouchard et al. 2019 found that increasing external electromechanical stimulation increased the rate of maturation for early hiPS-CMs [67]. Given this information, it can be further hypothesised that the cellular boundary conditions are not directly encouraging maturation, but rather, coordinating a stronger tissue level contractile behaviour. This enhanced and uniform contraction is effectually a self-reinforcing system, in which, the amplified contractile force, facilitated by structural alignment, serves to cyclicly stimulate the tissue construct and enhance the rate of cellular maturation. It can, therefore, be hypothesised that the developmental differences between structures can be attributed to the amplification of auto electromechanical stimulation that results from long range cellular order. Additionally, as maturity increases, so too does the magnitude of the external stimulation. This, in turn, encourages further maturation, creating an autologous system that parallels the work done by Bouchard et al. 2019 [67]. This effect is reduced for the pseudo-isotropic structure as the absence of long range cellular order disrupts the ability of cardiomyocytes to align and contract along the main axis of the scaffold, thus reducing the contractile forces of the tissues [35]. Therefore, it was found that while scaffold architecture did influence the cellular and functional performance of engineered cardiac tissue. Future work is needed to completely deconvolve the relationship between structure and tissue development.

6.4.1 Conclusion

Through a direct comparison, it has been shown that aligned macro-architecture is beneficial for both functional and cellular development of regenerative cardiac constructs. Additionally, the understanding of the role scaffold architecture plays in cellular development and tissue function for engineered cardiac tissue has been improved. It has also been hypothesised that the observed difference in maturity is a result of the long range cellular order and the consequent improved intra-cellular and intercellular contractile dynamics that serve to electromechanically self stimulate the whole construct. Further study is required to fully deconvolve the relationship highlighting an interesting future research direction. Taken together these results illuminate the importance of scaffold structure for hierarchical cardiac patch development and function at multiple length scales. This work can help inform the design of regenerative cardiac tissue for translational applications and the development of more physiologically relevant in vitro tissue culture/organoid models.

Chapter 7

Characterising collagen scaffold compliance to native myocardial strains using an *ex vivo* cardiac model

7.1 Introduction

After implantation, cardiac scaffolds will be subjected to a complex biomechanical environment of time-varying physio-mechanical changes in stresses, strains, and structural deformation [11]. The mechanical capacity of engineered tissue to biomimetically deform and simultaneously support the damaged native tissue is crucial for the success of engineered grafts [11]. There is, therefore, a great need for the characterisation of the diverse array of superficial strains that occur across the myocardium, and to characterise the relative compliance of regenerative scaffolds. This information will provide important insights into the long-term capabilities of engineered scaffolds.

In recent years, new technologies have been developed to measure the *in vivo* strains of the myocardium. Different non-invasive imaging techniques can be used to perform cardiac

strain imaging (CSI) such as ultrasound speckle-tracking echocardiography (STE), cardiac magnetic resonance image (cMRI) feature tracking, cMRI tissue tagging, and cardiac computed tomography (CCT) [58, 60]. STE is the most popular technique because of its relatively simple implementation and clinical availability [58, 61]. Two dimensional echocardiography allows for the analysis of complex mechanisms of myocardial deformation in time and space [61, 318, 319]. STE typically involves capturing and processing planar cross-sectional views of the heart, meaning the deformation across the surface of the myocardium is not characterised. Ferraiuoli et al. 2019, developed a 3D speckle tracking protocol across the surface of the myocardium in an *in vitro* haemodynamically loaded porcine heart platform [320]. A full-field strain map was produced for multiple beat cycles and local variations of principal strains were recorded across the epicardial surface [63, 321]. The *in vitro* haemodynamically loaded porcine heart model, however, fails to account for the native strains produced by myocardial contraction. Soltani et al. 2018, characterised the surface strains of the right ventricle during open heart surgery using optical imaging and speckle pattern tracking [46]. The obtained full-field measurements of native myocardial principal strains provided new insight into the biomechanics of the heart. The open heart surgery model has, however, only a limited field of view and is not applicable to test myocardial reaction to novel pharmaceuticals or regenerative scaffolds.

In this chapter, an *ex vivo* ovine cardiac perfusion model is used to enabled direct observation of the native surface myocardial movement during the cardiac cycle. The *ex vivo* cardiac model was used as a platform to observe and quantify the mechanical compliance of cardiac scaffolds with varied structural architectures and fixation methods to the native deformation of the superficial epicardium. Cardiac patches consisting of collagen scaffolds produced with either aligned or isotropic pore architectures were applied to the left ventricular wall using sutures or glue fixation. Through direct optical imaging and digital image correlation the

conformance of the acellular scaffolds to the native myocardial deformation patterns was assessed and compared. The performance of each scaffold condition was quantified through strain analysis and compared both with the surrounding myocardium and the control condition. Through direct observation of the physio-mechanical patch performance when adhered to live tissue, the influences of scaffold structure and fixation method can be quantified and compared to further inform the translational design of therapeutic cardiac tissue engineering.

7.2 Methods

The work in this chapter was done collaboratively with Dr. Clare Burdett, a member of the Cambridge Center for Medical Materials, in Cambridge, UK. Dr. Burdett's contributions were greatly appreciated and are specified in this section.

7.2.1 Scaffold fabrication

A 1 wt% suspension of insoluble type I bovine dermal collagen (Devro) was prepared according to the protocol laid out in section 3.1.2. Directionally freeze-cast scaffolds were fabricated using the controllable heat sink and mould system described in section 3.1.1. A 9 ml volume of collagen suspension was used. The heat sink was programmed to hold at -10 ^{o}C for 1 minute followed by cooling at a rate of 2 ^{o}C min^{-1}.

Isotropic scaffolds were fabricated in a freeze drier (VirTis SP Scientific Wizard 2.0). A 2 ml volume of collagen suspension was pipetted into standard 24-well plates (Corning, NY, USA), to a filling height of 8 mm. Well plates were placed on a Teflon block (10 mm thickness) and frozen in the freeze drier with a shelf temperature of -30 ^{o}C for 3 hours.

After solidification, scaffolds were dried, imaged and then cross linked to 30% according to the protocols described in sections 3.1.2 & 3.1.2.

Scaffold imaging

Prior to cross linking, scaffolds were imaged with both scanning electron microscopy and X-ray micro-computed tomography (μCT) as described in section 3.2.2. Reconstructions of μCT data were used to assess the pore sizes of both the directionally aligned and isotropic scaffolds according to the protocols described in sections 3.2.3 & 3.2.4

7.2.2 *Ex vivo* Cardiac model

The data from two cardiac reanimations are presented. Heart 1 was used to test glue fixation and Heart 2 was used to assess suture fixation and control dynamics.

A summary of the *ex vivo* cardiac model preparation and execution can be seen in Figure 7.1 and Table 7.1. The protocol is adapted from references [322–324]. The development of the protocol and the construction of the ex-vivo rig was done by Dr. Clare Burdett.

Ethical approval

Experiments were performed in accordance with the University Biomedical Support Service ethical recommendations.

Ovine cardiac donation after circulatory death

Animals were procured through collaboration with the Melbourn Abattoir in Melbourn, Cambridgeshire, England. Lambs (Breed: Taxel/Suffolk cross) between the ages of 7-10 months

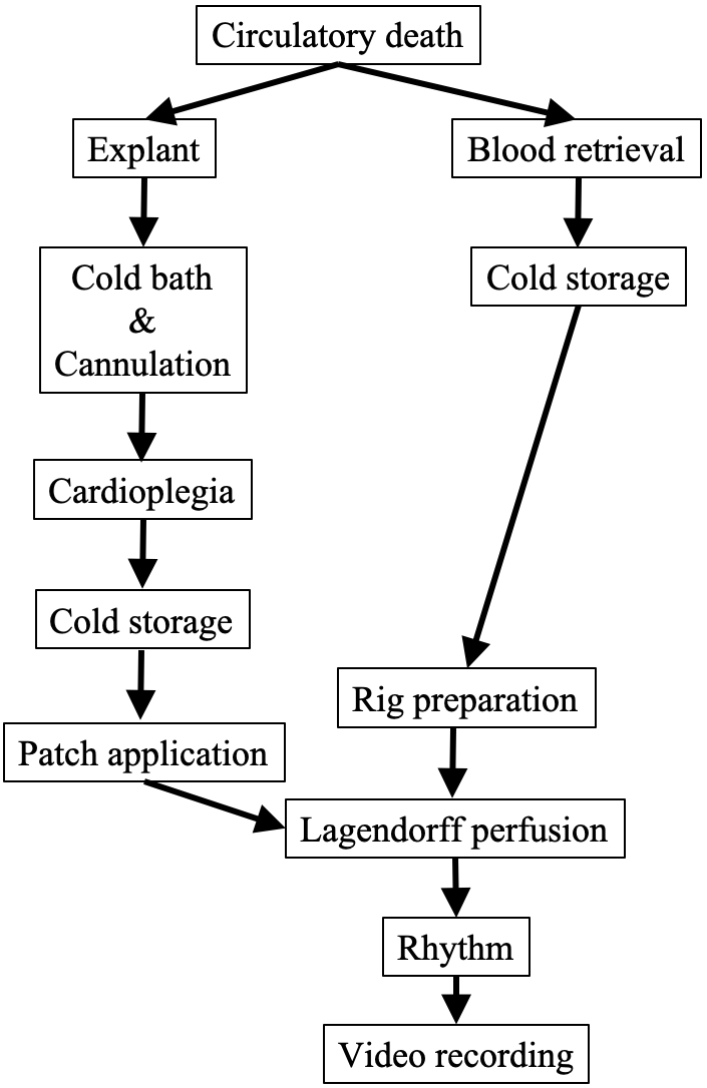

Fig. 7.1 The experimental protocol shown as a flow chart

old were stunned with a captive bolt pistol. Circulatory death was caused by exsanguination via opening of the superior vena cava. 800-1000 ml of blood was collected from the superior veno cava into a 5 L bucket pretreated with 50,000 units of heparin. All drug administration was overseen by Dr. Clare Burdett.

Table 7.1 Individual organ harvest and physical characteristics

Heart	Warm ischemic time (min)	Time to Plegia (min)	Cold ischemic time (min)	Post plegia weight (g)	Post cold ischemic weight (g)
1	7	5	81	462	522
2	6	5	103	400	400

Explant and cold storage

Hearts were explanted after 6-7 minutes of warm ischaemic time. The heart was immediately placed in a cold bath (0 ^{o}C) of normal saline solution (0.9%, Baxter) and cannulated through the aorta. The organ was initially flushed with normal saline (500 ml) supplemented with 12,500 units of heparin followed by 500 ml of cardioplegia solution comprised of 100 ml cardioplegia (Terumo IS849) and 400 ml Ringers solution (Baxter) supplemented with 6ml 8.4% sodium bicarbonate (Braun), 12,500 units heparin. After infusion with cardioplegia the heart was weighed and stored in cold (0 ^{o}C) natural saline solution. The individual organ weights, and processing times are summarized in Table 7.1. The cardiac dissection was overseen by Dr. Clare Burdett.

The *ex vivo* model

The Langendorff *ex vivo* cardiac perfusion rig was assembled according to Niu et al. 2013 [323]. A schematic of the assembly can be seen in Figure 7.2a. Briefly, the rig is set up such that oxygenated blood is pumped into the aorta, which then profuse the coronary arteries that supply the myocardium. The blood passively drains out of the pulmonary artery into a collection reservoir. The deoxygenated blood is then pumped through an oxygenator (Sorin inspire (LivaNova)) and perfused back through the aorta. Prior to cardiac reanimation the *ex vivo* rig was primed with 1000ml of priming solution. 700-800ml priming solution was drained and the blood 800-1000ml was strained through a Sorin reservoir filter and circulated through the rig. The cardiac rig was constructed by Dr. Clare Burdett.

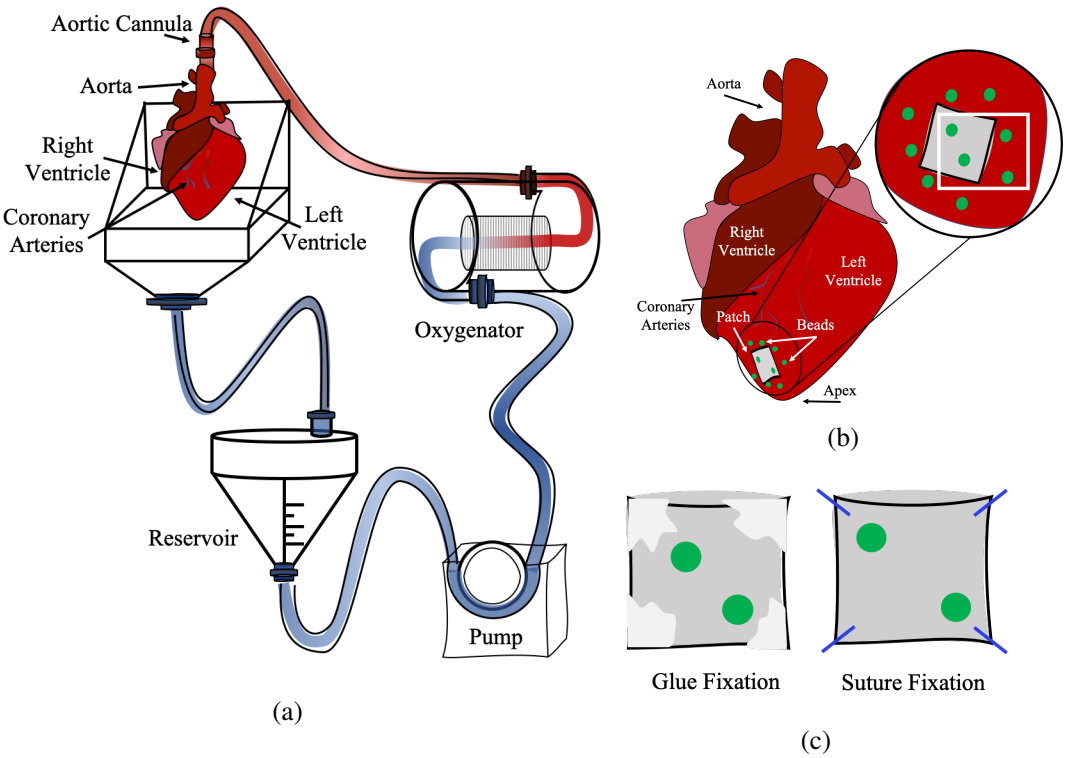

Fig. 7.2 Patch application and cardiac perfusion **(a)** Illustration of the Langendorff *ex vivo* cardiac perfusion set up, and the circulatory system in which the coronary arteries are supplied. **(b)** Illustration of the patch application site and applied bead pattern (green) for digital image tracking. The white rectangular outline indicates the two bead pairs used in analysis, with the bead pair on the grey patch denoted as the patch beads (note: this name is also utilized for the control condition where there is not a patch, instead beads are adhered directly to the myocardium where the patch would be located), and the bead pair directly medial to the patch beads denoted as the reference beads. **(b)** Illustration of the fixation methods; the glue fixation is depicted on the left where white regions at the corner of the patch indicate where glue was applied, the suture fixation is depicted on the right where blue sutures are depicted at each corner

7.2.3 Patch application

Scaffolds were sliced to a thickness of 2 mm; aligned structures were sliced in the longitudinal direction to maintain structural alignment. Squares (15 mm x15 mm) were cut and structures were hydrated in PBS.

Scaffolds were fixed to the anterior left ventricle proximal to the apex as shown in Figure 7.2b. Aligned scaffolds were fixed with the longitudinal pore orientation parallel to the native alignment of the superficial myocardium. For glue fixation, cyanoacrylate (0.05 ml, Loctite I.D.1365882) was applied to each corner of the scaffold. For suture fixation, prolene nonabsorbable monofilament (7-0 Aston) sutures were applied to each corner of the scaffold as illustrated in Figure 7.2c. 7-10 glass beads (green, ø=2 mm) were fixed to the region of interest on the myocardium with cyanoacrylate glue (Loctite I.D.1365882). The bead placement pattern can be seen in Figure 7.2b. In the control condition, beads were glued directly to the myocardium in the patch location. Additional beads were glued to the surrounding myocardium such that a pair of beads were applied proximal to the region of interest in a parallel orientation as shown in Figure 7.2b.

7.2.4 Cardiac reanimation

After patch application the hyperthermic heart was hooked up to the Langendorff *ex vivo* perfusion rig and warmed to 37 ^{o}C at a rate of 3 ^{o}Cmin^{-1}. Once warm 10 ml glucose 5%, 5 ml calcium 5%, 5 mg in 5 ml lidnocain were administered. Beating commenced spontaneously within 20 minutes of organ attachment to the perfusion rig. All drug administration was overseen by Dr. Clare Burdett.

7.2.5 Digital image recording

Video samples were recorded with a GoPro Hero 5 camera at 30 fps. Patches were exchanged at 20 minute intervals without interruption of the beating cycle.

7.2.6 Post application patch processing

After patch removal, patches were washed in PBS (2x5 min), 70% ethanol (2x5 min), and water (5x5 min) followed by freeze drying according to section 3.1.2. Dried scaffolds were then imaged with scanning electron microscopy according to section 3.2.2.

Calculation of characteristic parameters

Linear strain calculations

Bead positions in sample video frames were isolated through hue thresholding in ImageJ. The TrackMate plugin was used to track bead locations from frame to frame and position data were exported for processing. The distance between beads of interest was identified for the bead pair on the patch and the reference bead pair fixed directly to the myocardium. The bead pairs of interest are indicated by a white box in Figure 7.2b. The linear strain was calculated for each bead pair according to equation 7.1.

$$\varepsilon_L = \frac{\Delta L}{L_0} = \frac{L' - L_0}{L_0} \tag{7.1}$$

The variable L_0 is defined as the length between beads during diastole, identified as the reference length and is redefined for each beat to reduce the effects of sample drift. Similarly, L' is defined as the length between beads in the current frame as shown in Figure 7.3.

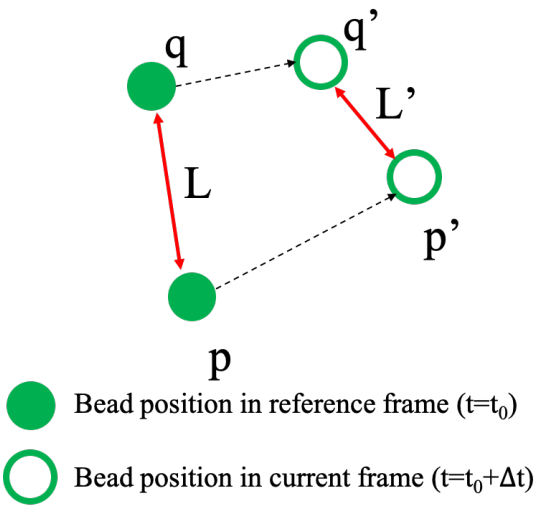

Fig. 7.3 Illustration of bead movement during contraction of the cardiac tissue.

The peak linear strain was identified for each beat and a linear strain ratio was calculated between the peak linear strain of the patch beads (ε_L^P) and the adjacent reference beads (ε_L^R). Peak linear strain between bead pairs was identified independently due to subtle temporal variability between locations. The linear strain ratio was defined $\varepsilon_L^P/\varepsilon_L^R$ and compared between conditions.

Digital image correlation and principal strain analysis

All bead positions (7-10 beads dispersed across the region) were used to calculate two-dimensional strain across the sample region. Bead position image stacks were prepared in MatlabR2020a. Position data were used to interpolate bead position between frames through path average interpolation such that the bead position was defined at 0.167 second intervals. Translation was removed by subtracting the bead position of the lateral most bead from all bead positions such that the position of the lateral most bead was fixed. However, all relative bead movement was maintained. Bead position images were plotted with circles of varying colour and radius in the interpolated bead positions to aid in subset tracking for two dimensional strain analysis.

Strain analysis was performed with Ncorr digital image correlation software according to section 3.2.6. A subset radius of 100 pixels and spacing of 15 pixels was used with high strain enabled.

Principal strains were calculated according to the protocol laid out in section 3.2.6 and component strain ratios between the patch region strain (ε^P) and the reference region strain (ε^R) were defined as $\varepsilon^P/\varepsilon^R$ and used to compare between conditions.

7.2.7 Statistics

Between 3 and 15 repetitions of each condition were executed. A t-test with a 95% confidence interval was used to determine statistical significance.

7.3 Results

7.3.1 Scaffold structure

Distinct scaffold architectures were achieved. The isotropic scaffolds were composed of a homogenous equiaxed pore structure and the aligned scaffolds displayed unidirectional pore alignment as shown in Figures 7.4a and 7.4b respectively. Pore sizes were comparable between scaffold structures, Figure 7.4c illustrates that both scaffold types had a broad range of pore diameters with average values of $97\pm50\ \mu m$ and $82\pm33\ \mu m$ for isotropic and the transverse plane of aligned scaffolds respectively.

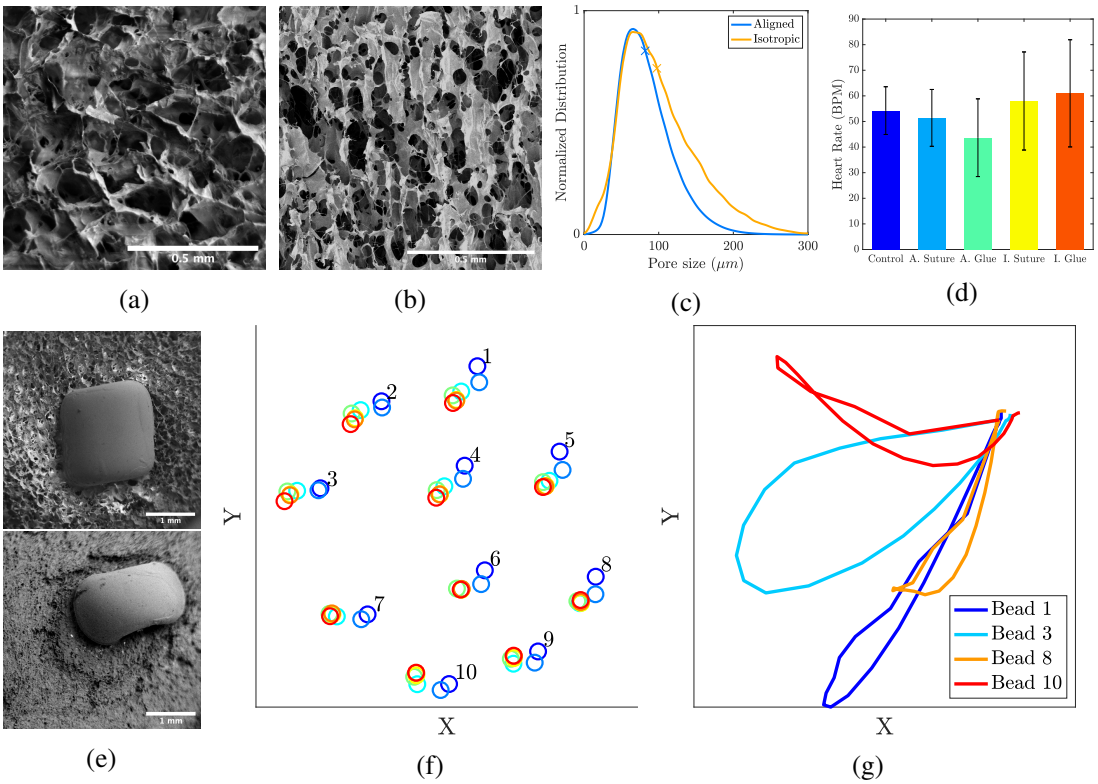

Fig. 7.4 Scaffold structure and native myocardial behaviour. **(a)** Scanning electron micrographs of an isotropic scaffold and **(b)** an aligned scaffold (scale bars: 0.5 mm). **(c)** Histogram of pore size distribution of both scaffold structures (isotropic: N=3; aligned N=6). **(d)** Sampled heart rate for each condition. Sampling repetitions for Control, A. Suture, A. Glue, I. Suture, and I. Glue are N=4, N=4, N=3, N=3, N=3 respectively. **(e)** Bead attachment to isotropic (top) and aligned (bottom) scaffolds. **(f)** Bead position evolution during contraction, blue represents early time points and red represents the final frames with 0.033 s between time points. **(g)** Representation of the dynamic displacement of four beads in (f) during a full contractile cycle. Scale bars in **(a)** and **(b)** are 0.5 mm and in **(e)** are 1 mm

7.3.2 Cardiac Reanimation

Cardiac reanimation occurred without pacing within 15 minutes of perfusion. A range of heart rates were sampled for each condition such that no condition was sampled over a distinct range as shown in Figure 7.4d.

Native myocardial dynamics

Beads were attached either directly to the myocardium or directly to the collagen scaffold as depicted in Figure 7.4e. The bead position displacement during contraction was tracked for each bead. Asymmetric displacement during the contractile cycle (from early ventricular diastole to late ventricular systole) was observed across the region of interest. Displacement was found to vary in space and time 7.4f. A comparison of bead positions 8 and 3, in Figure 7.4f, illustrates the spatial variation of bead displacement across the region. The displacement of bead 8 has a large y-component, whereas the displacement of bead 3 is predominantly in the x direction. Figure 7.4g demonstrates such variations in bead path during a contractile cycle. Similarly, temporal variations can be observed with significant displacement of bead 8 beginning within the first 0.033 seconds (blue marker), whereas significant displacement of bead 3 occurs later (green marker).

7.3.3 Patch Performance

Fixation

Hydrated scaffolds, irrespective of structural morphology, were found to conform to the shape of the myocardium upon application. Scaffolds were exchanged during active beating to compare conditions on the same heart. No observed tearing occurred during suture fixation as shown if Figure 7.5a. Scaffolds also remained fixed until removal.

Glue fixation resulted in stiffening of the scaffold in the regions of glue application as shown in Figures 7.5b and 7.5c for aligned and isotropic scaffolds respectively. The glue was absorbed into the scaffold through capillary action. The increased stiffness resulted in a greater interfacial stress between the patch and myocardium for the given strain applied

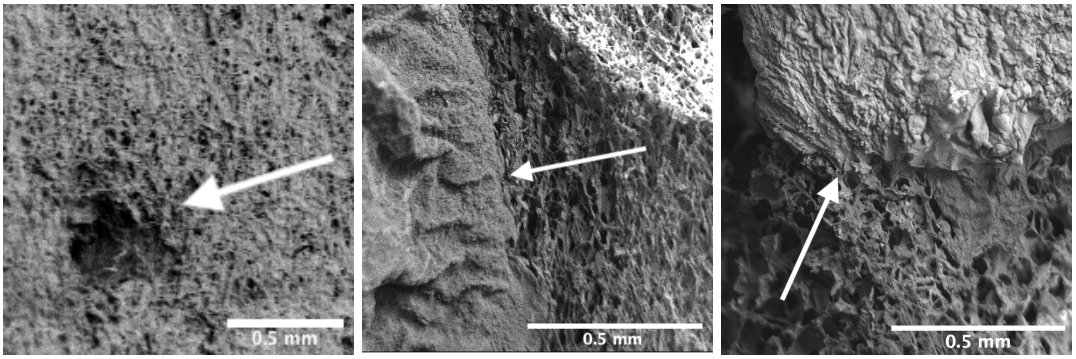

(a) (b) (c)

Fig. 7.5 Scanning electron micrographs of fixation methods showing **(a)** a suture perforation in an aligned scaffold, indicated by a white arrow, a glue globule on **(b)** an aligned and on **(c)** an isotropic scaffold.

by the native tissue. In some cases, the increased stiffness caused the myocardial strain to exceed the strain tolerance of the bond and interfacial de-bonding was observed. The scaffold deformation data for de-bonded scaffolds were not included in strain analysis.

Linear Strain

The linear strain was calculated between the bead pair adhered to the patch region (ε_L^P) and the reference bead pair adhered immediately medial to the patch region (ε_L^R). The change in the linear strains over the course of a beat, starting and ending in early diastole, can be seen in Figures 7.6a & 7.6b. The linear strains recorded for the control condition illustrate that the strain in the patch and reference region occur concurrently and the patch region is characterised by an increased strain magnitude relative to the reference region such that the linear strain ratio at peak strain is greater than one as shown in Figure 7.6a. The linear strain dynamics for the aligned patch with suture fixation were observed to be consistent with the control. Conversely, the sutured isotropic scaffold as well as both glue conditions were characterised by dramatically reduced strain in the patch region relative to the reference region as shown in Figure 7.6b. The linear strain ratios for each condition are compared in

Figure 7.6c. It was found that the aligned scaffold applied with suture fixation performed most similarly to the control condition, with no significant difference observed. All other conditions were found to perform similarly, characterised by significantly reduced linear strain in the patch region relative to the reference region.

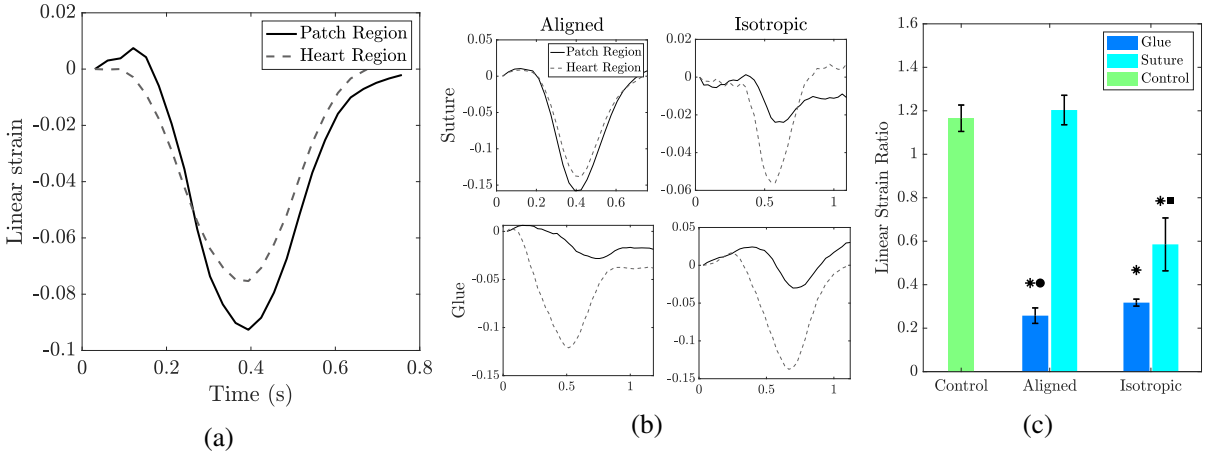

Fig. 7.6 The dynamic linear strain over the course of a beat (time) for **(a)** control and **(b)** patch conditions. **(c)** Mean peak linear strain ratios ($\varepsilon^P/\varepsilon^R$) for each condition, error bars indicate standard error, $*$ represents significance from control, ■ represents significance from aligned counter part with the same fixation, and • represents significance from suture counterpart with the same scaffold architecture. Beat repetitions for Control, A. Suture, A. Glue, I. Suture, and I. Glue are N=14, N=12, N=6, N=8, N=3 respectively.

Principal Strains

Two dimensional strain was calculated across the sampled field specified in Figure 7.2b. The native dynamics are illustrated by the control condition as shown in Figure 7.7. Figure 7.7a shows that principal strains occurred concurrently during a contractile cycle with opposite signs. The contractile component strain (ε_1) was found to be comparable in magnitude to the expansion component strain (ε_2). A similar trend was observed for both the patch and reference regions of interest, however the strain magnitudes were found to be increased as shown in Figure 7.7b. The strain ratios between the patch and reference regions for each

component strain were found to be stable during contraction with the ε_1 ratio greater than one while the ε_2 ratio was found to be less than one. The full-field strain during peak contraction is shown as a heat map in Figures 7.7c and 7.7d. The strains were found to be greater in the centre of the surface. Rectangular annotations indicate the patch region of interest (white) and the reference region of interest (black). It should be noted that the patch region is also used to describe the correlating region in the control condition where there is no patch, however the white square indicated is where a patch would be. Figures 7.7c and 7.7d also show component strain orientations. It can be seen that ε_1 strain vectors point uniformly in the longitudinal direction, while ε_2 strain vectors point circumferentially. These results are used as the model dynamics for comparison with the patch conditions.

The resultant principal strain dynamics for all patch conditions are displayed in Figure 7.8. Irrespective of patch condition it was found that component strain orientation was conserved, with contraction occurring along the longitudinal axis. Figures 7.8a-7.8c shows resultant strain profiles in the presence of an aligned patch with suture fixation. It can be seen that the component strain dynamics for both the patch and reference regions are similar to the control condition with constant strain ratios occurring above one for ε_1 and below one for ε_2. The strain heat maps are also similar to the control condition as shown in Figures 7.8b and 7.8c for ε_1 and ε_2 respectively.

The isotropic suture condition and both glue conditions displayed differences in resultant strain profiles when compared to the control. The sutured isotropic scaffold resulted in a reduced contractile strain ratio while the ε_2 strain remained unaffected as shown in Figure 7.8d. The ε_1 heat map displayed in Figure 7.8e also shows a distinct discrepancy in the patch region while the ε_2 heat map is less affected 7.8f. The resultant strain profiles for the glued patches are shown in Figures 7.8g-7.8i and Figures 7.8d-7.8l for aligned and isotropic

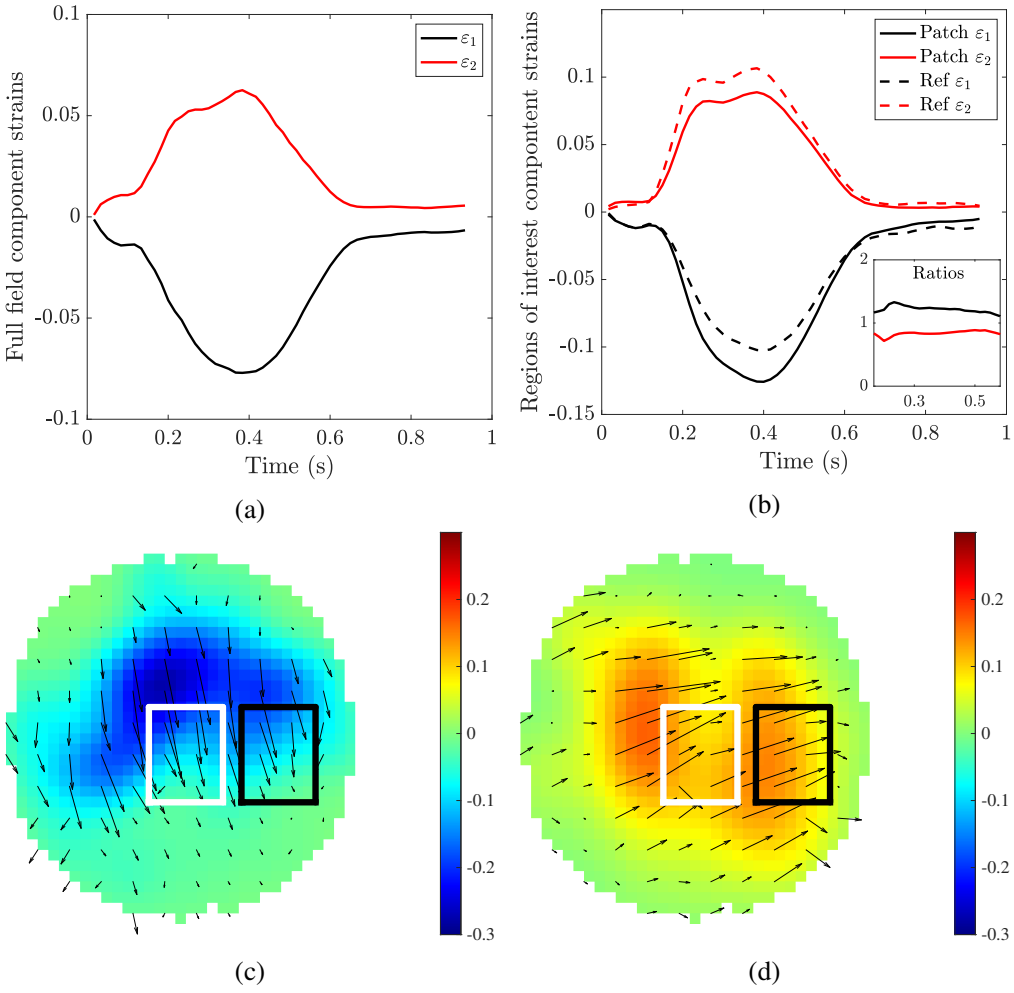

Fig. 7.7 2D strain analysis of the control condition. **(a)** Mean principal strains (ε_1 and ε_2) of the full field of view, **(b)** mean principal strains for the regions of interest, the patch region is where a patch would be placed, however, in the control condition there is no patch and the reference region is directly medial to the patch region. Insert shows the principal strain ratios ($\varepsilon_i^P / \varepsilon_i^R$) during contraction, where i represents the principal strain. **(c)** and **(d)** show full field isochrones of the principal strains ε_1 and ε_2 respectively. The white box indicates the patch region where the patch would be and the black box indicates the reference region

scaffolds respectively. Similar to the sutured isotropic scaffolds, a significant reduction in ε_1 magnitude was observed in the patch region relative to the reference region. While the ε_2 dynamics were different from the control condition, they were also consistent between the patch and reference regions for both scaffold types. The ε_2 values for both patch and

reference regions were found to be close to zero, causing high variability in the resultant strain ratios as shown in Figures 7.8g and 7.8d. Furthermore, the heat maps of peak ε_1 strain show a localised disruption in contractile strain. On the other hand, little disruption in the ε_2 heat maps were observed between the patch and reference regions. This indicates that contraction in the longitudinal direction was significantly affected by scaffold type and fixation while circumferential expansion was less affected by the same variable.

The component strain ratios for each condition were compared. Figure 7.9a shows that the native relationship between the patch and reference regions ε_1 strain was best replicated by the aligned scaffold applied with suture fixation. The principal strain ratios for other conditions were found to be significantly reduced when compared to the control condition. The ε_2 strain ratios, as shown in Figure 7.9b, were found to be more consistent between conditions than ε_1 and had values falling between 0.3 and 0.9. The ε_2 strain ratios for both the sutured aligned scaffolds and the glued isotropic scaffolds were found to be significantly different from the control condition. While scaffold structure was not found to produce significant differences when using glue fixation, the isotropic scaffold applied with sutures was found to produce a significantly reduced ε_2 strain ratio relative to its aligned counterpart.

Taken together these results demonstrate that scaffold architecture plays an important role in deformation mechanics and the capacity for engineered tissue to deform with the native myocardium. It was found that aligned scaffolds applied with the direction of alignment parallel to the native superficial myocardial alignment were better able to conform to the native myocardial contraction.

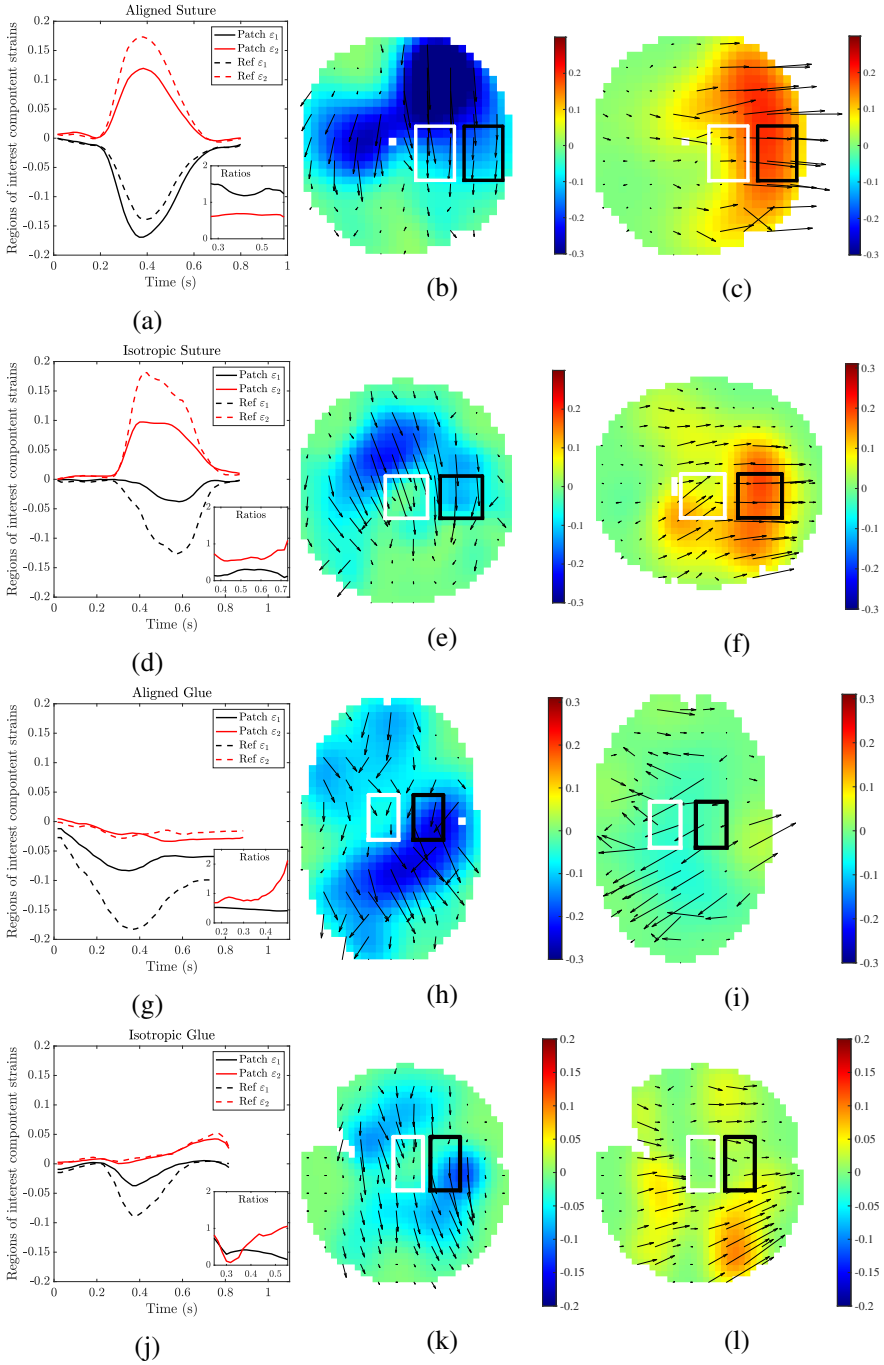

Fig. 7.8 Example principal strain measurements for each scaffold condition. The left column shows the mean principal strains for each region of interest (patch and reference regions) with insert of the principal strain ratios ($\varepsilon_i^P/\varepsilon_i^R$) during contraction. The middle and right columns show the full field isochrons of the principal strains ε_1 and ε_2 respectively. The white boxed area indicates the patch region and the black boxed area indicates the reference region. Example results are shown for each experimental condition: **(a)**-**(c)** aligned scaffold with suture fixation, **(d)**-**(f)** isotropic scaffold with suture fixation, **(g)**-**(i)** aligned scaffold with glue fixation, **(j)**-**(l)** isotropic scaffold with glue fixation

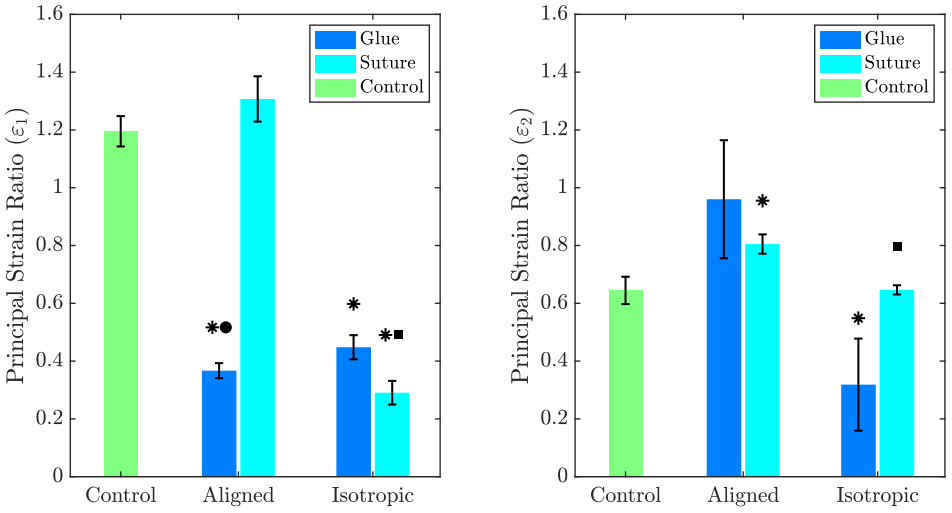

Fig. 7.9 Mean principal strain ratios ($\varepsilon_i^P/\varepsilon_i^R$) for each condition **(a)** ε_1 **(b)** ε_2, error bars indicate standard error, $*$ represents significance from control, ■ represents significance from aligned counter part with the same fixation, and • represents significance from suture counterpart with the same scaffold architecture. Beat repetitions for Control, A. Suture, A. Glue, I. Suture, and I. Glue are N=14, N=12, N=6, N=8, N=3 respectively

7.4 Discussion

The complex myocardial architecture has been widely studied and shown to consist of a helical arrangement of cellular bundles within the heart wall which form a complex three dimensional mesh. This results in torsional and compressive forces, causing complex deformations of the ventricular wall [325–328]. The resulting epicardial contraction occurs as a function of time and space across the superficial myocardium. Here the influences of scaffold architecture and fixation method on scaffold compliance with native surface deformation were studied. It was found that by tracking the dynamic position of beads adhered to the superficial myocardium in an *ex vivo* cardiac model the complex deformation profile could be directly observed. Through strain analysis of the native tissue and scaffold displacement, differences in the deformation profiles could also be quantified. While all scaffolds were found to adhere and conform to the static topography of the myocardium, scaffold structure

and fixation method significantly impacted the scaffolds compliance to native deformation dynamics.

7.4.1 Native myocardial dynamics

The native myocardial displacements of the inferior left ventricle, proximal to the apex, were characterised in the absence of scaffold application. An asymmetric contraction pattern was observed where the superficial epicardial movements were found to be a function of space and time across the muscle surface. This phenomenon is due to the complex layered architecture of the left ventricular wall. Pettegrew et al. 1864 identified opposing helical grains in the endocardial and epicardial layers near the ventricular apex [329]. The varied angles of alignment at different depths of the ventricular wall have been further explored in recent years and shown to contribute to the complex non-linear conduction pathways observed during ventricular contraction [51, 52, 325, 330–334]. The presence of an asymmetric contraction pattern, varying in space and time as illustrated in Figures 7.4f and 7.4g are consistent with previously reported results [46, 61, 63]. The complexity of deformation emphasises the need for a precise understanding of scaffold compliance to the dynamic native environment.

The *ex vivo* model in this study was executed in a Langendorff mode, where blood is circulated through the coronary artery system and not through the ventricular chambers. The myocardial displacement throughout the contractile cycle will, therefore, not describe the additional deformation caused by chamber filling and ejection. While the full *in vivo* cardiac deformations are not characterised in this study, it was found that the surface deformations of native myocardial contraction alone were sufficient to highlight functional differences in scaffold deformation mechanics through direct observation and subsequent strain analysis.

7.4.2 Patch performance

Four cardiac patch conditions were assessed. Acellular collagen scaffolds with aligned and isotropic scaffold architectures were adhered with either suture or glue fixation to determine the influence of both scaffold structure and fixation method on the mechanical deformation performance of regenerative cardiac scaffolds. Experiments were executed on two hearts. All glue conditions were performed on heart 1 while suture and control conditions were performed on heart 2. The processing of each heart is described in Table 7.1. While direct comparisons are made within this study, results would be strengthened by comparing the performance of all four conditions on a single heart.

Regenerative patch fixation was characterised by direct observation of adherence quality. The effects of fixation methods on scaffold structure were also assessed through scanning electron microscopy. Finally, the influences of fixation method as well as scaffold architecture on the dynamic strain throughout the cardiac cycle were compared. Two strain calculations were used to characterise the deformation of each condition relative to the surrounding myocardium. The linear displacement strain illustrates the changes in the one dimensional length between the bead pair adhered to the patch and between the bead pair adhered to the reference region. Component strain analysis produces a two dimensional description of the deformation dynamics across the full sampling field.

Fixation

Fixation method was found to influence the mechanical properties of the patch and resulted in varying qualities of adhesion. The cyanoacrylate glue fixative spread significantly as it was drawn up by capillary action into the porous scaffold as shown in Figures 7.5b and 7.5c. The glue stiffened when cured and reduced the strain tolerance of the glued region of the

patch. For scaffolds where glue spread was significant, the strain applied to the scaffold by the native myocardial contraction sometimes exceeded the strain tolerance of the glued patch and adhesion between the patch and the heart was lost. If glue remained localized, the bonding between the scaffold and the myocardium was maintained. Small external agitations, however, could trigger de-bonding. Considering the downstream requirements of the scaffold as a regenerative construct, the glue condition could also interfere with cellular repopulation of the structure in the glued regions due to the disruption of cellular binding chemistry caused by cyanoacrylate saturation and solidification. Cyanoacrylate is a common tissue glue and has been widely used for different surgical applications. In recent years, however, the development of flexible adhesives with stable bonding capabilities for internal use has been of growing interest in translational medical research and further study is needed to characterise adhesive capabilities of alternative tissue glues [335, 336].

Suture fixation avoided these issues and had no effect on scaffold stiffness although it did perforate the structure where the needle pierced the scaffold as shown in Figure 7.5a. Scaffolds which were adhered to the myocardium with sutures demonstrated stable fixation and no de-bonding was observed. The suture condition, therefore, provided superior adherence quality and stability when compared to glue fixation. The suture condition, also, does not disrupt the native surface chemistry of the collagen polymer, making it a superior option for regenerative medical scaffold fixation. The influence of fixation method on patch performance are further discussed in the subsequent sections.

Linear strain

Displacement strain analysis is an emerging tool in understanding the evolution of cardiac function [46]. The linear displacement strain gives a one dimensional description of the

deformation dynamics for the regions of interest and is commonly used to assess deformation observed through echocardiography [60, 61]. The linear strain was characterised for each condition and compared with the surrounding myocardium. It was found that for all conditions a shortening of the inter bead length was observed during the contractile cycle. This profile is consistent with previously reported results [61]. For the control condition the linear strain in the patch region (ε_L^P) was found to have a greater magnitude than that of the reference region (ε_L^R) as illustrated in Figure 7.6a. The strain ratio $\varepsilon^P/\varepsilon^R$ is used throughout this study for sample comparisons to account for variations in beat pattern and strain magnitudes that occur between samples. The linear strain ratio ($\varepsilon_L^P/\varepsilon_L^R$), for the control condition, without a patch, was found to be greater than one. This relationship was also observed with the presence of an aligned scaffold adhered with suture fixation, which resulted in a comparable strain ratio to the control condition as shown in Figure 7.6c. The inter bead length shortening was, however, significantly impaired by the presence of the sutured isotropic scaffold as well as scaffolds adhered with glue fixation, irrespective of scaffold structure as shown in Figure 7.6c. Deformation dynamics were further explored through two dimensional component strain analysis to better characterise the asymmetric surface deformation of the myocardium.

Component strains

Digital image correlation was performed on the bead displacement data such as that illustrated in Figure 7.4f. The Green-Lagrangian strain was calculated across the sampling field and the principal component strains were derived for sample analysis. Principal strains are independent of the original coordinate system and can illustrate expansion and compression along the principal axes where no shear occurs [321]. Quantification of full-field cardiac mechanical function through a principal strain analysis has been widely carried out. It enables the assessment of the complex behaviour of the myocardium using only normal

strain components including their magnitude and directions [321, 337–340]. While the low spatial resolution afforded by the widely spaced bead pattern in this work resulted in a high degree of variance in full-field strain measurements, the principal strain analysis was found to elucidate mechanical distinctions between patch conditions.

The average strain dynamics across the sampling field for the control condition were observed to have opposing directions such that as the myocardium stretched in one direction it compressed in the normal direction as shown in Figure 7.7a. This result was consistent for all conditions and in agreement with previous documentation regarding myocardial movement *in vivo* [46]. The component strains were found to have comparable magnitudes which contrasts the results of previous studies that report significantly increased ε_1 relative to the orthogonal strain [46, 63, 321]. The compressive strain (ε_1) in this chapter was found to be reduced when compared to previously reported dynamics of *in vivo* tissue [46]. This distinction can be attributed to the Langendorff *ex vivo* model, because additional strain that would occur *in vivo* due to chamber filling is not included in the deformation measurements taken in this chapter. Instead, the surface deformation of the myocardium due to the muscular contraction alone was analysed. Two regions of interest were identified for condition comparison. The strain dynamics of both the patch and reference regions for the control condition are shown in Figures 7.7c-7.7d. The strain dynamics for both regions were found to be comparable with constant strain ratios during the contractile cycle and serve as the standard to which all scaffold conditions are compared. Through analysis of the control condition, the orientation of principal strains was assessed. It was found that for the control and all scaffold conditions, the ε_1 principal axis is longitudinal while the orthogonal component points in the circumferential direction. This result is consistent with earlier reports which show that principal strain components of the natural myocardium (magnitude and direction) are largely influenced by the myocardial fibre orientations and that contractile strain occurs in the longitudinal direction [321, 338].

The strain dynamics after patch application were assessed and compared with the control condition. While some differences were observed for the ε_2 strain, circumferential strain was found to be relatively consistent between conditions as shown in Figure 7.9b. The dominant axis of myocardial deformation has been identified to be in the longitudinal direction, therefore, there is a particular interest in the strain dynamics along the ε_1 principal axis for each condition. It was found that the sutured aligned scaffold most accurately recapitulated the control dynamics. On the other hand, the sutured isotropic scaffold and both glue conditions resulted in significant disruptions in ε_1 dynamics. This result is evidenced by both a reduced ε_1 strain ratio and by localised strain reductions in the respective ε_1 heat maps shown in Figure 7.8. The resulting ε_1 strain ratios, summarised in Figure 7.9a, are consistent with the linear strain ratio results shown in Figure 7.6c. The consistency between these two results is due to the bead orientation, the patch and reference bead pairs used to calculate the linear strain are oriented parallel to the longitudinal axis, and therefore, the linear strain measurement is dominated by deformation along the longitudinal direction, similar to ε_1.

The improved compliance of the sutured aligned scaffold to the asymmetric contractile pattern of the native myocardium measured through both linear and principal strain analysis can be attributed to its asymmetric mechanical properties. Previous studies have shown that isotropic ice-templated collagen scaffolds have consistent compressive stiffness irrespective of the loading axis [249]. A study performed by Davidenko et al. in 2015 showed that the Young's modulus of isotropic scaffolds ranged from 2 to 6 kPa depending on the degree of cross linking [249]. Conversely, Brauer et al. 2019 discussed the compressive stiffness of ice-templated collagen scaffolds with anisotropic, aligned, pore architecture [341]. It was shown that the aligned scaffolds had asymmetric mechanical stiffness that was dependant on the direction in which the compressive stress was applied. Brauer et al. reported a compressive stiffness of between 2 and 4 kPa when scaffolds were loaded

parallel to the lamellar orientation and a compressive stiffness of 1 kPa when scaffolds were loaded perpendicular to lamellar orientation [341]. The stiffness of both of these scaffold types is similar to the passive mechanical stiffness of the native myocardium which has been recorded to be between 3 and 9 kPa [342, 343]. However, the passive mechanical stiffness of native myocardial tissue is shown to display asymmetric properties, similar to those of the anisotropic scaffolds, that vary depending on loading orientation [344]. It has been shown that native transmural myocardial samples have a higher stiffness when compressed in the longitudinal direction relative to the circumferential direction [344]. This result is attributed to the structural anisotropy of the native myocardial extracellular matrix. Thus, because the aligned scaffolds were applied such that the pore orientation matched the native alignment of the superficial epicardium, which near the apex is largely circumferential, the scaffold alignment is perpendicular to the principal axis of contraction. The principal axis of contraction has been shown to occur in the longitudinal direction, parallel to the alignment observed in the endocardium. The alignment orientations of the epicardium, endocardium and the patch can be seen in Figure 7.10. The aligned scaffolds in a circumferential orientation were, therefore, compliant to the native longitudinal contraction.

The different alignment orientations present at different depths within the myocardium have an important role in heart function. The cellular contraction in plane with the local alignment causes myocardial syncytia to shift in relationship to one another across the depth of the muscle. Syncytia sliding causes wall thickening and increased chamber contraction that optimises cardiac output. This phenomena is illustrated in Figure 2.2 in the literature review and discussed further in the work done by Nielles-Vallespin et al. 2017 [16]. Therefore, should a cell seeded scaffold be applied to epicardium, the pore alignment would enable the planar contraction of the scaffold to match that of the superficial most syncytia in the myocardium, closely replicating the behaviour of the native tissue. The asymmetric pore

orientation also provides the necessary mechanical compliance to collapse in the transverse direction as required by the longitudinal contraction of the whole organ.

Isotropic structures, in contrast, are characterised by an equiaxed pores and thus resist deformation equally in all directions. Taken together these mechanical profiles could help to explain the discrepancy observed in the suture condition due to scaffold structure. The restriction of compressive movement caused by the glue fixation method can instead be attributed to the extensive spreading of the glue medium observed during application as shown in Figures 7.5b-7.5c. The subsequent stiffening after the glue cured may interfere with the native myocardial deformation, as the fixation method will locally fix both the scaffold and the contacted superficial myocardium. Localised disruption in the deformation of the superficial epicardium and increased stiffness on the patch may contribute to the reduced deformation observed for the ε_1 strain.

7.4.3 Limitations

It has been shown that scaffold architecture and fixation method significantly impact the capacity of collagen scaffolds to conform to the native asymmetric deformations of the superficial epicardium. This work, however, is subject to some limitations. The Langendorff *ex vivo* model used in this chapter does not simulate myocardial deformation due to chamber filling. An *ex vivo* model in working mode would include ventricular chamber filling during diastole and the pumping action of the myocardium against an after load. Including these characteristics of myocardial action would enable an improved understanding of functional myocardial deformations. With regard to strain analysis, a large quantity of research has been done regarding speckle pattern optimisation for digital image correlation, it has been shown that a high density of distinct irregularly shaped speckles is optimal [321, 345, 346].

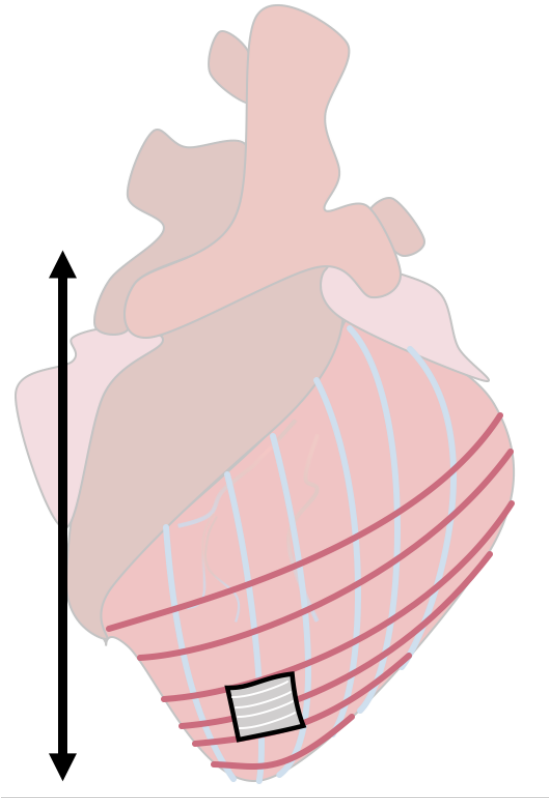

Fig. 7.10 Myocardial alignment and contraction. The red lines indicate the alignment of the epicardium, parallel to the patch alignment, blue lines indicate the alignment of the endocardium, parallel to the principal whole organ contractile direction indicated by the black arrow.

Improving the quality of speckle pattern as well as expanding the strain analysis to describe myocardial deformation in three dimensions would, therefore, improve the accuracy and uniformity of digital image correlation results [63].

7.5 Conclusion

Cardiac scaffolds are required to have the mechanical capacity to biomimetically deform to the complex physio-mechanical environment while simultaneously supporting the damaged

myocardium. Previously, the deformations of the superficial epicardium during the cardiac cycle have been unexplored. A few studies have utilised strain calculations to characterise the complex asymmetric epicardial movement [46, 63, 321]. In this chapter, direct optical imaging and strain analysis were utilised to characterise not only the native myocardial deformation, but the influences of scaffold structure and fixation on the capacity for regenerative scaffolds to recapitulate the complexity of the dynamic myocardium.

The application of an *ex vivo* ovine cardiac perfusion model enabled direct observation of the native surface myocardial movement during the cardiac cycle. Through direct optical imaging and bead tracking, tissue engineered collagen scaffolds with varied architecture and fixation were tested for conformance to native myocardial movement patterns. The contraction pattern and local strain components for each condition were analysed through digital image correlation and resultant strain dynamics for multiple cardiac cycles. The performance of each scaffold condition was characterised by the relative agreement with the surrounding myocardium and the control condition. It was found that both scaffold architecture and fixation method significantly influenced the deformation compliance of acellular cardiac patches. Scaffolds with aligned architecture applied with suture fixation were found to best replicate the native deformation of the superficial epicardium. This is likely to be due to the agreement between the dominant strain axis and the asymmetric mechanical properties of the scaffold. In contrast, the isotropic scaffold and both glue conditions were found to impair the contractile deformation of myocardium. Despite the limitations discussed above, conclusive evidence was found that aligned scaffolds adhered with suture fixation facilitate improved deformation mechanics that most accurately comply with the native environment when compared with isotropic scaffolds or scaffolds secured with glue fixation. These results improve the understanding of scaffold function and inform the design of regenerative cardiac scaffolds to improve translational functionality.

This work has provided initial understandings of the local strain patterns of the ventricular myocardium and the influences of tissue engineered structure and fixation on the translation of native strain dynamics to regenerative collagen scaffolds. It has also been demonstrated that strain analysis through digital image tracking is a valuable tool when characterising the functional capabilities of engineered scaffolds in a translational setting.

Chapter 8

Conclusions and Future directions

8.1 Conclusions

Ice templated collagen scaffolds have been shown to have great potential for use in regenerative cardiac applications [70, 76, 113]. The clinical application of regenerative cardiac tissue is, however, currently limited by a lack of scaffold structure that mimics the complex architecture of the myocardium [21]. The aim of this thesis has been to identify methods to tailor anisotropic collagen scaffold architecture and understand the influence of architectural order on the translational capacity of cardiac scaffolds through cellular response and physio-mechanical compliance to live tissue. In the early chapters of this work, fabrication methods were introduced and explored to enable direct control over pore size, architectural alignment and pore orientation. The relative importance of scaffold architecture was explored in the later chapters. *In vitro* studies revealed that long range scaffold alignment encouraged phenotypic cellular maturity and improved signalling and contractile synchronicity. Similarly, the use of an *ex vivo* cardiac model enabled direct observation of scaffold compliance to native myocardial deformations. It was shown that aligned scaffolds, that replicated the native mechanical asymmetries of the superficial epicardium were better able to match the native deformations relative to isotropic scaffold structures. Within this thesis, advanced

architectural control methodologies have been presented and the importance of scaffold anisotropy for the function of regenerative cardiac tissue has been highlighted.

8.1.1 Architectural control of ice-templated collagen scaffolds

One major challenge in the design and fabrication of regenerative scaffolds for cardiac applications is a lack of precise architectural control. Directional freeze casting was shown to produce collagen scaffolds with aligned lamellar structure, and further the rate of freezing was found to be negatively correlated with the degree to which structures aligned. In order to better understand the influence of physical parameters on the final lamellar alignment and pore size composition of ice-templated collagen scaffolds, the freezing front velocity was monitored during solidification. Two different freezing protocols were compared. It was found that by setting the heat sink temperature to linearly decrease, the freezing front velocity could be stabilised. This resulted in increased intra-scaffold pore size uniformity and a trend toward improved structural alignment relative to solidification with a constant heat sink temperature. By comparing pore sizes to the freezing front velocity, a power-law relationship was identified. This relationship enabled a physical based description of pore size control, independent of processing parameters. Consideration of the fundamental physical process by which ice-templating occurs and defining the pore size accordingly, led to the postulation of a fundamental link between isotropic and anisotropic freeze-casting processes.

Further to pore size control, replicating the native hierarchical structure with complex long range macro-architecture of cardiac scaffolds has been a persistent challenge in the design and fabrication of regenerative cardiac tissue. Here, a novel thermal control technique was developed to facilitate localised and specific control of complex lamellar alignment orientations during the solidification process. The technique was presented alongside a

simple, yet predictive, finite element model to serve as a design tool. It was demonstrated that by controlling the power and geometry of thermal sources embedded in the periphery of freeze-casting moulds, localised pore orientation could be controlled. Taken together the model and the novel heat source mould protocol enable localised control and design of bespoke scaffolds with complex architectural morphologies.

The architectural control protocols detailed in the early chapters of this thesis can be applied beyond the fabrication of regenerative cardiac tissue. These techniques can be used to inform the design and optimisation of specific and complex three dimensional ice-templated scaffolds for numerous clinical applications and *in vitro* model systems. Additionally, because ice-templating is a physical process these protocols can be expanded to applications in a number of fields and utilised with a host of different materials.

8.1.2 The influence of anisotropy on the functional capacity of regenerative cardiac tissue

Historically, regenerative cardiac tissue has been fabricated with gels or isotropic scaffolds [103, 155]. These formats do little to facilitate long range cellular order or to recapture the mechanical asymmetry of native tissue [181]. In the second half of this work the influence of anisotropy on translational cardiac capacity was assessed through cellular behaviour and physio-mechanical compliance to live tissue.

The influence of scaffold architecture on cell signalling and contractile dynamics was studied systematically through a direct comparison between an aligned scaffold that facilitated long range cellular order and a pseudo-isotropic scaffold. It was found that long range alignment encouraged significant increases in signalling synchronicity and directional contractility.

These findings were supported by phenotypic and cell structure assessment. It was found that cells seeded onto aligned scaffolds showed increased maturity and cardiogenic phenotypic markers. By observing the tissue level and cellular level effects of scaffold architecture, the design of cardiac scaffolds can be informed and future studies in cardiac tissue engineering can be optimised.

Further to cellular function, anisotropy was shown to significantly impact the physio-mechanical capacity of ice-templated collagen scaffolds [6, 50]. The superficial epicardium has a distinct and complex deformation pattern, variable in space and time, over the course of the contractile cycle [46]. The ability of regenerative scaffolds to comply with the native cardiac environment is paramount for successful engraftment [21]. To better understand the impact of scaffold architecture on the physio-mechanical compliance of regenerative structures an *ex vivo* cardiac model was used to enable direct observation of scaffold deformation. Through strain analysis it was found that aligned scaffolds were better able to conform to native epicardial dynamics when compared to isotropic structures. Furthermore, while suture fixation enabled free deformation, the use of glue fixation impaired the mechanical compliance of collagen scaffolds.

It was shown that aligned scaffolds facilitate improved long range cell signalling and contractility as well as increased cardiogenic phenotyping and maturity while maintaining the necessary physio-mechanical properties to conform to the native deformation of live tissue.

8.2 Further work

8.2.1 Expanding architectural control

The architectural control protocols presented in this thesis have expanded the range of complex scaffold architectures fabricated through ice-templating. By combining these techniques with previously established protocols, numerous avenues of research can be explored. Furthermore, the fundamental concepts can be utilised and expanded to produce scaffolds with specific and complex architectures for a wide range of applications.

Pore size control for interfacial tissue The strong link between processing parameters and the final scaffold pore architecture implies that by tailoring the freezing protocol, seamless scaffold structures can be produced with discrete regions of distinct pore sizes. A structure that seamlessly transitions between different pore structures could be used for three dimensional co-culture systems or implanted as a regenerative structure for interface tissues. To explore the capability of such scaffold fabrication, an interface scaffold was produced as a pilot study.

The preparation protocol for the interface structure is consistent with that presented in sections 3.1.1-3.1.2. The freezing conditions used are as follows. The cold finger was pre-cooled and held at a temperature of -60 ^{o} C. The mould was mounted onto the cold finger and allowed to commence solidification for 5 minutes with $T_B = -60\,^o$ C. The temperature at the cold finger mould interface was then ramped up to $T_B = -5\,^o$ C over the course of 1 minute and held at that temperature for the remainder of the solidification process. The resulting structure was lyophilised and imaged as described in sections 3.1.2 and 3.2.2. Pore size and alignment analyses were executed on reconstructed μCT images of three regions of interest measuring 2.5mm^2 in the xy-plane and 1 mm tall on the z-axis at the bottom, top and interface height of the final scaffold.

The resultant structure can be seen in Figure 8.1a. The initial proof of concept study resulted in a scaffold with small pores at the base of the scaffold and larger pores at the top as shown in Figures 8.1b-8.1c. The two pore morphologies were separated by a distinct interfacial region where large and small pores were found to co-exist. Further study is needed to fully understand the physical underpinnings of this technique and the range of scaffold structures that could be achieved.

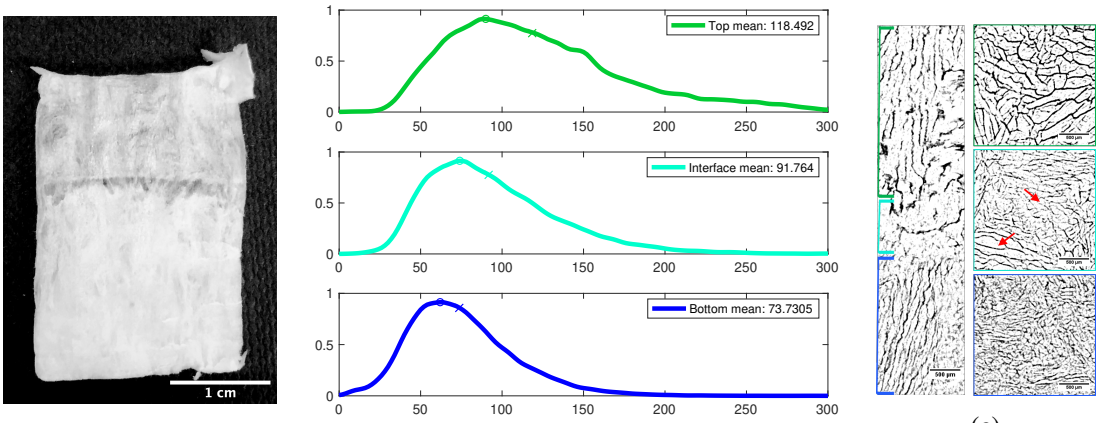

(a) (b) (c)

Fig. 8.1 Pore structure analysis of the interface scaffold. **(a)** photograph of a longitudinal slice of the pilot scaffold **(b)** the pore size distribution for each region of the pilot scaffold **(c)** μCT reconstructions on the longitudinal xz-plane and on the xy-plane for each region, bottom (blue), interface (Teal), Top (Green). Red arrows highlight the presence of large and small pores in the interface region

Understanding alignment In Chapter 4 it was found that the freezing protocol significantly influenced the degree of final lamellar alignment. The relationship between thermal parameters and the degree of final lamellar alignment has, however, not been fully investigated. Further exploration into processing parameters and the physical system may illuminate the processes that dictate the degree of lamellar alignment and enable the fabrication of scaffolds with a full range of architectural order from isotropic to fully aligned.

Expanding architectural complexity The protocol to achieve controlled and complex lamellar orientations presented in Chapter 5, can be expanded to increase the architectural complexity of ice-templated scaffolds that better replicate native tissue structures. The introduction of time varying thermal sources as well as varying the source/sink geometries could enable the fabrication of bespoke architectures. Additionally, the finite element model can be modified to enable targeted mould design and simulate protocols prior to experimentation.

Mechanical properties The influence of complex scaffold architecture on mechanical properties can be further explored. In a pilot study, the effects of lamellar curvature were tested. A scaffold with vertical, horizontal and curving architecture (lamellar alignment at approximately 34^o from vertical) were fabricated according to the protocols laid out in chapter 3. Each scaffold was cross linked to 30% according to the protocol in section 3.1.2 and cut into 5 mm tall cylinders with a 5 mm diameter biopsy punch. Scaffolds were fully rehydrated in DI water and hydrated compression testing with 5kN Tinius Olsen machine and a 5 N cell was executed.

Correlating mechanical properties with structural alignment, it was found that the stiffness of fully hydrated collagen scaffolds was largely dependent on the lamellar orientation angle relative to the compressive loading force as shown in Figure 8.2a. The modulus was found to increase as lamellar alignment approached a parallel orientation to the compressive load, where curved structures displayed intermediate stiffness. The stiffness, however, was more comparable to structures oriented perpendicular to the load as shown in Figure 8.2b. This result is in agreement with composite mechanics where the modulus has been shown to drop rapidly as the angle of orientation deviates from parallel to the loading direction [347]. Further study is needed, however, to understand the influence of more complex lamellar structures on the mechanical properties of ice-templated collagen scaffolds.

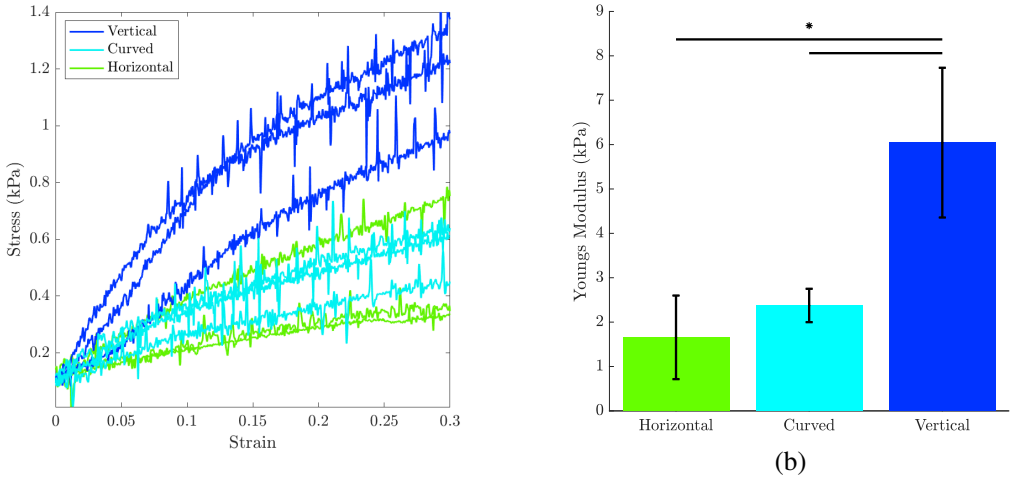

Fig. 8.2 Influence of pore orientation on stiffness. **(a)** Stress strain curves of hydrated collagen scaffolds achieved through compression testing. **(b)** Young's moduli of hydrated collagen scaffolds calculated from the linear region at 5% strain.

8.2.2 Further studies on scaffold architecture and translational functionality

Understanding how cellular behaviour is influenced by scaffold anisotropy has great impact on the future design and eventual clinical use of regenerative tissue. The studies conducted within this thesis indicate that biomimetic structures encourage improved cellular signalling, contractility, maturation and phenotypic development as well as improve the ability of scaffolds to conform to the dynamic physio-mechanical demands of the native myocardium. However, further study is needed to fully deconvolute the relationship between scaffold structure and regenerative tissue function for applications on the heart and other physiological systems.

Addition of scaffold functionalisation molecules The introduction of scaffold functionalisation molecules such as triple helical peptides (eg. GFOGER or GLOGEN) or growth

factors (eg. VEGF or HGF) to the collagen scaffolds could enhance cell binding and survival [348]. Functionalisation molecules have also been shown to enhance regenerative re-vascularization and de-novo matrix deposition [244, 247, 248]. Further study is needed to understand the combined effects of scaffold anisotropy and functionalisation.

Diversifying the cell source The current study used hESC derived immature cardiomyocytes. There is, however, a diverse array of cell types that contribute to the native myocardium. Introducing additional cell types, such as endothelial cells, may have a dramatic effect on regenerative tissue function and cellular behaviour. Further study into co-culture systems is needed to optimise and improve the development of regenerative tissue.

Influences of complex architecture The introduction of complex long range scaffold architecture in Chapter 6 laid the ground work for new studies that explore the influence of multidirectional lamellar structures on cell behaviour and construct function. Optical imaging, using the protocol laid out by He et al. 2019, could be utilised to track the conduction velocity and the signal activation time after point stimulation [73]. The isochrones could then be compared to the scaffold architecture. Characterisation of how scaffold orientation effects regenerative tissue function and directs cell signalling would help inform future design of regenerative cardiac constructs.

Expanding the *ex-vivo* model The *ex-vivo* cardiac model utilized in Chapter 7 enabled direct observation of scaffold behaviour when applied to the superficial epicardium. The model used was a Lagendorff model, however, which does not enable ventricular filling and ejection. Expanding the study to a working mode *ex vivo* model could allow for a greater understanding of scaffold perfaormance in the native myocardial environment. Furthermore, the study can be expanded to characterise the dynamics of other regions on the epicardium.

The *ex vivo* model for cardiac patch appraisal could also be expanded by incorporating cellularised patches onto the live myocardium. The cell seeded construct could then be assessed for not only deformation but also signalling pairing capabilities with the native epicardium and various adhesion techniques could be compared that encourage signalling integration between the regenerative patch and the myocardial musculature.

Beyond cardiac applications The influences of scaffold architecture on regenerative tissue can be expanded to other physiological systems. For example, aligned scaffold architectures have been found to encourage tendon cell phenotyping [26]. Further study into the influences of different scaffold architectures in different cell systems may improve the quality of regenerative tissue for a great range of physiological systems.

Conclusion Scaffold architecture has been found to greatly affect the success of regenerative cardiac constructs [21]. This work has examined the fabrication of regenerative cardiac constructs from the fundamental physics that prescribe scaffold architecture to its translational capacity when adhered to the living myocardium. The physics of directional freeze-casting has been utilised to control and dictate scaffold pore sizes and alignment. A novel freeze casting technique to afford three dimensional control of pore orientation was established and simulated. By utilising the predictive finite element model, bespoke scaffolds with complex pore orientations can be designed and fabricated for a wide range of biomedical applications. The influences of aligned scaffold architectures was also tested for cellular signalling and maturity as well as for the physio-mechanical demands when applied to the living myocardium. When tested through direct comparisons the scaffolds with defined long range order were found to enhance cellular and mechanical dynamics to better replicate the native behaviour of myocardial tissue. This thesis presents a longitudinal study

of ice-templated collagen scaffold design and assessment for cardiac applications; beginning with the fundamental physics that designate scaffold architecture and culminating with the examination of translational capacities when adhered to a live beating heart.

References

[1] World Health Organization. Cardiovascular Disease Fact Sheet. Technical report, The World Health Organization, 2020.

[2] Y. Li and D. Zhang. Artificial Cardiac Muscle with or without the Use of Scaffolds. *BioMed Research International*, 2017:1–15, 2017.

[3] V. Serpooshan, M. Zhao, S. A. Metzler, K. Wei, P. B. Shah, A. Wang, M. Mahmoudi, A. V. Malkovskiy, J. Rajadas, J. Butte, D. Bernstein, and P. Ruiz-lozano. The Effect of Bioengineered Acellular Collagen Patch on Cardiac Remodeling and Ventricular Function post Myocardial Infarction. *Biomaterials*, 34(36):1–15, 2014.

[4] F. J. O'Brien. Biomaterials and scaffolds for tissue engineering. *Materials Today*, 14(3):88–95, 2011.

[5] W. F. Daamen, S. T. M. Nillesen, T. Hafmans, J. H. Veerkamp, M. J. A. van Luyn, and T. H. van Kuppevelt. Tissue response of defined collagen-elastin scaffolds in young and adult rats with special attention to calcification. *Biomaterials*, 26(1):81–92, jan 2005.

[6] K. A. Faraj, D. Ph, T. H. V. A. N. Kuppevelt, and D. Ph. Construction of Collagen Scaffolds That Mimic the Three-Dimensional Architecture of Specific Tissues. *Tissue engineering*, 13(10):2387–2394, 2007.

[7] R. J. Daher, N. O. Chahine, A. S. Greenberg, N. A. Sgaglione, and D. A. Grande. New methods to diagnose and treat cartilage degeneration. *Nature Reviews Rheumatology*, 5(11):599–607, 2009.

[8] G. F. Muschler, C. Nakamoto, and L. G. Griffith. Engineering principles of clinical cell-based tissue engineering. *Journal of Bone and Joint Surgery - Series A*, 86(7):1541–1558, 2004.

[9] L. Griffith. Emerging Design Principles in Biomaterials and Scaffolds for Tissue Engineering. *Annals of the New York Academy of Sciences*, 961(1):83–95, jun 2002.

[10] Q.-Z. Chen, S. E. Harding, N. N. Ali, A. R. Lyon, and A. R. Boccaccini. Biomaterials in cardiac tissue engineering: ten years of research survey. *Materials Science and Engineering: R: Reports*, 59(1):1–37, 2008.

[11] F. Guilak. Functional tissue engineering: The role of biomechanics in reparative medicine. *Journal of Biomechanical Engineering*, 122(6):570–575, 2000.

[12] A. Atala. Engineering organs. *Current opinion in biotechnology*, 20(5):575–592, 2009.

[13] H. H. Lu, S. D. Subramony, M. K. Boushell, and X. Zhang. Tissue engineering strategies for the regeneration of orthopedic interfaces. *Annals of biomedical engineering*, 38(6):2142–2154, 2010.

[14] P. J. Yang and J. S. Temenoff. Engineering orthopedic tissue interfaces. *Tissue Engineering Part B: Reviews*, 15(2):127–141, 2009.

[15] A. Atala, F. Kurtis Kasper, and A. G. Mikos. Engineering complex tissues. *Science Translational Medicine*, 4(160):1–11, 2012.

[16] S. Nielles-Vallespin, Z. Khalique, P. F. Ferreira, R. de Silva, A. D. Scott, P. Kilner, L. A. McGill, A. Giannakidis, P. D. Gatehouse, D. Ennis, E. Aliotta, M. Al-Khalil, P. Kellman, D. Mazilu, R. S. Balaban, D. N. Firmin, A. E. Arai, and D. J. Pennell. Assessment of Myocardial Microstructural Dynamics by In Vivo Diffusion Tensor Cardiac Magnetic Resonance. *Journal of the American College of Cardiology*, 69(6):661–676, 2017.

[17] A. K. Lynn, S. M. Best, R. E. Cameron, B. A. Harley, I. V. Yannas, L. J. Gibson, and W. Bonfield. Design of a multiphase osteochondral scaffold. I. Control of chemical composition. *Journal of Biomedical Materials Research Part A*, 92A(3):1057–1065, mar 2010.

[18] J. D. Kretlow and A. G. Mikos. Bones to biomaterials and back again—20 years of taking cues from nature to engineer synthetic polymer scaffold. *Journal of Biomedical Materials Research Part A*, 98(3):323–331, 2011.

[19] J. Y. Tan, C. K. Chua, and K. F. Leong. Fabrication of channeled scaffolds with ordered array of micro-pores through microsphere leaching and indirect rapid prototyping technique. *Biomedical microdevices*, 15(1):83–96, 2013.

[20] L. Moroni, J. R. De Wijn, and C. A. Van Blitterswijk. 3D fiber-deposited scaffolds for tissue engineering: influence of pores geometry and architecture on dynamic mechanical properties. *Biomaterials*, 27(7):974–985, 2006.

[21] A. H. Nguyen, P. Marsh, L. Schmiess-Heine, P. J. Burke, A. Lee, J. Lee, and H. Cao. Cardiac tissue engineering: State-of-the-art methods and outlook. *Journal of Biological Engineering*, 13(1):1–21, 2019.

[22] K. M. Pawelec, S. M. Best, and R. E. Cameron. Collagen: a network for regenerative medicine. *Journal of materials chemistry. B*, 4(40):6484–6496, oct 2016.

[23] I. V. Yannas, D. S. Tzeranis, B. A. Harley, and P. T. C. So. Biologically active collagen-based scaffolds: advances in processing and characterization. *Philosophical Transactions of the Royal Society A: Mathematical, Physical and Engineering Sciences*, 368(1917):2123–2139, 2010.

[24] B. A. Harley, A. K. Lynn, Z. Wissner-Gross, W. Bonfield, I. V. Yannas, and L. J. Gibson. Design of a multiphase osteochondral scaffold III: Fabrication of layered scaffolds with continuous interfaces. *Journal of biomedical materials research. Part A*, 92(3):1078–1093, mar 2010.

[25] A. Lee, A. R. Hudson, D. J. Shiwarski, J. W. Tashman, T. J. Hinton, S. Yerneni, J. M. Bliley, P. G. Campbell, and A. W. Feinberg. 3D bioprinting of collagen to rebuild components of the human heart. *Science*, 365(6452):482–487, aug 2019.

[26] Z. Wang, W. J. Lee, B. T. Koh, M. Hong, W. Wang, P. N. Lim, J. Feng, L. S. Park, M. Kim, and E. S. Thian. Functional regeneration of tendons using scaffolds with physical anisotropy engineered via microarchitectural manipulation. *Science Advances*, 4(10):1–13, 2018.

[27] F. Copes, N. Pien, S. V. Vlierberghe, and F. Boccafoschi. Collagen-Based Tissue Engineering Strategies for Vascular Medicine. *Frontiers in Bioengineering and Biotechnology*, 7(July):1–15, 2019.

[28] H. Lu, Y.-G. Ko, N. Kawazoe, and G. Chen. Cartilage tissue engineering using funnel-like collagen sponges prepared with embossing ice particulate templates. *Biomaterials*, 31(22):5825–5835, 2010.

[29] M. J. W. Koens, P. J. Geutjes, K. A. Faraj, J. Hilborn, W. F. Daamen, and T. H. van Kuppevelt. Organ-specific tubular and collagen-based composite scaffolds. *Tissue Engineering Part C: Methods*, 17(3):327–335, 2011.

[30] H. Schoof, J. Apel, I. Heschel, and G. Rau. Control of pore structure and size in freeze-dried collagen sponges. *Journal of biomedical materials research*, 58(4):352–357, 2001.

[31] K. M. Pawelec, A. Husmann, S. M. Best, and R. E. Cameron. Ice-templated structures for biomedical tissue repair: From physics to final scaffolds. *Applied Physics Reviews*, 1(2), 2014.

[32] S. Deville, E. Saiz, and A. P. Tomsia. Ice-templated porous alumina structures. *Acta Materialia*, 55(6):1965–1974, 2007.

[33] P. Menasché, V. Vanneaux, A. Hagège, A. Bel, B. Cholley, I. Cacciapuoti, A. Parouchev, N. Benhamouda, G. Tachdjian, L. Tosca, J.-H. Trouvin, J.-R. Fabreguettes, V. Bellamy, R. Guillemain, C. Suberbielle Boissel, E. Tartour, M. Desnos, and J. Larghero. Human embryonic stem cell-derived cardiac progenitors for severe heart failure treatment: first clinical case report. *European Heart Journal*, 36(30):2011–2017, may 2015.

[34] S. D. Anker, A. J. S. Coats, G. Cristian, D. Dragomir, E. Pusineri, M. Piredda, L. Bettari, R. Dowling, M. Volterrani, and B.-A. Kirwan. A prospective comparison of alginate-hydrogel with standard medical therapy to determine impact on functional capacity and clinical outcomes in patients with advanced heart failure. *European heart journal*, 36(34):2297–2309, 2015.

[35] J. Liu, K. Miller, X. Ma, S. Dewan, N. Lawrence, G. Whang, P. Chung, A. D. Mcculloch, and S. Chen. Direct 3D bioprinting of cardiac micro-tissues mimicking native myocardium. *Biomaterials*, 256, 2020.

[36] W. Friess. Collagen–biomaterial for drug delivery. *European Journal of Pharmaceutics and Biopharmaceutics*, 45(2):113–136, 1998.

[37] J. K. Mouw, G. Ou, and V. M. Weaver. Extracellular matrix assembly: a multiscale deconstruction. *Nature reviews Molecular cell biology*, 15(12):771–785, 2014.

[38] D. J. Prockop. Collagens. In W. J. Lennarz and M. D. B. T. Lane, editors, *Encyclopedia of Biological Chemistry (Second Edition)*, pages 545–549. Academic Press, Waltham, 2013.

[39] D. J. S. Hulmes. Collagen Diversity, Synthesis and Assembly. In P. Fratzl, editor, *Collagen: Structure and Mechanics*, pages 15–47. Springer US, Boston, MA, 2008.

[40] S. Ricard-Blum. The collagen family. *Cold Spring Harbor perspectives in biology*, 3(1):4978–4978, jan 2011.

[41] K. T. Weber. Cardiac interstitium in health and disease: The fibrillar collagen network. *Journal of the American College of Cardiology*, 13(7):1637–1652, 1989.

[42] M. M. H. Marijianowski, P. Teeling, J. Mann, and A. E. Becker. Dilated cardiomyopathy is associated with an increase in the type I/type III collagen ratio: A quantitative assessment. *Journal of the American College of Cardiology*, 25(6):1263–1272, may 1995.

[43] G. A. Gray, I. S. Toor, R. F. P. Castellan, M. Crisan, and M. Meloni. Resident cells of the myocardium: more than spectators in cardiac injury, repair and regeneration. *Current opinion in physiology*, 1:46–51, 2018.

[44] D. Sharma, M. Ferguson, T. J. Kamp, and F. Zhao. Constructing biomimetic cardiac tissues: a review of scaffold materials for engineering cardiac patches. *Emergent Materials*, 2(2):181–191, 2019.

[45] L. Axel, V. J. Wedeen, and D. B. Ennis. Probing dynamic myocardial microstructure with cardiac magnetic resonance diffusion tensor imaging. *Journal of Cardiovascular Magnetic Resonance*, 16(89), 2014.

[46] A. Soltani, J. Lahti, K. Järvelä, S. Curtze, J. Laurikka, M. Hokka, and V. T. Kuokkala. An Optical Method for the In-Vivo Characterization of the Biomechanical Response of the Right Ventricle. *Scientific Reports*, 8(1):1–11, 2018.

[47] A. F. Corno, M. J. Kocica, and F. Torrent-Guasp. The helical ventricular myocardial band of Torrent-Guasp: potential implications in congenital heart defects. *European journal of cardio-thoracic surgery*, 29:61–68, 2006.

[48] I. J. LeGrice, B. H. Smaill, L. Z. Chai, S. G. Edgar, J. B. Gavin, and P. J. Hunter. Laminar structure of the heart: ventricular myocyte arrangement and connective tissue architecture in the dog. *American Journal of Physiology-Heart and Circulatory Physiology*, 269(2):571–582, 1995.

[49] A. J. Pope, G. B. Sands, B. H. Smaill, and I. J. LeGrice. Three-dimensional transmural organization of perimysial collagen in the heart. *American Journal of Physiology-Heart and Circulatory Physiology*, 295(3):1243–1252, 2008.

[50] S. Fleischer, A. Shapira, R. Feiner, and T. Dvir. Modular assembly of thick multifunctional cardiac patches. *Proceedings of the National Academy of Sciences of the United States of America*, 114(8):1898–1903, 2017.

[51] D. D. Streeter Jr and W. T. Hanna. Engineering mechanics for successive states in canine left ventricular myocardium: I. Cavity and wall geometry. *Circulation research*, 33(6):639–655, 1973.

[52] D. D. Streeter Jr, H. M. Spotnitz, D. P. Patel, J. ROSS Jr, and E. H. Sonnenblick. Fiber orientation in the canine left ventricle during diastole and systole. *Circulation research*, 24(3):339–347, 1969.

[53] S. Huang and D. E. Sosnovik. Molecular and Microstructural Imaging of the Myocardium. *Current cardiovascular imaging reports*, 3(1):26–33, feb 2010.

[54] P. W. Hales, J. E. Schneider, R. A. B. Burton, B. J. Wright, C. Bollensdorff, and P. Kohl. Histo-anatomical structure of the living isolated rat heart in two contraction states assessed by diffusion tensor MRI. *Progress in biophysics and molecular biology*, 110(2-3):319–330, 2012.

[55] G. B. Sands, D. A. Gerneke, D. A. Hooks, C. R. Green, B. H. Smaill, and I. J. Legrice. Automated imaging of extended tissue volumes using confocal microscopy. *Microscopy research and technique*, 67(5):227–239, 2005.

[56] H. M. Spotnitz, W. D. Spotnitz, T. S. Cottrell, D. Spiro, and E. H. Sonnenblick. Cellular basis for volume related wall thickness changes in the rat left ventricle. *Journal of molecular and cellular cardiology*, 6(4):317–331, 1974.

[57] K. B. Harrington, F. Rodriguez, A. Cheng, F. Langer, H. Ashikaga, G. T. Daughters, J. C. Criscione, N. B. Ingels, and D. C. Miller. Direct measurement of transmural laminar architecture in the anterolateral wall of the ovine left ventricle: new implications for wall thickening mechanics. *American Journal of Physiology-Heart and Circulatory Physiology*, 288(3):1324–1330, 2005.

[58] M. Tee, J. A. Noble, and D. A. Bluemke. Imaging techniques for cardiac strain and deformation: comparison of echocardiography, cardiac magnetic resonance and cardiac computed tomography. *Expert Review of Cardiovascular Therapy*, 11(2):221–231, feb 2013.

[59] A. Nasiraei Moghaddam, N. Saber, H. Wen, J. P. Finn, D. Ennis, and M. Gharib. Analytical method to measure three-dimensional strain patterns in the left ventricle from single slice displacement data. *Journal of Cardiovascular Magnetic Resonance*, 12(1):1–18, 2010.

[60] M. S. Amzulescu, M. De Craene, H. Langet, A. Pasquet, D. Vancraeynest, A. C. Pouleur, J. L. Vanoverschelde, and B. L. Gerber. Myocardial strain imaging: Review of general principles, validation, and sources of discrepancies. *European Heart Journal Cardiovascular Imaging*, 20(6):605–619, 2019.

[61] V. Mora, I. Roldán, E. Romero, A. Saurí, D. Romero, J. Pérez-Gozalbo, N. Ugalde, J. Bertolín, M. Rodriguez-Israel, C. Delgado, and J. Lowenstein. Myocardial Contraction during the Diastolic Isovolumetric Period: Analysis of Longitudinal Strain by Means of Speckle Tracking Echocardiography. *Journal of Cardiovascular Development and Disease*, 5(3):41, 2018.

[62] Y. Mizuguchi, Y. Oishi, H. Miyoshi, A. Iuchi, N. Nagase, and T. Oki. The Functional Role of Longitudinal, Circumferential, and Radial Myocardial Deformation for Regulating the Early Impairment of Left Ventricular Contraction and Relaxation in Patients With Cardiovascular Risk Factors: A Study With Two-Dimensional Strain Im. *Journal of the American Society of Echocardiography*, 21(10):1138–1144, 2008.

[63] P. Ferraiuoli, L. S. Fixsen, B. Kappler, R. G. Lopata, J. W. Fenner, and A. J. Narracott. Measurement of in vitro cardiac deformation by means of 3D digital image correlation and ultrasound 2D speckle-tracking echocardiography. *Medical Engineering and Physics*, 74:146–152, 2019.

[64] R. L. Mauck, M. A. Soltz, C. C. B. Wang, D. D. Wong, P.-H. G. Chao, W. B. Valhmu, C. T. Hung, and G. A. Ateshian. Functional tissue engineering of articular cartilage through dynamic loading of chondrocyte-seeded agarose gels. *Journal of biomechanical engineering*, 122(3):252–260, 2000.

[65] M. D. Buschmann, Y. A. Gluzband, A. J. Grodzinsky, and E. B. Hunziker. Mechanical compression modulates matrix biosynthesis in chondrocyte/agarose culture. *Journal of cell science*, 108(4):1497–1508, 1995.

[66] M. Hokka, N. Mirow, H. Nagel, M. Irqsusi, S. Vogt, and V.-T. Kuokkala. In-vivo deformation measurements of the human heart by 3D Digital Image Correlation. *Journal of Biomechanics*, 48(10):2217–2220, 2015.

[67] K. Ronaldson-Bouchard, K. Yeager, D. Teles, T. Chen, S. Ma, L. J. Song, K. Morikawa, H. M. Wobma, A. Vasciaveo, E. C. Ruiz, M. Yazawa, and G. Vunjak-Novakovic. *Engineering of human cardiac muscle electromechanically matured to an adult-like phenotype*, volume 14. Springer US, 2019.

[68] J. M. Bhalodiya, A. Palit, E. Ferrante, M. K. Tiwari, S. K. Bhudia, T. N. Arvanitis, and M. A. Williams. Hierarchical Template Matching for 3D Myocardial Tracking and Cardiac Strain Estimation. *Scientific Reports*, 9(1):1–13, 2019.

[69] A. Shradhanjali, B. D. Riehl, B. Duan, R. Yang, and J. Y. Lim. Spatiotemporal Characterizations of Spontaneously Beating Cardiomyocytes with Adaptive Reference Digital Image Correlation. *Scientific Reports*, 9(1):1–10, 2019.

[70] L. A. Macqueen, S. P. Sheehy, C. O. Chantre, J. F. Zimmerman, F. S. Pasqualini, X. Liu, J. A. Goss, P. H. Campbell, G. M. Gonzalez, S. J. Park, A. K. Capulli, J. P. Ferrier, T. Fettah Kosar, L. Mahadevan, W. T. Pu, and K. K. Parker. A tissue-engineered scale model of the heart ventricle. *Nature Biomedical Engineering*, 2(12):930–941, 2018.

[71] A. W. Feinberg, P. W. Alford, H. Jin, C. M. Ripplinger, A. Andreas, S. P. Sheehy, A. Grosberg, and K. K. Parker. Controlling the contractile strength of engineered cardiac muscle by hierarchal tissue architecture. *Biomaterials*, 33(23):5732–5741, 2012.

[72] Q. Wen, K. Gandhi, R. A. Capel, G. Hao, C. O'Shea, G. Neagu, S. Pearcey, D. Pavlovic, D. A. Terrar, J. Wu, G. Faggian, P. Camelliti, and M. Lei. Transverse cardiac slicing and optical imaging for analysis of transmural gradients in membrane potential and Ca2+ transients in murine heart. *Journal of Physiology*, 596(17):3951–3965, 2018.

[73] S. He, Q. Wen, C. OShea, R. Muu-Min, K. Kou, A. Grassam-Rowe, Y. Liu, X. Tan, X. Ou, P. Camelliti, D. Pavlovic, and M. Lei. A protocol for transverse cardiac slicing and optical mapping in murine heart. *Frontiers in Physiology*, 10:1–8, 2019.

[74] D. L. Mann and M. R. Bristow. Mechanisms and models in heart failure: the biomechanical model and beyond. *Circulation*, 111(21):2837–2849, 2005.

[75] B. M. Jackson, J. H. Gorman III, I. S. Salgo, S. L. Moainie, T. Plappert, M. St. John-Sutton, L. H. Edmunds Jr, and R. C. Gorman. Border zone geometry increases wall stress after myocardial infarction: contrast echocardiographic assessment. *American Journal of Physiology-Heart and Circulatory Physiology*, 284(2):475–479, 2003.

[76] R. Hashizume, Y. Hong, K. Takanari, K. L. Fujimoto, K. Tobita, and W. R. Wagner. The effect of polymer degradation time on functional outcomes of temporary elastic patch support in ischemic cardiomyopathy. *Biomaterials*, 34(30):7353–7363, 2013.

[77] M. A. Laflamme. Heart regeneration. *Nature*, 473:326–335, 2011.

[78] M. L. Steinhauser and R. T. Lee. Regeneration of the heart. *EMBO molecular medicine*, 3(12):701–712, 2011.

[79] P. Anversa and B. Nadal-Ginard. Myocyte renewal and ventricular remodelling. *Nature*, 415(6868):240–243, 2002.

[80] M. Mercola, P. Ruiz-Lozano, and M. D. Schneider. Cardiac muscle regeneration: lessons from development. *Genes & development*, 25(4):299–309, 2011.

[81] L. Yue, J. Xie, and S. Nattel. Molecular determinants of cardiac fibroblast electrical function and therapeutic implications for atrial fibrillation. *Cardiovascular research*, 89(4):744–753, 2011.

[82] W.-H. Zimmermann, I. Melnychenko, and T. Eschenhagen. Engineered heart tissue for regeneration of diseased hearts. *Biomaterials*, 25(9):1639–1647, 2004.

[83] G. Y. Koh, M. H. Soonpaa, M. G. Klug, and L. J. Field. Long-term survival of AT-1 cardiomyocyte grafts in syngeneic myocardium. *American Journal of Physiology-Heart and Circulatory Physiology*, 264(5):1727–1733, 1993.

[84] G. Y. Koh, M. G. Klug, M. H. Soonpaa, and L. J. Field. Differentiation and long-term survival of C2C12 myoblast grafts in heart. *The Journal of clinical investigation*, 92(3):1548–1554, 1993.

[85] B. A. Tompkins, M. Natsumeda, W. Balkan, and J. M. Hare. What is the future of cell-based therapy for acute myocardial infarction. *Circulation Research*, 120(2):252–255, 2017.

[86] Y. W. Liu, B. Chen, X. Yang, J. A. Fugate, F. A. Kalucki, A. Futakuchi-Tsuchida, L. Couture, K. W. Vogel, C. A. Astley, A. Baldessari, J. Ogle, C. W. Don, Z. L. Steinberg, S. P. Seslar, S. A. Tuck, H. Tsuchida, A. V. Naumova, S. K. Dupras, M. S. Lyu, J. Lee, D. W. Hailey, H. Reinecke, L. Pabon, B. H. Fryer, W. R. MacLellan, R. S. Thies, and C. E. Murry. Human embryonic stem cell-derived cardiomyocytes restore function in infarcted hearts of non-human primates. *Nature Biotechnology*, 36(7):597–605, 2018.

[87] K. L. Fujimoto, K. Tobita, W. D. Merryman, J. Guan, N. Momoi, D. B. Stolz, M. S. Sacks, B. B. Keller, and W. R. Wagner. An elastic, biodegradable cardiac patch induces contractile smooth muscle and improves cardiac remodeling and function in subacute myocardial infarction. *Journal of the American College of Cardiology*, 49(23):2292–2300, 2007.

[88] S. T. Wall, J. C. Walker, K. E. Healy, M. B. Ratcliffe, and J. M. Guccione. Theoretical impact of the injection of material into the myocardium: a finite element model simulation. *Circulation*, 114(24):2627–2635, 2006.

[89] R. Lanza, R. Langer, J. P. Vacanti, and A. Atala. *Principles of tissue engineering*. Academic press, 2020.

[90] M.-N. Giraud, C. Armbruster, T. Carrel, and H. T. Tevaearai. Current state of the art in myocardial tissue engineering. *Tissue engineering*, 13(8):1825–1836, 2007.

[91] C. P. Jackman, I. Y. Shadrin, A. L. Carlson, and N. Bursac. Human cardiac tissue engineering: from pluripotent stem cells to heart repair. *Current opinion in chemical engineering*, 7:57–64, 2015.

[92] M. Gonen-Wadmany, L. Gepstein, and D. Seliktar. Controlling the cellular organization of tissue-engineered cardiac constructs. *Annals of the New York academy of sciences*, 1015(1):299–311, 2004.

[93] Y. Yildirim, H. Naito, M. Didie, B.-C. Karikkineth, D. Biermann, T. Eschenhagen, and W.-H. Zimmermann. Development of a biological ventricular assist device: preliminary data from a small animal model. *Circulation*, 116(1):16–23, 2007.

[94] R. A. Li, W. Keung, T. J. Cashman, P. C. Backeris, B. V. Johnson, E. S. Bardot, A. O. T. Wong, P. K. W. Chan, C. W. Y. Chan, and K. D. Costa. Bioengineering an electro-mechanically functional miniature ventricular heart chamber from human pluripotent stem cells. *Biomaterials*, 163:116–127, 2018.

[95] E. J. Lee, D. E. Kim, E. U. Azeloglu, and K. D. Costa. Engineered cardiac organoid chambers: toward a functional biological model ventricle. *Tissue Engineering Part A*, 14(2):215–225, 2008.

[96] D. J. Richards, Y. Li, C. M. Kerr, J. Yao, G. C. Beeson, R. C. Coyle, X. Chen, J. Jia, B. Damon, R. Wilson, E. Starr Hazard, G. Hardiman, D. R. Menick, C. C. Beeson, H. Yao, T. Ye, and Y. Mei. Human cardiac organoids for the modelling of myocardial infarction and drug cardiotoxicity. *Nature Biomedical Engineering*, 4(4):446–462, 2020.

[97] J. Veldhuizen, J. Cutts, D. A. Brafman, R. Q. Migrino, and M. Nikkhah. Engineering anisotropic human stem cell-derived three-dimensional cardiac tissue on-a-chip. *Biomaterials*, 256, 2020.

[98] J.-H. Jang, C. B. Rives, and L. D. Shea. Plasmid delivery in vivo from porous tissue-engineering scaffolds: transgene expression and cellular transfection. *Molecular Therapy*, 12(3):475–483, 2005.

[99] R. M. Capito and M. Spector. Collagen scaffolds for nonviral IGF-1 gene delivery in articular cartilage tissue engineering. *Gene therapy*, 14(9):721–732, 2007.

[100] I. O. Smith, X. H. Liu, L. A. Smith, and P. X. Ma. Nanostructured polymer scaffolds for tissue engineering and regenerative medicine. *Wiley Interdisciplinary Reviews: Nanomedicine and Nanobiotechnology*, 1(2):226–236, 2009.

[101] K. Itaka, K. Osada, K. Morii, P. Kim, S.-H. Yun, and K. Kataoka. Polyplex nanomicelle promotes hydrodynamic gene introduction to skeletal muscle. *Journal of controlled release*, 143(1):112–119, 2010.

[102] L. E. Freed and G. Vunjak-Novakovic. Microgravity tissue engineering. *In Vitro Cellular & Developmental Biology-Animal*, 33(5):381–385, 1997.

[103] W. H. Zimmermann, K. Schneiderbanger, P. Schubert, M. Didié, F. Münzel, J. F. Heubach, S. Kostin, W. L. Neuhuber, and T. Eschenhagen. Tissue engineering of a differentiated cardiac muscle construct. *Circulation Research*, 90(2):223–230, 2002.

[104] H. A. Awad, D. L. Butler, G. P. Boivin, F. N. L. Smith, P. Malaviya, B. Huibregtse, and A. I. Caplan. Autologous mesenchymal stem cell-mediated repair of tendon. *Tissue engineering*, 5(3):267–277, 1999.

[105] R. G. Young, D. L. Butler, W. Weber, A. I. Caplan, S. L. Gordon, and D. J. Fink. Use of mesenchymal stem cells in a collagen matrix for Achilles tendon repair. *Journal of Orthopaedic Research*, 16(4):406–413, 1998.

[106] F. Guilak and C. T. Hung. Physical regulation of cartilage metabolism. In *Basic Orthopaedic Biomechanics. Philadelphia: Lippincott-Raven*, pages 259–300. 2005.

[107] W. M. Lai, J. S. Hou, and V. C. Mow. A triphasic theory for the swelling and deformation behaviors of articular cartilage. *Journal of biomechanical engineering*, 113:245–258, 1991.

[108] E. H. Frank and A. J. Grodzinsky. Cartilage electromechanics—II. A continuum model of cartilage electrokinetics and correlation with experiments. *Journal of biomechanics*, 20(6):629–639, 1987.

[109] F. Guilak, A. Ratcliffe, and V. C. Mow. Chondrocyte deformation and local tissue strain in articular cartilage: a confocal microscopy study. *Journal of Orthopaedic Research*, 13(3):410–421, 1995.

[110] P. Datta, V. Vyas, S. Dhara, A. R. Chowdhury, and A. Barui. Anisotropy Properties of Tissues: A Basis for Fabrication of Biomimetic Anisotropic Scaffolds for Tissue Engineering. *Journal of Bionic Engineering*, 16(5):842–868, 2019.

[111] Y. Miyagi, L. L. Y. Chiu, M. Cimini, R. D. Weisel, M. Radisic, and R.-K. Li. Biodegradable collagen patch with covalently immobilized VEGF for myocardial repair. *Biomaterials*, 32(5):1280–1290, 2011.

[112] M. Radisic, H. Park, S. Gerecht, C. Cannizzaro, R. Langer, and G. Vunjak-Novakovic. Biomimetic approach to cardiac tissue engineering. *Philosophical Transactions of the Royal Society B: Biological Sciences*, 362(1484):1357–1368, 2007.

[113] X. Lin, Y. Liu, A. Bai, H. Cai, Y. Bai, W. Jiang, H. Yang, X. Wang, L. Yang, N. Sun, and H. Gao. A viscoelastic adhesive epicardial patch for treating myocardial infarction. *Nature Biomedical Engineering*, 3(8):632–643, 2019.

[114] H. Jawad, N. N. Ali, A. R. Lyon, Q. Z. Chen, S. E. Harding, and A. R. Boccaccini. Myocardial tissue engineering: a review. *Journal of tissue engineering and regenerative medicine*, 1(5):327–342, 2007.

[115] J. R. Venugopal, M. P. Prabhakaran, S. Mukherjee, R. Ravichandran, K. Dan, and S. Ramakrishna. Biomaterial strategies for alleviation of myocardial infarction. *Journal of the Royal Society Interface*, 9(66):1–19, 2012.

[116] H. Takahashi, T. Yokota, E. Uchimura, S. Miyagawa, T. Ota, K. Torikai, A. Saito, K. Hirakawa, K. Kitabayashi, and K. Okada. Newly developed tissue-engineered material for reconstruction of vascular wall without cell seeding. *The Annals of thoracic surgery*, 88(4):1269–1276, 2009.

[117] J. Ashworth, M. Mehr, B. Paul, B. Serena, and C. Ruth. Cell Invasion in Collagen Scaffold Architectures Characterized by Percolation Theory. *Advanced Healthcare Materials*, 4(9):1317–1321, jan 2015.

[118] G. Vunjak-Novakovic, N. Tandon, A. Godier, R. Maidhof, A. Marsano, T. P. Martens, and M. Radisic. Challenges in cardiac tissue engineering. *Tissue Engineering Part B: Reviews*, 16(2):169–187, 2010.

[119] M. Radisic and G. Vunjak-Novakovic. Cardiac tissue engineering. *Journal-Serbian Chemical Society*, 70(3):541, 2005.

[120] M. Shin, O. Ishii, T. Sueda, and J. P. Vacanti. Contractile cardiac grafts using a novel nanofibrous mesh. *Biomaterials*, 25(17):3717–3723, 2004.

[121] O. Ishii, M. Shin, T. Sueda, and J. P. Vacanti. In vitro tissue engineering of a cardiac graft using a degradable scaffold with an extracellular matrix–like topography. *The Journal of thoracic and cardiovascular surgery*, 130(5):1358–1363, 2005.

[122] D. C. Tancred, B. A. O. McCormack, and A. J. Carr. A synthetic bone implant macroscopically identical to cancellous bone. *Biomaterials*, 19(24):2303–2311, 1998.

[123] S. H. Oh, S. G. Kang, E. S. Kim, S. H. Cho, and J. H. Lee. Fabrication and characterization of hydrophilic poly(lactic-co-glycolic acid)/poly(vinyl alcohol) blend cell scaffolds by melt-molding particulate-leaching method. *Biomaterials*, 24(22):4011–4021, 2003.

[124] A. S. Rowlands, S. A. Lim, D. Martin, and J. J. Cooper-White. Polyurethane/poly(lactic-co-glycolic) acid composite scaffolds fabricated by thermally induced phase separation. *Biomaterials*, 28(12):2109–2121, 2007.

[125] A. Khademhosseini and R. Langer. Microengineered hydrogels for tissue engineering. *Biomaterials*, 28(34):5087–5092, 2007.

[126] U. Cheema. *Three-dimensional collagen biomatrix development and control*. Woodhead Publishing Limited, 2013.

[127] H. Liu, E. B. Slamovich, and T. J. Webster. Less harmful acidic degradation of poly(lacticco-glycolic acid) bone tissue engineering scaffolds through titania nanoparticle addition. *International journal of nanomedicine*, 1(4):541–545, 2006.

[128] B. L. Seal, T. C. Otero, and A. Panitch. Polymeric biomaterials for tissue and organ regeneration. *Materials Science and Engineering: R: Reports*, 34(4):147–230, 2001.

[129] S. F. Badylak. The extracellular matrix as a biologic scaffold material. *Biomaterials*, 28(25):3587–3593, 2007.

[130] B. A. Harley, A. K. Lynn, Z. Wissner-Gross, W. Bonfield, I. V. Yannas, and L. J. Gibson. Design of a multiphase osteochondral scaffold. II. Fabrication of a mineralized collagen-glycosaminoglycan scaffold. *Journal of biomedical materials research. Part A*, 92(3):1066–1077, mar 2010.

[131] T. Eschenhagen, C. Fink, U. Remmers, H. Scholz, J. Wattchow, J. Weil, W. Zimmermann, H. H. Dohmen, H. Schäfer, and N. Bishopric. Three-dimensional reconstitution of embryonic cardiomyocytes in a collagen matrix: a new heart muscle model system. *The FASEB journal*, 11(8):683–694, 1997.

[132] J. A. Schaefer, P. A. Guzman, S. B. Riemenschneider, T. J. Kamp, and R. T. Tranquillo. A cardiac patch from aligned microvessel and cardiomyocyte patches. *Journal of tissue engineering and regenerative medicine*, 12(2):546–556, 2018.

[133] C. P. Jackman, A. M. Ganapathi, H. Asfour, Y. Qian, B. W. Allen, Y. Li, and N. Bursac. Engineered cardiac tissue patch maintains structural and electrical properties after epicardial implantation. *Biomaterials*, 159:48–58, 2018.

[134] D. Zhang, I. Y. Shadrin, J. Lam, H.-Q. Xian, H. R. Snodgrass, and N. Bursac. Tissue-engineered cardiac patch for advanced functional maturation of human ESC-derived cardiomyocytes. *Biomaterials*, 34(23):5813–5820, 2013.

[135] T. Arts, K. D. Costa, J. W. Covell, and A. D. McCulloch. Relating myocardial laminar architecture to shear strain and muscle fiber orientation. *American Journal of Physiology-Heart and Circulatory Physiology*, 280(5):2222–2229, 2001.

[136] K. D. Costa, Y. Takayama, A. D. McCulloch, and J. W. Covell. Laminar fiber architecture and three-dimensional systolic mechanics in canine ventricular myocardium. *American Journal of Physiology-Heart and Circulatory Physiology*, 276(2):595–607, 1999.

[137] S. Rohr, D. M. Schölly, and A. G. Kleber. Patterned growth of neonatal rat heart cells in culture. Morphological and electrophysiological characterization. *Circulation research*, 68(1):114–130, 1991.

[138] A. G. Kleber and Y. Rudy. Basic mechanisms of cardiac impulse propagation and associated arrhythmias. *Physiological reviews*, 84(2):431–88, 2004.

[139] N. Bursac, K. K. Parker, S. Iravanian, and L. Tung. Cardiomyocyte cultures with controlled macroscopic anisotropy: a model for functional electrophysiological studies of cardiac muscle. *Circulation research*, 91(12):45–54, 2002.

[140] A. W. Feinberg. Engineered tissue grafts: opportunities and challenges in regenerative medicine. *WIREs Systems Biology and Medicine*, 4(2):207–220, mar 2012.

[141] W. L. Stoppel, D. Hu, I. J. Domian, D. L. Kaplan, and L. D. Black III. Anisotropic silk biomaterials containing cardiac extracellular matrix for cardiac tissue engineering. *Biomedical materials*, 10(3):34105, 2015.

[142] K. M. Pawelec, H. A. van Boxtel, and S. G. J. M. Kluijtmans. Ice-templating of anisotropic structures with high permeability. *Materials science & engineering. C, Materials for biological applications*, 76:628–636, jul 2017.

[143] M. Silva, L. A. Cyster, J. J. A. Barry, X. B. Yang, R. O. C. Oreffo, D. M. Grant, C. A. Scotchford, S. M. Howdle, K. M. Shakesheff, and F. Rose. The effect of anisotropic architecture on cell and tissue infiltration into tissue engineering scaffolds. *Biomaterials*, 27(35):5909–5917, 2006.

[144] E. A. Phelps and A. J. Garcia. Update on therapeutic vascularization strategies. *Regenerative Medicine*, 4(1):65–80, dec 2008.

[145] H. C. H. Ko, B. K. Milthorpe, and C. D. McFarland. Engineering thick tissues - The vascularisation problem. *European Cells and Materials*, 14:1–18, jan 2007.

[146] V. Karageorgiou and D. Kaplan. Porosity of 3D biomaterial scaffolds and osteogenesis. *Biomaterials*, 26(27):5474–5491, 2005.

[147] K. Rezwan, Q. Z. Chen, J. J. Blaker, and A. R. Boccaccini. Biodegradable and bioactive porous polymer/inorganic composite scaffolds for bone tissue engineering. *Biomaterials*, 27(18):3413–3431, 2006.

[148] D. W. Hutmacher. Scaffolds in tissue engineering bone and cartilage. *Biomaterials*, 21(24):2529–2543, 2000.

[149] A. Eltom, G. Zhong, and A. Muhammad. Scaffold Techniques and Designs in Tissue Engineering Functions and Purposes: A Review. *Advances in Materials Science and Engineering*, 2019.

[150] G. Chen and N. Kawazoe. Preparation of Polymer Scaffolds by Ice Particulate Method for Tissue Engineering. In M. Ebara, editor, *Biomaterials Nanoarchitectonics*, pages 77–95. Elsevier Inc., 2016.

[151] W. Lin, W. Lan, Y. Wu, D. Zhao, Y. Wang, X. He, J. Li, Z. Li, F. Luo, H. Tan, and Q. Fu. Aligned 3D porous polyurethane scaffolds for biological anisotropic tissue regeneration. *Regenerative Biomaterials*, 7(1):19–27, 2019.

[152] Z. Wang and S. J. Florczyk. Freeze-FRESH: A 3D printing technique to produce biomaterial scaffolds with hierarchical porosity. *Materials*, 13(2):354, 2020.

[153] S. T. Kelley, R. Malekan, J. H. Gorman III, B. M. Jackson, R. C. Gorman, Y. Suzuki, T. Plappert, D. K. Bogen, M. G. S. J. Sutton, and L. H. Edmunds Jr. Restraining infarct expansion preserves left ventricular geometry and function after acute anteroapical infarction. *Circulation*, 99(1):135–142, 1999.

[154] J. Leor, S. Aboulafia-Etzion, A. Dar, L. Shapiro, I. M. Barbash, A. Battler, Y. Granot, and S. Cohen. Bioengineered cardiac grafts: a new approach to repair the infarcted myocardium? *Circulation*, 102(suppl_3):Iii–56, 2000.

[155] W. H. Zimmermann, C. Fink, D. Kralisch, U. Remmers, J. Weil, and T. Eschenhagen. Three-dimensional engineered heart tissue from neonatal rat cardiac myocytes. *Biotechnology and bioengineering*, 68(1):106–114, 2000.

[156] W.-H. Zimmermann, I. Melnychenko, G. Wasmeier, M. Didié, H. Naito, U. Nixdorff, A. Hess, L. Budinsky, K. Brune, and B. Michaelis. Engineered heart tissue grafts improve systolic and diastolic function in infarcted rat hearts. *Nature medicine*, 12(4):452–458, 2006.

[157] J. C. Chachques, J. C. Trainini, N. Lago, M. Cortes-Morichetti, O. Schussler, and A. Carpentier. Myocardial Assistance by Grafting a New Bioartificial Upgraded Myocardium (MAGNUM Trial): Clinical Feasibility Study. *Annals of Thoracic Surgery*, 85(3):901–908, 2008.

[158] C. A. Holladay, A. M. Duffy, X. Chen, M. V. Sefton, T. D. O'Brien, and A. S. Pandit. Recovery of cardiac function mediated by MSC and interleukin-10 plasmid functionalised scaffold. *Biomaterials*, 33(5):1303–1314, 2012.

[159] T. Mizuno, T. M. Yau, R. D. Weisel, C. G. Kiani, and R.-K. Li. Elastin stabilizes an infarct and preserves ventricular function. *Circulation*, 112(9):81–88, 2005.

[160] W. Dai, S. L. Hale, G. L. Kay, A. J. Jyrala, and R. A. Kloner. Delivering stem cells to the heart in a collagen matrix reduces relocation of cells to other organs as assessed by nanoparticle technology. *Regenerative Medicine*, 4(3):387–385, 2009.

[161] N. Derval, L. Barandon, P. Dufourcq, L. Leroux, J.-M. D. Lamazière, D. Daret, T. Couffinhal, and C. Duplàa. Epicardial deposition of endothelial progenitor and mesenchymal stem cells in a coated muscle patch after myocardial infarction in a murine model. *European journal of cardio-thoracic surgery*, 34(2):248–254, 2008.

[162] M. Giraud, E. Ayuni, S. Cook, M. Siepe, T. P. Carrel, and H. T. Tevaearai. Hydrogel-based engineered skeletal muscle grafts normalize heart function early after myocardial infarction. *Artificial organs*, 32(9):692–700, 2008.

[163] E. Bassat, Y. E. Mutlak, A. Genzelinakh, I. Y. Shadrin, K. B. Umansky, O. Yifa, D. Kain, D. Rajchman, J. Leach, and D. R. Bassat. The extracellular matrix protein agrin promotes heart regeneration in mice. *Nature*, 547(7662):179–184, 2017.

[164] T. J. Herron, A. M. D. Rocha, K. F. Campbell, D. Ponce-Balbuena, B. C. Willis, G. Guerrero-Serna, Q. Liu, M. Klos, H. Musa, and M. Zarzoso. Extracellular matrix–mediated maturation of human pluripotent stem cell–derived cardiac monolayer structure and electrophysiological function. *Circulation: Arrhythmia and Electrophysiology*, 9(4), 2016.

[165] J. Jang, H. J. Park, S. W. Kim, H. Kim, J. Y. Park, S. J. Na, H. J. Kim, M. N. Park, S. H. Choi, S. H. Park, S. W. Kim, S. M. Kwon, P. J. Kim, and D. W. Cho. 3D printed complex tissue construct using stem cell-laden decellularized extracellular matrix bioinks for cardiac repair. *Biomaterials*, 112:264–274, 2017.

[166] G. C. Engelmayr, M. Cheng, C. J. Bettinger, J. T. Borenstein, R. Langer, and L. E. Freed. Accordion-like honeycombs for tissue engineering of cardiac anisotropy. *Nature materials*, 7(12):1003–1010, 2008.

[167] D. Motlagh, T. J. Hartman, T. A. Desai, and B. Russell. Microfabricated grooves recapitulate neonatal myocyte connexin43 and N-cadherin expression and localization. *Journal of Biomedical Materials Research Part A: An Official Journal of The Society for Biomaterials, The Japanese Society for Biomaterials, and The Australian Society for Biomaterials and the Korean Society for Biomaterials*, 67(1):148–157, 2003.

[168] N. A. Geisse, S. P. Sheehy, and K. K. Parker. Control of myocyte remodeling in vitro with engineered substrates. *In Vitro Cellular & Developmental Biology-Animal*, 45(7):343–350, 2009.

[169] C. Chung, H. Bien, E. A. Sobie, V. Dasari, D. McKinnon, B. Rosati, and E. Entcheva. Hypertrophic phenotype in cardiac cell assemblies solely by structural cues and ensuing self-organization. *The FASEB Journal*, 25(3):851–862, 2011.

[170] K. K. Parker, J. Tan, C. S. Chen, and L. Tung. Myofibrillar architecture in engineered cardiac myocytes. *Circulation research*, 103(4):340–342, 2008.

[171] M. Bray, S. P. Sheehy, and K. K. Parker. Sarcomere alignment is regulated by myocyte shape. *Cell motility and the cytoskeleton*, 65(8):641–651, 2008.

[172] A. Grosberg, P.-L. Kuo, C.-L. Guo, N. A. Geisse, M.-A. Bray, W. J. Adams, S. P. Sheehy, and K. K. Parker. Self-organization of muscle cell structure and function. *PLoS computational biology biology*, 7(2), 2011.

[173] L. Ye, W.-H. Zimmermann, D. J. Garry, and J. Zhang. Patching the heart: cardiac repair from within and outside. *Circulation research*, 113(7):922–932, 2013.

[174] U. G. K. Wegst, M. Schecter, A. E. Donius, and P. M. Hunger. Biomaterials by freeze casting. *Philosophical transactions. Series A, Mathematical, physical, and engineering sciences*, 368(1917):2099–2121, apr 2010.

[175] J. Tan and W. M. Saltzman. Biomaterials with hierarchically defined micro- and nanoscale structure. *Biomaterials*, 25(17):3593–3601, aug 2004.

[176] L. Zhao, S. Mei, P. K. Chu, Y. Zhang, and Z. Wu. The influence of hierarchical hybrid micro/nano-textured titanium surface with titania nanotubes on osteoblast functions. *Biomaterials*, 31(19):5072–5082, jul 2010.

[177] J. E. Snyder, P. M. Hunger, C. Wang, Q. Hamid, U. G. K. Wegst, and W. Sun. Combined multi-nozzle deposition and freeze casting process to superimpose two porous networks for hierarchical three-dimensional microenvironment. *Biofabrication*, 6(1), mar 2014.

[178] J. J. Campbell, N. Davidenko, M. M. Caffarel, R. E. Cameron, and C. J. Watson. A multifunctional 3D co-culture system for studies of mammary tissue morphogenesis and stem cell biology. *PloS one*, 6(9), 2011.

[179] K. M. Pawelec, A. Husmann, S. M. Best, and R. E. Cameron. A design protocol for tailoring ice-templated scaffold structure. *Journal of the Royal Society Interface*, 11(92), 2014.

[180] M. Kuberka, D. Von Heimburg, H. Schoof, I. Heschel, and G. Rau. Magnification of the Pore size in Biodegradable Collagen Sponges. *The International Journal of Artificial Organs*, 25(1):67–73, jan 2002.

[181] E. N. Taylor, M. P. Hoffman, D. Y. Barefield, G. E. n. Aninwene, A. D. Abrishamchi, T. L. t. Lynch, S. Govindan, H. Osinska, J. Robbins, S. Sadayappan, and R. J. Gilbert. Alterations in Multi-Scale Cardiac Architecture in Association With Phosphorylation of Myosin Binding Protein-C. *Journal of the American Heart Association*, 5(3), mar 2016.

[182] R. R. Cooper and S. Misol. Tendon and ligament insertion. A light and electron microscopic study. *The Journal of bone and joint surgery. American volume*, 52(1):1–20, jan 1970.

[183] M. S. Conte. The ideal small arterial substitute: a search for the Holy Grail? *The FASEB Journal*, 12(1):43–45, jan 1998.

[184] E. L. W. De Mulder, P. Buma, and G. Hannink. Anisotropic porous biodegradable scaffolds for musculoskeletal tissue engineering. *Materials*, 2(4):1674–1696, 2009.

[185] T. Waschkies, R. Oberacker, and M. Hoffmann. Control of Lamellae Spacing During Freeze Casting of Ceramics Using Double-Side Cooling as a Novel Processing Route. *Journal of the American Ceramic Society*, 92:79–84, jan 2009.

[186] S. Deville. The lure of ice-templating: Recent trends and opportunities for porous materials. *Scripta Materialia*, 147:119–124, 2018.

[187] S. Deville, E. Saiz, R. K. Nalla, and A. P. Tomsia. Freezing as a path to build complex composites. *Science*, 311(5760):515–518, 2006.

[188] E. Munch, E. Saiz, A. P. Tomsia, and S. Deville. Architectural Control of Freeze-Cast Ceramics Through Additives and Templating. *Journal of the American Ceramic Society*, 92(7):1534–1539, 2009.

[189] A. Myerson. *Handbook of industrial crystallization*. Butterworth-Heinemann, 2 edition, 2002.

[190] M. Matsumoto, S. Saito, and I. Ohmine. Molecular dynamics simulation of the ice nucleation and growth process leading to water freezing. *Nature*, 416(6879):409–413, 2002.

[191] Y. Shirai, T. Sugimoto, M. Hashimoto, K. Nakanishi, and R. Matsuno. Mechanism of Ice Growth in a Batch Crystalljzer with an External Cooler for Freeze Concentration. *Agricultural and Biological Chemistry*, 51(9):2359–2366, 1987.

[192] K. M. R. Nuss, J. A. Auer, A. Boos, and B. Von Rechenberg. An animal model in sheep for biocompatibility testing of biomaterials in cancellous bones. *BMC musculoskeletal disorders*, 7(1):67, 2006.

[193] A. Husmann, K. Pawelec, C. Burdett, S. Best, and R. Cameron. Numerical simulations to determine the influence of mould design on ice-templated scaffold structures. *Journal of Biomedical Engineering and Informatics*, 1(1):47, 2015.

[194] J. A. Sekhar and R. Trivedi. Solidification microstructure evolution in the presence of inert particles. *Materials Science and Engineering: A*, 147(1):9–21, 1991.

[195] H. Esaka and W. Kurz. Columnar dendrite growth: experiments on tip growth. *Journal of crystal growth*, 72(3):578–584, 1985.

[196] L. Hadji. Morphological instability induced by the interaction of a particle with a solid-liquid interface. *The European Physical Journal B-Condensed Matter and Complex Systems*, 37(1):85–89, 2004.

[197] R. Asthana and S. N. Tewari. The engulfment of foreign particles by a freezing interface. *Journal of materials science*, 28(20):5414–5425, 1993.

[198] H. Schoof, L. Bruns, A. Fischer, I. Heschel, and G. Rau. Dendritic ice morphology in unidirectionally solidified collagen suspensions. *Journal of Crystal Growth*, 209(1):122–129, 2000.

[199] P. Divakar, K. Yin, and U. G. K. Wegst. Anisotropic freeze-cast collagen scaffolds for tissue regeneration: How processing conditions affect structure and properties in the dry and fully hydrated states. *Journal of the mechanical behavior of biomedical materials*, 90:350–364, feb 2019.

[200] V. Ayel, O. Lottin, M. Faucheux, D. Sallier, and H. Peerhossaini. Crystallisation of undercooled aqueous solutions: Experimental study of free dendritic growth in cylindrical geometry. *International journal of heat and mass transfer*, 49(11-12):1876–1884, 2006.

[201] J. Hallett. Experimental studies of the crystallization of supercooled water. *Journal of the Atmospheric Sciences*, 21(6):671–682, 1964.

[202] M. Müller-Stoffels, P. J. Langhorne, C. Petrich, and E. W. Kempema. Preferred crystal orientation in fresh water ice. *Cold Regions Science and Technology*, 56(1):1–9, 2009.

[203] S. Deville, E. Maire, A. Lasalle, A. Bogner, C. Gauthier, J. Leloup, and C. Guizard. In Situ X-Ray Radiography and Tomography Observations of the Solidification of Aqueous Alumina Particle Suspensions—Part I: Initial Instants. *Journal of the American Ceramic Society*, 92(11):2489–2496, 2009.

[204] H. Nakae and S. Wu. Behavior of ceramic particles at solid/liquid interface during solidification of metal matrix composites. *Key Engineering Materials*, 127-131:503–510, 1996.

[205] W. W. Mullins and R. F. Sekerka. Stability of a Planar Interface During Solidification of a Dilute Binary Alloy. *Journal of Applied Physics*, 35(2):444–451, feb 1964.

[206] R. Petrenko, V Whitworth. *Physics of ice*. aug 1999.

[207] S. Deville, E. Saiz, and A. P. Tomsia. Freeze casting of hydroxyapatite scaffolds for bone tissue engineering. *Biomaterials*, 27(32):5480–5489, 2006.

[208] H. Zhang, I. Hussain, M. Brust, M. F. Butler, S. P. Rannard, and A. I. Cooper. Aligned two-and three-dimensional structures by directional freezing of polymers and nanoparticles. *Nature materials*, 4(10):787–793, 2005.

[209] Y. Chino and D. C. Dunand. Directionally freeze-cast titanium foam with aligned, elongated pores. *Acta Materialia*, 56(1):105–113, 2008.

[210] N. O. Shanti, K. Araki, and J. W. Halloran. Particle redistribution during dendritic solidification of particle suspensions. *Journal of the American Ceramic Society*, 89(8):2444–2447, 2006.

[211] N. Davidenko, T. Gibb, C. Schuster, S. M. Best, J. J. Campbell, C. J. Watson, and R. E. Cameron. Biomimetic collagen scaffolds with anisotropic pore architecture. *Acta biomaterialia*, 8(2):667–676, 2012.

[212] M. W. Pot, K. A. Faraj, A. Adawy, W. J. Van Enckevort, H. T. Van Moerkerk, E. Vlieg, W. F. Daamen, and T. H. Van Kuppevelt. Versatile wedge-based system for the construction of unidirectional collagen scaffolds by directional freezing: Practical and theoretical considerations. *ACS Applied Materials and Interfaces*, 7(16):8495–8505, 2015.

[213] J. J. Campbell, A. Husmann, R. D. Hume, C. J. Watson, and R. E. Cameron. Development of three-dimensional collagen scaffolds with controlled architecture for cell migration studies using breast cancer cell lines. *Biomaterials*, 114:34–43, 2017.

[214] P. Pronk, C. A. I. Ferreira, and G. J. Witkamp. A dynamic model of Ostwald ripening in ice suspensions. *Journal of Crystal Growth*, 275(1-2):1355–1361, 2005.

[215] L. Rey and J. May. *Freeze-drying/lyophilization of pharmaceutical and biological products*. informa healthcare, New York City, 3 edition, 2016.

[216] K. M. Pawelec, A. Husmann, S. M. Best, and R. E. Cameron. Understanding anisotropy and architecture in ice-templated biopolymer scaffolds. *Materials Science and Engineering: C*, 37:141–147, 2014.

[217] N.-Y. Yuan, Y.-A. Lin, M.-H. Ho, D.-M. Wang, J.-Y. Lai, and H.-J. Hsieh. Effects of the cooling mode on the structure and strength of porous scaffolds made of chitosan, alginate, and carboxymethyl cellulose by the freeze-gelation method. *Carbohydrate Polymers*, 78(2):349–356, 2009.

[218] Q. Fu, M. N. Rahaman, F. Dogan, and B. S. Bal. Freeze-cast hydroxyapatite scaffolds for bone tissue engineering applications. *Biomedical Materials*, 3(2), 2008.

[219] S. Deville, J. Adrien, E. Maire, M. Scheel, and M. Di Michiel. Time-lapse, three-dimensional in situ imaging of ice crystal growth in a colloidal silica suspension. *Acta Materialia*, 61(6):2077–2086, 2013.

[220] F. J. O'Brien, B. A. Harley, I. V. Yannas, and L. Gibson. Influence of freezing rate on pore structure in freeze-dried collagen-GAG scaffolds. *Biomaterials*, 25(6):1077–1086, 2004.

[221] K. M. Pawelec, A. Husmann, S. M. Best, and R. E. Cameron. Altering crystal growth and annealing in ice-templated scaffolds. *Journal of materials science*, 50(23):7537–7543, 2015.

[222] S.-L. Chen and T.-S. Lee. A study of supercooling phenomenon and freezing probability of water inside horizontal cylinders. *International Journal of Heat and Mass Transfer*, 41(4-5):769–783, 1998.

[223] J. A. Searles, J. F. Carpenter, and T. W. Randolph. The ice nucleation temperature determines the primary drying rate of lyophilization for samples frozen on a temperature-controlled shelf. *Journal of pharmaceutical sciences*, 90(7):860–871, 2001.

[224] L. R. Maki, E. L. Galyan, M. M. Chang-Chien, and D. R. Caldwell. Ice nucleation induced by pseudomonas syringae. *Applied microbiology*, 28(3):456–459, sep 1974.

[225] M. A. Meyers, P.-Y. Chen, A. Y.-M. Lin, and Y. Seki. Biological materials: structure and mechanical properties. *Progress in Materials Science*, 53(1):1–206, 2008.

[226] S. Deville, C. Viazzi, J. Leloup, A. Lasalle, C. Guizard, E. Maire, J. Adrien, and L. Gremillard. Ice shaping properties, similar to that of antifreeze proteins, of a zirconium acetate complex. *PloS one*, 6(10), 2011.

[227] M. A. White, J. Conrad, S. N. Ellis, and R. Chen. Investigations of ice-structuring agents in ice-templated ceramics. *Journal of the American Ceramic Society*, 100(11):5066–5074, nov 2017.

[228] S. Deville, C. Viazzi, and C. Guizard. Ice-structuring mechanism for zirconium acetate. *Langmuir*, 28(42):14892–14898, 2012.

[229] T. Chen, A. Fowler, and M. Toner. Literature review: supplemented phase diagram of the trehalose–water binary mixture. *Cryobiology*, 40(3):277–282, 2000.

[230] Y. Roos and M. Karel. Amorphous state and delayed ice formation in sucrose solutions. *International journal of food science & technology*, 26(6):553–566, 1991.

[231] J. A. Lewis. Colloidal processing of ceramics. *Journal of the American Ceramic Society*, 83(10):2341–2359, 2000.

[232] I. Nelson, J. Varga, P. Wadsworth, M. Mroz, J. J. Kruzic, O. T. Kingstedt, and S. E. Naleway. Helical and Bouligand Porous Scaffolds Fabricated by Dynamic Low Strength Magnetic Field Freeze Casting. *Journal of the Minerals Metals and Materials Society*, 72(4):1498–1508, 2020.

[233] Y. F. Tang, K. Zhao, J. Q. Wei, and Y. S. Qin. Fabrication of aligned lamellar porous alumina using directional solidification of aqueous slurries with an applied electrostatic field. *Journal of the European Ceramic Society*, 30(9):1963–1965, 2010.

[234] T. A. Ogden, M. Prisbrey, I. Nelson, B. Raeymaekers, and S. E. Naleway. Ultrasound freeze casting: Fabricating bioinspired porous scaffolds through combining freeze casting and ultrasound directed self-assembly. *Materials & Design*, 164:107561, 2019.

[235] G. Shao, D. A. Hanaor, X. Shen, and A. Gurlo. Freeze Casting: From Low-Dimensional Building Blocks to Aligned Porous Structures—A Review of Novel Materials, Methods, and Applications. *Advanced Materials*, 32(17), 2020.

[236] Y. Zhang, L. Hu, and J. Han. Preparation of a Dense/Porous BiLayered Ceramic by Applying an Electric Field During Freeze Casting. *Journal of the American Ceramic Society*, 92(8):1874–1876, aug 2009.

[237] R. Yu, Y. Shi, D. Yang, Y. Liu, J. Qu, and Z.-Z. Yu. Graphene oxide/chitosan aerogel microspheres with honeycomb-cobweb and radially oriented microchannel structures for broad-spectrum and rapid adsorption of water contaminants. *ACS applied materials & interfaces*, 9(26):21809–21819, 2017.

[238] S. Barg, F. M. Perez, N. Ni, P. do Vale Pereira, R. C. Maher, E. Garcia-Tunon, S. Eslava, S. Agnoli, C. Mattevi, and E. Saiz. Mesoscale assembly of chemically modified graphene into complex cellular networks. *Nature communications*, 5, 2014.

[239] S. Wu, L. Li, H. Xue, K. Liu, Q. Fan, G. Bai, and J. Wang. Size controllable, transparent, and flexible 2D silver meshes using recrystallized ice crystals as templates. *ACS nano*, 11(10):9898–9905, 2017.

[240] S. Liao, T. Zhai, and H. Xia. Highly adsorptive graphene aerogel microspheres with center-diverging microchannel structures. *Journal of Materials Chemistry A*, 4(3):1068–1077, 2016.

[241] Y. Cui, H. Gong, Y. Wang, D. Li, and H. Bai. A thermally insulating textile inspired by polar bear hair. *Advanced Materials*, 30(14):1706807, 2018.

[242] A. A. Firsov, A. D. Nazarov, and I. P. Fomina. Biodegradable Implants Containing Gentamicin: Drug Release and Pharmacokinetics. *Drug Development and Industrial Pharmacy*, 13(9-11):1651–1674, jan 1987.

[243] L. M. Mullen, S. M. Best, R. A. Brooks, S. Ghose, J. H. Gwynne, J. Wardale, N. Rushton, and R. E. Cameron. Binding and release characteristics of insulin-like growth factor-1 from a collagen-glycosaminoglycan scaffold. *Tissue engineering. Part C, Methods*, 16(6):1439–1448, 2010.

[244] R. A. Hortensius and B. A. C. Harley. The use of bioinspired alterations in the glycosaminoglycan content of collagen–GAG scaffolds to regulate cell activity. *Biomaterials*, 34(31):7645–7652, 2013.

[245] D. J. Choi, S. M. Choi, H. Y. Kang, H.-J. Min, R. Lee, M. Ikram, F. Subhan, S. W. Jin, Y. H. Jeong, J.-Y. Kwak, and S. Yoon. Bioactive fish collagen/polycaprolactone composite nanofibrous scaffolds fabricated by electrospinning for 3D cell culture. *Journal of biotechnology*, 205:47–58, jul 2015.

[246] D. V. Bax, N. Davidenko, D. Gullberg, S. W. Hamaia, R. W. Farndale, S. M. Best, and R. E. Cameron. Fundamental insight into the effect of carbodiimide crosslinking on cellular recognition of collagen-based scaffolds. *Acta Biomaterialia*, 49:218–234, 2016.

[247] S. Battista, D. Guarnieri, C. Borselli, S. Zeppetelli, A. Borzacchiello, L. Mayol, D. Gerbasio, D. R. Keene, L. Ambrosio, and P. A. Netti. The effect of matrix composition of 3D constructs on embryonic stem cell differentiation. *Biomaterials*, 26(31):6194–6207, 2005.

[248] F. Yang, S.-W. Cho, S. M. Son, S. P. Hudson, S. Bogatyrev, L. Keung, D. S. Kohane, R. Langer, and D. G. Anderson. Combinatorial extracellular matrices for human embryonic stem cell differentiation in 3D. *Biomacromolecules*, 11(8):1909–1914, 2010.

[249] N. Davidenko, C. F. Schuster, D. V. Bax, N. Raynal, R. W. Farndale, S. M. Best, and R. E. Cameron. Control of crosslinking for tailoring collagen-based scaffolds stability and mechanics. *Acta biomaterialia*, 25:131–142, 2015.

[250] A. J. Engler, S. Sen, H. L. Sweeney, and D. E. Discher. Matrix Elasticity Directs Stem Cell Lineage Specification. *Cell*, 126(4):677–689, 2006.

[251] T. Yeung, P. C. Georges, L. A. Flanagan, B. Marg, M. Ortiz, M. Funaki, N. Zahir, W. Ming, V. Weaver, and P. A. Janmey. Effects of substrate stiffness on cell morphology, cytoskeletal structure, and adhesion. *Cell Motility*, 60(1):24–34, jan 2005.

[252] R. Pelham and Y. Wang. Cell locomotion and focal adhesions are regulated by substrate flexibility. *Proceedings of the National Academy of Science*, 94(25):13661–13665, 1997.

[253] T. L. Jenkins and D. Little. Synthetic scaffolds for musculoskeletal tissue engineering: cellular responses to fiber parameters. *Nature Partner Journal Regenerative Medicine*, 4(1), 2019.

[254] C. F. Guimarães, L. Gasperini, A. P. Marques, and R. L. Reis. The stiffness of living tissues and its implications for tissue engineering. *Nature Reviews Materials*, 5:351–370, 2020.

[255] J. Shepherd, D. Bax, S. Best, and R. Cameron. Collagen-fibrinogen lyophilised scaffolds for soft tissue regeneration. *Materials*, 10(6), 2017.

[256] J. Blumm and A. Lindemann. Characterization of the thermophysical properties of molten polymers and liquids using the flash technique. *High Temperature High Pressure*, 35(36):627–632, 2003.

[257] L. H. H. Olde Damink, P. J. Dijkstra, M. J. A. van Luyn, P. B. van Wachem, P. Nieuwenhuis, and J. Feijen. Cross-linking of dermal sheep collagen using a water-soluble carbodiimide. *Biomaterials*, 17(8):765–773, 1996.

[258] C. E. Ayres, B. S. Jha, H. Meredith, J. R. Bowman, G. L. Bowlin, S. C. Henderson, and D. G. Simpson. Measuring fiber alignment in electrospun scaffolds: a user's guide to the 2D fast Fourier transform approach. *Journal of biomaterials science. Polymer edition*, 19(5):603–621, 2008.

[259] I. V. Yannas, E. Lee, D. P. Orgill, E. M. Skrabut, and G. F. Murphy. Synthesis and characterization of a model extracellular matrix that induces partial regeneration of adult mammalian skin. *Proceedings of the National Academy of Sciences*, 86(3):933–937, 1989.

[260] F. J. O'Brien, B. A. Harley, I. V. Yannas, and L. J. Gibson. The effect of pore size on cell adhesion in collagen-GAG scaffolds. *Biomaterials*, 26(4):433–441, 2005.

[261] P. Zhao, H. Gu, H. Mi, C. Rao, J. Fu, and L. sheng Turng. Fabrication of scaffolds in tissue engineering: A review. *Frontiers of Mechanical Engineering*, 13(1):107–119, 2018.

[262] D. Odedra, L. Chiu, L. Reis, F. Rask, K. Chiang, and M. Radisic. Cardiac tissue engineering. In *Biomaterials for Tissue Engineering Applications*, pages 421–456. Springer, 2011.

[263] L. J. Chamberlain, I. V. Yannas, A. Arrizabalaga, H.-P. Hsu, T. V. Norregaard, and M. Spector. Early peripheral nerve healing in collagen and silicone tube implants: myofibroblasts and the cellular response. *Biomaterials*, 19(15):1393–1403, 1998.

[264] M. Ezra, J. Bushman, D. Shreiber, M. Schachner, and J. Kohn. Porous and Nonporous Nerve Conduits: The Effects of a Hydrogel Luminal Filler With and Without a Neurite-Promoting Moiety. *Tissue engineering. Part A*, 22(9-10):818–826, may 2016.

[265] S. J. Hollister. Porous scaffold design for tissue engineering. *Nature materials*, 4(7):518–524, 2005.

[266] R. Scaffaro, F. Lopresti, A. Maio, F. Sutera, and L. Botta. Development of polymeric functionally graded scaffolds: a brief review. *Journal of applied biomaterials & functional materials*, 15(2):107–121, 2017.

[267] A. Yousefi, M. E. Hoque, R. G. S. V. Prasad, and N. Uth. Current strategies in multiphasic scaffold design for osteochondral tissue engineering: a review. *Journal of biomedical materials research Part A*, 103(7):2460–2481, 2015.

[268] M. E. Davis, J. P. M. Motion, D. A. Narmoneva, T. Takahashi, D. Hakuno, R. D. Kamm, S. Zhang, and R. T. Lee. Injectable self-assembling peptide nanofibers create intramyocardial microenvironments for endothelial cells. *Circulation*, 111(4):442–450, 2005.

[269] A. Preiss, B. Su, S. Collins, and D. Simpson. Tailored graded pore structure in zirconia toughened alumina ceramics using double-side cooling freeze casting. *Journal of the European Ceramic Society*, 32(8):1575–1583, 2012.

[270] J. W. Valvano, J. R. Cochran, and K. R. Diller. Thermal conductivity and diffusivity of biomaterials measured with self-heated thermistors. *International Journal of Thermophysics*, 6(3):301–311, 1985.

[271] Q. L. Loh and C. Choong. Three-dimensional scaffolds for tissue engineering applications: role of porosity and pore size. *Tissue Engineering Part B: Reviews*, 19(6):485–502, 2013.

[272] B. Dhandayuthapani, Y. Yoshida, T. Maekawa, and D. S. Kumar. Polymeric scaffolds in tissue engineering application: a review. *International journal of polymer science*, 2011.

[273] C. Bayram, X. Jiang, M. Gultekinoglu, S. Ozturk, K. Ulubayram, and M. Edirisinghe. Biofabrication of Gelatin Tissue Scaffolds with Uniform Pore Size via Microbubble Assembly. *Macromolecular Materials and Engineering*, 304(11), nov 2019.

[274] S. Barg, D. Koch, and G. Grathwohl. Processing and properties of graded ceramic filters. *Journal of the American Ceramic Society*, 92(12):2854–2860, 2009.

[275] G. Ju, K. Reifsnider, and J.-H. Kim. Cathode Thermal Delamination Study for a Planar Solid Oxide Fuel Cell with Functional Graded Properties: Experimental Investigation and Numerical Results. In N. P. B. A. W. E. Lara-Curzio, editor, *Advances in Solid Oxide Fuel Cells II: Ceramic Engineering and Science Proceedings*, Ceramic Engineering and Science Proceedings, pages 161–173. jan 2006.

[276] G. H. Paulino, E. C. N. Silva, and C. H. Le. Optimal design of periodic functionally graded composites with prescribed properties. *Structural and Multidisciplinary Optimization*, 38(5):469–489, 2009.

[277] X. Miao and D. Sun. Graded/Gradient Porous Biomaterials. *Materials*, 3(1):26–47, dec 2009.

[278] D. Yang, Z. Zhao, F. Bai, S. Wang, A. P. Tomsia, and H. Bai. Promoting Cell Migration in Tissue Engineering Scaffolds with Graded Channels. *Advanced Healthcare Materials*, 6(18), sep 2017.

[279] K. F. Leong, C. K. Chua, N. Sudarmadji, and W. Y. Yeong. Engineering functionally graded tissue engineering scaffolds. *Journal of the Mechanical Behavior of Biomedical Materials*, 1(2):140–152, 2008.

[280] T. B. F. Woodfield, C. A. V. Blitterswijk, J. D. Wijn, T. J. Sims, A. P. Hollander, and J. Riesle. Polymer scaffolds fabricated with pore-size gradients as a model for studying the zonal organization within tissue-engineered cartilage constructs. *Tissue engineering*, 11(9-10):1297–1311, 2005.

[281] A. G. Mikos, S. W. Herring, P. Ochareon, J. Elisseeff, H. H. Lu, R. Kandel, F. J. Schoen, M. Toner, D. Mooney, A. Atala, M. E. Van Dyke, D. Kaplan, and G. Vunjak-Novakovic. Engineering complex tissues. *Tissue engineering*, 12(12):3307–3339, dec 2006.

[282] S. Mitragotri and J. Lahann. Physical approaches to biomaterial design. *Nature Materials*, 8(1):15–23, 2009.

[283] B. K. Connizzo, S. M. Yannascoli, and L. J. Soslowsky. Structure-function relationships of postnatal tendon development: a parallel to healing. *Matrix biology : journal of the International Society for Matrix Biology*, 32(2):106–116, mar 2013.

[284] M. J. W. Koens, K. A. Faraj, R. G. Wismans, J. A. der Vliet, A. G. Krasznai, V. Cuijpers, J. A. Jansen, W. F. Daamen, and T. H. Van Kuppevelt. Controlled fabrication of triple layered and molecularly defined collagen/elastin vascular grafts resembling the native blood vessel. *Acta biomaterialia*, 6(12):4666–4674, 2010.

[285] E. L. De Mulder, G. Hannink, T. H. Van Kuppevelt, W. F. Daamen, and P. Buma. Similar hyaline-like cartilage repair of osteochondral defects in rabbits using isotropic and anisotropic collagen scaffolds. *Tissue Engineering - Part A*, 20(3-4):635–645, 2014.

[286] C. M. Agrawal and R. B. Ray. Biodegradable polymeric scaffolds for musculoskeletal tissue engineering. *Journal of Biomedical Materials Research*, 55(2):141–150, may 2001.

[287] B. A. Aguado, J. C. Grim, A. M. Rosales, J. J. Watson-Capps, and K. S. Anseth. Engineering precision biomaterials for personalized medicine. *Science Translational Medicine*, 10(424), 2018.

[288] R. L. Creighton, J. Phan, and K. A. Woodrow. In situs 3D-patterning of electrospun fibers using two-layer composite materials. *Scientific Reports*, 10(1):1–14, 2020.

[289] L. Fan, J. L. Li, Z. Cai, and X. Wang. Creating Biomimetic Anisotropic Architectures with Co-Aligned Nanofibers and Macrochannels by Manipulating Ice Crystallization. *ACS Nano*, 12(6):5780–5790, 2018.

[290] T. Bhattacharjee, S. M. Zehnder, K. G. Rowe, S. Jain, R. M. Nixon, W. G. Sawyer, and T. E. Angelini. Writing in the granular gel medium. *Science Advances*, 1(8), sep 2015.

[291] T. J. Hinton, Q. Jallerat, R. N. Palchesko, J. H. Park, M. S. Grodzicki, H.-J. Shue, M. H. Ramadan, A. R. Hudson, and A. W. Feinberg. Three-dimensional printing of complex biological structures by freeform reversible embedding of suspended hydrogels. *Science Advances*, 1(9), oct 2015.

[292] H. Bai, Y. Chen, B. Delattre, A. P. Tomsia, and R. O. Ritchie. Bioinspired large-scale aligned porous materials assembled with dual temperature gradients. *Science Advances*, 1(11):1–9, 2015.

[293] S. S. Peppin, J. A. Elliott, and M. G. Worster. Solidification of colloidal suspensions. *Journal of Fluid Mechanics*, 554:147–166, 2006.

[294] T.-H. Huang, T.-H. Huang, Y.-S. Lin, C.-H. Chang, P.-Y. Chen, S.-W. Chang, and C.-S. Chen. Phase-Field Modeling of Microstructural Evolution by Freeze-Casting. *Advanced Engineering Materials*, 20(3):456, mar 2018.

[295] C. Yang, X. Zhu, X. Wang, J. Wang, and H. Huang. Phase-field model of graphene aerogel formation by ice template method. *Applied Physics Letters*, 115(11), sep 2019.

[296] S. A. Barr and E. Luijten. Structural properties of materials created through freeze casting. *Acta Materialia*, 58(2):709–715, 2010.

[297] V. Naglieri, H. A. Bale, B. Gludovatz, A. P. Tomsia, and R. O. Ritchie. On the development of ice-templated silicon carbide scaffolds for nature-inspired structural materials. *Acta Materialia*, 61(18):6948–6957, 2013.

[298] B. Platzer. Adrian Bejan: Convection Heat Transfer. John Wiley & Sons, Hoboken, New Jersey, 4th ed., 2013. *ZAMM - Journal of Applied Mathematics and Mechanics / Zeitschrift für Angewandte Mathematik und Mechanik*, 94(9), sep 2014.

[299] Q. T. Pham. Modelling heat and mass transfer in frozen foods: a review. *International Journal of Refrigeration*, 29(6):876–888, 2006.

[300] T. Barz, J. Emhofer, K. Marx, G. Zsembinszki, and L. F. Cabeza. Phenomenological modelling of phase transitions with hysteresis in solid/liquid PCM. *Journal of Building Performance Simulation*, 12(6):770–788, 2019.

[301] Z. Ma, N. Huebsch, S. Koo, M. A. Mandegar, B. Siemons, S. Boggess, B. R. Conklin, C. P. Grigoropoulos, and K. E. Healy. Contractile deficits in engineered cardiac microtissues as a result of MYBPC3 deficiency and mechanical overload. *Nature Biomedical Engineering*, 2(12):955–967, 2018.

[302] E. Tzatzalos, O. J. Abilez, P. Shukla, and J. C. Wu. Engineered heart tissues and induced pluripotent stem cells: macro-and microstructures for disease modeling, drug screening, and translational studies. *Advanced drug delivery reviews*, 96:234–244, 2016.

[303] N. T. Feric and M. Radisic. Maturing human pluripotent stem cell-derived cardiomyocytes in human engineered cardiac tissues. *Advanced drug delivery reviews*, 96:110–134, 2016.

[304] A. Eder, I. Vollert, A. Hansen, and T. Eschenhagen. Human engineered heart tissue as a model system for drug testing. *Advanced drug delivery reviews*, 96:214–224, 2016.

[305] B. M. Ogle, N. Bursac, I. Domian, N. F. Huang, P. Menasché, C. E. Murry, B. Pruitt, M. Radisic, J. C. Wu, and S. M. Wu. Distilling complexity to advance cardiac tissue engineering. *Science translational medicine*, 8(342):342ps13–342ps13, 2016.

[306] D. Iyer, L. Gambardella, W. G. Bernard, F. Serrano, V. L. Mascetti, R. A. Pedersen, A. Talasila, and S. Sinha. Robust derivation of epicardium and its differentiated smooth muscle cell progeny from human pluripotent stem cells. *Development*, 142(8):1528–1541, 2015.

[307] S. Mendjan, V. L. Mascetti, D. Ortmann, M. Ortiz, D. W. Karjosukarso, Y. Ng, T. Moreau, and R. A. Pedersen. NANOG and CDX2 pattern distinct subtypes of human mesoderm during exit from pluripotency. *Cell stem cell*, 15(3):310–325, 2014.

[308] A. M. Fenix, A. C. Neininger, N. Taneja, K. Hyde, M. R. Visetsouk, R. J. Garde, B. Liu, B. R. Nixon, A. E. Manalo, J. R. Becker, S. W. Crawley, D. M. Bader, M. J. Tyska, Q. Liu, J. H. Gutzman, and D. T. Burnette. Muscle-specific stress fibers give rise to sarcomeres in cardiomyocytes. *eLife*, 7:1–33, 2018.

[309] B. Angst, L. Khan, N. Severs, K. Whitely, S. Rothery, R. Thompson, A. Magee, and R. Gourdie. Dissociated Spatial Patterning of Gap Junctions and Cell Adhesion Junctions During Postnatal Differentiation of Ventricular Myocardium. *Circulation Research*, 80(1):88–94, jan 1997.

[310] J. Bargehr, L. P. Ong, M. Colzani, H. Davaapil, P. Hofsteen, S. Bhandari, L. Gambardella, N. Le Novère, D. Iyer, F. Sampaziotis, F. Weinberger, A. Bertero, A. Leonard, W. G. Bernard, A. Martinson, N. Figg, M. Regnier, M. R. Bennett, C. E. Murry, and S. Sinha. Epicardial cells derived from human embryonic stem cells augment cardiomyocyte-driven heart regeneration. *Nature Biotechnology*, 37(8):895–906, 2019.

[311] P. P. Sengupta, J. Korinek, M. Belohlavek, J. Narula, M. A. Vannan, A. Jahangir, and B. K. Khandheria. Left ventricular structure and function: basic science for cardiac imaging. *Journal of the American College of Cardiology*, 48(10):1988–2001, 2006.

[312] Z. Y. Lim, B. Maskara, F. Aguel, R. Emokpae, and L. Tung. Spiral wave attachment to millimeter-sized obstacles. *Circulation*, 114(20):2113–2121, 2006.

[313] W. R. Legant, A. Pathak, M. T. Yang, V. S. Deshpande, R. M. McMeeking, and C. S. Chen. Microfabricated tissue gauges to measure and manipulate forces from 3D microtissues. *Proceedings of the National Academy of Sciences*, 106(25):10097–10102, 2009.

[314] J. A. Thomson, J. Itskovitz-Eldor, S. S. Shapiro, M. A. Waknitz, J. J. Swiergiel, V. S. Marshall, and J. M. Jones. Embryonic stem cell lines derived from human blastocysts. *science*, 282(5391):1145–1147, 1998.

[315] K. Takahashi and S. Yamanaka. Induction of pluripotent stem cells from mouse embryonic and adult fibroblast cultures by defined factors. *cell*, 126(4):663–676, 2006.

[316] A. Guhr, S. Kobold, S. Seltmann, A. E. M. Seiler Wulczyn, A. Kurtz, and P. Löser. Recent Trends in Research with Human Pluripotent Stem Cells: Impact of Research and Use of Cell Lines in Experimental Research and Clinical Trials. *Stem cell reports*, 11(2):485–496, aug 2018.

[317] C. Eguizabal, B. Aran, S. M. Chuva de Sousa Lopes, M. Geens, B. Heindryckx, S. Panula, M. Popovic, R. Vassena, and A. Veiga. Two decades of embryonic stem cells: a historical overview. *Human Reproduction Open*, 2019(1), jan 2019.

[318] B. H. Bijnens, M. Cikes, P. Claus, and G. R. Sutherland. Velocity and deformation imaging for the assessment of myocardial dysfunction. *European Journal of Echocardiography*, 10(2):216–226, 2009.

[319] B. Bijnens, M. Cikes, C. Butakoff, M. Sitges, and F. Crispi. Myocardial motion and deformation: What does it tell us and how does it relate to function? *Fetal Diagnosis and Therapy*, 32(1-2):5–16, 2012.

[320] A. M. Leopaldi, K. Wrobel, G. Speziali, S. van Tuijl, A. Drasutiene, and W. R. Chitwood Jr. The dynamic cardiac biosimulator: a method for training physicians in beating-heart mitral valve repair procedures. *The Journal of thoracic and cardiovascular surgery*, 155(1):147–155, 2018.

[321] P. Ferraiuoli, B. Kappler, S. van Tuijl, M. Stijnen, B. A. de Mol, J. W. Fenner, and A. J. Narracott. Full-field analysis of epicardial strain in an in vitro porcine heart platform. *Journal of the Mechanical Behavior of Biomedical Materials*, 91:294–300, 2019.

[322] O. A. Mownah, M. A. Khurram, C. Ray, A. Kanwar, S. Stamp, D. Rees, J. Brassil, J. Majo, J. H. Dark, N. M. Carter, and D. Talbot. Development of an ex vivo technique to achieve reanimation of hearts sourced from a porcine donation after circulatory death model. *Journal of Surgical Research*, 189(2):326–334, 2014.

[323] Y. Niu, E. A. Herrera, R. D. Evans, and D. A. Giussani. Antioxidant treatment improves neonatal survival and prevents impaired cardiac function at adulthood following neonatal glucocorticoid therapy. *Journal of Physiology*, 591(20):5083–5093, 2013.

[324] J. Kobayashi, S. Luo, Y. Akazawa, M. Parker, J. Wang, D. Chiasson, M. K. Friedberg, C. Haller, and O. Honjo. Flow-targeted pediatric ex vivo heart perfusion in donation after circulatory death: A porcine model. *Journal of Heart and Lung Transplantation*, 39(3):267–277, 2020.

[325] R. S. Stephenson, P. Agger, P. P. Lunkenheimer, J. Zhao, M. Smerup, P. Niederer, R. H. Anderson, and J. C. Jarvis. The Functional Architecture of Skeletal Compared to Cardiac Musculature : Myocyte Orientation , Lamellar Unit Morphology , and the Helical Ventricular Myocardial Band. *Clinical Anatomy*, 29:316–332, 2016.

[326] N. B. Ingels Jr. Myocardial fiber architecture and left ventricular function. *Technology and Health Care*, 5(1, 2):45–52, 1997.

[327] P. P. Lunkenheimer, K. Redmann, J. Florek, U. Fassnacht, C. W. Cryer, F. Wübbeling, P. Niederer, and R. H. Anderson. The forces generated within the musculature of the left ventricular wall. *Heart*, 90(2):200–207, 2004.

[328] M. Smerup, P. Agger, E. A. Nielsen, S. Ringgaard, M. Pedersen, P. Niederer, R. H. Anderson, and P. P. Lunkenheimer. Regional and Epi-to Endocardial Differences in Transmural Angles of Left Ventricular Cardiomyocytes Measured in Ex Vivo Pig Hearts: Functional Implications. *The Anatomical Record*, 296(11):1724–1734, 2013.

[329] J. B. Pettigrew. XIV. On the arrangement of the muscular fibres in the ventricles of the vertebrate heart, with physiological remarks. *Philosophical Transactions of the Royal Society of London*, (154):445–500, 1864.

[330] R. H. Anderson, Y. H. Siew, K. Redmann, D. Sanchez-Quintana, and P. P. Lunkenheimer. The anatomical arrangement of the myocardial cells making up the ventricular mass. *European Journal of Cardio-thoracic Surgery*, 28(4):517–525, 2005.

[331] F. T. Guasp. *The cardiac muscle*. Editorial Gráficas Torroba, 1973.

[332] D. D. Streeter Jr and D. L. Bassett. An engineering analysis of myocardial fiber orientation in pig's left ventricle in systole. *The Anatomical Record*, 155(4):503–511, 1966.

[333] D. D. Streeter Jr, R. N. Vaishnav, D. J. Patel, H. M. Spotnitz, J. Ross Jr, and E. H. Sonnenblick. Stress distribution in the canine left ventricle during diastole and systole. *Biophysical Journal*, 10(4):345–363, 1970.

[334] R. A. Greenbaum, S. Y. Ho, D. G. Gibson, A. E. Becker, and R. H. Anderson. Left ventricular fibre architecture in man. *Heart*, 45(3):248–263, 1981.

[335] A. T. Trott. Cyanoacrylate Tissue Adhesives: An Advance in Wound Care. *JAMA*, 277(19):1559–1560, may 1997.

[336] N. Annabi, Y. N. Zhang, A. Assmann, E. S. Sani, G. Cheng, A. D. Lassaletta, A. Vegh, B. Dehghani, G. U. Ruiz-Esparza, X. Wang, S. Gangadharan, A. S. Weiss, and A. Khademhosseini. Engineering a highly elastic human protein-based sealant for surgical applications. *Science Translational Medicine*, 9(410), 2017.

[337] H. Azhari, J. L. Weiss, W. J. Rogers, C. O. Siu, E. A. Zerhouni, and E. P. Shapiro. Noninvasive quantification of principal strains in normal canine hearts using tagged MRI images in 3-D. *American Journal of Physiology-Heart and Circulatory Physiology*, 264(1):205–216, 1993.

[338] A. D. McCulloch, B. H. Smaill, and P. J. Hunter. Regional left ventricular epicardial deformation in the passive dog heart. *Circulation research*, 64(4):721–733, 1989.

[339] L. K. Waldman, Y. C. Fung, and J. W. Covell. Transmural myocardial deformation in the canine left ventricle. Normal in vivo three-dimensional finite strains. *Circulation research*, 57(1):152–163, 1985.

[340] H. Zhang, K. Iijima, J. Huang, G. P. Walcott, and J. M. Rogers. Optical mapping of membrane potential and epicardial deformation in beating hearts. *Biophysical journal*, 111(2):438–451, 2016.

[341] E. Brauer, E. Lippens, O. Klein, G. Nebrich, S. Schreivogel, G. Korus, G. N. Duda, and A. Petersen. Collagen Fibrils Mechanically Contribute to Tissue Contraction in an In Vitro Wound Healing Scenario. *Advanced Science*, 6(9):1801780, may 2019.

[342] N. Momtahan, N. Poornejad, J. A. Struk, A. A. Castleton, B. J. Herrod, B. R. Vance, J. P. Eatough, B. L. Roeder, P. R. Reynolds, and A. D. Cook. Automation of pressure control improves whole porcine heart decellularization. *Tissue Engineering Part C: Methods*, 21(11):1148–1161, 2015.

[343] C. F. Guimarães, L. Gasperini, A. P. Marques, and R. L. Reis. The stiffness of living tissues and its implications for tissue engineering. *Nature Reviews Materials*, 5(5):351–370, 2020.

[344] K. B. Gupta, M. B. Ratcliffe, M. A. Fallert, L. H. Edmunds Jr, and D. K. Bogen. Changes in passive mechanical stiffness of myocardial tissue with aneurysm formation. *Circulation*, 89(5):2315–2326, 1994.

[345] D. Lecompte, A. Smits, S. Bossuyt, H. Sol, J. Vantomme, D. Van Hemelrijck, and A. M. Habraken. Quality assessment of speckle patterns for digital image correlation. *Optics and lasers in Engineering*, 44(11):1132–1145, 2006.

[346] H. Schreier, J.-J. Orteu, and M. A. Sutton. *Image correlation for shape, motion and deformation measurements: Basic concepts, theory and applications*, volume 1. Springer, 2009.

[347] F. C. Campbell. *Structural composite materials*. ASM international, 2010.

[348] N. Davidenko, C. F. Schuster, D. V. Bax, R. W. Farndale, S. Hamaia, S. M. Best, and R. E. Cameron. Evaluation of cell binding to collagen and gelatin : a study of the effect of 2D and 3D architecture and surface chemistry. *Journal of Materials Science Materials in Medicine*, 27(10):148, 2016.